



HAL
open science

Thermo-hydrodynamics of an extended meniscus as unit-cell approach of pulsating heat pipe

Manoj Rao

► **To cite this version:**

Manoj Rao. Thermo-hydrodynamics of an extended meniscus as unit-cell approach of pulsating heat pipe. Thermics [physics.class-ph]. INSA de Lyon, 2015. English. NNT: 2015ISAL0080. tel-01247470

HAL Id: tel-01247470

<https://theses.hal.science/tel-01247470>

Submitted on 4 Jan 2016

HAL is a multi-disciplinary open access archive for the deposit and dissemination of scientific research documents, whether they are published or not. The documents may come from teaching and research institutions in France or abroad, or from public or private research centers.

L'archive ouverte pluridisciplinaire **HAL**, est destinée au dépôt et à la diffusion de documents scientifiques de niveau recherche, publiés ou non, émanant des établissements d'enseignement et de recherche français ou étrangers, des laboratoires publics ou privés.

Thèse

Thermo-hydrodynamics of an extended meniscus as unit-cell approach of pulsating heat pipe

Présentée devant

L'Institut National des Sciences Appliquées de Lyon

Ecole doctorale MEGA

(Mécanique, Énergétique, Génie civil, Acoustique)

Pour obtenir

Le grade de docteur

Par

Manoj RAO

Soutenance prévue le 18 Septembre 2015 devant la commission d'examen composée de:

Pr. Yves BERTIN	ENSMA, Institut Pprime , Poitiers
Pr. Lounès TADRIST	Université Aix-Marseille, IUSTI, Marseille
Pr. Sameer KHANDEKAR	IIT Kanpur, India
Dr. Vincent AYEL	ENSMA, Institut Pprime , Poitiers
Pr. Jocelyn BONJOUR	INSA de Lyon, CETHIL, Lyon
Pr. Frédéric LEFEVRE	INSA de Lyon, CETHIL, Lyon

Cette thèse a été préparée au Centre d'Énergétique et Thermique de Lyon (CETHIL UMR5008).

Abstract

This work makes an attempt to explain the self-sustained thermally-induced oscillations of a two-phase system consisting of an isolated confined liquid–vapour meniscus (a single liquid plug adjoining a vapour bubble) inside a circular capillary tube, the tube length being exposed to a net temperature gradient, thereby creating a continuous cycle of evaporation and condensation. This system represents the simplest ‘unit-cell’ version of a Pulsating Heat Pipe (PHP). The fundamental understanding of its transport behavior leading to self-sustained oscillations is vital for building the hitherto non-existent mathematical models of the complete PHP system. First, visualization of the oscillations of the unit-cell has been done under controlled thermal boundary conditions. Here, a unique and novel understanding of the system dynamics has been achieved by real-time synchronization of the internal pressure measurement with high-speed videography that was used to visualize and record the meniscus oscillations and the thin liquid film that is laid on the wall when the meniscus leaves the evaporator.

When the temperature difference increases between the heat source and the heat sink, different meniscus dynamics, with excellent repeatability, can be observed. The experimental results clearly demonstrated that evaporation of the liquid film is responsible for these patterns. The different components of evaporation and condensation processes were critically analysed. Two different modes of evaporation were observed inside the system: one at the triple-line and one at the liquid-vapour interface. Contrary to obvious interpretations, maximum pressure in the vapour bubble is achieved in the downward stroke, rather than the upward stroke. Thus, the system dynamics cannot be compared with gas-compression cycles; the presence of vapour coupled with transient phase-change processes give rise to singular transport phenomena. Such an interpretation of the meniscus motion and the resulting pressure cycles has not been considered by any of the existing mathematical models of PHPs.

By simple scaling arguments, it was demonstrated that there is a high probability of metastable states existing in the system, which essentially points towards considering non-equilibrium evaporation and condensation models for predicting the thermal transport. A simple transient analytical model of thermal transport in the liquid film

was developed which clearly explains the observed behavior. Existence of non-equilibrium conditions and their underlying effects on system dynamics need further exploration, both experimentally as well as analytically.

A numerical model was developed for the system consisting of a vapour plug and a liquid slug oscillating in a tube closed at one end and connected to a reservoir at a constant pressure at the other end. The modeling principle had been posed in previous work. Some modifications were never the less introduced in this work to take into account the peculiarities of the new experimental set-up and to improve the liquid film evaporation model in the light of the experimental results. Also a parametric study was carried out to understand the implications of the various factors on the working of such system. The results show that the classical correlations used to calculate pressure drops inside the liquid plug are relevant in the case of an oscillating flow. The results confirm that the dynamics of the film is the most important parameter of the system and has to be modeled by taking into account the nature of the liquid but also the nature of the wall. Therefore, the heat transfer equation in the wall has to be solved and coupled to the hydrodynamic behavior of the system. Considering that no comprehensive model of PHP system is available, the conclusions and directions provided in this study are important for building a broad understanding of these devices that remain a promising option to face the future need for thermal management of heat dissipating engineering systems.

Table of contents

Abstract	iii
Table of content	v
List of figures	ix
List of tables	xv
Nomenclature	xvii
Chapter 1: Introduction, Motivation and Background	1
1. Need for thermal passive management: Electronics cooling techniques	2
1.1. Two-phase passive cooling technologies	3
1.2. Heat pipe	5
2. Pulsating heat pipes (PHPs)	7
2.1. Different arrangements of PHP	9
2.2. Physical design parameters	10
2.3. Flow regimes in PHPs	12
2.4. Thermodynamics of PHPs	13
2.5. Hydrodynamics of PHPs	14
2.6. Heat transfer in a PHP	16
3. Two research approaches for understanding of PHP working	17
3.1. Studying PHPs as a complete system	17
3.2. PHP local level approach (“unit-cell” approach)	20
3.2.1. Single branch modeling	22
3.2.2. Single branch PHP experiments	24
4. Closing remarks, motivation of work and thesis chapter plan	26
References	28
Chapter 2: Literature review: Thermo-hydrodynamics of the extended meniscus related to single branch PHP	33
1. Thermo-physical parameters in a single branch PHP – The extended meniscus region	33
1.1. Capillary pressure and disjoining pressure	35
1.2. Fundamentals of extended meniscus region	36
1.2.1. Adsorbed or non-evaporating region	37
1.2.2. Intrinsic meniscus region	38
1.2.3. Thin film or transition region	39
1.3. The road ahead – The meniscus region	39
2. Hydrodynamic transport features of extended meniscus	40
2.1. Two phase flows in capillaries	41
2.2. Taylor bubble flows	42
2.3. Interfacial contact line and affecting parameters	44
2.3.1. Three-phase contact lines: Statics	44
2.3.2. Three-phase contact lines: Dynamics	50
2.3.3. Initial film thickness	56
2.3.4. Effect of interfacial contact line behaviour	59
2.3.5. Pressure drop in oscillating flows	62
3. Heat transfer characteristics of extended meniscus	63

3.1. Young-Laplace equation	64
3.2. Augmented Young-Laplace equation	65
3.3. Vaporization and condensation interfacial resistances	66
3.4. Experimental and modeling approaches for analyzing extended meniscus evaporation	72
4. Closing remarks	81
References	83
Chapter 3: Experimental setups and data processing	89
1. Experimental setup 1: Thermal dynamics of the simplest unit cell of PHP	89
1.1. Details of the experimental setup	91
1.2. Experimental procedure	96
1.3. Data processing	99
2. Experimental setup 2: Hydrodynamics of the meniscus inside the capillary (adiabatic experiments)	101
2.1. Details of the experimental setup	101
2.2. Experimental procedure	104
2.3. Data processing	105
3. Closing remarks	106
References	106
Chapter 4: Results and discussions- Single branch PHP experimentation and thin film dynamics	107
1. Experimental results of single branch PHP	107
1.1. Experimental boundary conditions	108
1.2. Meniscus oscillation with pressure variation	112
1.3. Actual vapour temperature versus the vapour saturated temperature	118
1.4. Dynamics of the liquid film	120
1.4.1. Experimental estimation of the vapour mass dynamics	120
1.4.2. Modeling of vapour mass dynamics	122
1.4.3. Comparison of model predictions with experiments	125
2. Theoretical analysis of unsteady heat transfer in the liquid thin film	131
2.1. Scaling arguments	132
2.2. Thermal response time of liquid thin film	137
2.3. Film thickness variation during phase-change	141
3. Closing remarks	146
References	148
Chapter 5: Modeling of single branch PHP	151
1. Modeling of the different components of the unit-cell system	152
1.1. Reservoir	153
1.2. Liquid slug	153
1.3. Vapour plug	156
1.4. Liquid film dynamics	157
1.5. Tube, evaporator and condenser	159
1.6. Resolution of the equations of the model	162
2. Comparison with the experimental data	163

2.1. Single phase pressure drop comparison with experiments	163
2.2. Thermal model of the evaporator	166
2.3. Liquid plug, vapor slug and liquid film dynamics	169
3. Parameter study	173
3.1. Influence of the properties of the fluid and of the tube	174
3.2. Influence of $h_{e,tl}$, $h_{e,lf}$ and h_{cond} on the dynamics of the system	177
4. Closing remarks	180
References	181
Chapter 6: Conclusion and future scope	183
1. Conclusions	183
2. Future scope	185
Appendix A	187
Appendix B	189
Appendix C	191
C.1 Experimental uncertainty analysis	191
C.2 Estimation of uncertainties	192
C.3 Calibration curves of measuring devices	194
References	194
Appendix D	195

List of figures

Number	Title	Page No.
Fig. 1.1	Range of heat transfer coefficients typically possible from various cooling technologies applied in contemporary thermal management systems (<i>Lin et al. [1.1]</i>)	03
Fig. 1.2	Heat transfer coefficient attainable with natural convection, single-phase liquid forced convection and boiling for different coolants (<i>Lasance [1.2]</i>)	04
Fig. 1.3	Typical heat pipe schematic	06
Fig. 1.4	Schematic of typical pulsating heat pipe (<i>Khandekar [1.3]</i>)	07
Fig. 1.5	Prototypes proposed by <i>Akachi et al. [1.8]</i>	08
Fig. 1.6	Different configurations of PHP, (a) Closed end (b) Closed loop (c) Closed loop with check valve (d) PHP with open ends	09
Fig. 1.7	Different flow regimes of PHP (<i>Xu et al. [1.12]</i>)	13
Fig. 1.8	Thermodynamic cycle of PHP (<i>Groll and Khandekar [1.14]</i>)	14
Fig. 1.9	Liquid slug in a PHP (<i>Khandekar et al. [1.15]</i>)	15
Fig. 1.10	Liquid slug in a PHP	16
Fig. 1.11	Schematic of a Unit cell PHP (single tube: single vapour plug – liquid slug)	21
Fig. 1.12	Lumped meniscus/wetting film model for the single-bubble PHP [<i>1.34, 1.39, 1.40</i>] and its key geometrical and physical parameters. The pressure at the right open end of the tube is imposed to the value P_{ext} by connecting the tube to a large reservoir	23
Fig. 1.13	Das et al. Setup in 2010 [<i>1.34</i>]	25
Fig. 1.14	Oscillations in the single bubble PHP (<i>Das et al. [1.34]</i>). Left: experimental measurement of the time evolution of meniscus position (x) and vapour pressure p (fig. 1.12). The meniscus position curve is cut from the bottom because the evaporator and adiabatic sections are opaque so that the meniscus is invisible there. Right: numerical modeling of the meniscus position (x) vapour pressure (p), vapour temperature (T) and film edge position (x_f)	26
Number	Title	Page No.
Fig. 2.1	Meniscus of radius R formed in a channel due to variations of surface energies of solid channel wall and liquid	35
Fig. 2.2	(a) Schematics of an extended meniscus in unit cell PHP (b) A typical comparison of capillary and disjoining pressure obtained by numerical simulation for meniscus formed by water in a	37

	micro-channel where $x=0$ is at intrinsic meniscus and increasing when move towards higher values of x (<i>Park et al. [2.4]</i>)	
Fig. 2.3	The flow patterns encountered in vertical upwards co-current flows (<i>Collier and Thome [2.18]</i>)	41
Fig. 2.4	Liquid slug in a PHP (<i>Khandekar et al. [2.19]</i>)	42
Fig. 2.5	(a) Contact angle of a fluid on solid substrate (b) The moving meniscus seen on three different length scales (<i>Khandekar et al. [2.19]</i>)	45
Fig. 2.6	(a) Contact angle hysteresis, (b) continuously varying physical and chemical in-homogeneity, and (c) sharp physical or chemical discontinuities at the surface (<i>Khandekar et al. [2.19]</i>)	53
Fig. 2.7	Variation of apparent contact angle with Ca as per Tanner's law. Inset shows experimental data by <i>Kavehpour et al. [2.29]</i>	55
Fig. 2.8	Variation of film thickness with Capillary number, as per five correlations mentioned therein	59
Fig. 2.9	Possible configurations of the plugs/ meniscus under oscillatory motion (<i>Tripathi et al. [2.44]</i>)	60
Fig. 2.10	Contact angle data superimposed on meniscus velocity, U , vs. time graph at an oscillating frequency of 0.5 Hz <i>Shekhawat et al. [2.45]</i>	61
Fig. 2.11	Nomenclature and geometry used in molecular flux derivation (<i>Carey [2.23]</i>)	68
Fig. 2.12	Modeling S^* with regards to thin-film setup (<i>Carey [2.23]</i>)	68
Fig. 2.13	(a) Experimental setup (top view) and details of capillary slot (b) Temperature distribution at the micro-region (<i>Hoffman and Stephan [2.62]</i>)	74
Fig. 2.14	(a) Schematic representation of the experimental set-up of the VCVB heat exchanger, cross-sectional view of the top-corner of the cuvette showing liquid meniscus and the adsorbed thin film region and schematic of the micro-region (b) Evaporative heat flux profile at the liquid–vapour interface of the evaporating meniscus region, The solid–liquid and liquid–vapour interface temperature profiles in the evaporating meniscus region as a function of the meniscus length and surface tension variation with the evaporating meniscus region (<i>Panchamgam et al. [2.63]</i>)	75
Fig. 2.15	(a) Experimental setup schematics (b) Infrared temperature maps of T_{top} and T_{bottom} at a heat flux of 1190 W/m^2 and different evaporation rates for Image of heptane meniscus on	76

fused quartz wafer (C) 1. Contour of heptane vapour concentration near the meniscus 2. Velocity contours in the vapour/air domain 3. Temperature contours (K) and stream traces showing thermocapillary convection in the meniscus (d) Wall temperature profiles near the contact line (*Dhavaleswarapu et al. [2.64, 2.65]*)

Fig. 2.16	(a) Experimental setup schematics (b) Linear local wall temperature distribution underneath the meniscus at different input heat fluxes and linear local heat flux distribution for different input heat fluxes (<i>Ibrahem et al. [2.66]</i>)	77
Fig. 2.17	Schematics of physical phenomenon of slip boundary condition, Marangoni convections and slope and curvature dependence of disjoining pressure in an extended meniscus	78
Fig. 2.18	(a) Experimental setup schematics (b) Vapour temperature as compared to saturation temperature (<i>Gully et al. [2.70]</i>)	79
Fig. 2.19	(a) Experimental setup schematics (b) Experimental results for wall temperature and % of heat transfer at various regions (<i>Chauris et al. [2.71]</i>)	81

Number	Title	Page No.
Fig. 3.1	Schematics of experimental setup 1- Thermal dynamics of the simplest unit cell of PHP	93
Fig. 3.2	Photograph of experimental setup 1- Thermal dynamics of the simplest unit cell of PHP	95
Fig. 3.3	Dimensions of experimental setup 1- Thermal dynamics of the simplest unit cell of PHP	95
Fig. 3.4	(a) Typical image from camera 1 of the complete unit cell PHP with meniscus (b) Schematic image from the camera 2 of the thin liquid film and triple line	98
Fig. 3.5	Thermodynamic state of unit cell PHP	100
Fig. 3.6	Schematics of the experimental setup 2: Hydrodynamics of the meniscus inside the capillary	103
Fig. 3.7	Actual photograph of the experimental setup 2: Hydrodynamics of the meniscus inside the capillary	104
Number	Title	Page No.
Fig. 4.1	Schematics of the various possible cases of contact line behaviour	109
Fig. 4.2	Represents the adiabatic experimental results for de-ionized water, motion of the triple line with respect to meniscus motion	110

	in a capillary and thus corresponds to the partial pinning of contact line	
Fig. 4.3	Temporal variations of pressure (right ordinate axis) in the vapour bubble along with location of meniscus (left ordinate axis, solid line) and triple-line (left ordinate axis, dotted line) for experimental condition of $T_e = 46^\circ\text{C}$ and (a) $T_c = 16^\circ\text{C}$, (b) $T_c = 20^\circ\text{C}$, (c) $T_c = 24^\circ\text{C}$ and (d) $T_c = 28^\circ\text{C}$ and $P_r = 0.5$ bar	113
Fig. 4.4	(a) Schematic explaining the events during one cycle of the meniscus motion. (b) Time evolution of the meniscus from the entrance in the evaporator (Stage A) as it passes towards the condenser (Stage J) and comes back to the evaporator (Stage T), is shown. The four zones are also highlighted (will be used in section 1.4.1)	115
Fig. 4.5	Temporal variations of pressure (right ordinate axis) along with temperature in the vapour bubble and saturation temperature $T_{\text{sat}} = f(P_v)$, for experimental boundary condition of $T_e = 46^\circ\text{C}$ and $T_c = 16^\circ\text{C}$, 20°C , 24°C and 28°C , respectively and $P_r = 0.5$ bar	119
Fig. 4.6	Temporal variations of location of meniscus (left ordinate axis, solid line), triple-line (left ordinate axis, dotted line) and mass of vapour (right ordinate axis) calculated using ideal gas equation (ref. and eq. 4.1) (at $T_e = 46^\circ\text{C}$ and (a) $T_c = 16^\circ\text{C}$, (b) $T_c = 20^\circ\text{C}$, (c) $T_c = 24^\circ\text{C}$, and (d) $T_c = 24^\circ\text{C}$, and $P_r = 0.5$ bar, showing the sensitivity of the vapour temperature on the mass of vapour)	121
Fig. 4.7	Temporal variations of location of meniscus and film thickness variation calculated using the analytical model as per eq. 4.7 (at $T_e = 46^\circ\text{C}$ and $T_c = 16^\circ\text{C}$, 20°C and 24°C , respectively, and $P_r = 0.5$ bar).	126
Fig. 4.8	Variation of Capillary number of the meniscus motion during one complete oscillation cycle	128
Fig. 4.9	Comparison of the empirical scaling correlations for predicting the initial film thickness lay down by a moving meniscus inside a tube	129
Fig. 4.10	Cumulated variation of vapour mass during one cycle separating four different contributions: Evaporation on the triple-line or on the liquid film in the evaporator and condensation on the liquid film or on the meniscus in the condenser ($T_e = 46^\circ\text{C}$ and $T_c = 16^\circ\text{C}$, first cycle)	131
Fig. 4.11	Unit cell of single branch PHP	133
Fig. 4.12	Thermal conductivity versus thermal diffusivity for a wide	134

	variety of homogeneous materials (closed circles-metals; squares-ceramics; triangles-glasses; open squares-polymers; open circles-liquids; and crosses-gases) (<i>Salazar [4.20]</i>)	
Fig. 4.13	Temporal variation of the liquid film thickness ($\delta_{lf,i} = 50 \mu\text{m}$) and its corresponding temperature at the conditions existing in the evaporator section of the present experiment for FC72 ($T_e = 55 \text{ }^\circ\text{C}$, $T_c = -3 \text{ }^\circ\text{C}$ and $P_r = 0.42 \text{ bar}$)	142
Fig. 4.14	Temporal variation of liquid film thickness ($\delta_{lf,i} = 50 \mu\text{m}$) at the conditions existing in the evaporator section of the present experiment for FC72 ($T_e = 55 \text{ }^\circ\text{C}$, $T_c = -3 \text{ }^\circ\text{C}$ and $P_r = 0.42 \text{ bar}$).	143
Fig. 4.15	Influence of the initial thickness of the liquid film on its evolution from initial condition to the final state of complete evaporation. During the initial period the film becomes thicker as it experiences condensation of vapour on it	144
Fig. 4.16	Temperature of the liquid film ($\delta_{lf,i} = 50 \mu\text{m}$) at different time in the conditions of the experiment at the condenser	145
Number	Title	Page No.
Fig. 5.1	Geometrical properties considered in the model	151
Fig. 5.2	Pressure drop measurement and various components involved in it	154
Fig. 5.3	Thermal model of the tube, the evaporator or the condenser	160
Fig. 5.4	Comparison of temporal variation of analytical and experimental pressure drop for the single phase liquid oscillating inside a capillary tube of 2mm along with the meniscus movement, where (a) for fluid FC72 oscillating at 1 Hz (b) for fluid FC72 oscillating at 1.5 Hz (c) for fluid pentane oscillating at 1 Hz (d) for fluid pentane oscillating at 1.5 Hz (here X-axis represents the location of meniscus in capillary tube, 0 corresponds to the closest location to reservoir during the oscillation)	164
Fig. 5.5	Comparison of three components contributing in theoretical pressure drop across the tube length L_t by dividing them with internal cross sectional area A, (i) Instantaneous momentum of the liquid slug ($d\mu/dt$), (ii) Gravitational term ($m_l g$) and (iii) Shear term (F_r) for (a) For fluid FC72 oscillating at 1 Hz (b) For fluid FC72 oscillating at 1.5 Hz (c) For fluid pentane oscillating at 1 Hz (d) For fluid pentane oscillating at 1.5 Hz	165
Fig. 5.6	Inner wall temperature of the tube at the contact with the liquid film	167
Fig. 5.7	Flow rate of evaporation of the liquid film	168
Fig. 5.8	Meniscus movement depending on the evaporator temperature	170
Fig. 5.9	Comparison of meniscus movement, triple line movement and vapor pressure for $T_e = 37.5^\circ\text{C}$ (in thermal model) and $T_e =$	171

	46°C (in experiments) for FC72 with $T_c = 16^\circ\text{C}$, $P_r = 0.5$ bar, for similar dimensions as described in chapter 3 experimental setup 1. $h_{e,tl} = 7.348 \times 10^6 \text{ W/m}^2\text{K}$; $h_{e,lf} = 7.273 \times 10^3 \text{ W/m}^2\text{K}$	
Fig. 5.10	Comparison of vapor temperature and saturation temperature corresponding to the vapor pressure with $T_e = 37.5^\circ\text{C}$, for similar conditions as experimental data presented in Fig.4.5 (a)	171
Fig. 5.11	Meniscus movement, triple line movement and vapor pressure with $T_e = 37.5^\circ\text{C}$ and $T_c = 16^\circ\text{C}$, for similar conditions as experimental data presented in Fig.4.6 (a)	172
Fig. 5.12	Meniscus movement, triple line movement and vapor pressure with $T_e = 37.5^\circ\text{C}$ and $T_c = 20^\circ\text{C}$, for similar conditions as experimental data presented in Fig.4.6 (b)	173
Fig. 5.13	Meniscus movement, triple line movement and vapor pressure with $T_e = 37.5^\circ\text{C}$ and $T_c = 24^\circ\text{C}$, for similar conditions as experimental data presented in Fig.4.6 (c)	173
Fig. 5.14	Inner wall temperature of the tube made of glass at the contact with the liquid film for water ($T_{sat} = 81^\circ\text{C}$; $T_e = 92^\circ\text{C}$; $T_c = 66^\circ\text{C}$; $h_{HS} = 20000 \text{ W/m}^2\text{K}$)	176
Fig. 5.15	Inner wall temperature of the tube made of copper at the contact with the liquid film for water ($T_{sat} = 81^\circ\text{C}$; $T_e = 92^\circ\text{C}$; $T_c = 66^\circ\text{C}$; $h_{HS} = 20000 \text{ W/m}^2\text{K}$)	177
Fig. 5.16	Meniscus dynamic for $T_e = 37.5^\circ\text{C}$ and $T_c = 16^\circ\text{C}$; $h_{e,tl} = 8.638 \times 10^6 \text{ W/m}^2\text{K}$; $h_{e,lf} = 3.212 \times 10^3 \text{ W/m}^2\text{K}$; $h_c = 800 \text{ W/m}^2\text{K}$	178
Fig. 5.17	Meniscus movement, triple line movement and vapor pressure with $T_e = 38.4^\circ\text{C}$; $T_c = 16^\circ\text{C}$; $h_{e,tl} = 5.579 \times 10^6 \text{ W/m}^2\text{K}$; $h_{e,lf} = 1.605 \times 10^3 \text{ W/m}^2\text{K}$; $h_c = 800 \text{ W/m}^2\text{K}$	179
Fig. 5.18	Meniscus dynamic for $T_e = 37.5^\circ\text{C}$ and $T_c = 16^\circ\text{C}$; $h_{e,tl} = 7.348 \times 10^6 \text{ W/m}^2\text{K}$; $h_{e,lf} = 7.273 \times 10^3 \text{ W/m}^2\text{K}$; $h_c = 800 \text{ W/m}^2\text{K}$	179
Fig. 5.19	Meniscus dynamic depending on the condensation heat transfer; $T_e = 37.5^\circ\text{C}$, $T_c = 16^\circ\text{C}$; $h_{e,tl} = 7.348 \times 10^6 \text{ W/m}^2\text{K}$; $h_{e,lf} = 7.273 \times 10^3 \text{ W/m}^2\text{K}$	180

Number	Title	Page No.
Fig. C.1	Calibration curve absolute pressure transducer	194
Fig. C.2	Calibration curve differential pressure transducer	194
Fig. D.1	Pentane results (meniscus location cannot be tracked completely because it was beyond the range of camera)	195

List of tables

Number	Title	Page No.
Table 2.1	Static equilibrium contact angle θ_{eq} range for various types of fluids	48
Table 3.1	The basic physical properties of fluids used	94
Table 3.2	Typical experimental measurements	99
Table 3.3	Typical experimental measurements	105
Table 4.1	Comparison of initial film thickness	130
Table 4.2	Order of magnitude of important time scales of the unit-cell elements	135
Table 5.1	Thermal effusivity $(K.\rho.C_p)^{1/2}$ of different substances in $W. s^{1/2}/K.m^2$.	175
Table C.1	Uncertainty in the measured variables	193

Nomenclature

Letter	Definition	SI Units
A	Area	(m ²)
\hat{a}	Acceleration	(m/s ²)
A'	Constants	(-)
A1	Constants	(-)
A2	Constants	(-)
B	Constants	(-)
C	Thermal capacitance per unit length	(J/m.K)
C _f	Coefficient of friction	(-)
C _p	Specific heat at constant pressure	(J/kg.K)
C _v	Specific heat at constant volume	(J/kg.K)
cp	Thermal capacity	(J/K)
D	Diameter	(m)
d	Diameter	(m)
F	Force	(N/m ²)
f	Frequency	(Hz)
g	Acceleration due to gravity	(m/s ²)
h	Heat transfer coefficient	(W/m ² .K)
\hat{h}	Enthalpy	(J/kg)
J	Flux of molecules	(-)
j	Constant	
K	Thermal conductivity	(W/m.K)
k _B	Boltzmann constant	(1.38×10 ⁻²³ m ² . kg/ s ² .K)
K1	Constants	(-)
K3	Constants	(-)
K4	Constants	(-)
L	Length	(m)
M'	Momentum	(kg.m/s)
\bar{M}	Molecular weight	(kg/mol)
m	Mass	(kg)
m''	Mass flux	(kg/m ²)
n	nodes	
N	Number of molecules	(-)
P	Pressure	(N/m ²)
\dot{Q}	Heat input rate	(W/m ²)
q''	Heat transfer	(W)
q1	Constants	(-)
R	Radius	(m)
\bar{R}	Thermal resistance	(-)
\bar{R}	Universal gas constants	(8.314 J.mol/K)
\dot{r}	Characteristics roughness	(-)
S	Spreading coefficient	(-)
s	Dimensionless parameter	(-)
T	Temperature	(K)

t	Time	(s)
u,v,w	Velocities in x,y,z directions respectively	(m/s)
V	Volume	(m ³)
X,x	Distance	(m)
x,y,z	Directions	(-)
Z	A function	(-)
z	Constant	(-)

Greek symbols

Symbol	Definition	SI Units
α	Thermal diffusivity	(m ² /s)
γ	Accommodation coefficient	(-)
δ	Thickness	(m)
θ	Contact angle	(°)
κ	Curvature	(-)
λ	Laplace constant	(m)
μ	Dynamic viscosity	(Pa.s)
ν	Kinematic viscosity	(m ² /s)
ρ	Density	(kg/m ³)
σ	Surface tension	(N/m)
τ	Shear stress	(N/m ²)
ϕ	Heat flux	(W/ m ²)
ω	Angular frequency	(rad/s)

Operator

	Definition	SI Units
Δ	Differences between	(-)

Subscripts

	Definition
a	Adiabatic section
ad	Adsorbed
acc	Accelerating
adv	Advancing
app	Apparent
c	Condenser/condensation
cap	Capillary
conv	Convection
cond	Conducting
d	Dead space due to connections
dis	Disjoining
e	Evaporator/evaporation
eq	Equilibrium
exp	Experimental

ext	External
HS	Heat sink or heat source
hyd	Hydraulic
i	Initial
int	Interface
l	Liquid
lf	Liquid film
lv	Liquid-Vapour
max	Maximum
meas	Measured
mol	Molecular
p	pressure
r	Reservoir
res	Residing
reg	Regular
s	Slug
sl	Solid-Liquid
so	Dry solid surface
st	Static
sv	Solid-Vapour
sat	Saturated
sens	Sensible
sign	Singularity
t	Total
tb	tube
th	Theoretical
tl	Triple line
v	Vapour
w	Wall
z	Constant

Abbreviations

	Definition
B/W	Black and white
CCD	Charge-coupled device
cond	Condensing
CETHIL	Centre d'Energétique et de Thermique de Lyon
CLOHP/CV	Closed loop oscillating heat pipe with checked valves
DC	Direct current
DVD	Digital video disk
Diff	Differential
eq	Equation
HP	Heat pipe
HS	Heat source or Heat sink
ID	Internal diameter
IR	Infra red

IRT	Infra red thermography
LV	Liquid-Vapour
OD	Outer diameter
OHP	Oscillating heat pipe
PHP	Pulsating heat pipe
SL	Solid-Liquid
SS	Stainless steel
SV	Solid-Vapour
TC	Thermocouple
TV	Television
TLC	Thermochromic liquid crystal
th	Theoretical
μ TC	Micro thermocouple

Chapter 1

Introduction, Motivation and Background

Since the beginning of 18th century that can be called as “machine age” of the earth, human has been making lot of efforts in revealing secrets of nature by discovering its governing laws. In this process, we are making machines to ease down the applied effort. As a basic rule of the nature, energy can be converted from one form to another and required work can be extracted. But still human is yet to achieve the highest possible efficiency. So most of the time this lost energy is in the form of unnecessary heat dissipation. Later this heat becomes responsible for underperformance of the system and environment hazards. In the same period, electronics has also made significant growth and contribution in developing new machines. The reliability of these electronics components is a major factor in the overall reliability. Continued miniaturization of electronic systems has resulted in a dramatic increase in the amount of heat generated per unit volume. Unless properly designed and controlled, high rates of heat generation result in high operating temperatures for electronic equipment, which will affect safety and reliability. While absolute power levels in microelectronic devices are relatively modest (a few tens to a few hundred watts), heat fluxes can be significant (~ 50 W/cm² in current electronic chips; up to 2000 W/cm² in semiconductor lasers). Further, temperatures at the chip surface must be kept low for both performance and reliability. Today's electronic system are normally rated for operation in the 0 to 70°C temperature range (commercial grade), -40 to 85°C (industrial grade) and -55 to 125°C (military grade). For certain applications, very low temperatures (even close to as 0 K) are ideal, as conductivity increases and approaches superconductivity at this temperature. For a rule of thumb and for today's electronics, "room temperature" is a good operating temperature regardless of theoretical advantages of superconductivity. Hence from above it is clear that for the reliable and safe working of electronics systems, there will always be a need to cool these electronics

components with suitable technique. In next section, common cooling techniques for the electronics are presented in brief.

1. Need for thermal passive management: Electronics cooling techniques

The only form of energy leaving the electronic device is the heat generated when the current flows through resistive elements; we know that the heat dissipation or cooling load of an electronic device is equal to its power consumption. We should always keep in mind that the most desirable form of cooling is natural convection cooling, since it does not require any moving parts, and thus it is inherently reliable, quiet, and, best of all. Simple ventilation holes on the case may be all we need for the cooling of low-power-density electronics such as a TV or a DVD player in a room, and a fan may be adequate for the safe operation of a home computer. But the thermal control of the electronics of an aircraft will challenge thermal designers, since the environmental conditions in this case will swing from one extreme to another in a matter of minutes. Various active/passive, single-/multi-phase, single/multi-component heat transfer strategies have evolved in the last decades to cater the increased demand of thermal management for such mini/micro systems and device. The existing heat transfer mechanisms can broadly classified as single-phase natural convection, single-phase forced convection, non-phase change multiphase techniques and phase-change multiphase heat transfer techniques. Typical range of heat transfer rates achievable from these techniques is summarized in *fig. 1.1* inspired by *Lin et al. [1.1]*.

This figure clearly indicates that multiphase heat transfer process, with phase change, provides significantly higher heat transfer coefficients than the single-phase forced convection or natural convection processes. Therefore, several multiphase techniques and their variants are used as cooling solutions in contemporary times. Some applications of modern heat transfer devices are, film cooling, spray/jet impingement cooling, wicked heat pipe, pulsating heat pipe and micro-channel heat sink with flow boiling, etc. Such devices have shown better thermal performance in terms of enhanced heat transfer coefficients and maximum heat handling capacity, in comparison to the air/liquid cooled forced or natural convective counterparts. Conventional natural

convection and single-phase convection have been widely studied in the past and largely understood. However, there are many open issues, which need to be explored in multiphase flow devices because of occurrence of wide variety of flow patterns, presence of interfaces, contact line motion etc., which result in complex flow and heat transfer physics in such systems. Keeping the area of research concentrated towards the heat pipes and more precisely towards pulsating heat pipes, first we will briefly discuss two phase passive cooling technology and then we will describe heat pipes in general and later will move deep in to the pulsating heat pipes research history and challenges.

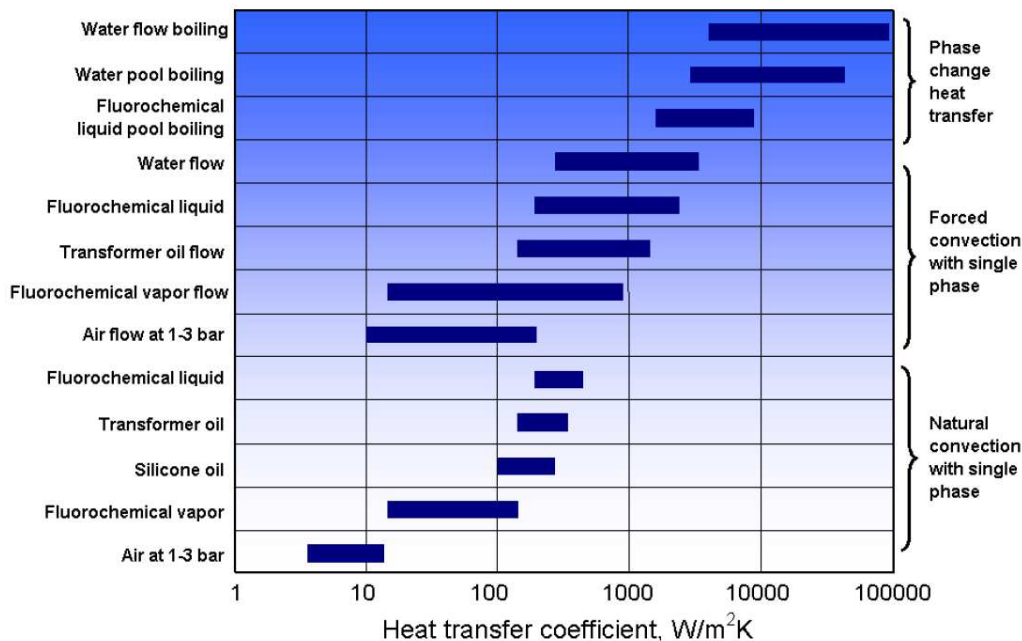


Fig. 1.1: Range of heat transfer coefficients typically possible from various cooling technologies applied in contemporary thermal management systems (*Lin et al. [1.1]*).

1.1. Two-phase passive cooling technologies

The operation of modern passive heat transfer devices is based on the combined action of three physical phenomena: phase-change, gravity and capillarity. These three phenomena are acting together but there may be some extreme conditions where capillary effects are negligible (i.e. thermosyphons) or gravity effects are less important (i.e. sintered HP). *Fig. 1.2* shows a comparison of various cooling techniques as a function of the attainable heat transfer in terms of the heat transfer coefficient. A

passive device is fully thermally driven: the heating power activates the evaporation/condensation process and the consequent vapour expansion, together with the capillary/gravity effect on the liquid phase, provide the “pumping power” which is needed to maintain the fluid circulation.

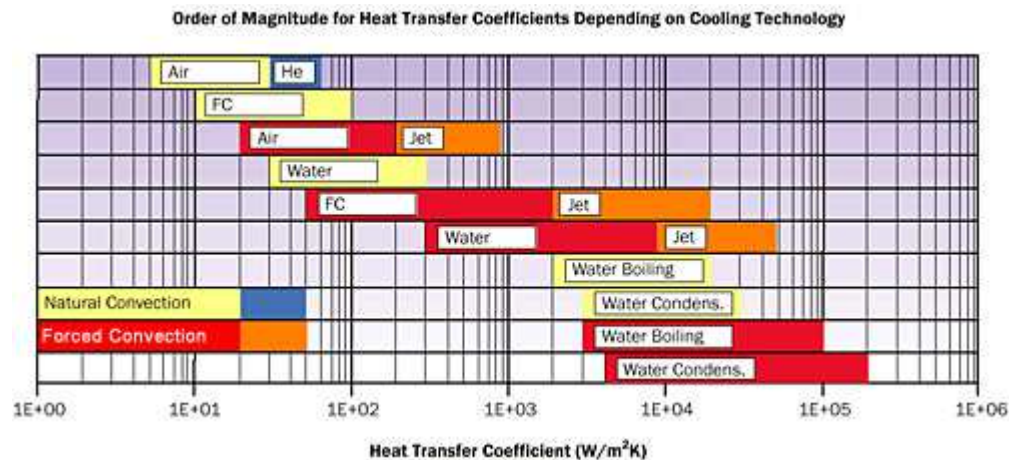


Fig. 1.2: Heat transfer coefficient attainable with natural convection, single-phase liquid forced convection and boiling for different coolants (*Lasance [1.2]*).

The passive two-phase heat transfer technology gives improved heat transfer capability: higher heat loads and higher heat fluxes (up to 200W/cm² of radial heat flux). Also they give improved performance: low thermal resistance down to 0.01 K/W, lower mass flow rates and relatively smaller size and weight. There is no need for external pumping work. Also have smaller temperature gradients and nearly isothermal operation regardless of variations in the heat load. Different types of two-phase passive heat transfer devices can be defined as: The heat pipe, capillary pumped loop and loop heat pipe, thermosyphon and pulsating heat pipe.

In the gravity assisted thermosyphon lower end of the tube is heated which results in the liquid evaporation and the vapour to move to the cold end of the tube where it is condensed. Since condensate is returned to the hot end by gravity, the evaporator must be situated at the lowest point. In modern devices this limitation is overcome by means of a wick structure, constructed for example from a few layers of fine gauze, which is fixed to the inside surface and returns the condensate to the evaporator by capillary

forces. In the heat pipe the evaporator position is not restricted and it may be used in any orientation. If, of course, the heat pipe evaporator happens to be in the lowest position, gravitational forces assist the capillary forces.

1.2. Heat pipe

A heat pipe is a heat transfer device that uses evaporation and condensation of a two-phase "working fluid" to transport large quantities of heat with a very small difference in temperature between the hot and the cold interfaces. As illustrated in *fig. 1.3*, a typical heat pipe consists of a sealed hollow tube made of a thermo-conductive metal such as copper or aluminum this tube can be divided in three sections: an evaporator or heat addition section, an adiabatic section, and a condenser or heat rejection section. When heat is added to the evaporator section of the heat pipe, the heat is transferred through the shell and reaches the liquid. When the liquid in the evaporator section receives enough thermal energy, the liquid vapourises. The vapour carries the thermal energy through the adiabatic section to the condenser section, where the vapour is condensed into the liquid and releases the latent heat of vaporization. The condensate is pumped back from the condenser to the evaporator by the driving force acting on the liquid. No external power is needed for a typical heat pipe. The phase-change heat transfer occurs almost in the quasi-equilibrium state. The heat pipe has a very high efficiency to transfer the thermal energy from a heat source to a heat sink. An operational heat pipe can provide an extra-high effective thermal conductivity and reach a higher level of temperature uniformity.

The thermal conductivity of heat pipes can be as high as 10,000 W/m.K, in contrast to copper, which has a thermal conductivity of around 400 W/m.K. The working fluid medium in a heat pipe can be selected from a variety of fluids, depending on the operating temperature and compatibility with the shell material. The heat pipe can be operated from a temperature lower than 4 K to a high temperature up to 3000 K. Because the evaporator and condenser of a heat pipe function independently, the heat pipe can be made into any shape, depending on the design requirement. Due to these unique features, the heat pipe has been widely used in a wide range of applications.

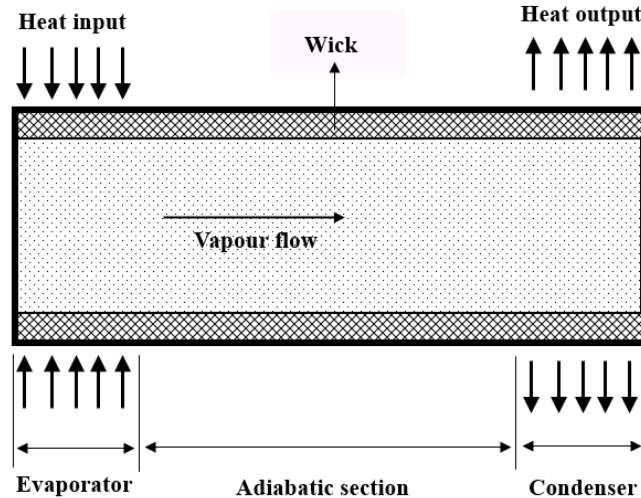


Fig. 1.3: Typical heat pipe schematic.

There are a number of limitations which affect the working of a heat pipe such as smooth flow of the working fluid, when the pumping pressure produced by the surface tension cannot overcome the summation of the total pressures; the heat transport occurring in the heat pipe reaches a limit known as the capillary limit. There are several other limitations disconnecting the return of the working fluid from the evaporator to the condenser or from the condenser to the evaporator. Among these are the boiling limit, sonic limit, entrainment limit, and viscous limit. When the heat flux added to the evaporator is sufficiently high, nucleate boiling occurs. The bubble formed in the wick significantly increases the thermal resistance, causing the heat-transfer performance to be significantly reduced. More importantly, when the heat flux is so high, the bubbles block the return of the working fluid and lead to a dry-out of the evaporator. The boiling limit plays a key role in a high heat flux heat pipe. When the vapour velocity is high and the cross-sectional area variation of the vapour space in a heat pipe cannot meet the flow condition, choked flow occurs and the vapour flow rate will not respond with the amount of heat added in the evaporator. This will lead to a sonic limit. The entrainment limit is due to the frictional shear stresses caused by the vapour–liquid interface. The viscous limit occurs in a low heat flux heat pipe, where the vapour pressure difference in the vapour phase cannot overcome the vapour pressure drop in the vapour phase. Now let us discuss PHP separately in detail.

2. Pulsating heat pipes (PHPs)

Like a conventional heat pipe, a pulsating or oscillating heat pipe, in short called as PHP\OHP, is not a cooling system, but a system to transport heat from a hot source or a heat source to a cold source or heat sink. The tube forming a PHP is bent many times in a symmetrical manner so that an evaporation section, adiabatic section and condenser section are formed (*fig. 1.4*). The tube is partially filled with a working fluid and remains in the state of liquid-vapour equilibrium in the operating conditions. Due to capillary forces, a series of liquid slugs and vapour bubbles of variable size are then formed within the tube. It is observed under certain boundary conditions, oscillations of the liquid slugs and vapour pockets are responsible for the transfer of heat from the evaporator to the condenser. The oscillation frequencies found typically are of the order of 0-10 Hz.

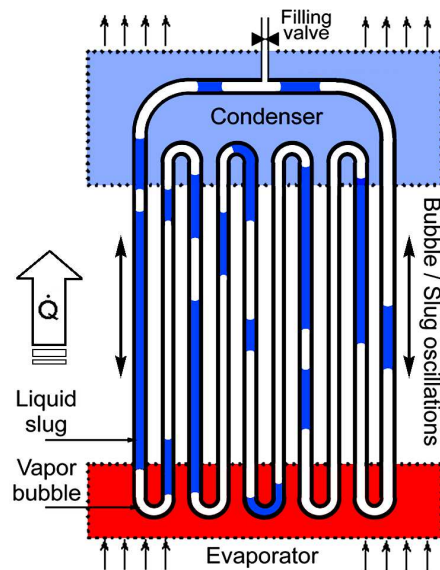


Fig. 1.4: Schematic of typical pulsating heat pipe (*Khandekar [1.3]*).

Due to these oscillations, a liquid slug arrives at the hot source and it partially evaporates due to overheating, which includes the pressure in the neighboring pockets of steam and pushes in turn the liquid slugs. It should be noted that this pressure can also be result of the expansion of the steam due to the contribution of sensible heat. Thus, the oscillations of the liquid slugs and vapour pockets are maintained due to the overheating of the wall and thus the evaporation of the liquid leads to a sudden

expansion of the fluid to the evaporator. Statistically, the number of such instances will always bring the liquid to the evaporator. Also the condensation of the superheated vapour at the condenser will locally lead to a pressure reduction, which also helps to maintain the oscillations. No external power is required to drive the device, internal oscillations being fully driven by the thermal non-equilibrium that is sustained inside the system due to external heating and cooling. Compared to other cooling solutions, PHPs are the simplest technology, from the point of view of manufacturing as compared to the family of heat pipes and thus more reliable and cheaper.

As stated above the pulsating heat pipe (PHP) is a non-equilibrium passive two-phase heat transfer device, first of its kind PHP was found to be described in 1971 in a Russian patent filed by *Smyrnov and Savchenkov* [1.4]. But in the 1990s, *Akachi* [1.5-1.7] patent the first of its kind of working pulsating heat pipe (PHP). The prototypes of Akachi are widely accepted and up till now exploited for further research (the actual pictures with the dimensions of such PHP are given in *fig. 1.5*).

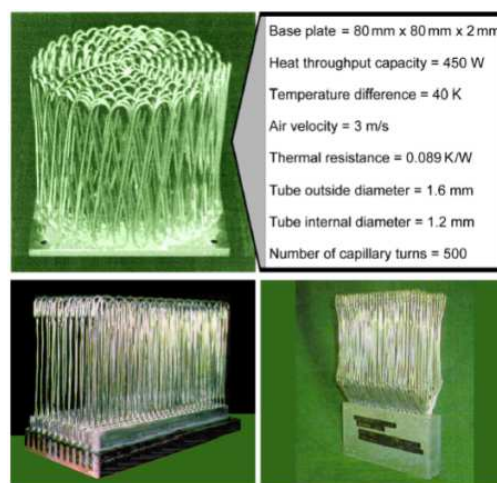


Fig. 1.5: Prototypes proposed by *Akachi et al.* [1.8].

As stated above PHP belongs to a category of wickless heat pipes, however with complex internal thermo-hydrodynamic transport processes, responsible for the self-sustained thermally driven oscillating two-phase Taylor bubble flow which in turn, leads to its unique heat transfer characteristics. However, still the technology is simple, the physics of flow and heat transfer within these systems is extremely complex and yet not

completely understood. Unlike conventional heat pipes, the study of these phenomena is complex because of unsteady oscillatory flow characteristics. Understanding how PHP works is not that easy due to the complexities of such phenomenon as two-phase flows in capillary tubes, evaporation and boiling in confined space. Also the pressure fields with statistical instabilities are all complex and varied phenomena governing these systems. To understand the PHP working and the challenges it propose, first let us discuss various terms and methodologies involved in it.

2.1. Different arrangements of PHP

The pulsating heat pipes (PHP) can be classified on the basis of how the tubes are connected to each other and how the flow of fluid takes place inside the tubes. The tube is bent back and forth parallel to itself, and the ends of the tube may be connected to one another in a closed loop, or pinched off and welded shut in an open loop (*fig. 1.6-a and 1.6-b*). As it is evident from the name PHP is that liquid-vapour combination oscillates inside these tubes, in addition to this oscillatory flow, the working fluid can also be circulated along with pulsations in the closed-loop PHP, resulting in heat transfer enhancement. Although an addition of a check valve (*fig. 1.6-c*) could improve the heat transfer performance of the PHPs by making the working fluid move in a specific direction, it is difficult and expensive to install these valves. Consequently, the closed-loop PHP without a check valve becomes the most favorable choice for the PHP structures. There can be another type of pulsating heat pipe in which one or both ends are left open without being sealed (*fig. 1.6-d*).

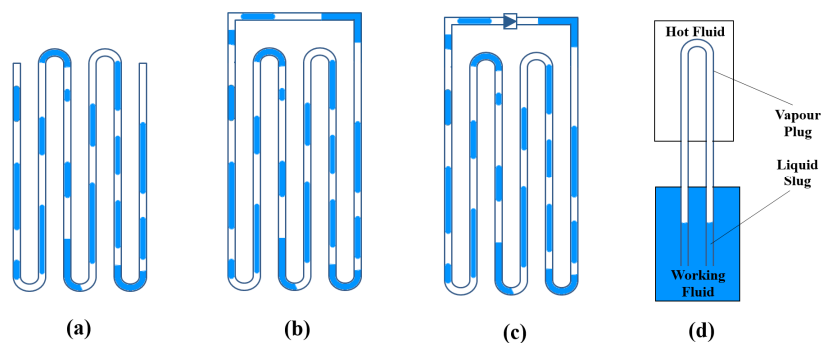


Fig. 1.6: Different configurations of PHP, (a) Closed end (b) Closed loop (c) Closed loop with check valve (d) PHP with open ends.

2.2. Physical design parameters

As explained previously a PHP is made up of a single tube bent in many turns of sufficiently small internal diameter so that the capillary forces are predominant with respect to the volume forces. The inner diameter of this tube must be small enough that surface tension forces dominate gravitational forces and distinct liquid slug and vapour plugs can form. For normal heat transfer fluids, this suggests the use of small, mini or micro ducts or channels for the construction of PHP. Due to significant differences of transport phenomena in mini-micro systems as compared to normal sized channels, it is important to define what is meant by the terms mini, meso and micro sizes of the channels. Merely categorizing on the basis of tube geometry is not enough, especially in the context of two-phase flows. The criterion ought to be based on the combination of the size and thermo-physical properties of the fluid under consideration. Channels are generally considered small when surface tension forces dominate the gravitational forces. A measure of the relative value of the two forces is given by the **Eötvös or Bond number**:

$$Bo = \sqrt{E\ddot{o}} = \sqrt{(D_{hyd}^2 g (\rho_l - \rho_v)) / \sigma} \quad 1.1$$

Where, Bo is the bond number, $E\ddot{o}$ is the Eötvös number, D_{hyd} is the hydraulic diameter of the tube, g is the acceleration due to gravity, ρ_l and ρ_v are the densities of liquid and vapour and σ is the surface tension of the fluid.

It is believed that values of the Bond number, ranges from 0.88 to $2\pi^2$, below which channels can be considered small, stated that, for $Bo < 1.84$, the channel can be considered as small. According to *Triplett et al. [1.9]*, the flow channels having D_{hyd} less than or equal to **Laplace constant λ** may be considered as microchannels, where:

$$\lambda = \sqrt{\sigma / (g \cdot (\rho_l - \rho_v))} \quad 1.2$$

Kew and Cornwell [1.10] give another interpretation of the same quantity in terms of the confinement of bubbles in a channel. They reported that channels having two-phase flow can be considered as mini systems when the **Confinement number** Co , as defined in eq. 1.3, is greater than 0.5.

$$Co = \frac{1}{D_{\text{hyd}}} \sqrt{\frac{4\sigma}{g(\rho_l - \rho_v)}} = \frac{2\lambda}{D_{\text{hyd}}} \quad 1.3$$

Under such conditions, the two-phase flows typically have a confined bubble flow regime which is unique to mini systems, as also is the case with PHPs. As the hydraulic diameter goes on decreasing, the effect of Bond number on various hydrodynamic parameters goes on increasing. In fact, all classification numbers, Bo , $E\ddot{o}$, Co , or the constant λ , consider the effect of fluid density, surface tension and channel size on two-phase flow. If we estimate the relevant threshold critical diameters i.e. transition diameters for considering a channel as ‘micro’, for common working fluids respectively, for the entire range of operating pressures, we notice that there are considerable differences in the threshold diameters, as defined above by various criteria; so far, no unified methodology is available. Such systems with mini or smaller systems where the Bond number is less than 2, will also be called as ‘capillary’ systems. The foregoing discussion has important implications in defining a PHP. The definition of a threshold diameter needs to be decided so that distinct liquid plugs and vapour slugs can be formed without separation, stratification or agglomeration, at least under adiabatic conditions. Thus, rather than a certain fixed diameter which classifies the boundary between classical macroscale systems and PHPs, there is a finite transition zone wherein PHPs can effectively function as truly pulsating/oscillating heat transfer devices (*Khandekar and Groll [1.11]*).

Apart from choosing appropriate diameter for a PHP, higher surface tensions will increase the maximum allowable diameter and also the pressure drop in the tube. Larger diameter will enable improved performance, but an increased pressure drop will require greater bubble pumping and thus a higher heat input to maintain pulsating flow. A low latent heat will cause the liquid to evaporate more quickly at a given wall temperature and a higher vapour pressure; the liquid slug oscillating velocities will be

increased and the heat transfer performance of the PHP will be improved. A high specific heat will increase the amount of sensible heat transferred. Because the majority of the total heat transfer in a PHP is due to sensible heat, a fluid with a high specific heat is desirable. A low dynamic viscosity will reduce shear stress along the wall and will consequently reduce pressure drop in the tube. This will reduce the heat input required to maintain a pulsating flow. The rate of change in pressure with respect to temperature at saturated conditions $(dp/dT)_{\text{sat}}$ affects the rate at which bubbles grow and collapse. At a high value of $(dp/dT)_{\text{sat}}$, the difference between vapour pressure in the evaporator and condenser will be increased and the performance of a PHP will be improved by enhanced oscillatory motion of liquid slugs.

The charge ratio is the volume of the liquid divided by the total internal volume of the PHP. If the charge ratio is too low, there is not enough liquid to perpetuate oscillating slug flow and the evaporator may dry out. If the charge ratio is too high, there will not be enough bubbles to pump the liquid, and the device will act as a single phase thermosyphon. *Khandekar [1.3]* shows that generally charge ratios ranging from 20% to 80% will allow the device to operate as a true pulsating heat pipe. The number of turns of bent tube in the PHP may affect thermal performance and may negate the effect of gravity. By increasing the number of turns, there are more distinct locations for heat to be applied. The fluid within each turn may be either liquid or vapour, the heating of which creates differences in pressure at each turn. It is these pressure differences that drive the pulsating flow. If a PHP only has a few turns, it may not operate in the horizontal or top heat modes, but a PHP with many turns can operate at any orientation because of the perturbations in each turn.

2.3. Flow regimes in PHPs

In a PHP, different flow regimes can be observed as shown by *Xu et al. [1.12]* (*fig. 1.7*). If the vapour bubbles are smaller than the diameter of the tube (a, b, c), the flow is said **dispersed bubble**; this corresponds to a low nucleation which continues to the evaporator. There is no coalescence effect and, most often, bubbles are condensed before reaching the condenser. When these bubbles become numerous, they can coalesce and form vapour pockets (f, g, h) or long bubbles. It is then intermittent regime

compound vapour pockets called as **Taylor Bubbles**, separated by liquid slugs. The liquid and vapour phases flow randomly inducing fluctuations in pressure and velocity.

The length of the vapour pockets depends on the surface tension of the fluid and is bounded by pocket breaking phenomena. When speed becomes high, the vapour is not any more in contact with the wall; it forms a cylindrical channel, surrounded by a liquid ring. The flow is then said **annular** (i, j). The work in the literature shows that the heat transfer occurs by both sensible heat and latent heat. Depending on the type of flow, one or the other of these transfer modes is dominant. The transfer with phase change is favored in the annular flow while the sensible heat is predominant in Taylor Bubble flow [Yang et al. \[1.13\]](#).

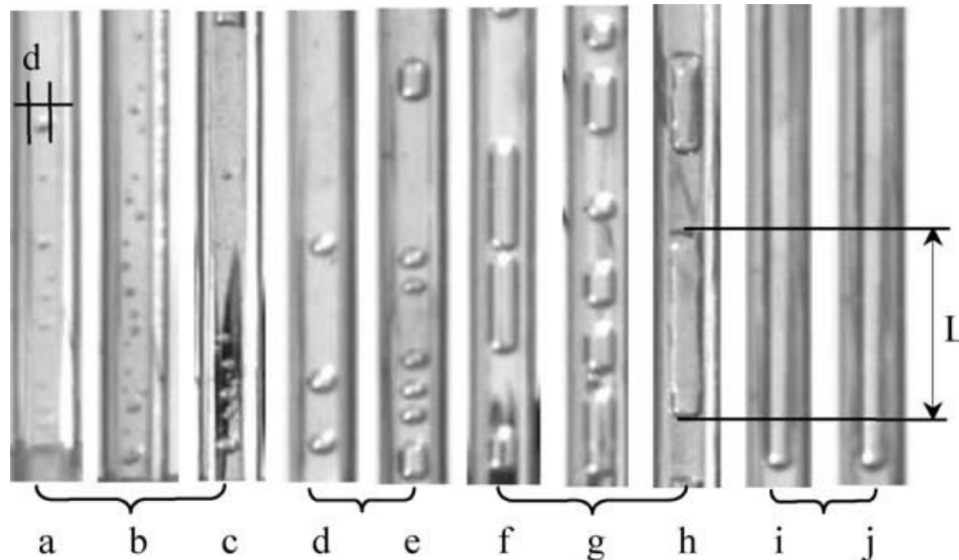


Fig. 1.7: Different flow regimes of PHP ([Xu et al. \[1.12\]](#)).

2.4. Thermodynamics of PHPs

Although simple in their construction, PHPs become complicated devices when one tries to fully understand their operation: the thermodynamics driving PHP operation needs to be looked carefully. Heat addition and rejection and the growth /extinction of vapour bubbles drive the flow in a PHP. Even though the exact features of the thermodynamic cycle are still unknown, [Groll and Khandekar \[1.14\]](#) described it in general terms using a pressure/ enthalpy diagram as seen in [fig. 1.8](#). The temperature and vapour quality in

the evaporator and condenser are known, or can be assumed, so the state at the outlets of the evaporator and condenser are known. Starting at the evaporator inlet, (point A on the $P-\hat{h}$ diagram), the processes required to get to point B on the diagram can be simplified to heat input at a constant pressure combined with isentropic pressure increase due to bubble expansion. As one travels through the adiabatic section from the evaporator to the condenser, the pressure decreases isenthalpically. The thermodynamic process between the condenser's inlet and outlet are complicated, but can be simplified to constant pressure condensation with negative isentropic work. An isenthalpic pressure drop in the adiabatic section completes the cycle. Because of the numerous assumptions made in this description, thermodynamic analysis is insufficient to study PHPs.

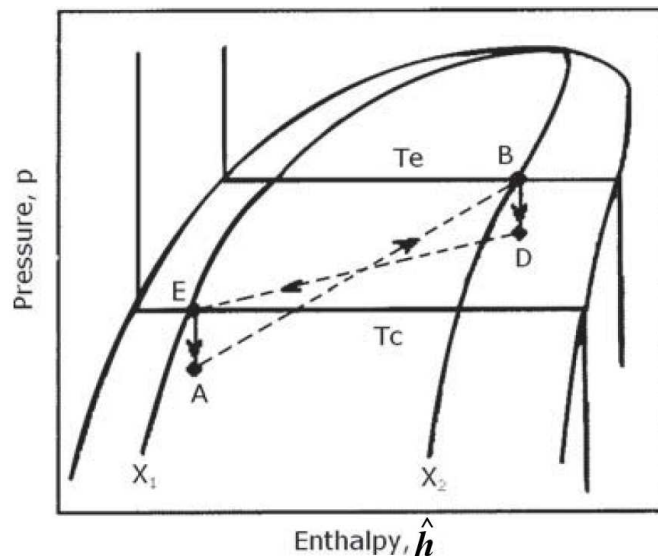


Fig. 1.8: Thermodynamic cycle of PHP (*Groll and Khandekar [1.14]*).

2.5. Hydrodynamics of PHPs

Fluid flow in a capillary tube consists of liquid slugs and vapour plugs moving in unison. The slugs and plugs initially distribute themselves in the partially filled tube. The liquid slugs are able to completely bridge the tube because surface tension forces overcome gravitational forces. There is a meniscus region on either end of each slug caused by surface tension at the solid/liquid/vapour interface. Due to the capillary dimensions of the PHP tube, a train of liquid slugs and vapour bubbles having menisci on their edges is

formed due to surface tension. Usually a liquid thin film exists around the bubbles. The contact angle of menisci, liquid thin film stability and its thickness depend on the fluid-solid combination and the operating parameters. Liquid slugs and vapour bubbles move against the gravity vector, either in its direction or at an angle to it, depending on the global PHP orientation and location of slugs/ bubbles in the up-header or down-header tubes. A detailed review on hydrodynamics parameters of pulsating heat pipes has been done by *Khandekar et al. [1.15]*, in which they show that the liquid slugs and vapour bubbles are subjected to pressure force F_1 and F_2 (*fig. 1.9*), from the adjoining slugs/bubbles. These are not only caused due to phase-change mass transfer but also due to capillary forces. The liquid slugs and vapour bubbles experience internal viscous dissipation as well as wall shear stress. Their relative magnitude decides the predominant force to be considered.

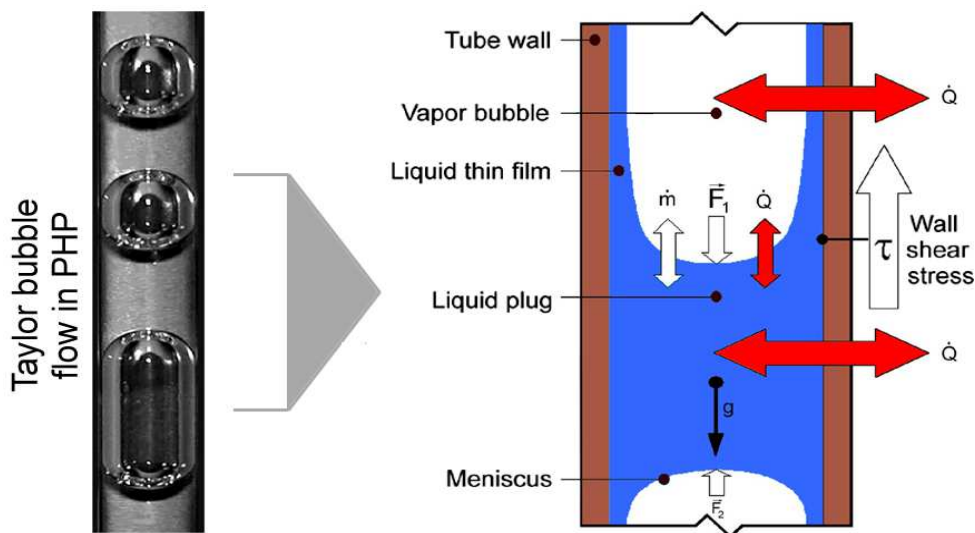


Fig. 1.9: Liquid slug in a PHP (*Khandekar et al. [1.15]*).

The slugs are separated by plugs. The vapour plug is surrounded by a thin liquid film trailing from the slug. *Fig. 1.10* shows the control volume for one liquid slug in a PHP and the forces acting on it *Shafii et al. [1.16]*. Motion of the i^{th} liquid slug within the PHP with an inner diameter of D and cross-sectional area of A can be described by the simplified momentum equation given by *Shafii et al. [1.16, 1.17]*:

$$\frac{dm_{li} v_{li}}{dt} = [P_{vi} - P_{v(i+1)}] A - \pi D L_{li} \tau \quad 1.4$$

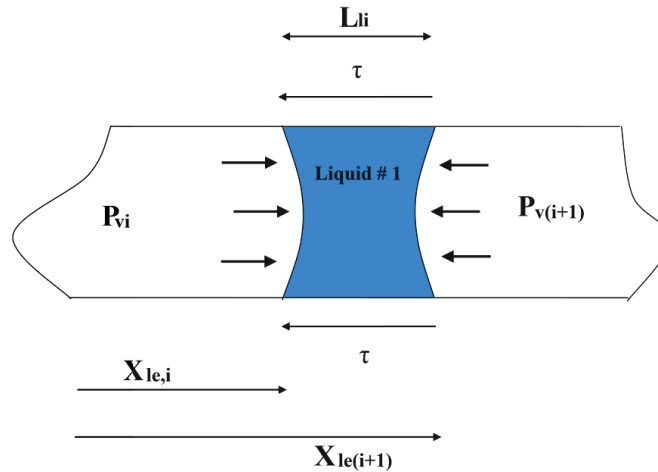


Fig. 1.10: Liquid slug in a PHP.

where, m_{li} , v_{li} , and L_{li} are the mass, velocity and length of the i^{th} liquid slug, respectively. The difference between vapour pressures of the i^{th} and the $(i+1)^{\text{th}}$ vapour plug, P_{vi} and $P_{v(i+1)}$, are the driving force for the oscillatory flow. The shear stress, τ , depends on whether the liquid flow is laminar or turbulent. A detail analysis about the hydrodynamics in a PHP will be discussed in chapter 2.

2.6. Heat transfer in a PHP

In order to properly evaluate total heat transfer in a pulsating heat pipe, the radial heat transfer between the pipe wall and the working fluid, the evaporative heat transfer, and the condensation heat transfer must all be considered. As the liquid slugs oscillate, they enter the evaporator section of the PHP. Sensible heat is transferred to the slug as its temperature increases, and when the slug moves back to the condenser end of the PHP, it gives up its heat. Latent heat transfer generates the pressure differential that drives the oscillating flow. The phase change heat transfer takes place in the thin liquid film between the tube wall and a vapour plug and in the meniscus region between the plug and slug, which requires complex analysis. Detailed understanding of such parameters will help in predictive modeling of the PHP. As we know that the evaporation/condensation dynamics is responsible for self sustained oscillations in a PHP. The heat

transfer in a PHP can be explained when and where it taking place, like in starting nucleate boiling for the formation of the bubbles, later there will be evaporation and condensation at the film. Heat transfer in thin films is a complex phenomenon and few researches have been found in this subject. In chapter 2 the terminologies and parameters affecting the thin film heat transfer will be explained.

3. Two research approaches for understanding of PHP working

Since the invention of PHP, several researchers have been putting efforts to understand and decode the physics involved in it. Most of the researches available on the PHPs are based on parametric studies without much explaining the physics behind it. In recent past there have been attempts to model a PHP by approximating various parameters affecting it. Recently it was also discussed that there is a need first to understand the local level physics happening in a PHP rather than directly going towards whole system modeling. In this direction unit cell approach (single tube: single vapour plug – liquid slug) for PHPs have been modeled and some of the researchers started building experiments based up on these modeling. There are also thoughts of some researchers that the unit cell approach (single tube: single vapour plug – liquid slug) is not exactly replicating the real PHP as it does not include the multiple vapour bubble – liquid slug interactions which may be the principle cause of PHP working. Let us now see how these two approaches (i) PHP studies as complete system (ii) Unit cell approach (single tube: single vapour plug – liquid slug) yields the various results and observation.

3.1. Studying PHPs as a complete system

Research on PHPs has seen an unprecedented increase during the last 15 years, almost 25 years after the system has been patented in its most popular layout by Akachi. Unfortunately, major part of the literature does not provide universally applicable generic knowledge base on these systems; it generally focuses on one particular PHP structure or type, designed for a specific application. In these type of works, the PHP is usually characterized by the temperature difference measured between the condenser and the evaporator for a given applied heat flux. Nevertheless, each PHP has its own geometrical and thermo-physical properties (inner and outer diameters, length, closed

or open-loop devices, evaporator, condenser and adiabatic lengths, number of turns, material of the tube, etc.) and is filled with a specific working fluid having also its own thermo-physical properties (latent heat, wettability and for both vapour and liquid phases: thermal conductivity and capacity, density, viscosity, etc.), and is tested in specific experimental conditions (heat load at the evaporator, ambient and condenser temperatures). A detailed review on advanced and unsolved issues in pulsating heat pipes has been done by *Zhang and Faghri [1.18]*. It was shown that there were several attempts to develop correlations for the overall Nusselt number in terms of non-dimensional groups of parameters. However, they all have a quite narrow range of applicability and fail if applied to other PHP prototypes. The number of relevant parameters to characterize a PHP is therefore so large that it is difficult to explicitly discriminate the effect of one parameter among the others in this type of experiments. As a result, one can find several research papers dealing with the same parameter and having conflicting conclusions. To overcome these difficulties, some authors developed non-dimensional expressions based on different numbers like the Jacob, the Karman, the Prandtl or the Kutateladze numbers and taking into account the number of turns (All these numbers are defined in *Appendix-A*). This occurs because the dynamic behavior of the PHPs may change strongly at slight variation of its parameters.

Systematic studies of the multi-bubble multi-turn PHPs are rare and concern mostly the qualitative description of its regimes. Nevertheless, this approach has also failed so far to provide a universal understanding of the PHP because the basic physical phenomena and the extent of parameters responsible for system dynamics are not yet well understood. More detailed quantitative information on the local measurement that would concern the menisci and film dynamics inside the PHP is lacking. Regarding the heat transfer in PHPs as a system, there have been various efforts taken by the researchers; here we are mentioning some of the important of them. *Khandekar et al. [1.19]* did a visualization and semi-empirical modeling on a closed loop PHPs. They showed that in the normal operation of the device, flow boiling occurs in closed loop PHPs. The type and magnitude of internal flow is a direct consequence of the applied heat flux, geometry and the inclination angle of operation and also showed importance of Bo on the functioning of PHPs. They said that, with very low input heat

fluxes, nucleate pool boiling or free convection nucleate boiling may be the only dominant phenomena in a PHP. A little increase in the heat flux will slowly give rise to nucleate flow boiling. On the other extreme, continuous increase of input heat flux will result in a condition where nucleate boiling may be completely suppressed and convective flow boiling becomes the dominant phenomenon (e.g. if annular flow quickly develops in the evaporator and heat transfer takes place through the liquid film–vapour interface). In nucleate boiling, the heat transfer coefficient is primarily dependent upon the heat flux and practically not at all upon the flow velocity. On the contrary, in convective boiling, the heat transfer coefficient is primarily influenced by the velocity of flow or by the mass flux, but on the other hand is scarcely influenced by the heat flux. Vapour mass quality is an additional independent variable for convective boiling. *Lee et al. [1.20]* conducted a visual study of the flow in a closed-loop oscillation heat-pipe with ethanol by varying in the inclination angles, filling ratios and working temperatures. They reported that oscillations of the bubble caused by nucleate boiling and vapour oscillation, and departure of small bubbles are considered as the representative flow pattern at the evaporator and adiabatic section, respectively.

Qu and Ma [1.21] did a theoretical analysis to determine the primary factors affecting the startup characteristics of a pulsating heat pipe. They found that the wall surface condition, evaporation in the heating section, superheat, bubble growth, and vapour bubbles trapped in cavities at the capillary inner wall affect the startup of oscillating motion in the pulsating heat pipe. Based on their experimental visualization they concluded that when the nucleate boiling occurs at the capillary inner wall, a large amount of vapour is produced. *Bhuwakietkumjohn and Rittidech [1.22]* investigated the internal flow patterns and heat transfer characteristics of a closed-loop oscillating heat-pipe with check valves (CLOHP/CV). It was found that the flow patterns occurred as annular flow + slug flow, slug flow + bubble flow and dispersed bubble flow + bubble flow respectively. There are two main phenomena occurring inside a CLOHP/CV, i.e., liquid slug and vapour slug counter-current flow phenomenon and boiling phenomenon. Bubble formation, formation of slugs or plugs, and boiling behavior conditions, are all important in understanding the heat transfer phenomena.

3.2. PHP local level approach (“unit-cell” approach)

Researchers agree that the oscillations are driven by an instability that appears due to coupling of the adiabatic vapour compression and evaporation/condensation mass exchange. Changing the nature of the fluid or the condenser temperature brought into focus a very wide range of behaviors that could not be explained in the absence of the general understanding of phenomena that occur inside the PHP. Indeed, the instability that causes the oscillations is yet to be studied. One has to begin with a system of a minimal complexity which is a straight capillary heated from one and cooled from the other end containing a single oscillating bubble *fig. 1.11*. This can be an important research effort dealt with systems of the reduced complexity with only one vapour bubble and/or liquid plug.

Although such a system seems to be simple, it contains the main phenomena involved in the multi-bubble PHP. One can mention evaporation/condensation of liquid continuous menisci and wetting films, motion of menisci and contact lines (film edges), viscous friction during the bubble motion among other phenomena that govern the PHP dynamics. Some of them have been extensively studied for stationary case. For example, evaporation of stationary liquid menisci in capillaries was studied in relation with the conventional heat pipes. On the other hand, the motion of constrained bubbles in capillaries (Taylor bubbles) is well studied under isothermal conditions (e.g. *Reinelt [1.23] and Bico and Quéré [1.24]*). It has been discovered that the viscous dissipation inside the wetting films left on the tube walls behind the moving liquid meniscus makes an important contribution to the overall pressure drop. Furthermore, the dissipation (and the pressure drop) is larger when the meniscus advances along the dry wall with respect to the wall with already deposited wetting film *Bico and Quéré [1.24]*. This shows the importance of the contact lines, the number of which might be large in the multibubble PHP.

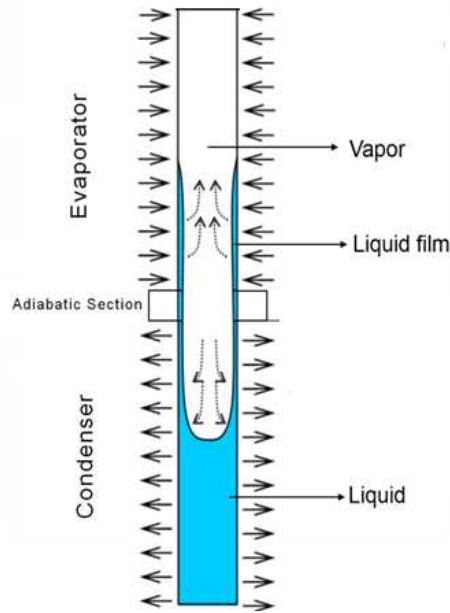


Fig. 1.11: Schematic of a Unit cell PHP (single tube: single vapour plug – liquid slug).

The evaporation at the contact lines and in the thin films has been actively studied (*Nikolayev [1.25]*). The evaporation in the constrained bubble geometry is studied in the domain of convective boiling (*Thome et al. [1.26]*). The dewetting in capillaries is also considered (*Callegari et al. [1.27]*). The oscillation of bubbles at isothermal conditions has been studied by *Lips and Bonjour [1.28]*. However, the conjunction of phase change and oscillating dynamics introduces new challenges. Some of them are related to inertial effects in particular with the oscillations in a capillary in isothermal case [*1.24, 1.29, 1.30*]. A first experiment of visualization of self-sustained oscillation of liquid meniscus in a capillary with evaporation/condensation was performed by *Lagubeau [1.31]*. It permitted to determine the main factors that determine the oscillation period.

Recently, since 2010, the number of works dealing with the physical phenomena occurring in the PHP (with PHPs of 1-2 bubbles) has remarkably increased [*1.32-1.36*]. This shows an acknowledgement by scientific community of the necessity of fundamental studies related to the PHP. Research at the local scale (i.e. at the scale of one bubble and one liquid plug), although few, were addressed quite early, in order to augment the knowledge on basic phenomena which are responsible for the oscillations

and the heat transfer in the system. In recent past researchers have done significant work to understand the basic governing physics of such simplified single branch systems. There are many researchers tried to model and performed experiments on such systems. Most of the system level models for PHPs are developed by using an average value of heat transfer coefficient (constant over time) to predict the convective heat transfer regime inside the evaporator. But in miniature unsteady devices, the fluid-dynamic conditions quickly change over time and the heat transfer coefficient can be strongly influenced by this transient, especially in the boiling regime. In next section we will discuss various modeling and experimental approaches taken by researchers.

3.2.1. Single branch modeling

From a modeling perspective, this approach was initiated by *Zhang and Faghri [1.37, 1.38]* and *Dobson [1.39, 1.40]*, who studied theoretically the governing mechanisms of a single branch of the PHP, consisting of one vapour bubble and one liquid slug. *Das et al. [1.34]* developed a similar approach including the two phase equilibrium that occurs locally at the liquid vapour-interface, especially along the time-varying wetting thin film which gets laid down by the liquid plug during its journey from the evaporator towards the condenser and through which the major part of the heat and mass transfer occurs. This film was shown to be responsible for the large flow oscillations observed in the system. In this work, an instability analysis of this system was also performed. The evaporation rate was assumed to be proportional to the difference of the temperatures of the vapour and the walls in contact with it. In the vapour bubble evolution equation this leads to terms analogous to those of sensible heat transfer between the vapour and the tube walls. It is well known from general considerations of thermal resistance that during the meniscus evaporation, an important contribution to the heat and mass transfer comes from thin liquid films that may cover the interior of the capillary. The local two-phase equilibrium exists at the interface of microscopically thin films *Quéré et al. [1.29]* so that the interface is at saturation or very close to it. This effect was completely neglected in the above mentioned works. *Dobson [1.39, 1.40]* has included a film in his single bubble PHP model. He introduced a lumped description of the liquid-vapour meniscus and the wetting films. However the film mass exchange was not related

to the liquid–vapour equilibrium and the mass exchange was proportional to the difference of temperatures of the vapour and the wall, just like in the other works that did not treat the films at all. The single-bubble model of *Zhang and Faghri [1.37]* has taken a step forward by rigorously showing that the most part of heat and mass exchange occurs via the films in the PHP. The shape of the curved meniscus including the film has been calculated. It is felt that to understand the working of the unit cell PHP it is eminent to understand the thin film behavior in two phase heat and mass transport systems. Globally, the existing models describe oscillations of small amplitude. During these oscillations, the meniscus is located mostly in the condenser section. This means basically that the evaporation in such models is almost inexistent, which contradicts most experimental results where strong amplitude meniscus oscillations are observed. At each oscillation the meniscus sweeps both the condenser and evaporator. These limitations have been successfully overcome within a film evaporation/condensation model *Das et al. [1.34]*. It uses the lumped meniscus geometry (*fig. 1.12*) and accounts for the two-phase equilibrium at the vapour–liquid interface. It explains large amplitude oscillations. An analytical expression describing the oscillations in the single-bubble PHP in the horizontal position has been established.

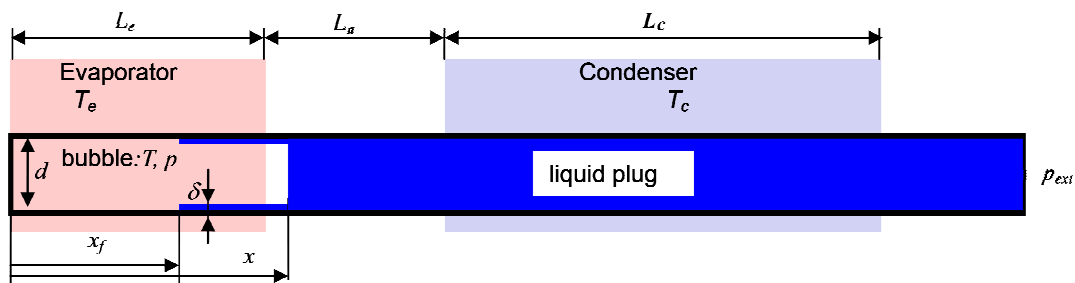


Fig. 1.12: Lumped meniscus/wetting film model for the single-bubble PHP [1.34, 1.39, 1.40] and its key geometrical and physical parameters. The pressure at the right open end of the tube is imposed to the value P_{ext} by connecting the tube to a large reservoir.

The approach of *Dobson [1.39, 1.40]* has been extended by *Shafii et al. [1.16, 1.17]* to model the PHP with multiple vapour bubbles, liquid plugs and tube bends. The local

scale modeling has been extended to several PHP branches with many liquid plugs and vapour bubbles [1.41-1.46].

As was noted earlier, exhaustive mathematical modeling of the phenomena occurring inside a PHP is yet an unaccomplished task. The models which are available for pressure drop and heat transfer coefficients are indeed very much simplified; they not only ignore the complex physics of the ‘unit-cell’, but the singular characteristics of oscillating hydrodynamics of Taylor bubbles also remain completely unaddressed.

3.2.2. Single branch PHP experiments

Looking the literature related to experimental studies on PHPs, the local approach to study its characteristics is comparatively even scarcer. Local heat transfer measurements in non-boiling Taylor bubble flow, in the context of pulsating heat pipes, have been recently addressed. Many research groups have shown that the flow field in single phase liquid flows gets significantly modified by slipping Taylor bubbles of gas/vapour through it, which eventually leads to enhanced heat transfer [1.47-1.49]. Continuing on these lines, *Mehta and Khandekar* [1.50] recently studied the heat transfer characteristics of pulsating Taylor bubble-train flow in square mini-channels using IRT, the frequency of imposed flow fluctuations similar to those encountered in PHPs. The main objective of the study was to observe the effects of externally imposed pulsations on local heat transfer taking place in a unit cell, comprising of a Taylor liquid slug trapped between two adjacent gas bubbles. The controlling parameter of the study was liquid and gas flow rates and imposed flow frequencies. The study indicated that liquid slug distribution is one of the important parameter for improving thermal performance of PHPs. Perturbing the Taylor bubble-train flow with imposed frequencies may conditionally lead to enhancement in the heat transfer in comparison to steady continuous Taylor bubble-train. The sensible heating/cooling transport capability of the liquid slugs can be altered by controlling the wake generated by the adjoining Taylor bubbles. Interfacial slip created by intermittent flow conditions, was the major cause for heat transfer enhancement. A similar experiment performed in cryogenic conditions was presented by *Bonnet et al.* [1.51, 1.52] in 2011 and in 2013 respectively. Compared to the previous experiment, their system was totally opaque; a thin micro-thermocouple

was used to measure the time varying temperature of the vapour, which showed that the vapour plug tended to be superheated in this single branch PHP experiment. This is a major result as this hypothesis had never been verified before, although it was proposed earlier by *Khandekar [1.3]*.

In the similar lines the work had been started by our group at CETHIL. In 2010, *Das et al. [1.34]* presented the first experimental data of the simplest ‘unit-cell’ version of a pulsating heat pipe consisting of one liquid plug and one vapour bubble. Their experimental setup was close to a real-PHP and also the theoretical configuration was previously studied by *Dobson [1.39, 1.40]*. It consisted of a capillary tube closed at one end and connected to a reservoir at a constant pressure at the other end (*fig. 1.13*). A single liquid plug adjoining a vapour bubble made to thermally auto-oscillate inside this tube, which was heated on one side and cooled down on the other side, thereby creating a continuous cycle of evaporation and condensation. The movement of the meniscus was recorded in the cooled section of the tube, while the heated section, made of copper, was opaque. The vapour pressure was also measured during the oscillations.

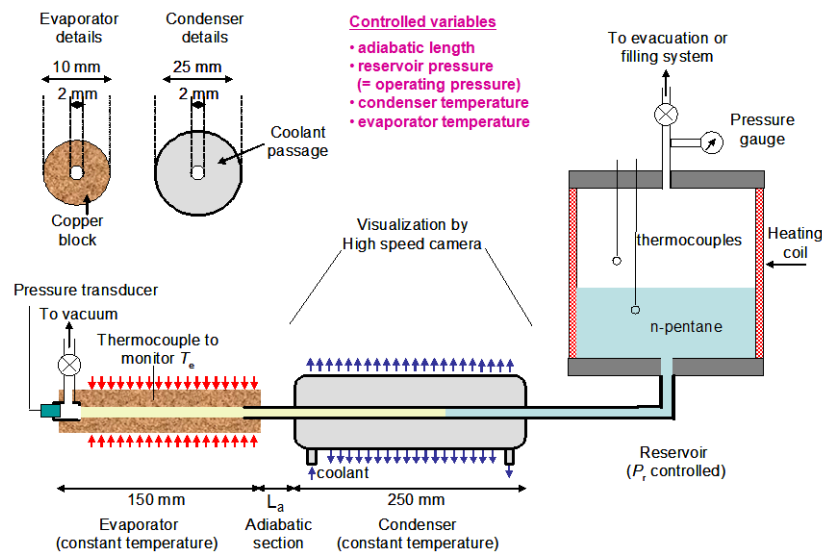


Fig. 1.13: Das et al. Setup in 2010 [1.34].

The model developed by *Das et al. [1.34]* has been compared with this single bubble experiment. The working fluid is n-pentane. The temperature T_c of the condenser

section of the tube is controlled by a transparent heat exchanger in which a coolant (water) is circulating. A vapour bubble is confined by the liquid at the closed side of the tube. The meniscus oscillations occur depending on the experimental conditions. Their frequency was about 3 Hz and the meniscus dynamics was observed in the transparent condenser with a high speed camera; the pressure of the vapour plug was also monitored (fig 1.14, left). The comparison with a theoretical model shows a reasonable agreement (fig. 1.14, right), at least regarding the orders of magnitude and the general trend.

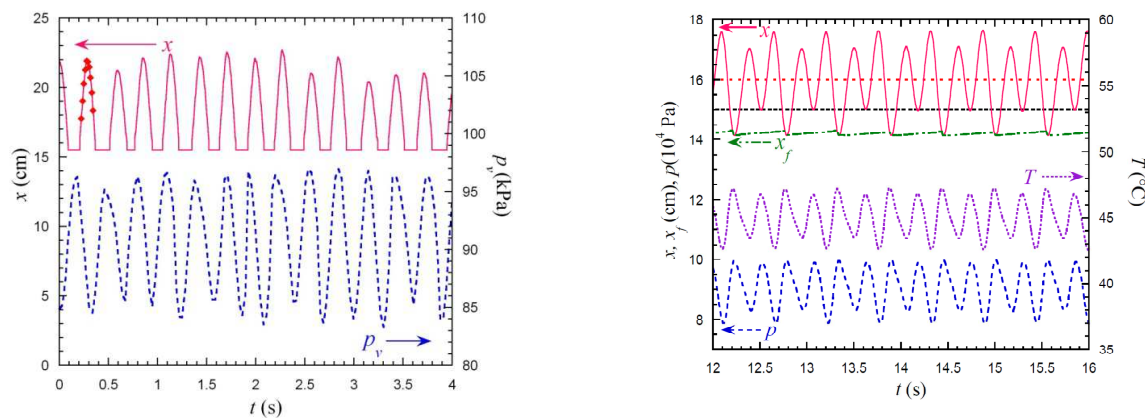


Fig. 1.14: Oscillations in the single bubble PHP (Das et al. [1.34]). Left: experimental measurement of the time evolution of meniscus position (x) and vapour pressure p (fig. 1.12). The meniscus position curve is cut from the bottom because the evaporator and adiabatic sections are opaque so that the meniscus is invisible there. Right: numerical modeling of the meniscus position (x) vapour pressure (p), vapour temperature (T) and film edge position (x_f).

4. Closing remarks, motivation of work and thesis chapter plan

As we have seen above, many efforts have been put recently on the topic of PHPs and the associated fundamental knowledge, but still the progress is very slow. The main reason for the slowness of the progress is the following. A large majority of the experimental studies of the PHP available in the literature concern the multi-bubble prototypes. However, it is technically impossible performing measurements (of pressure, temperature, etc.) for each individual bubble because both its ends move. For

the multi-bubble case, the measurements are thus limited to averaged over all bubbles values which cannot provide enough information necessary to understand the PHP functioning. In addition, the oscillations are much less chaotic than in the multi-bubble case, so that a smaller meniscus visualization area is sufficient. As explained previously, CETHIL (*Das et al. [1.34]*) had started experimenting single branch PHP. Some important experimental limitations were present in the work of *Das et al. [1.34]*. The experimental setup was not fully transparent, except the condenser section as indicated earlier, and therefore the internal hydrodynamic phenomena could not be observed in totality. Besides, the connection between the opaque metal evaporator and the glass condenser section was to induce some flow perturbations having potential impact on the smooth meniscus movement to a certain extent. Furthermore, experiments were done without any synchronization of the internal pressure measurements with the videography.

Das et al. [1.34] developed a simplified model based on the balance equations. This model conserves the main features of the multibubble PHP, the most important of which is the existence of self-sustained oscillations. This work shows a strong sensitivity of the modeling results to several parameters (or rather physical phenomena), on which the information is not yet available in the open literature. There is strong need to perform experiments (in particular those concerning the viscous dissipation) for a geometry where a single vapour bubble or liquid plug will travel along the capillary. In these experiments it is interesting to observe (i) the behavior of the wetting films, in particular their thickness and length, (ii) the viscous dissipation (pressure drop) during the oscillating bubble motion, and (iii) the vapour thermodynamics.

Looking in to the above discussion it is thought that a predictive modeling of the PHP is impossible without availability of reliable information on these phenomena. There is need to understand this combined system (solid-liquid-vapour system in a single branch PHP constituted of a channel wall, liquid meniscus and vapour plug) locally for finding the parameters affecting their thermo-hydrodynamics. It is visible that the thin film laid by the liquid on the channel walls plays an important role in working of PHP. Therefore it is required to understand the hydrodynamics and heat transfer characteristics of this

region which consists of thin film, solid wall and vapour, which in general is referred to as extended meniscus region.

In this respect as there are hardly any open literature available for thin films and their influence on working of PHPs, in chapter 2 we will be discussing the thermo-hydrodynamic and heat transfer features of combined solid-liquid-vapour system or extended meniscus with available literature. The chapter 2 will give us the directions to move ahead. Based up on the outcomes of chapter 1 and chapter 2, a methodology will be designed to solve the problem for which later in chapter 3, the experimental setup design and data processing will be presented. Chapter 4 will include detail analysis of experimental results and comparison of the experimental results with the available numerical models. In chapter 5 the numerical model developed will be illustrated and the results will be compared with the experiments. Chapter 6 will illustrate the conclusion of the thesis and future scope of work.

References

- 1.1 S. Lin, K. Sefiane, J. Christy, Prospects of confined flow boiling in thermal managements of Microsystems, *Appl. Therm. Eng.* 22 (2002) 825-837.
- 1.2 C. Lasance, Technical data column, *Electronics Cooling*, January 1997.
- 1.3 S. Khandekar, Thermo-Hydrodynamics of closed loop pulsating heat pipes, Ph.D. thesis, (2004).
- 1.4 G. Smyrnov, G. Savchenkov, former USSR Patent, Patent Number 504065, (1975).
- 1.5 H. Akachi, US Patent, Patent Number 4921041, (1990).
- 1.6 H. Akachi, US Patent, Patent Number 5219020, (1993).
- 1.7 H. Akachi, US Patent, Patent Number 5490558, (1996).
- 1.8 H. Akachi, F. Polasek, P. Stulc, Pulsating Heat Pipes, *Proc. 5th International Heat Pipe Symposium Melbourne, Australia*, (1996) 208–217.
- 1.9 K.A. Triplett, S.M. Ghiaasiaan, A. Khalik, S.I. Le-Mouel, B.N. McCord, Gas-Liquid two-phase flow in microchannels Part II: Void fraction and pressure drop, *Int. J. Multiphase Flow*, 25 (1999) 395-410.

- 1.10 P.A. Kew, K. Cornwell, Correlations for the prediction of boiling heat transfer in small-diameter channels, *J. Appl. Therm. Eng.*, 17 (1997) 705-715.
- 1.11 S. Khandekar, M. Groll, On the definition of pulsating heat pipes: An overview, *Proceedings of 5th Minsk International Conference*, Minsk, Belarus (2003).
- 1.12 J.L. Xu, Y.X. Li, T.N. Wong, High speed flow visualization of a closed loop pulsating heat pipe, *Int. J. Heat Mass Transfer*, 48 (2005) 3338–3351.
- 1.13 H. Yang, S. Khandekar, M. Groll, Performance characteristics of pulsating heat pipes as integral thermal spreaders *Int. J. Ther. Sci.* 48/4 (2009) 815-824.
- 1.14 M. Groll, S. Khandekar, Pulsating Heat Pipes: Progress and prospects, *Proc. International Conference on Energy and the Environment*, Shanghai, China, 1 (2003) 723–730.
- 1.15 S. Khandekar, P.K. Panigrahi, F. Lefèvre, J. Bonjour, Local hydrodynamics of flow in a pulsating heat pipe: a review, *Front. Heat Pipes*, 1, 023003 (2010) 1–20.
- 1.16 M.B. Shafii, A. Faghri and Y. Zhang, Thermal modeling of unlooped and looped pulsating heat pipes, *ASME J. Heat Transfer*, 123 (2001) 1159–1171.
- 1.17 M.B. Shafii, A. Faghri, Y. Zhang, Analysis of heat transfer in unlooped and looped pulsating heat pipes, *International Journal of Numerical Methods for Heat & Fluid Flow*, vol. 12/5, (2002) 585–609.
- 1.18 Y. Zhang, A. Faghri, Advances and unsolved issues in pulsating heat pipes, *Heat Tran. Eng.*, 29(1) (2008) 20–44.
- 1.19 S. Khandekar, P. Charoensawan, M. Groll, P. Terdtoon, Closed loop pulsating heat pipes Part B: visualization and semi-empirical modeling, *Appl. Therm. Eng.* 23 (2003) 2021–2033.
- 1.20 W.H. Lee, H.S. Jung, J.H. Kim, J.S. Kim, Flow visualization of oscillating capillary tube heat pipe, 11th International Heat Pipe Conference, Tokyo, Japan, (1999) 131-136.
- 1.21 W. Qu, H.B. Ma, Theoretical analysis of startup of a pulsating heat pipe, *Int. J. Heat Mass Transfer* 50 (2007) 2309–2316.
- 1.22 N. Bhuwakietkumjohn, S. Rittidech , Internal flow patterns on heat transfer characteristics of a closed-loop oscillating heat-pipe with check valves using ethanol and a silver nano-ethanol mixture, *Exp. Therm. Fluid Sci.*, 34 (2010) 1000–1007.
- 1.23 D.A. Reinelt, The rate at which a long bubble rises in a vertical tube, *J. Fluid. Mech.* 175 (1987) 557-565.
- 1.24 J.Bico, D. Quéré, Falling slugs, *J. Colloid Interface Sci.* 243 (2001) 262-264.

- 1.25 V.S. Nikolayev, Dynamics of the triple contact line on a nonisothermal heater at partial wetting *Phys. Fluids*, 22 (2010) 082105.
- 1.26 J.R. Thome, V. Dupont, A. Jacobi, Heat transfer model for evaporation in microchannels, Part I: Presentation of the model, *Int. J. Heat Mass Transfer*, 47 (2004) 3375-3385.
- 1.27 G. Callegari, A. Calvo, J.P. Hulin, Dewetting processes in a cylindrical geometry, *Eur. Phys. J.* 16 (2005) 283-290.
- 1.28 S. Lips, J. Bonjour, Oscillating two-phase flow in a capillary tube,: experiments and modeling, *Proc. 14th Int. Heat Pipe Conf., Florianopolis, Brazil, (2007)*.
- 1.29 D. Quéré, E. Raphaël, J.-Y. Ollitrault, Rebounds in a capillary tube, *Langmuir*, 15 (1999) 3679-3682.
- 1.30 E. Lorenceau, D. Quéré, J.-Y. Ollitrault, C. Clanet, Gravitational oscillations of a liquid column in a pipe, *Phys. Fluids*, 14 (2002) 1985-1992.
- 1.31 G. Lagubeau, Propulsion par moteur pop-pop, Master's thesis, supervisor: D. Quéré, PMMH-ESPCI, Paris (2006).
- 1.32 S. Lips, A. Bensalem, Y. Bertin, V. Ayel, C. Romestant, J. Bonjour, Experimental evidences of distinct heat transfer regimes in pulsating heat pipes (PHP), *Appl. Therm. Eng.*, 30 (2010) 900-907.
- 1.33 S. Das, V.S. Nikolayev, F. Lefèvre, B. Pottier, S. Khandekar, J. Bonjour, Thermally induced two-phase oscillating flow inside a capillary tube *Int. J. Heat Mass Transfer*, 53 (2010) 3905 - 3913.
- 1.34 S.P. Das, F. Lefèvre, S. Khandekar, J. Bonjour, Parametric study of a two-phase oscillating flow in a capillary tube, *Proc. 15th Int. Heat Pipe Conference, Clemson, USA, (2010)*.
- 1.35 A. Tripathi, S. Khandekar, P.K. Panigrahi, Oscillatory contact line motion inside capillaries, *Proc. 15th Int. Heat Pipe Conference, Clemson, USA, (2010)*.
- 1.36 T. Inoue, T. Kouduma, R. Senjayaand Y. Suzuki, Bubble generation in oscillating heat pipe, *Proc. 15th Int. Heat Pipe Conference, Clemson, USA, (2010)*.
- 1.37 Y. Zhang, A. Faghri, Heat transfer in a pulsating heat pipe with open end, *International J. Heat Mass Transf.*, 45 (2002) 755-764.
- 1.38 Y. Zhang, A. Faghri, M.B. Shafii, Analysis of liquid-vapour pulsating flow in a U-shaped miniature tube, *Int. J. Heat Mass Transf.*, 45 (2002) 2501-2508.
- 1.39 R.T. Dobson, Theoretical and experimental modeling of an open oscillatory heat pipe including gravity, *Int. J. Therm. Sci.* 43(2) (2004) 113-119.

- 1.40 R.T. Dobson, An open oscillatory heat pipe water pump, *Appl. Therm. Eng.*, 25(4) (2005) 603–621.
- 1.41 V.S. Nikolayev, A dynamic film model of the pulsating heat pipe, *J. Heat Transfer*, 133 (8) (2011) 081504.
- 1.42 V.S. Nikolayev, Towards predictive modeling of pulsating heat pipes, in: *Proc. 16th International Heat Pipe Conference*, INSA Lyon, Lyon, France, (2012).
- 1.43 M. Mameli, M. Marengo, S. Khandekar, Towards Quantitative Validation of a Closed Loop Pulsating Heat Pipe Numerical Model, invited lecture in *Proc. 16th Int. Heat Pipe Conf.*, INSA, Lyon, France (2012).
- 1.44 M. Mameli, M. Marengo, S. Zinna, Numerical model of a multi-turn closed loop pulsating heat pipe: Effects of the local pressure losses due to meanderings, *Int. J. Heat Mass Transf.*, 55 (2012) 1036–1047.
- 1.45 R. Senjaya, T. Inoue, Oscillating heat pipe simulation considering bubble generation Part I: Presentation of the model and effects of a bubble generation, *Int. J. Heat Mass Transfer* 60 (2013) 816–824.
- 1.46 V.S. Nikolayev, Dynamics of the triple contact line on a nonisothermal heater at partial wetting *Phys. Fluids*, 22 (2010) 082105.
- 1.47 A.K. Bajpai, S. Khandekar, Thermal transport behavior of a liquid Plug Moving Inside a Dry Capillary Tube, *Heat Pipe Sc. Tech.*, 3(2-4) (2012) 97–124.
- 1.48 A. Majumder B. Mehta, S. Khandekar, Local nusselt number enhancement during gas-liquid Taylor bubble flow in a square mini-channel: An experimental study, *Int. J. Thermal Sci.*, 66 (2013) 8–18.
- 1.49 B. Mehta, S. Khandekar, Taylor bubble-train flows and heat transfer in the context of pulsating heat pipes, *Int. J. Heat Mass Transfer*, 79 (2014) 279–290.
- 1.50 B. Mehta, S. Khandekar, Measurement of local heat transfer coefficient during gas-liquid Taylor bubble train flow by infrared thermography, *Int. J. Heat Fluid Flow*, 45 (2014) 41–52,
- 1.51 F. Bonnet, P. Gully, V.S. Nikolayev, Experimental study of a single branch cryogenic pulsating heat pipe: first results, in: *Proc. Eurotherm Sem. on gravitational effects on liquid-vapour phase change*, IUSTI, Hyeres, France, (2011).
- 1.52 F. Bonnet, P. Gully, V.S. Nikolayev, N. Luchier, T.Q. Tran, Evaluation of the vapour thermodynamic state in PHP, *17th Int. Heat Pipe Conf.*, October 13-17, Kanpur, India, (2013).

Chapter 2

Literature review: Thermo-hydrodynamics of extended meniscus related to single branch PHPs

As discussed in the previous chapter, universal thermal performance modeling of Pulsating Heat Pipes (PHP) requires local, spatio-temporally coupled, flow and heat transfer information of self-sustained thermally-driven oscillating Taylor bubble flow, under different operating conditions. Local hydrodynamic characteristics such as velocities, lengths, shapes/profiles of bubbles/slugs, their dynamic contact angles, thickness of the liquid film that surrounds the bubbles, enhanced mixing/ flow circulation within the liquid slugs and net pressure drop along the flow, etc., are needed to predict local heat transfer methodology and thus the global thermal performance. Hence it is necessary to understand first, what are the parameters which are important in studying the local level or unit cell approach in a single branch PHP. The methods to define the nature and target continuum of the problem are not well defined in available open literature. Hence here we are trying to prepare a state of the art using the related knowledge available in this field. To start with, let us go insight in the thermo-physical parameters involved in working of a single branch PHP and later we will see the issues and their solution methodologies.

1. Thermo-physical parameters in a single branch PHP – The extended meniscus region

As we saw capillary dimensions of the PHP tube, a liquid slug and vapour bubble having meniscus on their edge is formed due to surface tension. Usually, a liquid thin film exists around the bubble. The interfacial interactions of menisci, liquid thin film stability and its thickness depend on the fluid-solid combination and the operating parameters. It is widely accepted and observed in a PHP that the thin film is let on the wall when the meniscus moves from its extreme position in the evaporator towards the

condenser. Some experimental results clearly show that evaporation of the thin film is responsible for the oscillation observed experimentally in PHP studies. The films in PHP are thicker than in capillary heat pipes and are extensively of hydrodynamic origin; their thickness depends on the meniscus velocity. The heat transfer depends however on the contact line effects that define the film length. To the best of our knowledge, there are no explicit studies available in open literature related to pulsating thin film evaporation.

In general this problem can be tackled using the available knowledge on thermo-hydrodynamics for the so called extended meniscus by keeping in virtue our main goal of understanding the working of self-sustained thermally driven oscillating Taylor bubble flows for single plug and meniscus pulsating heat pipe system (single branch PHP).

As it is shown in chapter 1, the thin film region is responsible for high heat transfer rates because of very low thermal resistance across the liquid film. Some liquid also get adsorbed in the solid wall, but the very small scales involved in this adsorbed region is not of much interest while studying the PHP functioning. Most of the studies available for this region are in the colloidal science theory and hardly gives any help in solving our PHP problem as an engineering point of view. So this state of art will mostly focus on ‘Intrinsic meniscus region (bulk liquid)’ and ‘Thin film region’. This thin film region and intrinsic meniscus region in combined can be called as ***extended meniscus region***. In other words “extended meniscus” stands for a region of space that extends from the bulk liquid to the vapour around the liquid-vapour interface and triple line. We found that most of the researches are based upon the steady film evaporations, which give the general physics behind the static film evaporation and hardly talks about its engineering applications. To add in to it, thermally induced pulsations in meniscus and vapour system which are typically found in a PHP, will only complicate the solution. By generalising the problem to the basic level, it can be compared and evaluated using standard solutions given by researchers for static thin film heat transfer. This may help us in understanding and solving the thin film heat transfer problem in unit cell PHPs. So it is evident that the meniscus and thin film region is the driving factor and should be the area of interest to understand the happenings at local level of a single branch PHP

system. Let us disintegrate this region and factors involved in understanding it and for that knowing capillary and disjoining pressure is vital.

1.1. Capillary pressure and disjoining pressure

The capillary effect comes from the variations of surface energy between different interfaces. In a capillary channel, a pressure jump attributed to the capillary forces occurs between at the interface of two fluids that forms a meniscus of radius R (fig. 2.1). This resultant jump is commonly known as **capillary pressure** P_{cap} .

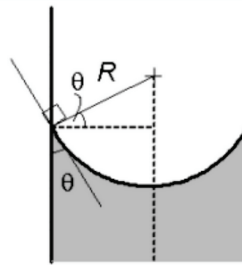


Fig. 2.1: Meniscus of radius R formed in a channel due to variations of surface energies of solid channel wall and liquid.

Adsorption of substances on the solid surface may limit the spreading of liquids over the surfaces. When wetting liquid films are very thin, the attractive forces between solid and liquid act to pull liquid in to the film layer as if the pressure in the film layer reduces below vapour pressure by an amount P_{dis} , which is known as **disjoining pressure** P_{dis} . By convention, if the affinity of the liquid for the solid draws liquid in to the film, P_{dis} is taken negative. *Derjaguin [2.1]* first conceptualized disjoining pressure as a means of explaining solid-liquid thin-film interactions. A typical power law correlation (*Potash and Wayner [2.2]*) for the disjoining pressure in term of film thickness δ_{lf} and constants A and B is given as:

$$P_{dis} = -A \delta_{lf}^B \quad 2.1$$

For non-polar liquids, the primary cause of disjoining pressure is London dispersion forces resulting from the interaction of the positive nucleus of one molecule with the

electrons of another molecule (*Wee et al. [2.3]*). This is the weakest of the van der Waals forces but nevertheless given the size scale involving in the extended meniscus region, these van der Waals forces will play a significant role in analyzing such systems.

1.2. Fundamentals of extended meniscus region

To understand the construction of the extended meniscus region, let us first go through the different aspects of this region. When a liquid wets a solid wall in a tube, the meniscus is formed. Subsequently this region can further be divided into three sub regions, as shown in *fig. 2.2*, (i) An adsorbed or non evaporating region, here liquid is adsorbed on the tube wall where the capillary forces are negligible and disjoining pressure plays a predominant role (ii) An evaporating thin film or transition region where effects of long-range molecular forces (disjoining pressure) as well as capillary forces are felt; (iii) An intrinsic meniscus region where capillary forces dominate and there is no influence of disjoining pressure.

Looking the historical developments in the understanding of above mentioned sub regions, *Derjaguin et al. [2.1]* developed an analytical theory and showed that the rate of evaporation from a capillary does not depend on the vapour diffusion through the gas only but also on the transport of liquid through the film caused by the film thickness gradient and near the adsorbed region, the disjoining pressure is dominant. According to him, the disjoining action could explain the deviation from the laws of hydrostatics that exists in the thin wetting film. Transitioning towards the bulk region or intrinsic meniscus, there is a changeover of dominance as disjoining pressure diminishes and capillary pressure is more prominent.

Potash and Wayner [2.2] studied the transport processes occurring in a two-dimensional evaporating extended meniscus where the fluid flow results from both capillarity and disjoining pressure. They found that, the pressure gradient for fluid flow includes the effect of disjoining pressure and the presence of an adsorbed superheated film results in a smooth transition between the evaporating and non-evaporating portions of the extended meniscus.

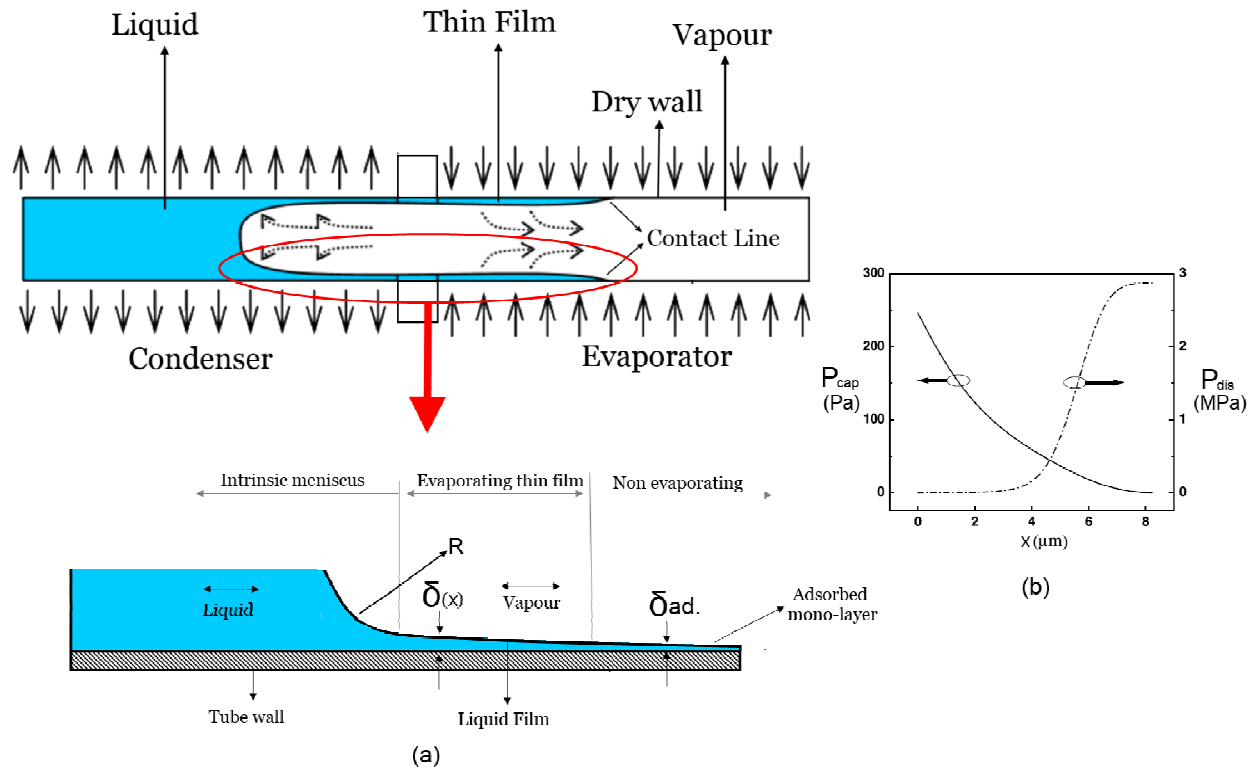


Fig. 2.2: (a) Schematics of an extended meniscus in unit cell PHP (b) A typical comparison of capillary and disjoining pressure obtained by numerical simulation for meniscus formed by water in a micro-channel where $x=0$ is at intrinsic meniscus and increasing when move towards higher values of x (*Park et al. [2.4]*).

These above two researchers set a benchmark for the further refinement of the knowledge in the meniscus region. Later various researchers worked on this problem by taking above work as a base and proposed the solution methods to tackle the thermo-hydrodynamics of this region. Since the clear distinction arrived among the behaviours of these sub regions, the knowledge is increasing day by day. By looking developments in these defined sub regions (adsorbed region, intrinsic meniscus region and thin film region), we can shortlist the factors which are of our interest and can directly apply in the study of the local level governing physics of single branch PHP.

1.2.1. Adsorbed or non-evaporating region

The adsorbed region as shown in *fig. 2.2* is on the nanometer scale and is governed by several key attributes. The variation of properties in the interfacial region between two

phases is actually continuous, and the values of the properties in this region are generally different from those in the bulk phase. For a pure vapour in contact with solid wall, attraction between solid and vapour molecules can thus increase the density of vapour molecules in the interface region near solid surface. The excess vapour density above bulk value is the amount said to be adsorbed onto the surface. Taking in to account the size and scale of this region, it is mainly characterized by the supremacy of van der Waals forces between the liquid and solid wall (*Wee et al. [2.3]*). This leads to the inability of the superheated liquid molecules to evaporate within the adsorbed region, as they are restrained by these overwhelming adhesive forces (*Wee et al. [2.3] and Stephane [2.5]*). It is these adhesive forces that prevent evaporation that allow the region to be considered of uniform thickness δ_{ad} (*fig. 2.2*) and of unspecified length [*2.5-2.9*]. This thickness however is temperature dependent. It is thus concluded that the imposed curvature value within the adsorbed region is almost zero. The thickness of the adsorbed region is sometimes given a constant value estimated from the size scale of the problem, (*Park et al. [2.4, 2.10]*).

However, it is now known that minor changes to the adsorbed film thickness can result in large changes in thin-film flow and evaporation rate (*Lin and Faghri [2.11]*). *Wayner [2.12]* showed that the adsorbed film thickness varies with temperature and concludes that using a constant value will miscalculate the total heat transport through the thin-film. A final best guess is valid that within the adsorbed layer, considering the size and scale of this region, it is understood that the fluid temperature is identical to that of the solid wall [*2.3, 2.9, 2.13*].

1.2.2. Intrinsic meniscus region

The intrinsic meniscus region as shown in *fig. 2.2*, is the bulk region can be the best identifiable part of the liquid vapour interface, and can be seen with the bare eye, whether it is observed as a graduated cylinder or a bucket. In the many prior representations, it is like a concave meniscus. The capillary pressure is dominant, with an insignificant contribution of disjoining pressure [*2.3, 2.4, 2.8*]. It is for this reason that the bulk region is governed by the Young-Laplace equation (explained in section 3

of this chapter) and is often considered to have a constant curvature (*Stephan [2.5]*). This constant curvature is often used as a far-field boundary condition when determining the transition from the thin-film region to the bulk meniscus (*Stephan [2.5]*). The concavity of a meniscus is determined by the cohesive interaction of the liquid with the substrate (*Polansky [2.14]*). In a concave meniscus, the liquid molecules have a greater affinity for the solid substrate than the bulk liquid. The evaporative mass flux contribution in intrinsic meniscus region is tiny as compared to that of the thin-film region. This has been distinguished in several works of (*Wang et al. [2.13]* and *Buffone et al. [2.15]*).

1.2.3. Thin film or transition region

Referring to thin film region (*fig. 2.2*), *Potash and Wayner [2.2]* studied the transport processes occurring in a two-dimensional evaporating region, where the fluid flow resulted from both capillarity and disjoining pressure. *Wee et al. [2.3]* also endorsed this concept. As mentioned in the intrinsic meniscus section constant curvature was found for that region and the termination of this constant curvature can be called as the beginning of the thin-film region. Defining the beginning of the thin-film region can also be done with confidence, as it transitions to the adsorbed region when curvature is zero *Wee et al. [2.3]* and *Wang et al. [2.8]*. *Wang et al. [2.16, 2.17]* defined the thin-film region as ending at a location when the disjoining pressure drops to 1/2000th of $P_{\text{dis-ad}}$, the disjoining pressure in the non evaporating or adsorbed region. Thin-film heat transfer is seen to increase with an increase in disjoining pressure, and decrease with increasing liquid viscosity.

1.3. The road ahead – The meniscus region

However slope and curvature dependences of the disjoining pressure may in fact lead to enhanced values of the heat transfer coefficient close to the adsorbed film region and reduced values of the same for axial locations progressively towards the intrinsic meniscus, as compared to the predictions from the more traditional considerations. Such considerations may be potentially important for a more precise and improved design of cooling strategies for thermal management of electronic devices with the aid of

micro-scale heat pipes. The suggested modifications in the theoretical treatment become progressively more significant as the disjoining pressure becomes more and more significant, as compared to the standard capillary pressure. This is indeed the case in the thin film region, especially towards the vanishingly thin limit of the meniscus profile.

The heat transfer is greatly influenced by hydrodynamic and thermodynamic characteristics of contact line or triple line (three phase contact line) where liquid-vapour interface joins the tube wall. In the case of evaporation in capillaries (PHPs) a similar situation with a stationary or moving three phase contact line appears that is governing the liquid-vapour meniscus evaporation. Very strong shear is required to make these thin films flow. The flow exists only near meniscus and near contact line. Keeping in mind the proposed analytical solutions for the typical static thin films heat transfers, to improve or validate them for a unit cell heat transfer problem along with coupling of heat transfer with the Taylor bubble hydrodynamics. The discussion can majorly be divided in 2 parts;

(a) Hydrodynamics transport features of extended meniscus.

(b) Heat transfer characteristics of extended meniscus.

2. Hydrodynamic transport features of extended meniscus

As discussed earlier, this extended meniscus region normally begins with the thin film generation in two phase flows in capillaries. To understand the phenomenon happening at the extended meniscus region, first we need to know the origin of it and parameters affecting the hydrodynamics of this region. We need to go through two phase flows in capillaries. Later we will discuss the major factors involved in understanding hydrodynamics of such flows in relation to the extended meniscus. These factors arise from the solid-liquid mutual interactions and governing physics of this combined liquid-solid system. These interactions are in the form of interfacial tensions and their resulting behavior. Majorly saying in understanding hydrodynamics of an extended meniscus, entire boundary phenomena involved in these interfacial interaction are important like contact angle, contact line statics and dynamics. Also the contact line motion and pressure drops occurring due to these interactions, will also influence the

study of the extended meniscus and further to the overall local level understanding of single branch PHP system.

2.1. Two phase flows in capillaries

When a liquid phase and a vapour or gas phase coexist in a channel, the phase distribution can take up variety of configurations, known as flow patterns. The particular flow pattern depends on the channel geometry, conditions of pressure, flow, and heat flux if the channel is heated. The mechanisms of transport of heat, momentum and mass in two-phase flow conditions are severely affected by the distribution of phases in the channel. It is therefore desirable to detect what are the flow pattern or successive flow patterns are present so that a hydrodynamic or heat transfer theory appropriate to that pattern can be chosen. Various flow patterns encountered in vertical upwards co-current flows are shown schematically in *fig. 2.3* (Collier and Thome [2.18]).

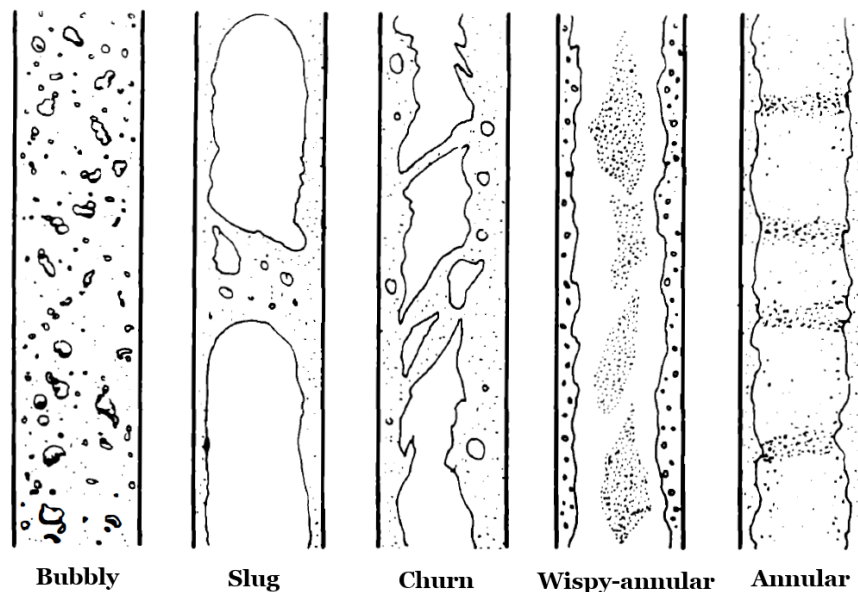


Fig. 2.3: The flow patterns encountered in vertical upwards co-current flows (Collier and Thome [2.18]).

In all of the flow patterns **slug flow** is the predominant flow pattern in the PHP working as stated by *Khandekar et al. [2.19]*. It is one of the vital multi-phase flow pattern often taking place in two-phase flow systems. In this type of flow, the motion of

a gas/vapour bubble (entrapped between liquid slugs) is observed which are also similar to the flow pattern found in PHPs (as shown in *fig. 2.4*). Slug flow belongs to a class of intermittent flows that has very typical features. There is an inherent random/statistical constituent for such a flow because of intermittent phase reversal which results in fluctuations of pressure and velocity. The nose of the bubble has a characteristic spherical cap and the gas in the bubble is separated from the pipe wall by a slowly descending film of liquid. The liquid flow is contained in liquid slugs which separate successive gas bubbles. These slugs may or may not contain smaller entrained gas bubbles carried in the wake of the large bubble. The length of the main gas bubble can vary evidently. The two-phases may be composed of an either gas-liquid two-component system or single component, vapour-liquid system. Capillary slug flow or **Taylor bubble flow** is one of the sub-classes of conventional slug flow; as noted, this particular pattern appears when surface tension dominates over gravitational body force¹. Due to this, capillary slug flows exist in horizontal as well as in vertical orientations. Also, flow is essentially laminar and predominantly viscous (*Khandekar et al. [2.19]*).



Fig. 2.4: Liquid slug in a PHP (*Khandekar et al. [2.19]*).

2.2. Taylor bubble flows

Taylor slug flow conditions are typically characterized by a sequence of long bubbles which are trapped in between liquid plugs. The diametrical size of these bubbles is nearly comparable to the pipe diameter while their axial length scale can be several times the pipe diameter. A thin liquid film always separates the bubbles from the channel wall. The thickness of this film varies from millimeter scale to micro scale

¹ *i.e., in the presence of the terrestrial gravity field, when the channel diameter reduce at least down to millimeters or μ meters.*

depending upon the dimensions, geometry, flow velocity, orientation of the channel and the thermo-physical properties of the fluid, channel used and heat flux if the channel is heated. The intermittent liquid plugs may also have small diameter bubbles (much smaller than the pipe diameter) entrapped inside them (*Khandekar et al. [2.19]*), this tendency reduces as the Bond number decreases. Taylor bubbles are characterized by strong geometric constraints. *Bretherton [2.20]* observed that a Taylor bubble does not raise spontaneously in water-filled vertical capillary under the effect of gravity for $Bo < 1.8$; this value can also be used to define small channels. *Khandekar et al. [2.19]* stated that the presence of the film that separates the bubble from the wall is responsible for the bubble velocity but is different than the liquid velocity. The recirculation patterns within the liquid slugs improve heat and mass transfer from liquid to wall and interfacial mass transfer from gas/vapour to liquid. Thus, Taylor flow offers many advantages for carrying out heat mass and momentum transfer operations compared with other patterns and with single-phase laminar flow.

The film surrounding the bubbles is the only bridge between two successive slugs, and mostly, its thickness is very small in comparison with the tube diameter. For practical estimation of mass transfer coefficients across the boundaries, properties such as thickness of film that surrounds the bubbles, bubble shape and velocity, bubble and slug length, flow patterns in the liquid slug, and pressure drop, are some of the primary focus of interest. The flow and heat transfer are influenced by the dynamics of a very small group of bubbles or typically, isolated slug bubbles, rather than the averaged behavior of a large population of bubbles. This, in principle, improves the prospects of developing mechanistic models. Such development needs to be facilitated by localized experimental observations of slug-bubble systems with synchronized measurements of the resulting fluctuations in local conditions such as temperature, pressure and wall heat flux. Mass transfer characteristics are also affected by the local hydrodynamic properties of the flow. The main forces acting on slug-bubble system are due to surface tension, viscosity, inertia, gravity (body forces), applied tangential shear stress and the force associated with the disjoining pressure at the molecular level. This gives rise to primary non-dimensional numbers. For details please refer to *Appendix-A*.

It has also been found that the surface energy (surface wetting capability) of the wall may have great impact on the interfacial film dynamics when a confined bubble is flowing along with liquid in a mini /microchannel (*Aussilous and Quéré [2.21]*). Modeling multi-phase fluid flow at the micro-scale with the assumption of simple disjoining pressure and liquid surface tension may not be accurate (*Akbar and Ghiaasiaan [2.22]*). To predict the shape, length and pressure drop under Taylor bubble flows, it is important to understand the basic physics of governing the interfacial region. In this regard now we will discuss the various parameters involved in defining the interfacial region.

2.3. Interfacial contact line and affecting parameters

When a gas or vapour phase is introduced in a liquid phase, a chance of formation of three-phase contact lines between the parent fluid, the dispersed phase and the solid channel/duct (where fluid is in contact). These three-phase contact lines are in addition to the gas-liquid two-phase interfaces. Possibility of formation of three-phase contact lines in a PHP is high, especially in the evaporator section where bubble formation and growth of confined bubbles takes place. Elsewhere in the PHP, the Taylor bubbles usually travel with a liquid film around them. In the case of unit cell approach of the single liquid slug and single vapour slug in a single branch PHP, there is a strong chance of formation of three phase contact line. The understanding of statics and dynamics of three phase contact line will give us chance to look it in more insight of the problem.

2.3.1. Three-phase contact lines: Statics

Three-phase triple contact lines are said to be formed when materials in different phases, e.g. solid, liquid and gas (or vapour) intersect. Common examples are a liquid droplet spreading on a solid surface or a liquid meniscus in a capillary tube. The angle between the tangents at the liquid /gas interface and the liquid /solid interface is known as the **contact angle θ** of the liquid on the solid surface.

Typically, when a liquid spreads on a solid surface in the presence of the third phase (gas or vapour), several equilibrium states can be achieved from non-wetting state to

(theoretical) complete wetting state as shown in *fig. 2.5 (a)*. This wetting phenomenon of a solid, by a given liquid, and the ultimate equilibrium state is governed by physical chemistry, statistical physics, short and long-range forces and fluid dynamics. The condition for static equilibrium of a triple contact line involving an ideal solid (perfectly smooth and chemically homogeneous), liquid and a gas/vapour is stated in eq. 2.2 and called as the Young's equation (*Carey [2.23]*);

$$\sigma_{sv} - \sigma_{sl} - \sigma_{lv} \cos(\theta) = 0$$

2.2

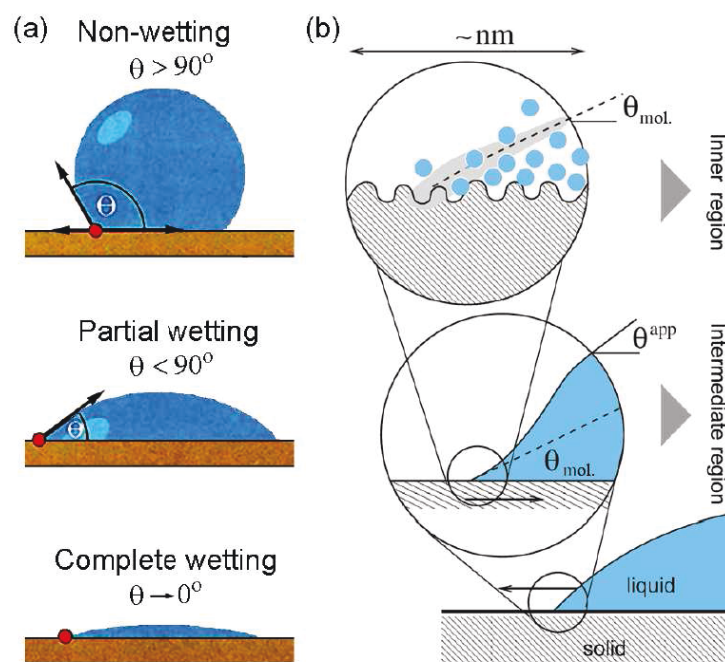


Fig. 2.5: (a) Contact angle of a fluid on solid substrate (b) The moving meniscus seen on three different length scales (*Khandekar et al. [2.19]*).

In the case of adsorption of liquid on the solid wall, there is the retention at the interface of solid, liquid or gas molecules, atoms, or ions by a solid or a liquid. As we know that the film formation widely depends up on the wettability of the interface surface, adsorption may affect the wetting of a liquid on a solid in at least two ways. First concentration of molecules at the liquid-vapour interface can reduce interfacial tension, and this reduced interfacial tension directly affects the contact angle, which may affect the wettability. Second this concentration of molecules at the interface can also alter

interfacial tension of the solid-vapour interface. Including this effect in eq. 2.2, modifies the contact angle as (*Carey [2.23]*):

$$\sigma_{lv} \cos \theta = (\sigma_{sv} - \pi_s) - \sigma_{sl} \quad 2.3$$

Where, $\pi_s = (\sigma_{sv} - \sigma'_{sv})$ and σ'_{sv} is the interfacial tension without adsorption

As we know high energy surfaces such as metals or glass have large values of interfacial tension of the solid-vapour interface (σ_{sv}), which may affect the contact angle appreciably. This indicates that adsorption on a solid surface may affect its wetting characteristics.

The equilibrium wetting conditions of a liquid on a solid surface can also be stated in terms of the **equilibrium Spreading coefficient, S_{eq}** . The spreading coefficient indicates the tendency of liquid to wet and spread into a thin liquid film. Which also represents the surface free energy per unit area σ_{sv} relative to its value for complete wetting, i.e.:

$$S_{eq} = \sigma_{sv} - (\sigma_{sl} - \sigma_{lv}) = \sigma_{lv} (\cos \theta - 1) \quad 2.4$$

For complete wetting, the equilibrium spreading coefficient S_{eq} is zero while for partial wetting conditions it is a negative quantity. As noted above, systems may not achieve complete equilibrium, at least in the time frame of the experiments, and to deal with such conditions, the initial spreading coefficient is defined as follows:

$$S_i = \sigma_{so} - (\sigma_{sl} + \sigma_{lv}) \quad 2.5$$

The **initial spreading coefficient S_i** , is a more relevant quantity of interest, especially under dynamical conditions of the contact line. Note that σ_{so} is the surface tension of the dry solid surface, contrary to σ_{sv} which is the surface tension of the solid surface in equilibrium with the gas or vapour. It is known that this latter quantity is

always lower than the former because of adsorption of gas/vapour molecules which lowers the surface tension of the solid. Thus, S_i is always larger than S_{eq} .

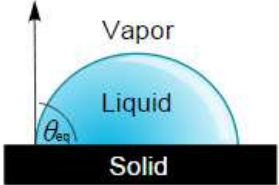
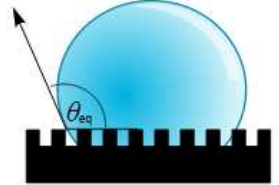
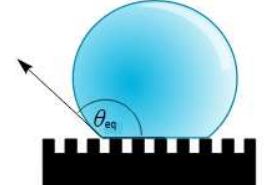
For the cases where equilibrium is not reached and S_i is negative (which means that S_{eq} is also more negative), the contact line will display a finite **static contact angle** θ_{st} which will not be the same as the earlier defined contact angle θ . When S_i is positive, although the droplet will spread and tend to flatten, there is no surety whether S_{eq} will necessarily be zero or negative. Thus, the drop may initially spread and if enough time is given for achieving true equilibrium, it may either become a case of complete wetting ($S_{eq} = 0$) or it may retract back to a case of partial wetting ($S_{eq} < 0$). In general, though, if S_i is large and positive, the equilibrium state is usually characterized by $S_{eq} = 0$, however there can be exceptions when $S_{eq} < 0$. It is difficult to get values of S_{eq} and even more difficult to estimate S_i ; careful experiments are the only meaningful alternatives for engineering applications.

Consequently, the contact angle depends not only on the thermo-physical properties of the liquid, but also on the physico-chemical structure of the solid substrate. If all the respective interfacial tensions are known, the equilibrium static contact angle can thus be estimated. But the SV (Solid- Vapour) and SL (Solid-Liquid) tensions are not only difficult to estimate but predictive theories are also weak. Also, validity of eq. 2.2 is restricted to ideal surfaces, which are rarely found in engineering practices.

This makes the Young's equation eq. 2.2 rather impractical and, frequently careful experiments are needed to estimate the '**static equilibrium contact angle** θ_{eq} '. It must be noted that true 'thermodynamic' equilibrium (mechanical, chemical and thermal) may be extremely difficult to achieve, especially for non-volatile fluids; at least, mechanical equilibrium (force balance) is mandatory in the definition of θ_{eq} . It is in this light that Young's equation eq. 2.2 is best derived by considering a reversible change in contact position, using global energetic arguments, i.e. the nature of the contact line region, over which intermolecular forces are acting, is not considered. Accordingly, θ_{eq} is understood to be measured macroscopically, on a scale above that of long range

intermolecular forces. Depending on this equilibrium contact angle, solid substrates, for a given fluid, may behave as in table 2.1;

Table 2.1: Static equilibrium contact angle θ_{eq} range for various types of fluids

Fluid type	Static equilibrium contact angle θ_{eq} Range	Schematic
Hydrophilic	$0^\circ \leq \theta_{eq} \leq 90^\circ$	
Hydrophobic	$90^\circ \leq \theta_{eq} \leq 150^\circ$	
Super-hydrophobic	$150^\circ \leq \theta_{eq} \leq 180^\circ$	

We know that the PHPs are also made up of tubes which are real time engineering surfaces, both physically and chemically heterogeneous. Therefore, efforts are needed to restore to systematic experimental work to get the real picture of actual contact angles. In doing such experiments and subsequent post-processing of the data, there are two more related issues which need careful consideration (i) ‘Apparent’ nature of the contact angle and its hysteresis, and, (ii) pinning of contact lines.

The scale at which we look at the three-phase contact line manifests a dramatic change in our perception of the contact angle, which the liquid-gas interface makes with the liquid-solid interface. This is explained in *fig. 2.5-b* (Khandekar et al. [2.19]). From a macroscopic viewpoint, wherein the length scale is of the order of capillary radius (or the droplet radius, in case of spreading droplets), the angle which the liquid-gas interface makes with the liquid-solid interface is termed as the **apparent contact**

angle θ^{app} ('apparent dynamic contact angle', if the contact line is moving). As we move to smaller scales from the 'outer' macroscopic regions, and approach towards the contact line, we pass through an 'intermediate' or proximal region where there is interplay of viscous and surface tension forces. This region is characterized by a rapid change in the interface slope. A point of inflection is evident in this region where the interface profile turns from concave to convex. Moving further closer to the contact line, we eventually reach the 'inner region'. This region is of the order of nanometers and characterized by interaction of molecular long-ranged forces. The interface here is constantly under thermal and diffusive fluctuations and it is not possible to uniquely determine the contact angle. Thus, for all practical purposes, we shall use and refer to the 'apparent' contact angle (and drop repetitive use of the word 'apparent'), unless stated otherwise.

The surfaces which are neither smooth nor chemically homogeneous require some corrections for the contact angle theory. Under such situations, the static contact angle turns out to be non-unique and it is observed that it depends on the way the surface was "prepared". Experiments involving the estimation of wettability are extremely sensitive to physical and chemical heterogeneities of the substrate. *Wenzel [2.24]* has developed correlations for 'apparent contact angle θ^{app} ' by taking influence of physical roughness (for a chemically homogeneous surface):

$$\cos \theta^{app} = r \cos \theta_{eq} \quad 2.6$$

Indeed usually roughness refers to an average distance between peaks and troughs expressed in ' μm ', which is not the case here. Here θ^{app} is the apparent contact angle, r is a characteristics parameter for the roughness ($r = 1$ is a smooth surface and $r > 1$ is a rough surface). It embodies two types of behaviors. If $\theta_{eq} < 90^\circ$ (hydrophilic substrate), we will have $\theta^{app} < \theta_{eq}$ since $r > 1$. Likewise, if $\theta_{eq} > 90^\circ$ (hydrophobic substrate), we will have $\theta^{app} > \theta_{eq}$. It is known that these angles can be sufficiently tuned by varying solid roughness. The same line of reasoning can be applied to a surface that is physically homogeneous but having n chemically heterogeneous species on its surface, which gives the Cassie-Baxter's relation:

$$\cos \theta^{\text{app}} = \sum_{i=1}^n \tilde{f}_i \cos \theta_{\text{eq-}i}; \text{ Where, } \sum_{i=1}^n \tilde{f}_i = 1 \quad 2.7$$

Here, θ^{app} is the apparent contact angle on the chemically inhomogeneous surface, $\theta_{\text{eq-}i}$ are the respective contact angles on the n chemically homogeneous surfaces respectively, \tilde{f}_i is the fractional area occupied by the i^{th} specie. Therefore, the apparent angle θ^{app} (which is restricted to the interval $(\theta_{\text{eq-}1}, \theta_{\text{eq-}n})$) is given by an average involving the angles characteristic of each constituent, but the average is applied to the cosines of these angles. Thus, we see that the contact angle of a liquid on a substrate depends on the roughness and chemical homogeneity of the surface; the three-phase contact line of the drop is deformed due to the physical and/or chemical topographic heterogeneities (this is true whenever the length scale of the three phase contact line is larger than the typical length scale of the physical/ chemical in-homogeneity).

2.3.2. Three-phase contact lines: Dynamics

Most classical work on dynamics of spreading is confined to two major arrangements; (i) forced flow in a capillary tube and (ii) spontaneous spreading of a droplet on a smooth horizontal surface. It is also important to note that these classical theories of contact line dynamics are usually restricted to cases where there is (a) no hysteresis of contact angles (b) gravitational effects are negligible (Bond number tending to zero), and, (c) practically no inertia effects Weber number tending to zero. Another limitation of these experiments, which have tried to isolate the interplay of purely viscous and surface tension forces, is that most experiments have been performed on dry surfaces for fluids with $\text{Si} > 0$. Furthermore, for the experiments with forced flow in capillary tubes, the effect of capillary diameter for a given liquid, i.e Bond Number, on the dynamics has not been extensively studied although there are clear indications that such dependency exists.

In general, for experiments involving submersion of a solid plate in free surface of a liquid with very slow moving constant velocity, two distinct values of the apparent contact angles are seen. These angles are known as **apparent advancing** θ_{adv} and **receding** θ_{res} angles respectively, depending on the direction of motion, as shown in

fig. 2.6-a. The difference between the advancing and receding contact angles is known as **contact angle hysteresis**. It is generally acknowledged to be a consequence of three factors: (i) surface in-homogeneity, (ii) surface roughness, and (iii) impurities on the surface. This can be more clearly understood by considering *fig. 2.6-b* which shows the sketch of the wetting behavior on a substrate with a continuously varying physical topography (chemical texture is homogeneous) and continuously varying chemical texture (physical topography is uniform). *Fig. 2.6-b* (i) shows that if the drop size is smaller than the topography, then the drop shape is not affected by the topography. But if the drop size is bigger than the physical topography then the global shape of the drop will be affected due the deformation of the three phase contact line due to the topography. Similarly, for a substrate with a gradient in wettability, as shown in *fig. 2.6-b(ii)*, the drop shape will be deformed due to the variation of the contact angles around the three-phase contact line of the drop. If, on the other hand, the substrate has sharp topography or wettability pattern then situation is very different, as shown in *fig. 2.6-c*.

At such sharp discontinuities, Young's equation eq. 2.2 becomes ill-defined. As a result, the three-phase contact line gets locally immobilized which is known as the pinning of contact line. The contact angle at the discontinuous boundary can have any value in between the smaller angle θ^- on the more hydrophilic part and the larger value θ^+ on the more hydrophobic part. The contact line then becomes immobilized and its position gets fixed to the line of discontinuity as long as the contact angle falls into the free range between θ^- and θ^+ .

In case of an operating PHP, none of these assumptions may be valid and most hydrodynamics is under pre-wetted conditions. Nevertheless, the available theory of spreading provides fundamental insights into the phenomena under consideration. The contact angle formed between a flowing liquid meniscus or a front and a solid surface is achieved by a balance between the capillary forces and the viscous forces. These two forces can be conveniently scaled by the Capillary number defined as:

$$Ca = \mu \cdot \frac{U}{\sigma} \quad 2.8$$

Where, μ is dynamic viscosity of the fluid, U its velocity and σ its surface tension. The viscous drag force on the liquid slug inside a capillary tube and the capillary force on the slug, scale respectively as:

$$F_{\text{drag}} \approx \left(\mu \cdot \frac{U}{R} \right) \left(\frac{L_s}{R} \right) (\pi R^2) \text{ and } F_{\text{cap}} \approx \sigma \cdot (2\pi R) \quad 2.9$$

Where R is the capillary radius and L_s is the slug length.

Thus, we deduce the scaling ratio of the drag and the capillary force as:

$$\left(\frac{F_{\text{drag}}}{F_{\text{cap}}} \right) \approx \left(\mu \cdot \frac{U}{\sigma} \right) \left(\frac{L_s}{2R} \right) \approx \text{Ca} \left(\frac{L_s}{2R} \right) \quad 2.10$$

It is clear that increasing liquid slug length L_s increases the net drag force vis-à-vis the capillary forces. Estimation of capillary forces require explicit knowledge of the dynamic apparent contact angles, both advancing and receding, when a unit-cell (Taylor bubble along with the adjoining liquid slug) train is passing through a capillary tube. One of the earliest mention of a ‘universal’ law between the velocity of spreading and the apparent advancing contact angle is highlighted by the work of *Rose and Heins [2.25]* who could correlate $\cos(\theta_a)$ with the velocity of the contact line. For capillary tubes which are already pre-wetted with a thin layer of liquid, eq. 2.11 was found to be suitable (*Khandekar et al. [2.19]*):

$$\tan(\theta_{\text{adv}}) = 3.4(\text{Ca})^{1/3} \quad 2.11$$

Hoffman [2.26] did two sets of experiments: (a) with silicon oils having complete wetting, i.e. $S_i > 0$ and (b) with liquids having non-zero static contact angle. For the former range of experiments and $\text{Ca} \rightarrow 0$, he found a rather universal relation between θ_{adv} and Ca :

$$Ca = A_1 (\theta_{adv})^{q_1}$$

2.12

The $\log(\tan(\theta_{adv}))$ vs. $\log(Ca)$ has a slope of $1/3$ but it is obvious that eq. 2.11 cannot be valid for values of θ_{adv} approaching 90° .

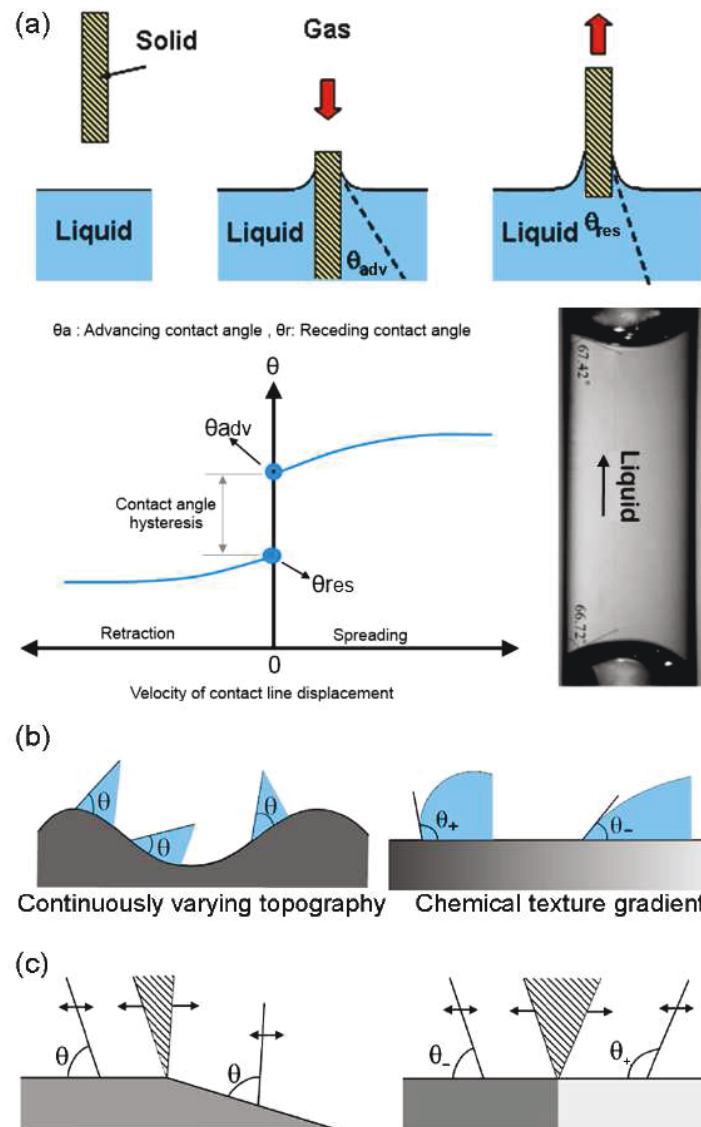


Fig. 2.6: (a) Contact angle hysteresis, (b) continuously varying physical and chemical in-homogeneity, and (c) sharp physical or chemical discontinuities at the surface (*Khandekar et al. [2.19]*).

where, $q_1 = 3.0 \pm 0.5$. In the experiments at low Ca, θ_{adv} first increases as $(Ca)^{1/3}$ but ultimately $\theta_{adv} \rightarrow \pi$ as $Ca \rightarrow 1$. For the second series of experiments, the data could be represented by the form:

$$Ca = A_2 (\theta_{adv} - \theta_{st}) \quad 2.13$$

Where, θ_{adv} is advancing contact angle, θ_{st} is static contact angle and A_2 is constant. While there are many assumptions and underlying limitations in the above 'laws', it is remarkable to note that these relations hold for liquids having different spreading coefficient $S_i > 0$, i.e., the magnitude of spreading coefficient apparently does not have any influence. A systematic theoretical and experimental study in a dry capillary was conducted by *Tanner [2.27]* and a simple cubic relation between the apparent dynamic advancing contact angle and Ca was established:

$$\theta_{adv} \sim K_1 (Ca)^{1/3} \quad 2.14$$

Optical observations of spreading silicone oil drops by Tanner, showed that the droplet profile had an inflection near the edge, consistent with the existence of a pressure gradient arising from surface tension, which caused the spreading motion. The edge profile was predictable and the analysis showed that the edge velocity was approximately proportional to the cube of the slope at the inflection. The relationship given by (eq. 2.13 or 2.14) is therefore referred to as Tanner's Law or Hoffman-Tanner law. *Fig. 2.7* shows the typical variation of the Tanner law curve by taking K_1 equal to 1.92. Other improved forms, by taking a somewhat stronger power law with the exponent of Ca equal to 0.39 and constant K_1 equal to 3.4 and more detailed treatment by incorporating a weak logarithmic dependency of the constant K_1 which gives:

$$\theta_{adv} \sim K_3 \left(Ca \cdot \ln(K_4 Ca^{2/3}) \right)^{1/3} \quad 2.15$$

All these variants of Hoffman-Tanner law are valid for low Ca ranging from 10^{-6} - 10^{-2} , under the assumptions discussed earlier in this section. For dynamic systems

with non-zero static contact angle, the Hoffman-Tanner Law can be slightly modified and extended as:

$$\theta_{\text{adv}}^3 - \theta_{\text{st}}^3 = A_3 \cdot \text{Ca} \quad 2.16$$

If Ca is small, linearization of (eq. 2.16) leads to *Berthier* [2.28]:

$$\theta_{\text{adv}} = \left(\theta_{\text{st}}^3 + A_3 \cdot \text{Ca} \right)^{1/3} \approx \theta_{\text{s}} \left(1 + \frac{1}{3 \left(A_3 \cdot \frac{\text{Ca}}{\theta_{\text{st}}^3} \right)} \right)$$

Or 2.17

$$\theta_{\text{adv}} - \theta_{\text{st}} = \frac{1}{3} \left(A_3 \cdot \frac{\text{Ca}}{\theta_{\text{st}}^3} \right)$$

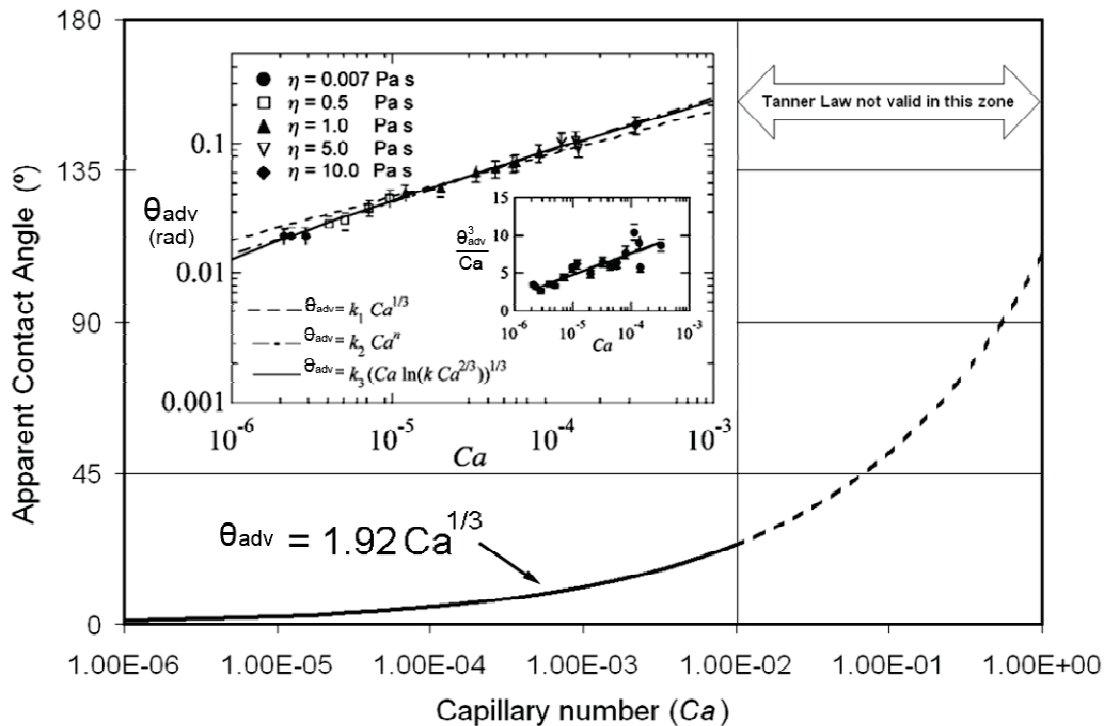


Fig. 2.7: Variation of apparent contact angle with Ca as per Tanner's law. Inset shows experimental data by *Kavehpour et al.* [2.29].

These equations inform us that the advancing contact angle is larger than the static contact angle and a receding contact angle is smaller than the static contact angle. This observation has been frequently reported qualitatively in the context of PHPs also.

2.3.3. Initial film thickness

Characteristics of the liquid film in micro-scale two phase flows are not fully understood, and thus designing two-phase flow systems still remains as a difficult task. It is reported that the thickness of the liquid film is one of the most important parameters for predicting two phase flow heat transfer in micro tubes, *Thome et al. [2.30]*; *Kenning et al. [2.31]*; *Qu and Mudawar [2.32]*. The thin film thickness is of particular interest as most of the heat transfer that takes place in PHP is believed to occur in this region. When gas bubble displaces a wetting fluid in a capillary, a liquid film is deposited on the capillary between the gas bubble and the inside wall as shown in the pioneering work of *Fairbrother and Stubbs [2.33]*. To find the initial thickness of this laid film is still an issue of debate between scientific communities. Many researches have been conducted to investigate the characteristics of liquid film both experimentally and theoretically. The classical Landau-Levich problem of dip coating, in which an immersed plate is dragged out slowly to allow deposition of thin film of coating, has been a long studied and understood phenomena since its inception in 1942. Since then, various aspects of it has been investigated and well understood. Predicting the instability of the film formed, knowing the thickness of the coating as a function of capillary number, effects of surface tension, and many more critical aspects of dip coating have been well researched and documented. This has paved way to numerous industrial application of dip coating process. In this background, the idea of extending the dip coating predictions to flow in a capillary tube is attempted here.

Early on it was known that the film thickness follows the scaling $(\delta/R) \sim Ca^{1/2}$ for Ca ranging from 10^{-5} to 10^{-1} . Seminal analytical work, with some simplified assumptions by *Bretherton [2.20]* established the scaling as $(\delta/R) \sim Ca^{2/3}$, the theory being valid for creeping flows at low Ca ranging from 10^{-3} to 10^{-2} and bubble Weber number much lower than 1. Although, the theory is based on low Ca assumption, it under-predicts the

film thickness at the lower range of Ca. This discrepancy has been explained by various mechanistic models and arguments (*Goldsmith and Mason [2.34]*; *Schwartz et al. [2.35]*), the most convincing being the effect of variable surface tension in the film and the bubble cap region, which in turn increases the film thickness at low Ca (*Ratulowski and Chang [2.36]*). Many experiments have confirmed the scalings, some results being close to Bretherton's theory while some more closely following that proposed by *Fairbrother and Stubbs [2.33]*. Various numerical studies, especially at high Ca, have been done in the context of Taylor bubbles not only to predict the bubble film thickness but also the Taylor bubble shape (*Edvinsson and Irandoust [2.37]*; *Giavedoni and Saita [2.38]*; *Heil [2.39]*). The effect of inertia (average flow Reynolds number) is also felt on the bubble shape and film thickness; it is non-monotonic but not profound. With increasing Reynolds number, the film thickness first decreases slightly and then somewhat increases. In addition, ripples and capillary waves can be seen on the interface. Moreover, the Froude number also affects the bubble shape as the significance of body forces increase; this is especially true while comparing upward and downward Taylor bubble flows. Increasing Ca also leads the shape of the back of the Taylor bubble to change from convex to concave (*Taha and Cui [2.40]*).

For low bubble velocities as in the case of very viscous fluids as in *Bretherton [2.20]*, the deposited film thickness is governed by momentum balance between viscous and capillary forces. For the fluids with low viscosity which we use in pulsating heat pipes like water, ethanol and FC72, we need to take in account higher fluid velocities so as to take inertial forces in to account in momentum balance. Keeping in this view, *Aussilous and Quéré [2.21]* have taken two systems with regard to viscosity and fluid velocity range: a visco-capillary regime for fluids with low velocity and high viscosity, using empirical Taylor's law: $\delta/R \approx Ca^{2/3}/(1+Ca^{2/3})$, applicable up to $Ca = 1$; and a visco-inertial regime, corresponding to higher fluid velocities with non negligible inertial effects in the film deposition mechanisms. They introduced a correcting factor taking into account the inertial effects by introducing the Weber number.

Recently *Han and Shikazono [2.41]* have performed a large experimental study of liquid film thickness measurements for bubbles in steady motion and under acceleration. By

applying a scaling analysis to the forces acting on the bubble to fit their experimental data, they proposed the following relationship to estimate the film thickness in laminar flow conditions:

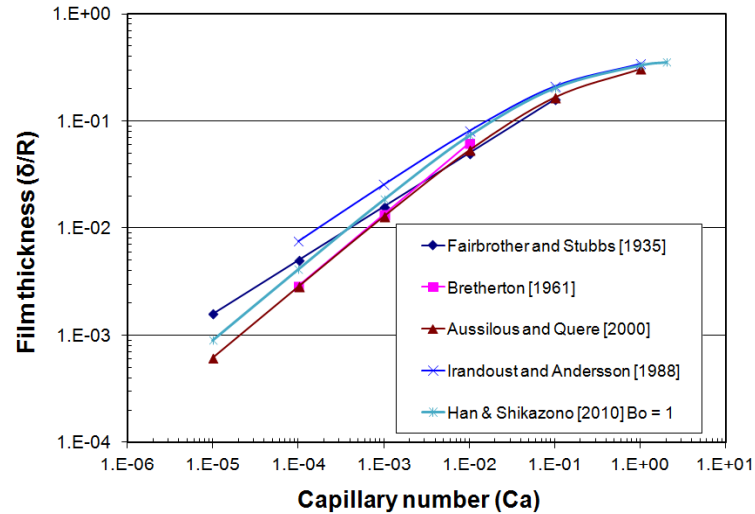
$$\left(\frac{\delta}{D}\right) = \min\left[\left(\frac{\delta}{D}\right)_{\text{steady}}, \left(\frac{\delta}{D}\right)_{\text{acc}}\right] \quad 2.18$$

Where δ is the liquid film thickness at the beginning of the flat film region which follows the bubble nose region. Values of the thickness under steady and accelerated conditions are obtained by empirical expressions: in their experiment, when the flow is accelerated the velocity profile in the preceding liquid slug strongly affects the liquid film formation (the liquid film becomes much thinner as flow is accelerated). Experimental correlation for the initial liquid film thickness under accelerated condition is proposed by introducing the Bond number. In order to develop precise micro-scale two-phase heat transfer models, it is necessary to consider the effect of flow acceleration on the liquid film formation.

Fig. 2.8 shows the variation of film thickness with Capillary number by using five commonly available correlations, as listed therein, along with their validity range. The effect of high Ca region is well captured by the correlations of *Aussilous and Quéré* [2.21], which at low Ca, overlaps with the Bretherton's theory. For proposed correlation by *Han and Shikazono* [2.41], Bo is taken equal to unity for the sake of comparison. As seen from the figure, all of the correlations results closely match with each other and hence it can be said that for assumption of initial film thickness by use of any of these will not make any significant error.

In the context of a PHP, looking into the experiments available so far with common working fluids like water, ethanol, acetone, and common refrigerants etc., typical Ca will be ranging from 10^{-4} to 10^{-1} (*Xu et al.* [2.43]). Systematic PHP visualization experiments are needed to quantify the film thickness regimes likely to be encountered in practice under oscillatory conditions. This is especially important in the adiabatic section which has substantial contribution in the overall pressure drop. In the evaporator and

condenser sections of the PHP the situation is more complicated due to phase-change processes.



Fairbrother and stubbs [1935]

$$\frac{\delta}{R} = 0.50(Ca)^{1/2}$$

Irandoust and Andersson [1988]

$$\frac{\delta}{R} = 0.36[1 - \exp(-3.08(Ca)^{0.54})]$$

Bretherton [1961]

$$\frac{\delta}{R} = 1.34(Ca)^{2/3}$$

Aussilous and Quere [2000]

$$\frac{\delta}{R} = \frac{1.34(Ca)^{2/3}}{1 + 2.5(1.34(Ca)^{2/3})}$$

Han & Shikazono [2010]

$$\frac{\delta}{R} = 2 \cdot \left(\frac{0.968 \cdot Ca^{2/3} \cdot Bo^{-0.414}}{1 + 4.838 Ca^{2/3} \cdot Bo^{-0.414}} \right)$$

Fig. 2.8: Variation of film thickness with Capillary number, as per five correlations mentioned therein.

2.3.4. Effect of interfacial contact line behaviour

At present, the dynamics of the fluid surrounding the contact line, and hence the contact line motion itself, is not fully understood. *Tripathi et al. [2.44]* explained that, depending on the wettability of the fluid on the solid wall, in conjunction with the applied external surface and body forces, there can be three types of oscillatory contact line motion of the liquid gas/vapour meniscus confined in a tube viz. (a) No pinning - the average velocity of contact line scales with the average bulk liquid velocity, (b)

Partial pinning - there is a phase lag in the contact line velocity and the bulk fluid velocity, and (c) Full pinning, the contact line is motionless while the bulk liquid moves/oscillates. Further, in cases (a) and (b), there can also be contact angle hysteresis in advancing and receding strokes.

These possible cases are shown qualitatively in *fig. 2.9* (2D axisymmetric representation); cases *fig. 2.9-a, b, c* show three different stages during oscillating flow of single meniscus without pinning, partial pinning and full pinning respectively. Similarly, *fig. 2.9-d, e, f* show liquid slug without pinning, partial pinning and full pinning respectively. These different behaviors of the contact line motion will greatly affect the functioning of the PHP. A detail study using various fluids is required to fully understand the behaviours of the fluid solid interactions and subsequently the overall effect on PHP working.

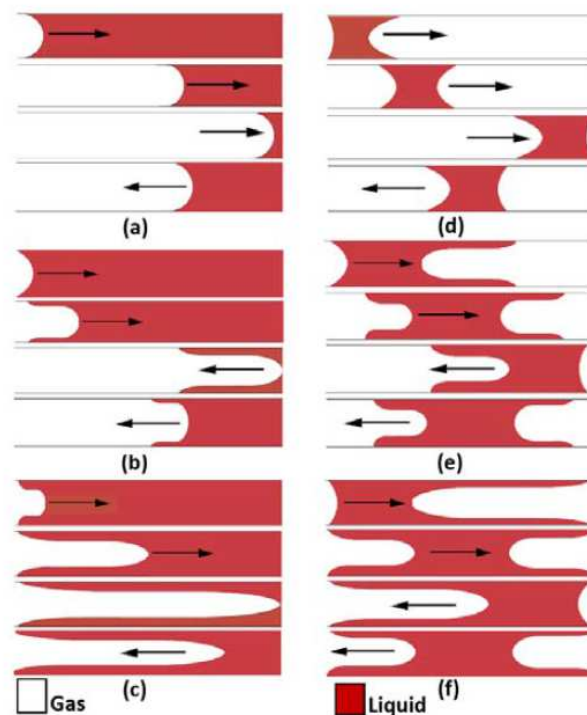


Fig. 2.9: Possible configurations of the plugs/ meniscus under oscillatory motion (*Tripathi et al. [2.44]*).

Shekhawat et al. [2.45] have studied the interfacial contact line behavior of the single oscillating meniscus formed between a long liquid slug and air, inside a square capillary

tube (2.0 mm x 2.0 mm). It was seen that the advancing contact angle was more than the receding contact angle. *Fig. 2.10* represents the evaluation of the meniscus velocity and the contact angle. The contact angle and the velocity display coherent oscillations.

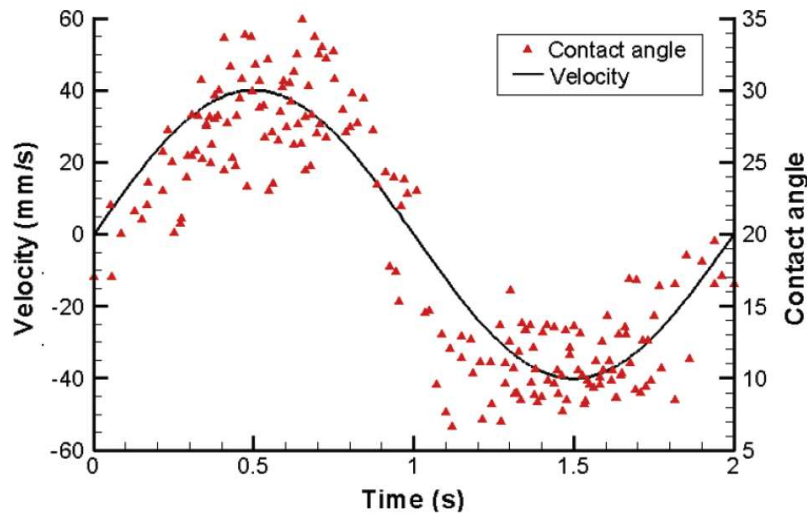


Fig. 2.10: Contact angle data superimposed on meniscus velocity U vs. time graph at an oscillating frequency of 0.5 Hz *Shekhawat et al. [2.45]*.

Recent studies by *Lips and Bonjour [2.46]* and *Lips et al. [2.47]* on adiabatic oscillations of menisci also brought to the fore the importance of dynamic contact angle in the Taylor bubble flows and the dissymmetry between the advancing and receding contact angles. Along with the contact line motions, the advancing and receding meniscus plays an important role in the heat transfer of the thin film. *Kandlikar et al. [2.48]* showed that for the stationary meniscus, the contact angle is almost independent of the wall superheat. In the case of a moving meniscus, as the surface velocity increases, the receding contact angle was found to vary whereas the advancing contact angle found to remain almost constant. *Mukherjee [2.49]* numerically simulated a steady evaporating meniscus on a moving heated wall in two dimensions. More than 99% of the evaporation is found to take place through the receding interface as compared to the advancing interface. The local wall heat transfer varies significantly along the meniscus base. The advancing contact region shows the highest heat transfer due to transient conduction in the liquid from the heated wall. The wall heat transfer coefficient is found to increase with increase in wall velocity and the advancing contact angle but remains

unaffected with changes in wall superheat or the receding contact angle. Conclusive evidence is yet to arrive for the PHP studies for the meniscus motion inside the capillaries.

2.3.5. Pressure drop in oscillating flows

The pressure drop inside a single unit cell oscillating meniscus can be studied as the pressure drop in Taylor bubble train flows. The common models for pressure drop in Taylor bubble train flows are because of two primary reasons (i) dominance of surface tension in slug flows, which is neglected in these models (ii) additional and unique flow field attributes in terms of velocity patterns in the liquid slug and vapour bubbles, which is also ignored in conventional models. *Chen et al. [2.50]* have shown that even after the inclusion of surface tension effects in terms of Bond number and Weber number, all the available experimental data sets on pressure drop in slug flows cannot be comprehensively predicted. This necessarily means that improved models should not only include the effect of surface tension but should also address to resolve the effect of flow fields in the unit cell on the overall pressure drop. *Khandekar [2.19]* showed that all mathematical models for pulsating heat pipes use extremely simplistic pressure drop correlations, typically the Hagen-Poiseuille model. Further, the statistical measure of bubble/liquid slug lengths in the adiabatic section of the pulsating heat pipe is not yet fully resolved vis-à-vis the operating boundary conditions. Unless these issues are studied, proper pressure drop estimation in the adiabatic section of the device cannot be achieved. The fact that the Taylor bubble flow is also oscillating, further complicates the estimation. Very little information is available on oscillating Taylor bubble flows, and extensive experimentation is required to incorporate the pressure drop due to oscillating flows in the proposed models of the PHPs.

The brief state of the art we have brought in this section indicates that the friction of Taylor slug flows like in an extended meniscus of PHP may strongly depend on the wall property, effective dynamic contact angles and hysteresis in a mini /microchannel (*Berthier [2.28] and Taha and Cui, [2.51]*). The former will depend on the interactions between the fluid, gas/vapour, and the surface properties of the wall. Furthermore, due

to the complexities of micro scale thermal capillary effects and the aspect ratio of the mini/micro channel, the relationship between the interfacial liquid film thickness, velocity profiles, friction, plug/slug menisci shape, dynamic contact angle hysteresis, is also not well understood *Chamarthy [2.52]*.

3. Heat transfer characteristics of extended meniscus

In order to understand the oscillatory flow pattern in PHP, it is essential to model the simultaneous phase change heat and mass transfer in Taylor-Bubble flows in small scale channels. *Magnini et al. [2.53]* stated that Taylor Bubble flow is efficient heat transfer mechanism because of recirculating flows within liquid slugs, evaporation of thin liquid film surrounding the bubble and presence of large interfacial area which enhance heat and mass transfer. They performed a numerical study of the hydrodynamics and heat transfer of elongated Taylor Bubble in a microchannel. Their numerical results reveal that the bubble shows an exponential time-law growth which is in agreement with theoretical models. Also, thin-film evaporation is the dominant heat transfer mechanism in the liquid film region between the wall and bubble while convection is found to strongly enhance the heat transfer in the intrinsic meniscus region. Recently the importance of Taylor bubble flows in enhancing the heat transfer characteristics is recently shown by *Mehta [2.54]*. He found that injection of Taylor bubbles provides an efficient means of heat transfer enhancement, up to 1.2 to 2.0 times, as compared to fully developed laminar single-phase liquid flow. While in many systems, capillary flows are uni-directional in nature or are employed in this way, there are many instances where the flow is either oscillating or pulsating in nature, as in the case of PHPs. These oscillations/ pulsations may be externally controlled, thermally driven or alternatively an effect of the dynamic instabilities which are inherent part of two-phase boiling/condensation systems. There is scarcely any work on oscillatory Taylor bubble flows. So it is important to see the factors affecting heat transfer characteristics of extended meniscus and available solution methods. While at the scale of thin films, PHPs are always governed by transient phenomena, most of the literature available is focused on single Taylor Bubble growth during flow boiling without accounting for heat transfer in the micro-layer near the liquid–gas–solid three phase contact region.

It is well known that during phase-change heat transfer across menisci, an important contribution comes from the extended meniscus covering the interior of the capillary. This was primarily shown by *Potash and Wayner [2.2]*, who studied that heat flux profile and demonstrated that, the heat flux reached a maximum in the evaporating thin-film portion. *Wayner et al. [2.55]* showed that heat-transfer coefficient at interline region of an adsorption controlled wetting film varies from zero at interline to a value equal to the liquid-vapour interfacial heat-transfer coefficient over a relatively short distance. Later numerous investigations [2.8, 2.56, 2.57] indicate that it is within this region that high heat transfer rates occur as a result of small conductive resistance and fluid flow driven by the capillary and disjoining pressure gradients.

Hence, *Taha and Cui [2.40]* stated that this liquid film formed between confined vapour bubble and tube wall plays an important role in heat exchange, since local heat and mass transfer is effectively enhanced at the thin liquid film region. This also justifies the increasing thin-film thickness $\delta_{(x)}$ (refer *fig. 2.2*) as compared to adsorbed region. It is this increasing film thickness that allows sufficient evaporation, resulting from the decay of disjoining pressure (*Polansky [2.14]*). Solving the resulting interface profile is an important point in studying thin films. The total heat transfer resistance is composed of the diffusional resistance of the liquid film and evaporation at vapour-liquid interface. There are very few experimental studies available on heat transfers in thin film for such cases. In most of the available studies, the thin film evaporation model is solved analytically or numerically. Due to lack of experimentation, concrete conclusion is yet to arrive. Let us now see the available solution techniques for evaluating thin film heat transfer and how we can correlate these solutions for our extended meniscus problem.

3.1. Young-Laplace Equation

The Young-Laplace equation comes about when performing a thermodynamic analysis of interfacial tension effects. The equation can be derived from the consideration of two fluids (I and II) in equilibrium separated by a planar (fixed shape) interface region. If this fixed shape restriction is relaxed and deformation of the interface is allowed, both

the area and curvature of the interface can change. The pressure difference across the interface can be represented as:

$$P_I - P_{II} = \sigma \frac{dA_i}{dV_I} \quad 2.20$$

Eq. 2.20 can be further simplified for a curved interface like a bubble with radii r_1 and r_2 (leading and lagging interface radii) respectively at leading and lagging face:

$$P_I - P_{II} = \sigma \left(\frac{1}{r_1} + \frac{1}{r_2} \right) = \sigma \kappa \quad 2.21$$

Where, κ is the curvature.

Eq. 2.21 is referred to as the Young-Laplace equation and relates the pressure difference across the interface to the interfacial tension and the geometry of the interface at equilibrium (*Carey [2.23]*). It is noted that this above equation is applicable for the interface between two fluid phases of a pure substance.

3.2. Augmented Young-Laplace Equation

The augmented Young-Laplace equation, much like the Young-Laplace equation is used to analyse the thermodynamic effects of the interfacial tension across the thin-film interface. In performing this analysis, disjoining pressure, capillary pressure, liquid pressure and vapour pressure must all be accounted for. It is the augmented Young-Laplace equation that provides the means for a continuum analysis of an evaporating thin-film meniscus. *Wayner et al. [2.55]* first used the augmented Young-Laplace equation in analysis. The equation is presented below:

$$P_v - P_l = P_{cap} + P_{dis} \quad 2.22$$

Eq. 2.22 is representative of the force balance present in the system. Using eq. 2.22 and the suitable evaporation model, one can determine the thin-film profile and heat transfer characteristics.

Schonberg et al. [2.58] used a concept of augmented Young-Laplace model for an evaporating meniscus in a microchannel. It was found that the heat flux is a function of the long range Van-Der-Waals dispersion force. The apparent contact angle, which represents viscous losses near the contact line, has a large effect on the heat flow rate because of its effect on capillary suction and the area of the meniscus. The liquid pressure differs from the pressure of the vapour phase due to capillarity and long-range Van-Der-Waals dispersion forces, which are relevant in the ultrathin film formed at the leading edge of the meniscus. Important pressure gradients in the thin film cause a substantial apparent contact angle for a completely wetting system.

3.3. Vaporization and condensation interfacial resistances

Our primary interest is to calculate the local evaporation/condensation mass flux associated with interfacial temperature and pressure jump that occurs across a liquid-vapour interface. This problem can be solved when we look the problem at molecular level. Due to motion of vapour molecules near the liquid-vapour interface plays a significant role in heat flux limitations of vaporization and condensation processes. For such cases, one classical approach is the use of an accommodation coefficient, which attempts to quantify the molecular behaviour at an interface. Accommodation coefficient came in to picture when molecular transport at the liquid-vapour interface was analysed as an extension of kinetic theory of gases (*Carey [2.23]*).

Using Maxwell's velocity distribution from kinetic theory of gases and obtaining a relationship for the fraction of the molecules with speeds in a specified range, regardless of direction using a simple cubical geometry (*fig. 2.11* considering the motion of molecules). We will find the flux of molecules passing through assumed surface of S^* per unit area and per unit time in such cube. A molecule with a y -component velocity (v) and any u and w must lie within distance $v\Delta t$ of the surface at the beginning of the time interval in order to pass through it. The fraction of molecules having a y -component of velocity between some value v and $v+dv$ and having any u and w is found by integrating over all possible values of u and w , obtains the following relation:

$$\frac{dN_v}{n} = \left(\frac{m}{2\pi k_B T} \right)^{1/2} \cdot \exp\left(\frac{-mv^2}{2k_B T} \right) dv \quad 2.23$$

Where, N is number of molecules, m is mass of one molecule, k_B is Boltzmann constant, T is temperature in Kelvin.

Above eq. 2.23 shows that only molecules within a fraction of $v\Delta t/L_y$ of the total cube volume will pass through surface S^* in the time interval Δt . Allowing the total number of molecules within the control volume to be represented by n , the flux of molecules with velocity v in the y direction that will pass through S^* per unit area per unit time is equal to:

$$dJ_v = \left(\frac{v\Delta t}{L_y} \right) dn_v \left(\frac{1}{L_x L_z} \right) \left(\frac{1}{\Delta t} \right) \quad 2.24$$

Where, J is the flux of molecules and L is the characteristics length

Combining eq. 2.23 and 2.24 and integrate over all values of v (0 to ∞), the total rate at which molecules pass through S^* :

$$J_n = \left(\frac{1}{4} \right) \left(\frac{N}{V} \right) \left(\frac{8k_B T}{\pi m} \right) = \left(\frac{\bar{M}}{2\pi \bar{R}} \right)^{1/2} \left(\frac{P}{mT^{1/2}} \right) \quad 2.25$$

where, \bar{M} is the molecular weight of the considered species, P is the pressure and \bar{R} is the universal gas constant.

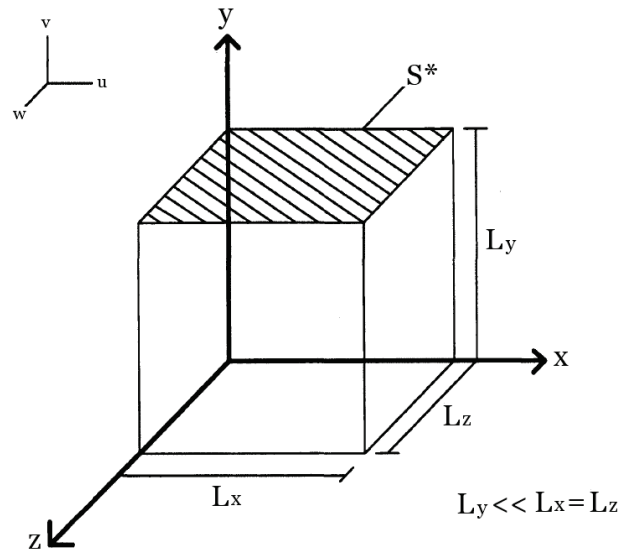


Fig. 2.11: Nomenclature and geometry used in molecular flux derivation (*Carey [2.23]*).

Applying eq. 2.25 across the liquid-vapour interface of the thin-film meniscus, giving further insight into the molecular motion. Let us consider the case of evaporation, and place S^* at an infinitesimal distance outside of the liquid interface (in the vapour phase) such as represented in *fig. 2.12*.

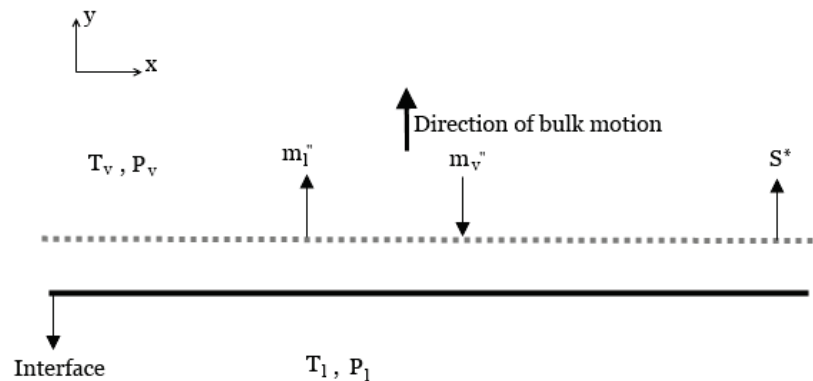


Fig. 2.12: Modeling S^* with regards to thin-film setup (*Carey [2.23]*).

From *fig. 2.12*, the net mass flux can be written as:

$$\mathbf{m}_{\text{net}}'' = \mathbf{m}_1'' - \mathbf{m}_v'' \quad 2.26$$

Now, for the case of evaporation and for a bulk velocity of the vapour w_o , *Schrage [2.59]* developed a relationship in which he defines the molecular flux for the vapour field whilst incorporating the effect of the bulk velocity:

$$J_{nv+} = Z(s) \cdot \left(\frac{\bar{M}}{2\pi RT} \right)^{1/2} \left(\frac{P}{m} \right) \quad 2.27$$

$$J_{nv-} = Z(-s) \cdot \left(\frac{\bar{M}}{2\pi RT} \right)^{1/2} \left(\frac{P}{m} \right) \quad 2.28$$

where 's' is a dimensionless parameter and represented as:

$$s = \frac{w_o}{\left(2RT / \bar{M} \right)^{1/2}} \quad 2.29$$

And function Z defined as:

$$Z(s) = \exp(s^2) + s\pi^{1/2}(1 + \text{erf}(s)) \quad 2.30$$

$$Z(-s) = \exp(s^2) - s\pi^{1/2}(1 - \text{erf}(s)) \quad 2.31$$

Where erf(s) is error function (also called the Gauss error function)

Eq. 2.27 and 2.28 represent the molecular flux with a bulk velocity in the positive and negative y direction respectively. As seen below in eq. 2.32, in the case of vaporization, eq. 2.27 is utilized.

In addition to the effect of bulk motion only a fraction γ_e of the molecules crossing the surface S^* in the negative y direction is actually due to vaporization. The remaining $1 - \gamma_e$ is due to the reflection of the vapour molecules that strike the interface but do not condense. The fraction of molecules crossing the surface S^* in positive y direction that

condense and are not reflected is represented as γ_c . If no phase change occurs at the interface, equilibrium requires that $\gamma_e = \gamma_c = \gamma$. In some cases γ_e and γ_c are assumed to be equal even for the dynamic case when phase change occurs at the interface (*Carey [2.23]*). These γ_e and γ_c often referred as vaporization/ evaporation, condensation **accommodation coefficients**. The portion of the mass flux m_1'' that actually enters the liquid phase upon striking the liquid using concept of accommodation coefficients can be given as:

$$m_1'' = \begin{cases} m\gamma_e J_{nv+} \rightarrow \text{Vaporization} \\ m\gamma_c J_{nv-} \rightarrow \text{Condensation} \end{cases} \quad 2.32$$

Eq. 2.27 represents the evaporative mass flux in the vapour field. In essence, considering the vaporization case, the equation represents the fraction of molecules with a positive y-component velocity that are indeed evaporating.

Similarly, within the liquid phase, an equation representing the fraction of molecules that successfully leave the liquid phase and are released into the vapour phase is generated:

$$m_2'' = m\gamma_e J_n \quad 2.33$$

Now, the new net mass flux equation across the interface is written as:

$$m_{\text{int}} = m_2'' - m_1'' \quad 2.34$$

Substituting 2.32, 2.33 in 2.34 we get:

$$m_{\text{int}}'' = \left(\frac{\bar{M}}{2\pi\bar{R}} \right)^{1/2} \left(\frac{Z(s)\gamma_c P_v}{T_v^{1/2}} - \frac{\gamma_e P_l}{T_l^{1/2}} \right) \quad 2.35$$

Eq. 2.35 provides the foundation for the Kelvin-Clapeyron model used in the solution of the thin-film meniscus, and provides a reasonable means of quantifying the pressure and temperature jump at the liquid-vapour interface. The Kelvin-Clapeyron model, developed by *Wayner [2.12]* is a linearized version of eq. 2.35.

Both of these γ_e and γ_c coefficients will be individually defined: *Marek and Straub [2.58]* state the evaporation coefficient as originally defined by Knudsen as:

$$\gamma_e = \frac{\text{molecules transferred to the vapour phase}}{\text{molecules emitted from the liquid phase}} \quad 2.36$$

An evaporation coefficient less than unity imply incomplete evaporation as not all of the molecules emitted from the liquid phase are released. A value of unity would imply perfect evaporation (*Marek and Straub [2.60]*).

Marek and Straub [2.60] state condensation coefficient:

$$\gamma_c = \frac{\text{molecules absorbed by the liquid phase}}{\text{molecules impinging on the liquid phase}} \quad 2.37$$

Much like the case of evaporation, a condensation coefficient less than one represents incomplete condensation, with a value of one representing full condensation (*Marek and Straub [2.60]*).

It is common practice within thin-film research to equate $\gamma_e = \gamma_c = \gamma$. It is important to realize that this does not imply a zero net mass flux and thus equilibrium. The only case where equating these coefficients implies equilibrium is when the denominator of eq. 2.36 and 2.37 are equal, which also suggests that there would be no bulk velocity in the vapour field ($w_0 = 0$). *Carey [2.23]* and *Schrage [2.59]* show that in such case, the function $Z(s)$ would tend to unity, the pressure and temperature jump across the interface would not exist and as a result eq. 2.35 would yield a result of zero evaporative mass flux. In the case where $\gamma_e = \gamma_c = \gamma$ and the denominators of the respective terms

do not equate, there would still be a net mass flux at the interface. This assumption is generally accepted in the absence of the knowledge of the individual accommodation coefficients. However as *Schrage [2.59]* states, this assumption is suspect. Furthermore, little experimental work has been done in quantifying accommodation coefficients given the molecular nature of the problem. Some authors also reported that in cases of extreme fluid purity, accommodation coefficient should tend to unity.

3.4. Experimental and modeling approaches for analyzing extended meniscus evaporation

The bulk transport mechanisms of liquid-vapour system in a capillary tube needs understanding of localized experimental observations of such systems, with synchronized measurements of the resulting fluctuations in local conditions such as temperature, pressure and wall heat flux. Very few experimental and numerical studies are available for heat transfer in extended meniscus region. The measurement of temperature gradient near the thin film region is always a challenging task. In such cases to predict the liquid-vapour thermodynamics inside such systems, require the precise dynamic measurement of the liquid-vapour temperature, which is still challenging due to its vibrant nature and also due to the unavailability² of the reliable temperature measurement techniques in such small microscopic systems. In addition, for predicting the dynamics of the liquid-vapour system in such cases of single branch PHP, the issue of dependence of thermal response and sensitivity of the temperature sensor will arise due to induced oscillating motion. There is strong need to develop appropriate temperature measuring techniques for liquid-vapour system to fasten the understanding. There are many experimental/numerical observations available for static extended meniscus evaporation problem, but there is a strong need to extend these studies to the moving meniscus. Let us now go through some of the experimental/numerical approaches and observations applied to the static extended meniscus evaporation.

² The most of the temperature measurement techniques are intrusive in nature and may influence the system functioning.

Most of the time, it was assumed that the vapour near the extended meniscus region is having uniform saturated temperature corresponding to the vapour pressure. *Stephan and Busse [2.61]* developed a model for the radial heat transfer of a grooved heat pipe evaporator. They showed that the common assumption of an interface temperature equal to the saturation temperature of the vapour can lead to a large over prediction of the heat transfer coefficient and there is presence of an inverse pressure gradient in the liquid phase, which is necessary for transporting the liquid in the micro region to the evaporating surface. These in turn lead to a significant decrease of the volatility of the liquid and a corresponding rise of the interface temperature above T_{sat} . They also observed that the temperature in the micro-region drastically drops and a high heat transfer is obtained at that region; up to 50 % of evaporation takes place in this small region. The length of the micro-region depends on the wetting characteristic which is represented by the local apparent contact angle. Thus, the dynamic apparent contact angle is a very important process parameter. The resulting adhesion forces cause a steady transition of the evaporating meniscus into a flat non evaporating film of microscopic thickness, which is adsorbed on the 'dry' part. Several authors [2.56-2.58] numerically computed thickness profiles of a heptane meniscus on silicon and compared that with the experimental data. They concluded that significant resistance to heat transfer was present in the contact line region due to conduction, interfacial forces and viscous stresses.

Hoffman and Stephan [2.62] measured temperatures beneath an evaporating meniscus using thermochromic liquid crystals. They found significant temperature drop near the micro-region³ due to presence of a high evaporative heat flux. *Fig. 2.13* illustrates their experimental setup and the temperatures at various regions of extended meniscus. The wall temperature increase to a higher value in the adsorbed film region is due to decreased heat transfer.

³ this "micro region" corresponds to the thin film region described in section 1.2 of this chapter.

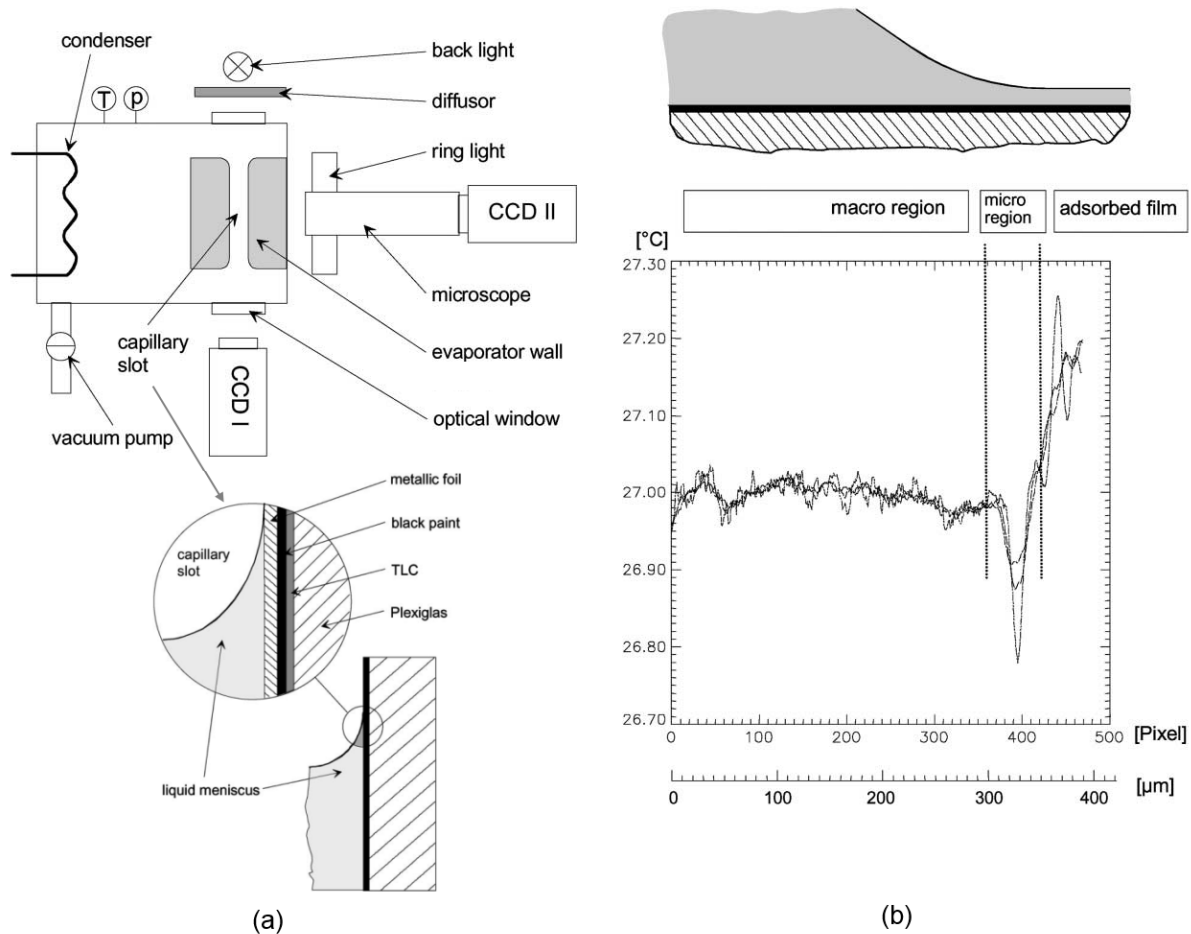


Fig. 2.13: (a) Experimental setup (top view) and details of capillary slot (b) Temperature distribution at the micro-region (*Hoffman and Stephan [2.62]*).

Panchangam et al. [2.63] studied physicochemical phenomena occurring in the contact line region of an evaporating meniscus by experiments and numerical model. They demonstrated the existence of a slip at the solid–liquid interface, which explain the high mass flow rates in the evaporating pentane meniscus.

There was a sharp dip in the solid–liquid interfacial temperature profile in the meniscus region demonstrating that the evaporating meniscus acts as a large heat sink. This insight into the solid–liquid interface temperature profile was made possible by including the effect of heat conduction in the solid substrate. The outside solid surface temperature also shows a dip due to the presence of the heat sink. The possibility of a non-uniform vapour temperature has been explored. It is proposed that the vapour

temperature obtained using model, has a dip in the evaporating region. *Fig. 2.14* shows the experimental setup and few important results of their experiments and model.

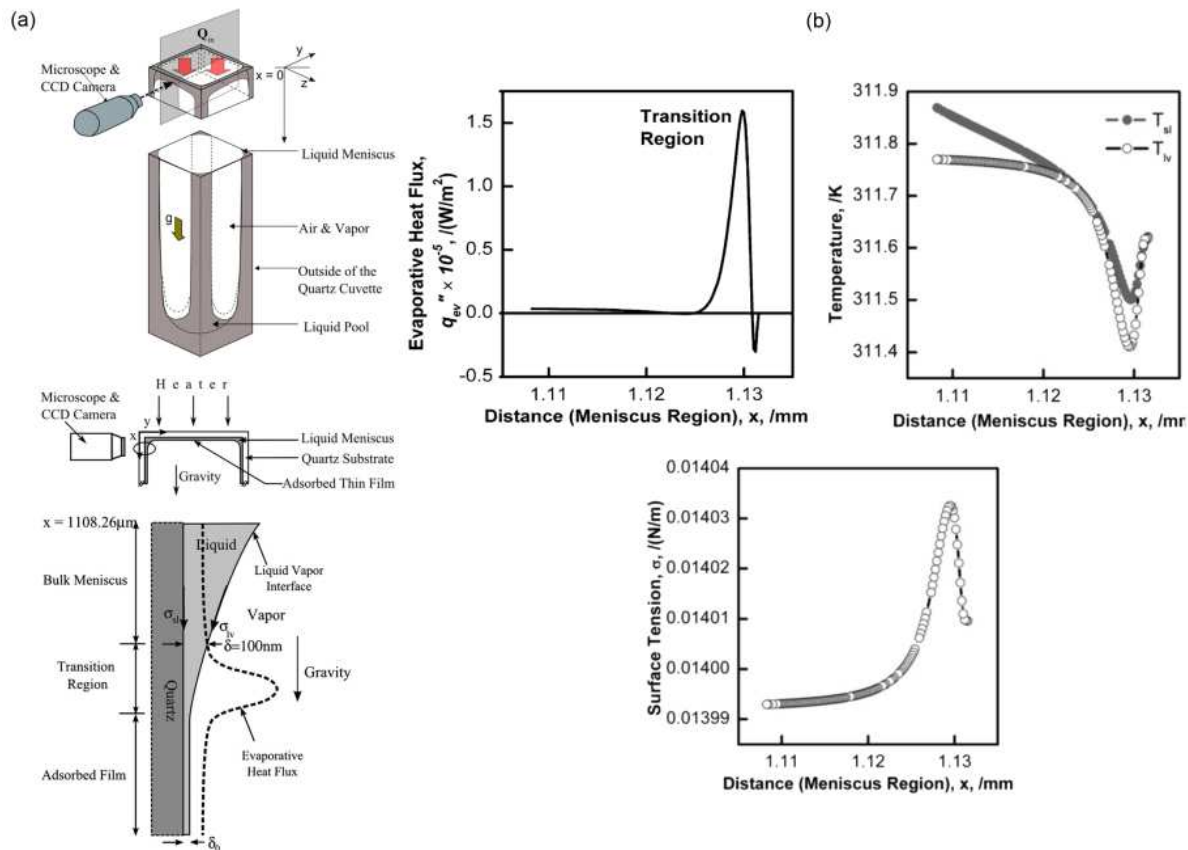


Fig. 2.14: (a) Schematic representation of the experimental set-up of the heat exchanger, cross-sectional view of the top-corner of the cuvette showing liquid meniscus and the adsorbed thin film region and schematic of the micro-region (b) Evaporative heat flux profile at the liquid–vapour interface of the evaporating meniscus region, The solid–liquid and liquid–vapour interface temperature profiles in the evaporating meniscus region as a function of the meniscus length and surface tension variation with the evaporating meniscus region (*Panchamgam et al. [2.63]*).

Using microscale infrared thermography *Dhavaleswarapu et al. [2.64]* demonstrated a distinct temperature drop at the triple line, indicating the effectiveness of thin-film heat transfer. This temperature drop was found to increase with increasing applied heat flux. Their approximate heat balance analysis shows that nearly 70% of the heat transfer takes place from a sub-region (extent of the meniscus adjacent to the contact line). The

sub-region heat transfer was found to increase with an increase in heat flux and increase in evaporation rate. *Dhavaleswarapu et al. [2.65]* also developed a numerical model for evaporation from a steady, liquid–vapour interface into air. The high vapour diffusion fluxes near the contact line demonstrate the strength of thin-film evaporation. *Fig. 2.15* shows the experimental setup and few important results of their experiments and model.

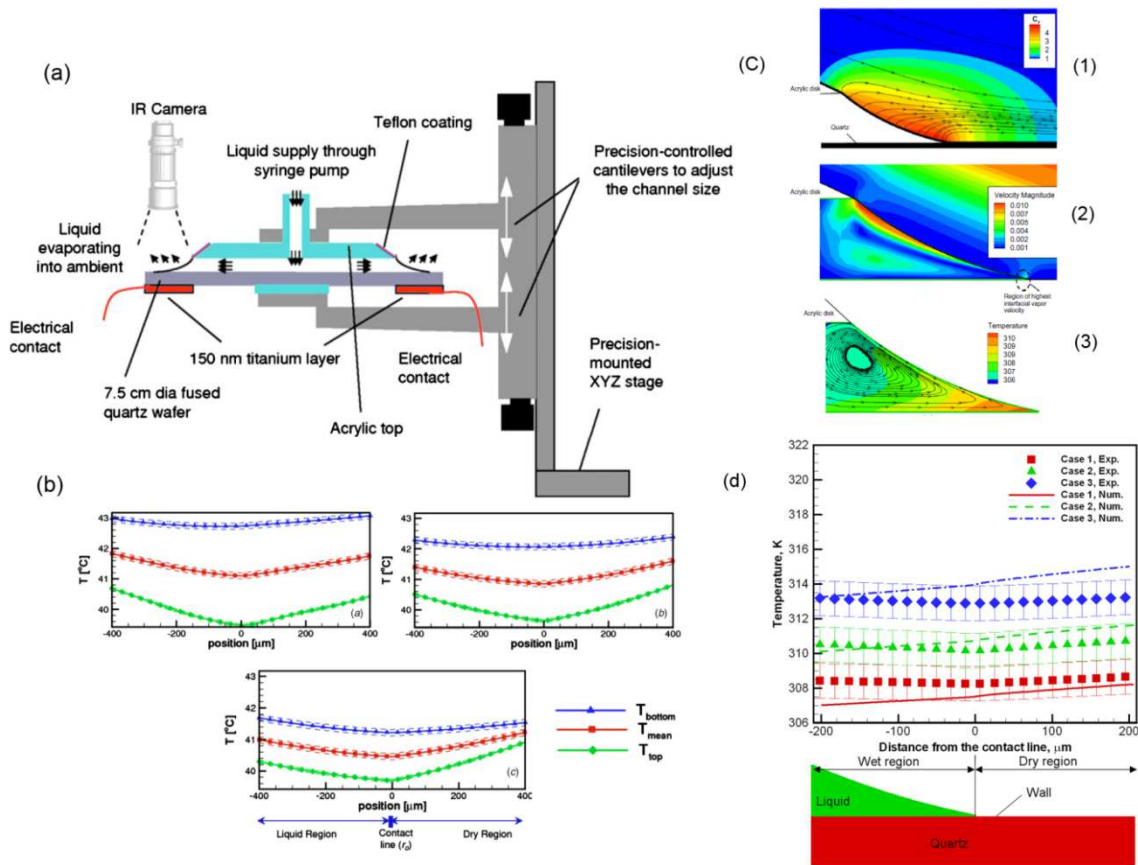


Fig. 2.15: (a) Experimental setup schematics (b) Infrared temperature maps of T_{top} and T_{bottom} at a heat flux of 1190 W/m^2 and different evaporation rates for Image of heptane meniscus on fused quartz wafer (C) 1. Contour of heptane vapour concentration near the meniscus 2. Velocity contours in the vapour/air domain 3. Temperature contours (K) and stream traces showing thermocapillary convection in the meniscus (d) Wall temperature profiles near the contact line (*Dhavaleswarapu et al. [2.64, 2.65]*).

Ibrahim et al. [2.66] used an infrared thermography system to measure the two dimensional temperature distributions underneath a single evaporating meniscus in the

contact line area. Due to extremely high local evaporation rates, a temperature difference up to 12 K between the wall temperatures at the contact line area and the bulk liquid has been observed. High local heat fluxes could be observed at contact line area with values up to 5.4–6.5 times higher than the mean input heat fluxes.

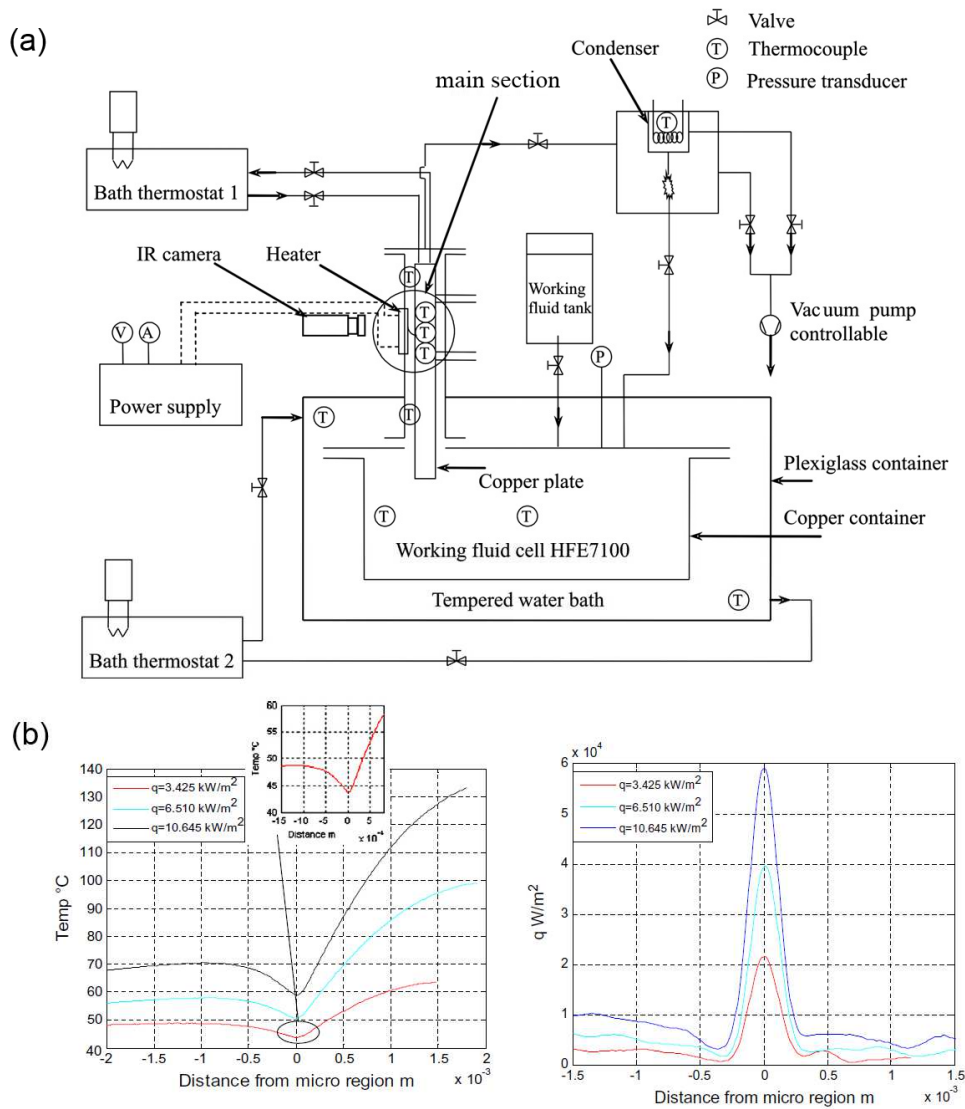


Fig. 2.16: (a) Experimental setup schematics (b) Linear local wall temperature distribution underneath the meniscus at different input heat fluxes and linear local heat flux distribution for different input heat fluxes (*Ibrahim et al. [2.66]*).

Fig. 2.16 shows their experimental setup and linear local wall temperature distribution underneath the meniscus at different input heat fluxes and linear local heat flux distribution for different input heat fluxes.

Within a liquid plug, the basic studies suppose the existence of a static thin film in contact with the wall of the micro-channel. However, close to three phases contact line, such assumption turns out to be incorrect as there are non continuous interactions between particles. *Park et al. [2.4]* proposed a mathematical model which includes the vapour region and a slip boundary condition. The implications of interfacial slip on thin film evaporation phenomenon in a rectangular micro channel have also been studied by *Biswal et al. [2.67]*. The thin film is usually assumed to be flat; however, near the three phase line, a slope exists; such slope can affect the thin film model. They have demonstrated that the film thickness profiles as well as the pertinent heat transfer characteristics may indeed be sensitively dependent on the slope and curvature dependences of the disjoining pressure. Fundamentally, such sensitive dependences may be attributed to the disparate number densities and attractive potential strengths in the constituent liquid and vapour phases. From their detailed analysis it has been inferred that slope and curvature dependences of the disjoining pressure is likely to give rise to thicker liquid films and consequently to lower local heat transfer coefficients. The physical phenomena involved are summarized in *fig. 2.17*.

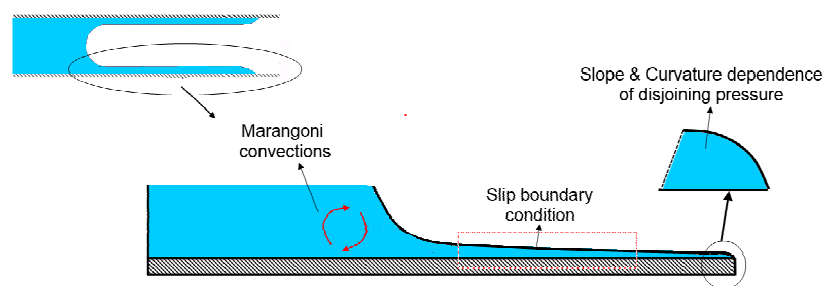


Fig. 2.17: Schematics of physical phenomenon of slip boundary condition, Marangoni convections and slope and curvature dependence of disjoining pressure in an extended meniscus.

Recently *Nikolayev [2.68]* stated that thin films in PHP are of different nature than wetting films (~ 10 nm thickness) like in capillary heat pipes, which are much thinner than in PHP (≥ 10 μm thickness). PHP films are of different origin and appear due to receding motion of menisci. The startup of oscillations in a unit-cell PHP has been studied by *Nikolayev [2.69]*. He assumed that strong temperature gradients exist inside the vapour phase. While the liquid-vapour interface is at saturation temperature, the vapour bulk temperature may deviate from it being either superheated or super-cooled. Few attempts have been made in this regard in predicting the vapour thermodynamic state in systems like unit cell PHPs.

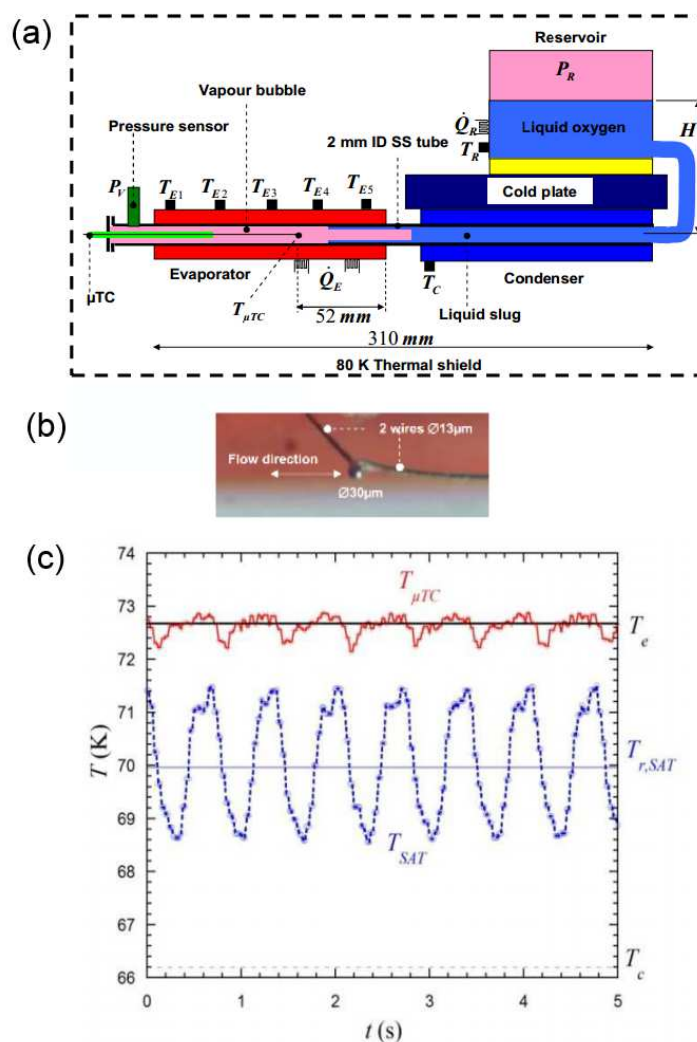


Fig. 2.18: (a) Experimental setup schematics (b) Micro thermocouple schematics (c) Vapour temperature as compared to saturation temperature (*Gully et al. [2.70]*).

Gully et al. [2.70] studied this problem in a unit branch PHP aiming at measuring and calculating the vapour state in a horizontal single branch PHP. The experimental setup uses oxygen at cryogenic state as operating fluid. Microscopic thermocouples were employed for the direct vapour temperature measurement. The vapour was found superheated and the vapour temperature oscillates around the evaporator temperature. As this temperature measurement technique is intrinsic in nature, it may influence the system behavior and also the issue of dependence of thermal response and sensitivity of the sensor will arise due to induced oscillating motion of meniscus and vapour. *Fig. 2.18* shows their schematics of experimental setup and the vapour temperature as compared to the saturation temperature.

Chauris et al. [2.71] studied an experimental analysis of the heat and mass transfers involved in evaporation of a thin liquid film deposited downstream a semi-infinite slug flow in a heated capillary tube (Copper tube of 200 mm length and 2 mm inner and 2.4 mm outer diameters) using water as working fluid keeping the target of understanding working of pulsating heat pipe (*fig. 2.19-a*). They have done temperature measurements on the outer wall of the tube by infrared thermography, which is used to determine the meniscus location during its passage through the heated test section, so as to ensure that the triple line followed the thin film.

They found that the transfers through the thin liquid film are mainly driven by heat conduction through film thickness and evaporation at its interface. Also compared to thin film length, the meniscus radius remains very small. As a result, the cumulated heat transfers in this zone are low (up to 10% of overall heat transfers) compared to those of the thin liquid film (*fig. 2.19-b*). Experimental identification of the thin liquid length subjected to evaporation confirmed that the latter is a primary function of heat flux density at the inner wall (including the stored heat) and of the deposited thin film initial thickness (through the capillary number). They also generated a generic correlation (for water) of first-order evaluation of the thin liquid film length as function of heat flux density at the wall, initial deposited film thickness and fluid properties.

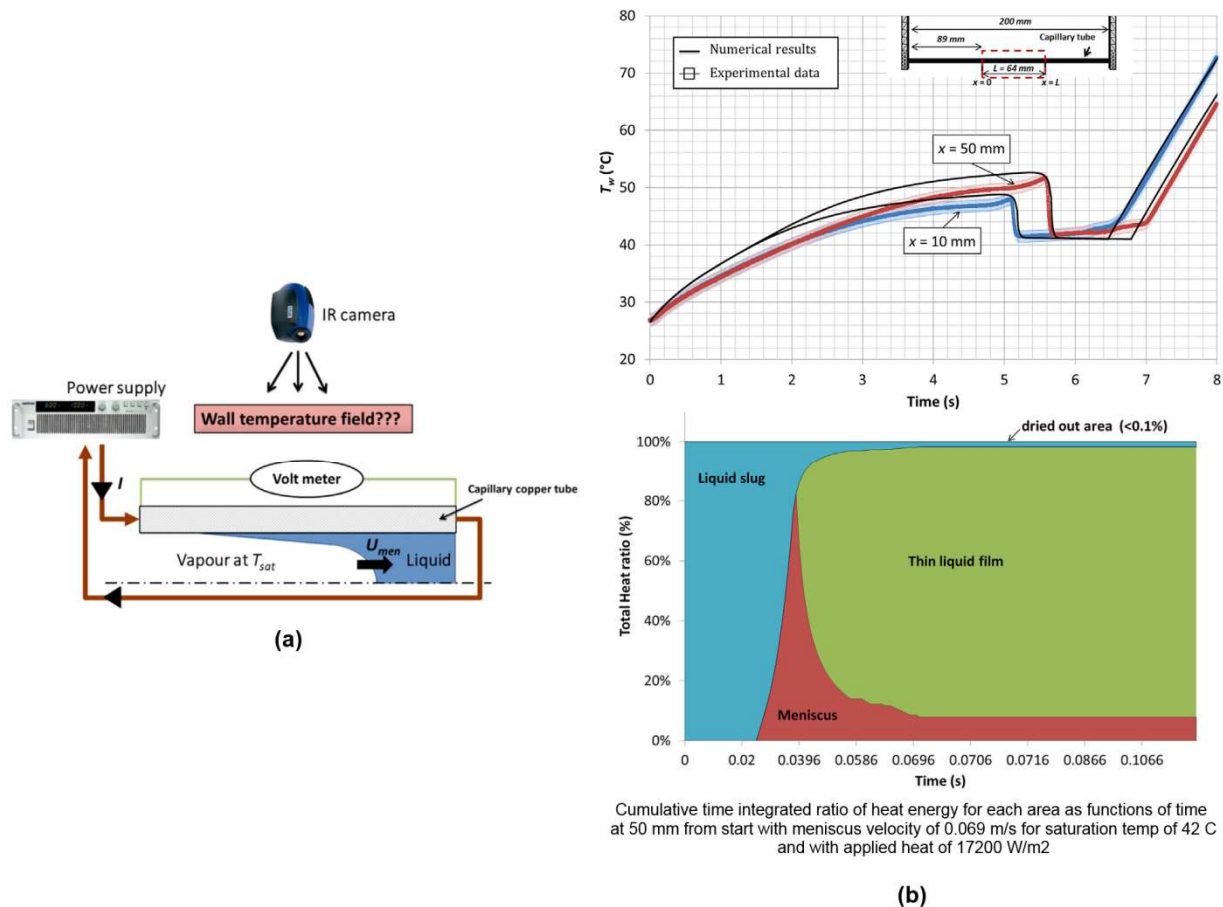


Fig. 2.19: (a) Experimental setup schematics (b) Experimental results for wall temperature and % of heat transfer at various regions (*Chauris et al. [2.71]*).

There are hardly any experimental studies those directly focused on extended meniscus region of a PHP without which the complete understanding of the pulsating-evaporating-condensing systems is quite difficult. Measurement of vapour dynamics inside the unit cell PHP system is a challenge and unfolding of such phenomenon will lead to better understanding of the systems like PHPs.

4. Closing remarks

Looking in to the above literature it is strongly believed that a focused effort is needed to move towards a better understanding of the functioning of the single branch PHPs and ultimately real PHPs. Here we are giving the outcome of the literature survey and salient points of course of action.

- The evaporation/condensation dynamics plays a key role in the oscillations. It is clear that the major part of mass transfer occurs via the wetting film (if it exists) or in the vicinity of the triple vapour-liquid-wall contact line when the film is evaporated. The evaporation rate depends strongly on the film area. However, the film dynamics during the oscillations is poorly understood, only a preliminary study is available.
- The pressure drop in the PHP appears due to three sources of viscous dissipation in the liquid: (i) liquid-wall shear stress (ii) the viscous dissipation at the meniscus (wetting films and contact lines) and (iii) effect of the tube exhaust in the reservoir and tube bends. While the first source is well studied, two others are not understood deeply enough. The information on the second source is very scarce while the third is studied only at stationary flow. However, the liquid motion is oscillating in the PHP and the inertial effects play important role.
- The vapour thermodynamic state is a very important but yet not studied for understanding the oscillation mechanism of a PHP. In some modeling approaches the vapour is allowed to be overheated due to its compression. It is assumed in the others to be at saturation temperature corresponding to its pressure, which is a behavior analogous to that observed (there are many cases of non-equilibrium) in conventional heat pipes. We think that while the vapour-liquid interface is at saturation, the temperature of the vapour bulk can be higher than the saturation temperature due to the compression. The strong temperature gradients in the vapour domain may get formed near its boundaries due to the weakness of the heat diffusion in vapour. If the vapour thermodynamic state was always at saturation curve, it could not be compressed and thus would not play the role of a spring providing the return force for the oscillation. The vapour compression would simply cause the condensation. The vapour states (both its pressure and temperature) need to be measured experimentally to verify this hypothesis.
- Another important parameter is the oscillatory instability which causes oscillations and has not been yet understood. This issue is however critical because if the system

is globally stable at some system parameters, the PHP might stop functioning. Such failures have indeed been observed experimentally. A parametric study of the instability needs to be carried out both theoretically and experimentally (different fluids, temperatures, pressures) in order to determine the oscillation threshold.

References

- 2.1 B. Derjaguin, N. Churaev, V. Muller, Surface forces. New York: Consultants Bureau, (1987).
- 2.2 M. Potash Jr., P.C. Wayner Jr., Evaporation from a two-dimensional extended meniscus, *Int. J. Heat Mass Transfer*, 15 (1972) 1851-1863.
- 2.3 S. K. Wee, K. D. Kihm, and K.P. Hallinan, Effects of the liquid polarity and the wall slip on the heat and mass transport characteristics of the micro-scale evaporating transition film, *Int. J. Heat Mass Transfer*, 48 (2005) 265-278.
- 2.4 K. Park, K.J. Noh, K.S. Lee, Transport phenomena in the thin-film region of a micro-channel, *Int. J. Heat Mass Transfer*, 46 (2003) 2381- 2388.
- 2.5 K. Stephan, Influence of dispersion forces on phase equilibria between thin liquid films and their vapour, *Int. J. Heat Mass Transfer*, 45 (2002) 715 - 4725.
- 2.6 S. DasGupta, I.Y. Kim, P.C. Wayner Jr., Use of the Kelvin-Clapeyron equation to model an evaporating curved micro-film, *J. Heat Transfer*, 116 (1994) 1007-1015.
- 2.7 J. Zhao, Y. Duan, X. Wang B. Wang, Effects of superheat and temperature-dependent thermophysical properties on evaporating thin liquid films in microchannels, *Int. J. Heat Mass Transfer*, 54 (2011) 1259-1267.
- 2.8 H. Wang, S. V. Garimella, J. Y. Murthy, An analytical solution for the total heat transfer in the thin-film region of an evaporating meniscus," *Int. J. Heat Mass Transfer*, 51 (2008) 6317- 6322.
- 2.9 W. Qu, T. Ma, J. Miao, J. Wang, Effects of radius and heat transfer on the profile of evaporating thin liquid film and meniscus in capillary tubes, *Int. J. Heat Mass Transfer*, 45 (2002) 1879-1887.
- 2.10 K. Park, K.S. Lee, Flow and heat transfer characteristics of the evaporating extended meniscus in a micro-capillary channel, *Int. J. Heat Mass Transfer*, 46 (2003) 4587-4594.
- 2.11 L. Lin, A. Faghri, Heat transfer in micro region of a rotating miniature heat pipe, *Int. J. Heat Mass Transfer*, 42 (1999) 1363-1369.
- 2.12 P. C. Wayner Jr., Intermolecular forces in phase-change heat transfer: 1998 Kern award review, *AIChE Journal*, 45 (1999) 2055-2068.

- 2.13 H. Wang, S. V. Garimella, J. Y. Murthy, Characteristics of an evaporating thin film in a microchannel, *Int. J. Heat Mass Transfer*, 50 (2007) 3933 – 3942.
- 2.14 J. Polansky, Numerical model of an evaporating thin film meniscus, Carleton University Press, Ottawa, Ontario, Canada, (2011).
- 2.15 C. Buffone, K. Sefiane, J.R.E. Christy, Experimental investigation of the hydrodynamics and stability of an evaporating wetting film placed in a temperature gradient, *Appl. Therm. Eng.*, 24 (2004) 1157-1170.
- 2.16 H. Wang, S. V. Garimella, J.Y. Murthy, Characteristics of an evaporating thin film in a microchannel, *Int. J. Heat Mass Transfer*, 50 (2007) 3933–3942.
- 2.17 H. Wang, S.V. Garimella, J. Y. Murthy, Transport from a volatile meniscus inside an open microtube, *Int. J. Heat Mass Transfer*, 51 (2008) 3007–3017.
- 2.18 J. Collier, J. Thome, Convective boiling and condensation, 3rd edition, Oxford Engineering Science Series.
- 2.19 S. Khandekar, P.K. Panigrahi, F. Lefèvre, J. Bonjour, Local hydrodynamics of flow in a pulsating heat pipe: A Review, *Front. Heat Pipes*, 1, 023003 (2010) 1–20
- 2.20 F.P. Bretherton, The Motion of long bubbles in tubes, *J. Fluid Mech.*, 10 (1961), 166-188.
- 2.21 P. Aussillous, D. Quéré, Quick deposition of a fluid on the wall of a tube, *Phys. Fluids*, 12 (2000) 2367-2371.
- 2.22 M.K. Akbar, S.M. Ghiaasiaan, Simulation of Taylor flow in capillaries based on the volume of fluid technique,” *Ind. Eng. Chem. Res.*, 45 (2006) 5396-5403.
- 2.23 V.P. Carey, Liquid-Vapour phase-change phenomena, 2nd ed., Taylor and Francis (2007).
- 2.24 R.N. Wenzel, Resistance of solid surfaces to wetting by water, *Industrial Engineering and Chemistry*, 28 (1936) 988-990.
- 2.25 W. Rose, R.W. Heins, Moving interfaces and contact angle rate-dependency, *J. Colloid Sci.*, 17 (1962) 39-48.
- 2.26 R.L. Hoffman, A study of advancing interface, *J. Colloid Interface Sci.*, 50 (1975) 228-241.
- 2.27 L.H. Tanner, The spreading of silicone oil drops on horizontal surfaces, *J. Phys. D: Appl. Phys.*, 12 (1979) 1473-1484.
- 2.28 J. Berthier, Microdrops and digital microfluidics, William Andrew Inc., New York, USA (2008).

- 2.29 H.P. Kavehpour, B. Ovrin, G.H. McKinley, Microscopic and macroscopic structure of the precursor layer in spreading viscous drops, *Phys. Rev. Lett.*, 91 (2003) 196104.
- 2.30 J.R. Thome, V. Dupont, A.M. Jacobi, Heat transfer model for evaporation in microchannels. Part I: presentation of the model, *Int. J. Heat Mass Transfer*, 47 (2004) 3375–3385.
- 2.31 D.B.R. Kenning, D.S. Wen, K.S. Das, S.K. Wilson, Confined growth of a vapour bubble in a capillary tube at initially uniform superheat: Experiments and modeling, *Int. J. Heat Mass Transfer*, 49 (2006) 4653–4671.
- 2.32 W. Qu, I. Mudawar, Measurement and correlation of critical heat flux in two-phase micro-channel heat sinks, *Int. J. Heat Mass Transfer*, 47 (2004) 2045–2059
- 2.33 F. Fairbrother, A. E. Stubbs, The bubble-tube method of measurement, *J. Chem. Soc.*, 1 (1935) 527-529.
- 2.34 H.L. Goldsmith, S.G. Mason, The flow of suspensions through tubes II. Single large bubbles,” *Journal of Colloid Science*, 18 (1963) 237-261.
- 2.35 A.M. Schwartz, S.B. Tejada, Studies of dynamic contact angles on solids, *J. Colloid Interface Sci.*, 38(2) (1972) 359-375.
- 2.36 J. Ratulowski, H.C. Chang, Transport of gas bubbles in capillaries, *Phys. Fluids*, A 1(10) (1989) 1642-1655.
- 2.37 R.K. Edvinsson, S. Irandoust, Finite element analysis of Taylor Flow, *AIChE Journal*, 42(7) (1996) 1815-1823.
- 2.38 M.D. Giavedoni, F.A. Saita, The axisymmetric and plane case of a gas phase steadily displacing a newtonian liquid - A simultaneous Solution to the governing equations, *Phys. Fluids*, 9(8) (1997) 2420-2428.
- 2.39 M. Heil, Finite reynolds number effects in the Bretherton Problem, *Phys. Fluids*, 13(9) (2001) 2517–2521.
- 2.40 T. Taha, Z.F. Cui, CFD modeling of slug flow inside square capillaries, *Chem. Eng. Sci.*, 61 (2006) 665-675.
- 2.41 Y. Han, N. Shikazono, Measurement of liquid film thickness in micro square channel. *International Journal of Multiphase Flow* 35 (2009), 896-903.
- 2.42 M.G. Cooper, A.J. Lloyd, The microlayer in nucleate pool boiling, *Int. J. Heat Mass Tr.* 12 (1969) 895-913
- 2.43 J. Xu, Y. Li, T. Wong, High speed flow visualization of a closed loop pulsating heat pipe, *Int. J. Heat Mass Transfer*, 48(16) (2005) 3338-3351.

- 2.44 A. Tripathi, S. Khandekar, P. K. Panigrahi, Oscillatory contact line motion inside capillaries, 15th International Heat Pipe Conference (15th IHPC) Clemson, USA, (2010).
- 2.45 Y.S. Shekhawat, S. Khandekar, P.K. Panigrahi, Hydrodynamic study of an oscillating meniscus in a square mini-channel, Proceedings of International Conference on Micro/ Nanoscale Heat and Mass Transfer, Shanghai, China, (2009).
- 2.46 S. Lips, J. Bonjour, Oscillating two-phase flow in a capillary tube: Experiments and modeling,” Proceedings of 14th International Heat Pipe Conference, Florianopolis, Brazil (2007).
- 2.47 S. Lips, A. Bensalem, Y. Bertin, V. Ayel, C. Romestant, J. Bonjour, Experimental evidences of distinct heat transfer regimes in pulsating heat pipes, Appl. Therm. Eng., 30 (2010) 900-907.
- 2.48 S.G. Kandlikar, W.K. Kuan, A. Mukherjee, Experimental study of heat transfer in an evaporating meniscus on a moving heated surface, Transactions of the ASME J. Heat Transfer, 127 (2005) 244-252.
- 2.49 A. Mukherjee, Contribution of thin-film evaporation during flow boiling inside microchannels, Int. J. Therm. Sci., 48 (2009) 2025–2035.
- 2.50 I.Y. Chen, K.S. Yang, C.C. Wang, An empirical correlation for two-phase frictional performance in small diameter tubes, Int. J. Heat Mass Transfer, 45(17) (2002) 3667-3671.
- 2.51 T. Taha, Z.F. Cui, Hydrodynamics of slug flow inside capillaries, Chem. Eng. Sci., 59 (2004) 1181-1190.
- 2.52 P. Chamrathy, H.K. Dhavaleswarapu, S.V. Garimella, J. Murthy and S.T. Wereley, Visualization of convection patterns near evaporating meniscus using Micro-PIV, Exp. Fluids, 44 (2008) 431-438.
- 2.53 M. Magnini, B. Pulvirenti, J. Thome, Numerical investigation of hydrodynamics and heat transfer of elongated bubbles during flow boiling in a microchannel, Int. J. Heat Mass Transfer, 59 (2013) 451–471.
- 2.54 B.Mehta, Local convective thermal transport in single-/two phase non-pulsating and pulsating flows in square mini-channels, PhD Thesis IIT Kanpur, India (2014).
- 2.55 P.C. Wayner Jr., Y. Kao, L. LaCroix, The interline heat-transfer coefficient of an evaporating wetting film, Int. J. Heat Mass Transfer, 19 (1976) 487- 492.

- 2.56 S. Dasgupta, J.A. Schonberg, P.C. Wayner Jr., Investigation of an evaporating extended meniscus based on the augmented Young–Laplace equation, *J. Heat Transfer*, 115 (1993) 201–208.
- 2.57 S. DasGupta, J.A. Schonberg, I.Y. Kim, P.C. Wayner Jr., Use of the augmented Young–Laplace equation to model equilibrium and evaporating extended meniscus, *J. Colloid Interface Sci.*, 157 (1993) 332–342.
- 2.58 J.A. Schonberg, S. Dasgupta, P.C. Wayner Jr., An augmented Young–Laplace model of an evaporating meniscus in a microchannel with high heat flux, *Exp. Therm. Fluid Sci.*, 10 (1995) 163–170.
- 2.59 R.W. Schrage, A theoretical study of interphase mass transfer, Columbia University Press, (1953).
- 2.60 R. Marek, J. Straub, Analysis of the evaporation coefficient and the condensation coefficient of water, *Int. J. Heat Mass Transfer*, 44 (2001) 39–53.
- 2.61 P.C. Stephan and C.A. Busse, Analysis of the heat transfer coefficient of grooved heat pipe evaporator walls, *Int. J. Heat Mass Transfer*, 35(2) (1992) 383–391.
- 2.62 C. Höffman and P. Stephan, Microscale temperature measurement at an evaporating liquid meniscus, *Exp. Therm. Fluid Sci.* 26 (2002) 157–162.
- 2.63 S.S. Panchamgam, A. Chatterjee, J.L. Plawsky, P.C. Wayner Jr, Comprehensive experimental and theoretical study of fluid flow and heat transfer in a microscopic evaporating meniscus in a miniature heat exchanger, *Int. J. Heat Mass Transfer*, 51(2008) 53–68.
- 2.64 H.K. Dhavaleswarapu, S.V. Garimella, J.Y. Murthy, Microscale temperature measurements near the triple line of an evaporating thin liquid film, *J. Heat Transfer*, 131 (2009) 061501-1.
- 2.65 H.K. Dhavaleswarapu, J.Y. Murthy, S.V. Garimella, Numerical investigation of an evaporating meniscus in a channel, *Int. J. Heat Mass Transfer*, 55 (2012) 915–924.
- 2.66 K. Ibrahim, M.F. Abd Rabbo, T. Gambaryan–Roisman, P. Stephan, Experimental investigation of evaporative heat transfer characteristics at the 3-phase contact line, *Exp. Therm. Fluid Sci.*, 34 (2010) 1036–1041.
- 2.67 L. Biswal, S.K. Som, S. Chakraborty, Thin film evaporation in microchannels with slope- and curvature-dependent disjoining pressure, *Int. J. Heat Mass Transfer*, 57 (2013) 402–410.
- 2.68 V.S. Nikolayev, Oscillating menisci and liquid films at evaporation/condensation, Keynote Lecture #3, 17th International Heat Pipe Conference (17th IHPC), Kanpur, India,(2013).

- 2.69 V.S. Nikolayev, Oscillatory instability of the gas-liquid meniscus in a capillary under the imposed temperature difference, *Int. J. Heat Mass Transfer*, 64 (2013) 313 -321.
- 2.70 P. Gully, F. Bonnet, V.S. Nikolayev, N. Luchier, T.Q. Tran, Evaluation of the vapour thermodynamic state in PHP, 17th International Heat Pipe Conference (17th IHPC), Kanpur, India, (2013).
- 2.71 N. Chauris, V. Ayel, Y. Bertin, C. Romestant, Evaporation of a liquid film deposited on a capillary heated tube: Experimental analysis by infrared thermography of its thermal footprint, *Int. J. Heat Mass Transfer*, 86 (2015) 492–507.

Chapter 3

Experimental setups and data processing

As discussed in the Chapter 1 and 2, for better understanding of PHPs it is necessary to quantify the physical phenomena happening inside a single branch PHP using unit-cell approach. We can divide this problem keeping two main objectives in focuses, which need to be studied, and for which we developed two experimental setups:

- (a) **Thermal dynamics of the simplest version of PHP, namely the single branch PHP:** The first experimental set-up is designed to give us the understanding of the heat transfer mechanism inside a single-branch PHP along with the better insight to the thermally-driven self-sustained meniscus oscillations. This insight information obtained can lead us to the dynamics of thin film and its behaviour. This will enable to move closer to the governing physics of oscillating phase change systems like PHPs.
- (b) **Hydrodynamics of the meniscus inside the capillary:** The second experimental setup is designed to obtain the hydrodynamics behavior of different oscillating fluids inside a capillary tube by controlling the flow by external pressure variations in adiabatic condition. Mainly this setup is designed to estimate single phase frictional pressure drop and to observe contact line motion in oscillating conditions for various fluids.

1. Experimental setup 1: Thermal dynamics of the simplest unit cell of PHP

As discussed earlier in chapter 1, in 2010, *Das et al. [3.1]* presented the first experimental data of the simplest ‘unit-cell’ version of a pulsating heat pipe. This system consisted of a 2.0 mm ID capillary tube, heated on one end and cooled on the other end, with one liquid plug and one vapour bubble. They were able to obtain thermally-driven

auto-oscillations in such a ‘unit-cell’ system under a definite range of operating experimental conditions. Their experimental setup was close to the theoretical configuration previously studied by *Dobson [3.2, 3.3]*. Temporal variation of vapour pressure was recorded. The passive thermally-driven auto-oscillations of the liquid plug were observed; however, the visualization was restricted to only the condenser section. There were some important limitations with the approach of *Das et al. [3.1]*, which are listed herein:

- (i) Experiments were done without any synchronization of the internal pressure measurements with the videography. As will be discussed subsequently, this led to serious shortcomings in the interpretation of the results.
- (ii) The experimental setup was not fully transparent. The evaporator, made of copper, was opaque, and therefore the internal hydrodynamic phenomena could not be observed in totality; only, the condenser section was visible. This restricted data interpretation.
- (iii) The connection between the opaque metal evaporator and the adiabatic section/condenser which was made of glass, presented several flow perturbations that might have disturbed the smooth meniscus movement to a certain extent.
- (iv) For modeling the internal oscillatory phenomena of the meniscus existing between the vapour bubble and the liquid plug, they introduced an improved and coherent ‘evaporation/ condensation’ model, as against the earlier simplified ‘superheated vapour models’ *[3.2-3.5]*. While this improvement could indeed predict the large amplitude oscillations observed in their experiments, the possibility of metastable conditions and/or non-equilibrium heat transfer of the liquid thin film were not considered by them.

In this background, here we developed a novel experimental setup which is an improved version of the test bench, as was originally proposed by *Das et al. [3.1]*, overcoming all its limitations listed above. As we know the primary objective of this study is to enhance the fundamental understanding of the phenomena guiding the self-sustained thermally-

induced two-phase oscillatory flows in the capillary tube of PHPs. Compared to the previous setup of *Das et al. [3.1]*, the new design of the experimental bench is;

- (i) Entirely transparent made up of glass in order to comprehensively observe the liquid film dynamics not only in the condenser, but also in the evaporator section too.
- (ii) The capillary tube is placed in a vertical heater-up position, intentionally providing the most unfavorable and demanding conditions for PHPs to operate.
- (iii) The setup utilizes a seamless tube connection between the condenser and the evaporator sections, thus completely avoiding any flow perturbations due to geometrical or constructional singularities.
- (iv) It is also possible to observe a thin film lay inside the evaporator in some cases of experiments. Furthermore an additional high speed camera is used in experimental setup for the definite understanding of dynamics of thin film with synchronize visualization for thin film movement inside the tube, meniscus movement and vapour pressure measurement.
- (v) The vapour pressure measurements are now fully synchronized in real-time with the high speed videography camera.

These singular improvements of the setup has led to a drastic improvement in the overall understanding of the complex thin-film evaporation and ensuing pressure fluctuations inside the unit-cell. In fact, as will be explained later, some of the interpretations are so unique that it is likely to catalyze a new perspective in mathematical description of the phenomena.

1.1. Details of the experimental setup

The experimental setup consists of a basic single branch PHP with one liquid plug and one vapour bubble in a vertical capillary tube of circular cross-section. The transparent capillary tube, made of glass, is closed at one end and connected to a reservoir maintained at a constant pressure at the other end. Its inner diameter is

2 mm. The liquid plug oscillates between a heat source (evaporator section length = 200 mm) located near the closed side and a heat sink (condenser section length = 200 mm) located near the reservoir. In between, an adiabatic section separates the condenser and the evaporator (length = 10 mm). Thermal insulations are provided at desired places to avoid heat losses. In the following, the heat source and the heat sink will often be termed ‘evaporator’ and ‘condenser’ from an analogy with conventional heat pipes. One should however be aware that strictly speaking, this terminology is not fully adequate in the present system, since condensation can also occur in the evaporator. The basic schematic of the experimental setup with all the instrumentation is shown in the *fig. 3.1* and the details of the instruments used in the will be discussed in next section.

Referring to the *fig. 3.1*, the evaporator and the condenser are transparent heat exchangers, whose temperature is controlled by two thermostatic baths with an overall accuracy of $\pm 1\text{K}$. A third thermostatic bath is used to control the temperature of the reservoir ($\pm 0.2\text{K}$), and thus its saturation pressure. The two-phase oscillatory flow is characterized by simultaneous vapour pressure measurements and meniscus displacement tracking in sync with each other. An absolute pressure sensor (supplied by Kistler®, piezo-resistive sensor type 4007B, operating range of 0-5 bar, (accuracy $\pm 0.1\%$ of full-scale reading) is located at the closed end of the tube. To avoid condensation of working fluid due to atmospheric conditions at connections of pressure sensor and unit cell system, this place is maintained at suitable temperature by external heating and insulation. Two high speed cameras (PhotronFastcam® 1024-PCI and SA-3, respectively) are simultaneously used to track the meniscus displacement and movement of the triple-line.

A DC powered light source is used along with these two cameras for the better illumination for capturing the clear image of meniscus and thin film movement. A K-type thermocouple of diameter $80\ \mu\text{m}$ is also inserted from the top of the tube to measure the temperature of the vapour, as shown in *fig.3.1*. A GRAPHTEC data acquisition system is used for recording the data and also for triggering the cameras. This data acquisition device also has inbuilt standard noise filtering algorithms. The

pressure and temperature measurements are synchronized with the two video cameras with external trigger in the data acquisition system. The photograph of the actual setup is shown in *fig.3.2*.

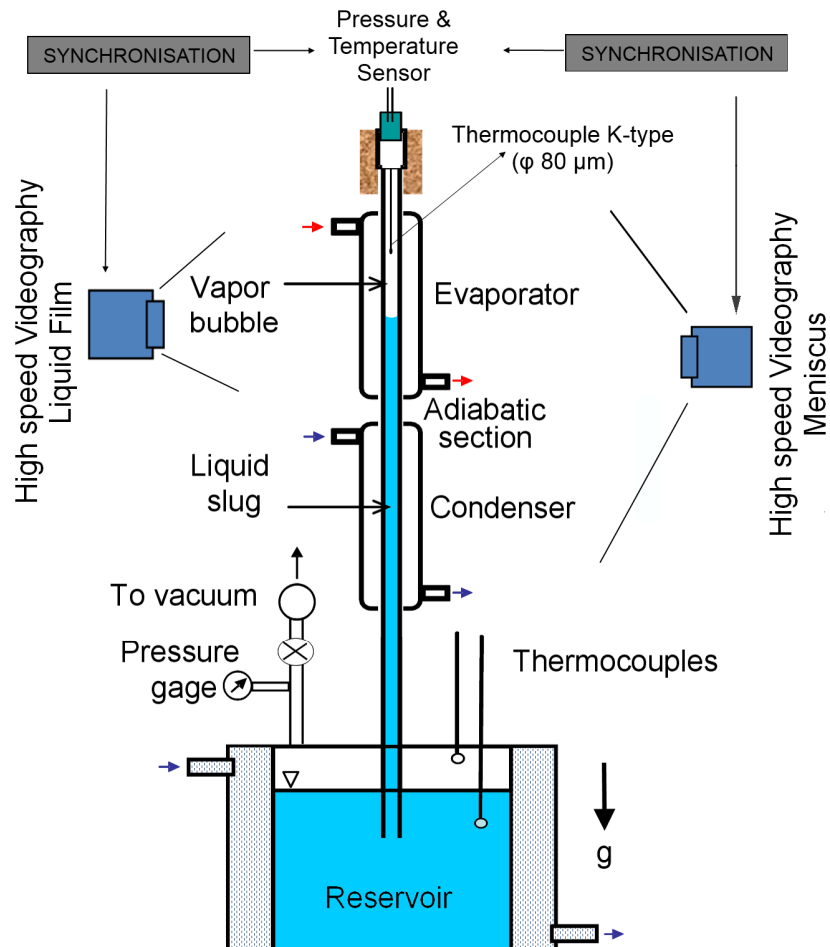


Fig. 3.1: Schematics of experimental setup 1- Thermal dynamics of the simplest unit cell of PHP.

The experiments are performed using various fluids (De-ionized water, Ethanol, Pentane and FC72) to cover the whole range of boiling points at atmospheric pressure. These fluids are also chosen as they can be used in future cooling systems which require an operating temperature range in between 0-100°C. The fundamental physical properties of these fluids are given below in Table 3.1.

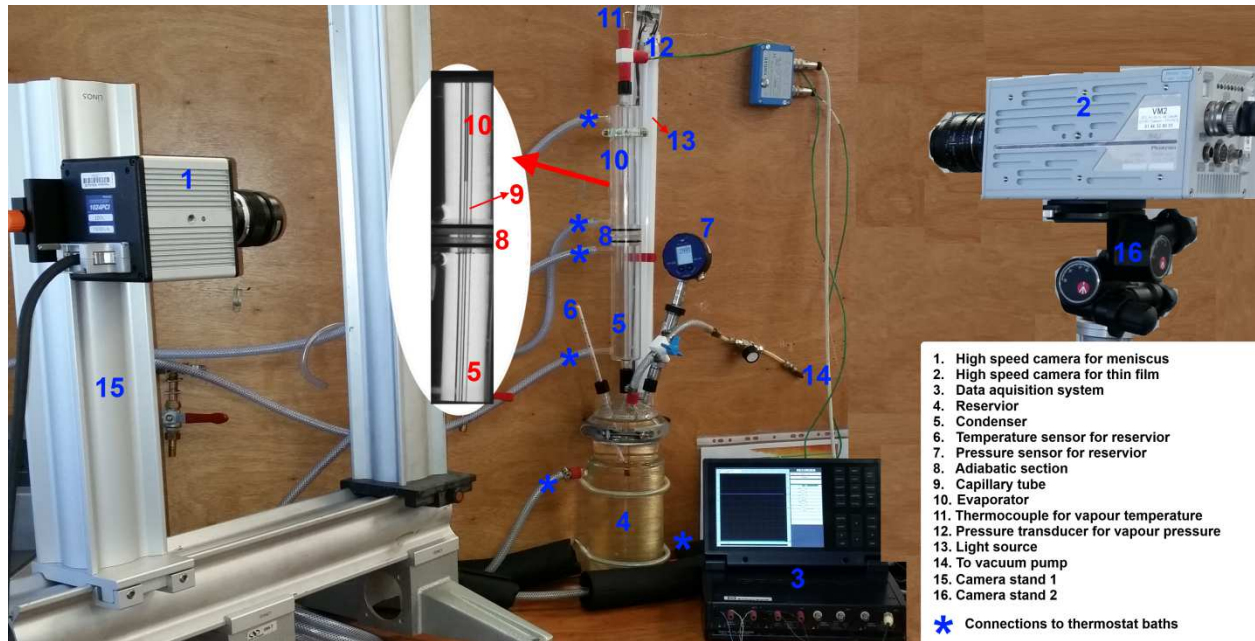
Table 3.1: The basic physical properties of fluids used

Properties	Pentane	FC72 ¹	Ethanol	De-ionized water	Units
Boiling pt. - 1 atm	35.9	56	78.37	100	°C
Density ρ at 20°C	626	1680	789	996.8	kg/m ³
Dynamic Viscosity μ at 20°C	0.24x10 ⁻³	0.64x10 ⁻³	1.074x10 ⁻³	0.8796x10 ⁻³	Pa.s
Kinematic Viscosity ν at 20°C	0.33x10 ⁻⁶	0.38x10 ⁻⁶	1.4x10 ⁻⁶	0.8824x10 ⁻⁶	m ² /s
Surface tension σ at 20°C	0.015	0.01	0.0224	0.0728	N/m
Thermal conductivity at 20°C	0.136	0.057	0.17	0.6	W/m.K
Latent heat of vaporization at 1 atm	357	88	855	2260	kJ/kg
Refractive index at 20°C	1.358	1.251	1.3575	1.33	-

As discussed earlier the evaporator and condenser sections are made transparent to track the meniscus and thin film movement. These evaporator and condenser which act as heat exchangers are made up of high quality borosilicate glass with suitable connections to accommodate the capillary tube. These two evaporator and condenser are identical in dimensions and shape. Evaporator and condenser are joined to each other using a specially made adiabatic section which holds these two along with the capillary tube. This adiabatic section is made up of Plexiglas and thus provides desired insulation from heat transfer interactions between evaporator and condenser. The

¹ FC72 - - 3M™ Fluorinert™ (Perfluorohexane (C₆F₁₄) or tetradecafluorohexane) is a clear, colorless, fully-fluorinated liquid. FC-72 is thermally and chemically stable, compatible with sensitive materials, nonflammable, practically nontoxic and leaves essentially no residue upon evaporation. This unique combination of properties makes Fluorinert liquid FC-72 ideal for many electronics applications, including quality and reliability testing. It is used in one formulation of the electronic cooling liquid/insulator Fluorinert for low-temperature applications due to its low boiling point of 56 °C and freezing point of -90 °C.

capillary tube is also made up of borosilicate glass and precisely cut and cleaned for the use.



1. High speed camera for meniscus
 2. High speed camera for thin film
 3. Data acquisition system
 4. Reservoir
 5. Condenser
 6. Temperature sensor for reservoir
 7. Pressure sensor for reservoir
 8. Adiabatic section
 9. Capillary tube
 10. Evaporator
 11. Thermocouple for vapour temperature
 12. Pressure transducer for vapour pressure
 13. Light source
 14. To vacuum pump
 15. Camera stand 1
 16. Camera stand 2
- * Connections to thermostat baths

Fig. 3.2: Photograph of experimental setup 1- Thermal dynamics of the simplest unit cell of PHP.

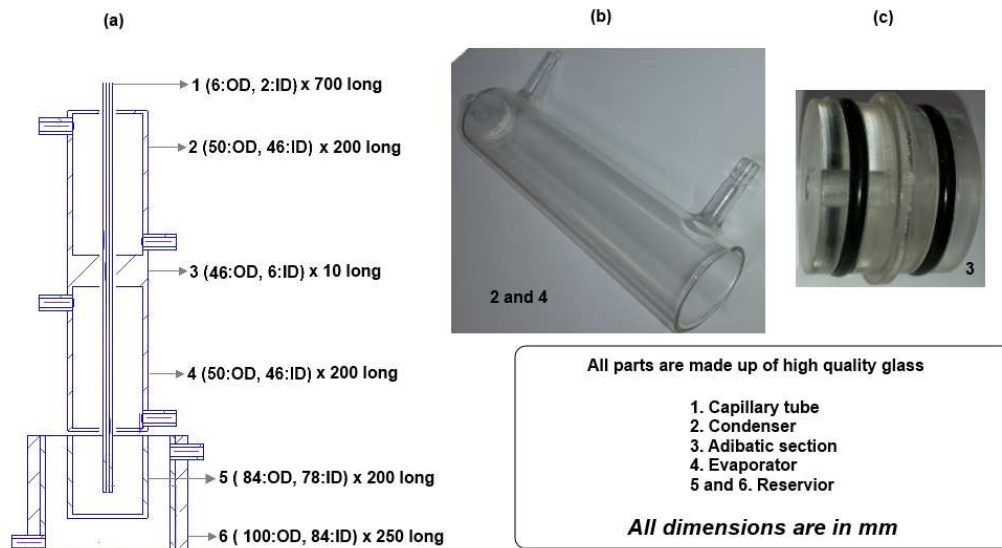


Fig. 3.3: Dimensions of experimental setup 1- Thermal dynamics of the simplest unit cell of PHP.

The reservoir used for our experiments is specially designed to store the working fluid of the PHP and also an internal jacket is integrated in it for heating and cooling of working fluid. All the parts, tubing and capillary tubes are assembled using leak proof vacuum fittings made of Teflon (can work in range of $-50\text{ }^{\circ}\text{C}$ to $150\text{ }^{\circ}\text{C}$). *Fig. 3.3* gives the dimensions of the important parts and actual photographs of evaporator, condenser and adiabatic section.

1.2. Experimental procedure

All the parts are thoroughly cleaned and assembled, then vacuum tightness of the complete assembly is ensured. Before the experiments starts, the system is completely evacuated to remove the non condensable gases using a vacuum pump ($< 10^{-5}$ mbar). The reservoir is then filled with the working fluid. After filling the liquid, all the non condensable gases present inside are removed. The volume of the reservoir is huge compared to that of the tube so that the oscillations inside the tube have negligible effects on the pressure within it. The capillary tube is always dipped inside the liquid irrespective of level of liquid in it. The changing in level affects the hydrostatic pressure at the exhaust of the tube, but in 3rd place of decimal, since the height of liquid above the exhaust of the tube is greater than 100 mm. Two high speed cameras, vapour pressure sensor and vapour temperature sensor are then verified for the synchronization.

There is some volume which is present inside the system which is not contributing to the PHP phenomenon but actually affecting its performance. This volume exists there due to the connections of pressure and temperature sensors at the vapour space at the end of capillary as shown in *fig. 3.2* by T junction. This volume we termed as the dead volume. To measure this dead volume, the empty weight of the connections (T junction) which is used to connect the thermocouple and the pressure transducer was measured, with help of a highly precise mass balance of METTLER TOLEDO. Then, the system is filled with water and the total weight measured again. The difference of weights was then divided by density of water to get the dead volume inside this T junction. This process was repeated several times to minimize the error. This dead volume was then found to be equal to $2.83 \times 10^{-6} \text{ m}^3 (\pm 5\%)$.

To get acquainted to the overall behavior of the experimental setup, it was necessary to determine the appropriate boundary conditions such as evaporator temperature, condenser temperature and reservoir pressure combination in which the self sustained thermally driven oscillations are obtained. It was observed that meniscus oscillates inside the capillary tube for certain combinations of above mentioned boundary conditions; these oscillations are sometimes regular, irregular, repetitive or random in nature. In some of the cases little external excitation is needed to start the first oscillation and in some cases it is automatically started. As we know that due to instabilities involved in the PHPs in general, several experiments were performed by varying the condenser/ evaporator temperature and reservoir pressure combinations. Due to imposed thermal gradient, meniscus oscillations of various shapes and size are observed. Out of these various experimental observations it is later on found that only a few with regular and repetitive patterns are useful to reach on logical conclusion.

With the help of vapour pressure/ temperature sensors and two high speed cameras, vapour pressure, vapour temperature, meniscus movement and triple line movement (if visible) are recorded in synchronization with each other. Also the respective reservoir pressure, condenser temperature and evaporator temperature are noted. The measurements recorded by these two cameras are in the form of B/W images. The meniscus is clearly observable in these images. Also when the thin film is observed its motion is observed by tracking the triple line motion, this motion is clearly distinguished by difference in the contrasts in the raw images. To get an accurate and reliable measurement we recorded 1000 data points per second.

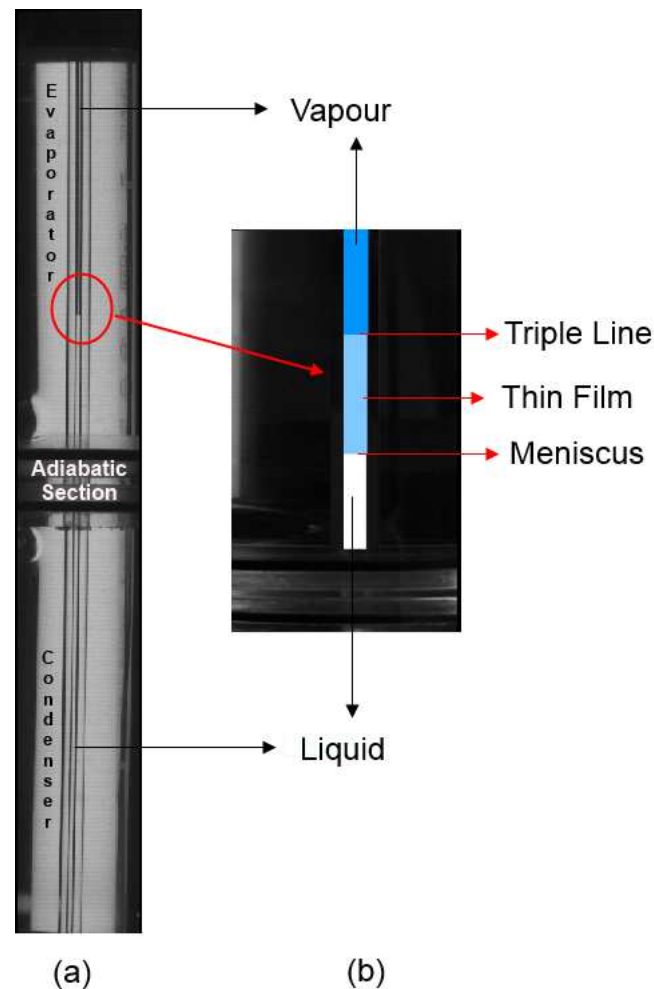


Fig. 3.4: (a) Typical image from camera 1 of the complete unit cell PHP with meniscus
(b) Schematic image from the camera 2 of the thin liquid film and triple line.

Fig. 3.4-a a typical image from camera 1 of the meniscus inside the capillary tube and *fig. 3.4-b* shows a schematic image from the camera 2 of the thin liquid film and triple line, this image is modified and represented schematically because it was quite difficult to get recognizable contrast of three zones on paper (liquid, thin film and vapour). Although it is difficult to represent the image of the triple line here, using the appropriate image processing technique it is possible to distinguish between the contrasts of various regions (thin film, vapour and liquid).

To summarize, the outcomes of the experimental measurements are the combination of following items shown in Table 3.2.

Table 3.2: Typical experimental measurements

Item	Symbol
Evaporator temperature	T_e
Condenser temperature	T_c
Reservoir pressure	P_r
Temporal variation of the vapour pressure	$P_v(t)$
Temporal variation of the vapour temperature	$T_v(t)$
Images of the meniscus for each time instance	
Images of the triple line (if visible) for each time instance	

1.3. Data processing

The pressure and temperature data are filtered using inbuilt standard noise filtering algorithms embedded in the data acquisition system. There are two cameras used for capturing the photographs of complete capillary tubes for meniscus movement tracking (Camera 1), photographs of evaporator capillary tube for tracking thin film movement (Camera 2) by observing the triple line (if visible) movement. These images are processed with code developed in MATLAB image processing tools. The code is available in [Appendix-B](#) for the purpose of archival. The outcome of this image processing is the position of meniscus inside the capillary tube in terms of pixel coordinates and later converted in actual distance by using appropriate scaling. Same is done for the case of triple line movement.

A schematic is shown in [fig. 3.5](#) for represents thermodynamic state of typical experimental results. Instantaneous vapour temperature $T_v(t)$, vapour pressure $P_v(t)$ and vapour volume $V_v(t)$ are measured. Referring to [fig. 3.5](#), the experiment provides the instantaneous location of the meniscus inside the capillary tube during its oscillatory motion. In other words, the instantaneous volume of vapour $V_v(t)$ can be estimated, neglecting the microscopic volume which the liquid film occupies. This volume is composed of the volume of vapour inside the tube and the constant dead volume which, which explained previously in section 1.2 of this chapter, is due to the connections of measuring instruments.

Using these data, the vapour mass dynamics $m(t)$ can be estimated using an adequate equation of state: as a first approximation, it will be convenient to adopt the simple assumption of ideal gas equation, when taking for granted $T_v(t)$ is always above the saturation temperature. The argument in support of using this hypothesis is that, the thermodynamic state of the system is far away from critical point and the and also has moderate ΔP and ΔT .

$$m_v(t) = \frac{P_v(t) \times V_v(t)}{\bar{R} \times T_v(t)} \times \bar{M} \tag{3.1}$$

where, \bar{R} is the universal gas constant and \bar{M} is the molecular weight of the fluid.

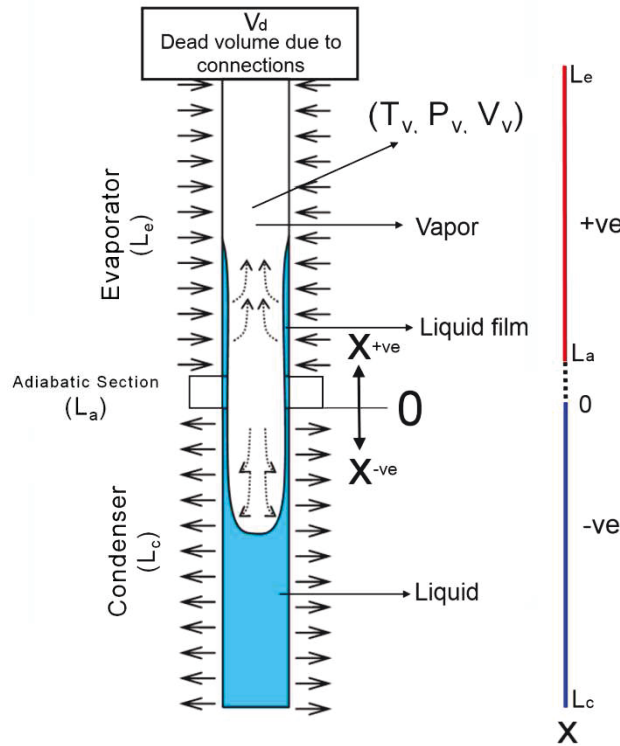


Fig. 3.5: Thermodynamic state of unit cell PHP.

Later this information coupled to the temporal movement of the triple line, enables to estimate the time-dependent thinning of the liquid film in the evaporator section. Finally, a simple mass balance equation in the evaporator provides an estimation of the initial thickness of the film. Hence, the dynamics of the film in the evaporator can be

completely derived. This part of the data processing will be discussed during the detail discussion about the meniscus dynamics and thin film dynamics in the chapter 4.

2. Experimental setup 2: Hydrodynamics of the meniscus inside the capillary (adiabatic experiments)

As discussed earlier in chapter 1 and 2, the singularities and friction play an important role in modeling the single branch PHPs. To overcome these problems, ideal solution is to obtain two-phase frictional pressure drop for a single branch PHP. But as it is quite difficult to build such experimental system to measure two phase pressure drop, also at same time modeling is also quite difficult as discussed in section 2.3.5 of chapter 2. Keeping this in mind, *Das et al. [3.1]* have incorporated the single phase frictional pressure drop for the oscillating flow inside the capillary tube in their model. Hence it will be interesting to verify this approximation using frictional pressure drop experiments for single phase oscillating fluids. The key is to develop an experimental setup which has similar in dimensions to setup 1 (as discussed in section 1 of this chapter) and then measuring the pressure drop in adiabatic conditions for oscillating fluid within similar frequency range. This verification will give clues either to verify the assumptions used in the model developed by *Das et al. [3.1]* or may lead to totally new findings. Also it will be interesting to see the contact line behaviour of the thin film laid by the fluids (if visible) during the oscillations inside the capillary tube (as discussed in section 2.3.4 of chapter 2).

2.1. Details of the experimental setup

Keeping above objectives in focus we built a new experimental setup using the same dimensions as of setup 1, as discussed in the previous section. The size of the capillary tubes is kept 2 mm internal diameter and 6 mm outer diameter. The length of this capillary tube taken as 700 mm. This tube is dipped inside the same reservoir used in the setup 1 described above.

A KELLER made (model PD23 measuring up to 1000 mbar with accuracy of 0.1% of full scale) differential pressure transducer is connected at one end of the capillary tube and

other end to the reservoir, so as to measure the pressure difference during the oscillations of the meniscus. This differential pressure transducer is capable of measuring the dynamic signal with a maximum output capturing frequency of 1000 Hz. The differential pressure transducer requires an external power supply of appropriate DC voltage. Experiments have been done in vertical orientation as to see influence of this pressure drop on the results obtained from experimental setup 1.

The liquid inside the reservoir-capillary tube system is externally excited using a pressure function generator (made by Elveflow model AF1) connected at the reservoir to move the meniscus in desired oscillating pattern. Elveflow® provides the microfluidic flow control system using piezo technology and enables a blazing fast flow change in our system. It gives a stable and pulse less flow while remaining extremely reactive. The exit of the Elveflow pressure function generator is connected to the reservoir tank in which the capillary tube is dipped, the connection (tubing) from Elveflow to the reservoir is kept long enough to obtain smooth pulse. These external excitation to the liquid, generated similar conditions of meniscus oscillations of the thermally induced oscillations inside the capillary tube similar to as we find a typical single branch PHP. Teflon vacuum fittings are used to connect all the tubing's of the experimental setup.

Similarly to previous experiments a high speed camera (SA-3) is simultaneously used to track the meniscus displacement. Also a DC powered light source is used along with this camera for the better illumination to capture the clear images during meniscus movement.

A GRAPHTEC data acquisition system is used for recording the data. This data acquisition device also has inbuilt standard noise filtering algorithms to filter the unnecessary noise. The pressure measurements are synchronized with the video camera with external trigger in the data acquisition system. The schematic of the actual setup is shown in *fig. 3.6*. These experiments are done in adiabatic conditions and without evaporator and condensers to facilitate the better view of the meniscus and thin film. *Fig. 3.7* shows the actual photograph of the experimental setup. To quantify the validity of standard frictional pressure drop correlations in such case of oscillatory motion of

fluid oscillating inside the capillary, Pentane and FC72 are used at atmospheric conditions in typical range of frequencies of a PHP.

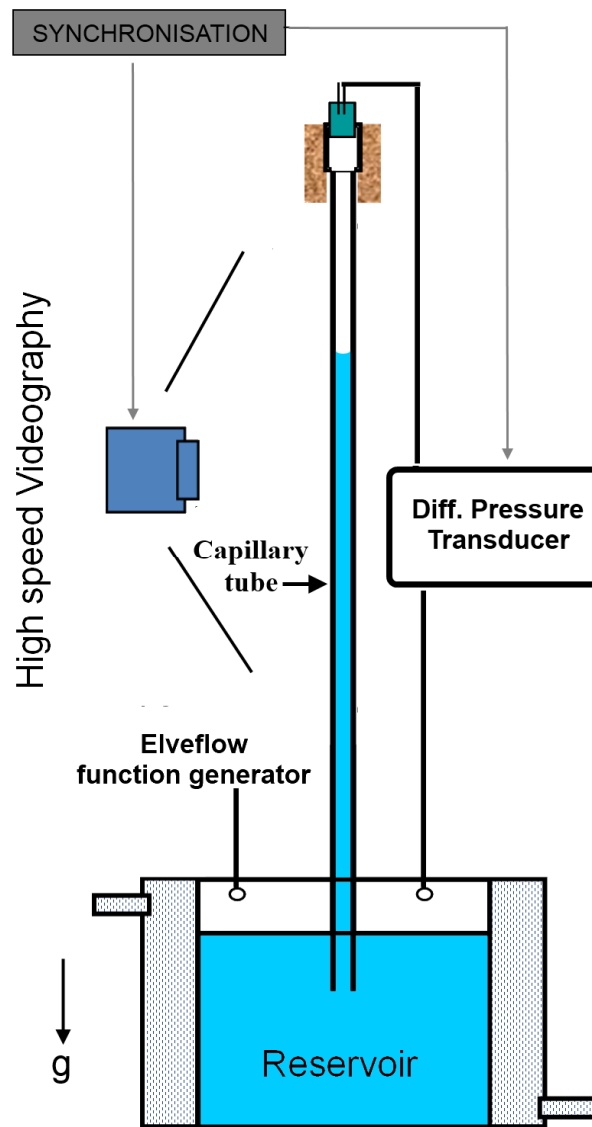
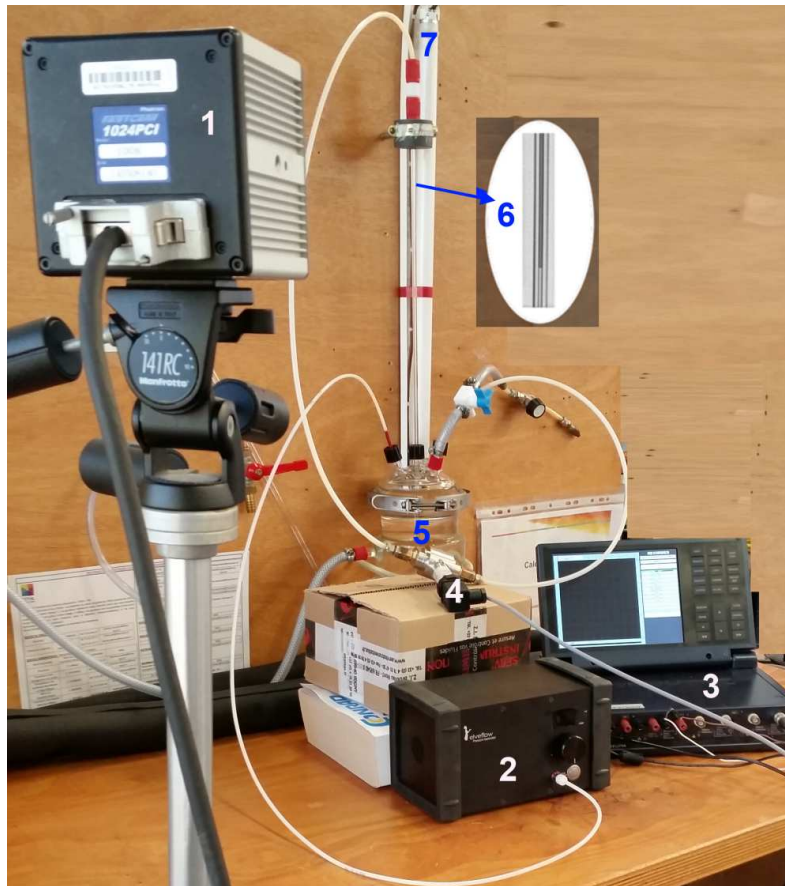


Fig. 3.6: Schematics of the experimental setup 2: Hydrodynamics of the meniscus inside the capillary.



1. High speed camera
2. Elveflow pressure function generator
3. GRAPHT|EC data acquisition system
4. KELLER PD23 differential pressure transducer
5. Reservoir
6. Glass capillary tube of 2mm internal diameter
7. Background DC white light source

Fig. 3.7: Actual photograph of the experimental setup 2: Hydrodynamics of the meniscus inside the capillary.

2.2. Experimental procedure

All the parts are thoroughly cleaned and assembled with ensuring for leakages. The reservoir is then filled with the working fluid (Pentane and FC72). The volume of the reservoir is huge compared to that of the capillary tube so that the oscillations inside the tube have negligible effects on the frictional pressure drop within it. The capillary tube is always dipped inside the liquid in reservoir. The external pressure function generator excites the fluid inside the reservoir in desired pattern which is then transferred to

oscillate it inside the capillary. Thus the liquid level in reservoir is maintained at highest level to get smooth oscillations.

The pressure function generator device is then connected to the reservoir. This connection (tubing) should not come in contact with liquid in reservoir to avoid entering of liquid in pressure function generator device. With the help of pressure function generator we can generate various types of pressure signals, e.g. sinusoidal, triangular, square or flat with various frequencies and amplitudes. For the purpose of uniformity we have chosen the sinusoidal pressure function for all of the experiments so that the meniscus oscillates in regular periodic motion. The frequency of these excitation signals is kept in the range of the frequencies found typically in the case of our single branch PHP experiments (0-2 Hz). The meniscus movement is in the form of B/W images recorded along with in synch temporal variation of differential pressure. The outcomes of the experimental measurements are the combination of the items shown in Table 3.3.

Table 3.3: Typical experimental measurements

Item	Symbol
Fluid	
Images of the meniscus for each time instance	
Frequency	f
Temporal variation of differential pressure	ΔP

2.3. Data processing

The differential pressure measured is then converted to calculate the actual differential pressure across the two ends of the capillary tube (as the other end of differential pressure transducer were connected to the reservoir) using suitable calculations. Camera used for capturing the capillary tube for meniscus movement tracking and for tracking thin film movement by observing the triple line (if visible) movement gives the B/W images. These images are processed with code developed in MATLAB using image processing tools. The method is similar to as discussed in section 1.2 of this chapter. The detail data processing of this part will be discussed further in chapter 5 while analyzing

the results as it involves some acquaintance with the terminologies involved in modeling such phenomenon.

3. Closing remarks

- These experimental setups leads us to encouraging results which we feel are helpful to enhance the understanding of the single branch PHP, are discussed in chapter 4 and 5.
- Uncertainties involved and calibration of some of the instruments in these experiments are discussed separately in the *Appendix-C*.

References

- 3.1 S. Das, V. Nikolayev, F. Lefèvre, B. Pottier, S. Khandekar and J. Bonjour, Thermally induced two-phase oscillating flow inside a capillary tube Int. J. Heat Mass Transfer, 53 (2010) 3905 – 3913
- 3.2 R.T. Dobson, Theoretical and experimental modelling of an open oscillatory heat pipe including gravity, Int. J. Therm. Sci. 43(2) (2004) 113–119.
- 3.3 R.T. Dobson, An open oscillatory heat pipe water pump, Appl. Therm. Eng., 25(4) (2005) 603–621.
- 3.4 M.B. Shafii, A. Faghri, Y. Zhang, Thermal Modeling of Unlooped and Looped Pulsating Heat Pipes, ASME J. Heat Transfer, 123 (2001) 1159–1171.
- 3.5 M.B. Shafii, A. Faghri, Y. Zhang, Analysis of Heat Transfer in Unlooped and Looped Pulsating Heat Pipes, International Journal of Numerical Methods for Heat & Fluid Flow, vol. 12/5, (2002) 585–609.

Chapter 4

Results and discussions - Single branch PHP experimentation and thin film dynamics

The scientific objectives of this work are to investigate the main physical effects that govern oscillations of a meniscus in both theoretical and experimental approach of a single branch PHP. Energy is supplied to the system mainly via evaporation/condensation, which occurs mainly through the wetting films. In this context a holly collaboration of CETHIL, France and IIT Kanpur, India with the help of CEFIPRA¹ came in to existence a few years ago to contribute the march towards decoding the physics of a PHP. This work is also a part of such journey. The film dynamics is studied in two different ways viz. first by experiments and then second by the theoretical modeling. In this sense, chapter 4 compromise of mainly two parts;

- (i) In the first section, we will be discussing the experimental results obtained using setup 1 and setup 2 as explained in the section 1 and section 2 of the chapter 3. This will give an opportunity to discuss the overall thermo-hydrodynamics involved in the studied systems of a single branch PHP.
- (ii) In second section a simplified theoretical analysis of unsteady heat transfer in the liquid thin film in context of single branch PHPs will be performed using analytical models.

The results presented here are already published (*Rao et al. [4.1, 4.2]*) in peer reviewed journal in previous years.

1. Experimental results of single branch PHP

As discussed in chapter 1 and 2 self-sustained thermally-induced oscillations of a meniscus in a two-phase system consisting of a liquid plug and a vapour bubble in a

¹ CEFIPRA joint project between CETHIL, France and IIT Kanpur, India # 4408-1

capillary tube are needed to be studied to understand the working of single branch PHP and ultimately, of full scale PHP. In this respect as explained in chapter 3 we developed two experimental setups. In this section we will be discussing the heat transfer mechanism inside the single branch PHP along with present our overview on thin film contribution to working of a single branch PHP.

1.1 Experimental boundary conditions

As discussed in chapter 3, the experiments are performed using various fluids (De-ionized water, Ethanol, FC72 and Pentane). The exact starting conditions of such systems cannot be determined using the available knowledge. Therefore for all of the fluids, we have tried various combinations of reservoir pressure, evaporator temperature and condenser temperature to find the correct combination of above three for obtaining self-sustained-thermally induced oscillations of the working fluid inside the system. We were successfully able to find such suitable combination for the FC72 and pentane but with de-ionized water and ethanol, we were not able to find any combination of reservoir pressure (0.2 to 1 bar), evaporator temperature (-10 to 120°C) and condenser temperature (-10 to 120°C) that would result in visible oscillations. Later on, analyzing the results for FC72, we found that the thin film laid by the meniscus on evaporator wall during receding motion towards the condenser plays an important role in maintaining the oscillations (refer section 1.4 below). So the non functioning of our system with de-ionized water and ethanol can be due to the phenomenon assumed by *Tripathi et al. [4.3]*, they explained that, depending on the wettability of the fluid on the solid wall, in conjunction with the applied external surface and body forces, there can be three types of oscillatory contact line motion of the liquid gas/vapor meniscus confined in a tube viz. (a) No pinning - the average velocity of contact line scales with the average bulk liquid velocity, (b) Partial pinning - there is a phase lag in the contact line velocity and the bulk fluid velocity, and (c) Full pinning, the contact line is motionless while the bulk liquid moves/ oscillates. *Fig. 4.1* represents schematics of the possible cases of contact line behaviour for various fluids. In this figure temporal meniscus movement is plotted along with the relative temporal movement of triple line (thin film is laid when meniscus moves downwards). In first scenario when fluid exhibits full contact line

pinning, the triple line is shown by red colour which doesn't move at all with respect to the meniscus and believed to be pinned to the wall. For no pinning case the triple shown by green colour moves along with the meniscus and hence have zero relative velocity with meniscus movement. In the case of partial pinning which is represented by blue line the triple line movement behaviour will lay in the zone in between green and red dotted lines. The slope of this blue dotted line will depend upon the interfacial properties of the fluid and solid.

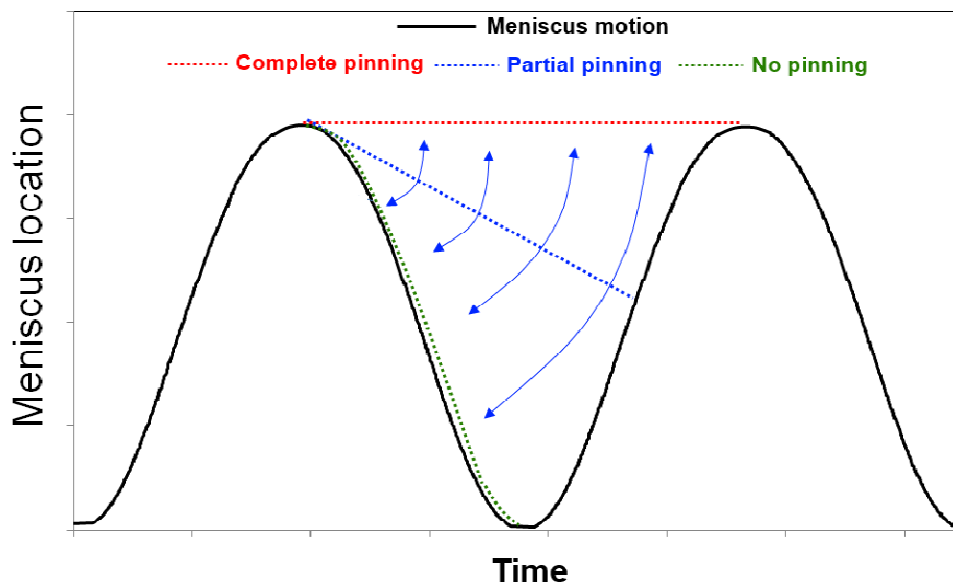


Fig. 4.1 Schematics of the various possible cases of contact line behaviour.

To verify this hypothesis we have done the experiments in adiabatic conditions (refer section 2 of chapter 3) to observe the relative film motion with meniscus. It is found that, it possible to observe the motion of triple line in the case of de-ionized water. *Fig. 4.2* represents the adiabatic experimental results of the motion of the triple line with respect to meniscus motion in a capillary and thus corresponds to the partial pinning of contact line as described by *Tripathi et al. [4.3]*. Looking into *fig. 4.1* we can say that the contact line is not pinned and also the de-pinning rate is not that high. So this can be a case of partial pinning.

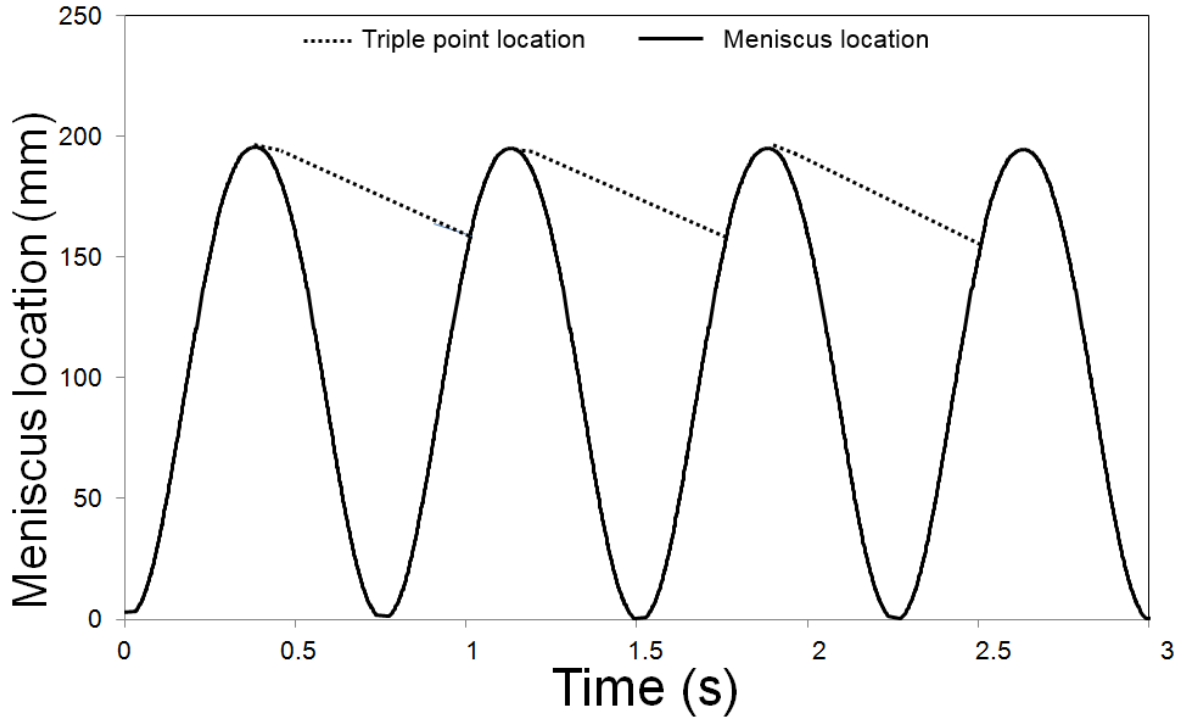


Fig. 4.2: Represents the adiabatic experimental results for de-ionized water, motion of the triple line with respect to meniscus motion in a capillary and thus corresponds to the partial pinning of contact line.

We believe that this movement of the contact line may be responsible for the non sustainable oscillations in the case of de-ionized water. Similarly in the adiabatic experiments of the FC72, Ethanol and Pentane it is not able to visualize the triple line movement; hence it will be difficult to comment on the contact line behaviour of these fluids. But as in the heat transfer experiments we saw the motion of the triple line for the FC72 (refer section 1.2 below), so we feel it is can be a case of full pinning, and also although the movement of triple line is not visible for Pentane heat transfer experiments but it sustains thermally-induced oscillations, hence it may be a case of full pinning. As we described earlier that neither the self-sustained thermally-induced oscillations are obtained for the Ethanol, nor we able to see its triple line movement in adiabatic experiments, so it can be a case of partial pinning or no pinning. This invisibility of the triple line movement (thin film) in the case of Ethanol and Pentane may be due to either the very thin film formation which is not observable using the camera or refractive index is not favorable to capture.

Although this contact line behaviour may not be the only cause of non self-sustained thermally-induced oscillations, it may be affected by physical properties, interfacial behaviour or tube material in the case of water and ethanol. In this respect a model is developed and solved to incorporate such parameters to know their relative influence on oscillations, which will be discussed in chapter 5.

So here onwards only results of FC72 will be discussed for a set of parameters to understand the governing mechanism of the single branch PHP. Similar kinds of results are also obtained for the Pentane but without the recording of the thin film location, these results are presented in the [Appendix-D](#) for the purpose of archival.

In the following, experimental results are discussed for various operating boundary conditions of FC72 as working fluid. The reservoir is maintained at a constant pressure of 0.5 bar, corresponding to a saturation temperature of 37.2°C. The evaporator temperature T_e is kept constant at 46°C while the condenser temperature T_c is varied from 0°C to 32°C. It is observed that when T_c is kept below 16°C (large temperature difference between the evaporator and condenser) or above 28°C (low temperature difference between the evaporator and condenser) the meniscus moves rather randomly and hence, it is very hard to obtain repeatability in such results. For the condenser temperature in between 16°C to 28°C systematic repeatable oscillations of vapour pressure and meniscus movement and thin film movement are observed. Therefore, the results presented in the next sections are taken in this range to arrive at meaningful conclusions which can contribute in attaining the objectives of this research.

Note: For the figures (fig. 4.3 to 4.8) presented in this section, the location $X = 0$ corresponds to the bottom of the adiabatic section. Locations defined by $X > L_a$ are in the evaporator section (represented by red line on primary Y-axis) while those defined by $X < 0$ are in the condenser section (represented by blue line on primary Y-axis).

1.2 Meniscus oscillation with pressure variation

Fig. 4.3 shows the temporal variation of vapour pressure in the vapour bubble, along with the location of the meniscus and the triple-line, for four cases of the experimentally applied boundary conditions ($T_e = 46^\circ\text{C}$ and $T_c = 16^\circ\text{C}$, 20°C , 24°C and 28°C , respectively). Three complete meniscus motion cycles are presented for each condenser temperature. It is observed that meniscus movement and pressure variation are quasi-periodic and nicely repeatable for all of the cases. When the meniscus moves towards the condenser (downward motion), a thin liquid film gets drained or laid on the tube wall. As it will be explained later, this film drainage by the moving meniscus is responsible for the large amount of vapour generation at the evaporator, which, in turn, leads to the oscillation of the liquid plug. By looking at the video of meniscus motion, it is possible to distinctly observe three different zones inside the tube: a dark zone corresponding to the liquid plug, a clear zone corresponding to the vapour slug, and an in-between zone where the contrast is neither dark nor clear that corresponds to this thin liquid film, which gets laid down during meniscus downward motion.

Furthermore, under proper lighting conditions and controlled focus, it is also possible to clearly observe the liquid film vanishing with time, i.e., evaporation of the film from the glass surface is unmistakably recorded. The movement of the triple-line towards the condenser is also clearly observable. We consider that the liquid film vanishes when the contrast value observed on the video is similar to the contrast value due to the vapour. However, as the contrast depends on the thickness of the liquid film, the sensitivity of the camera is probably not able to distinguish film-remnants which are extremely thin. Therefore, subsequent analysis is based till the location where the difference of contrast is just vanishing. However, one should keep in mind that the absence of explicit quantitative data points does not mean with certainty that the liquid film has indeed totally vanished; a few monolayers of liquid may still be remaining. Nevertheless, the recorded information certainly enables to bring some essential information for qualitative interpretations.

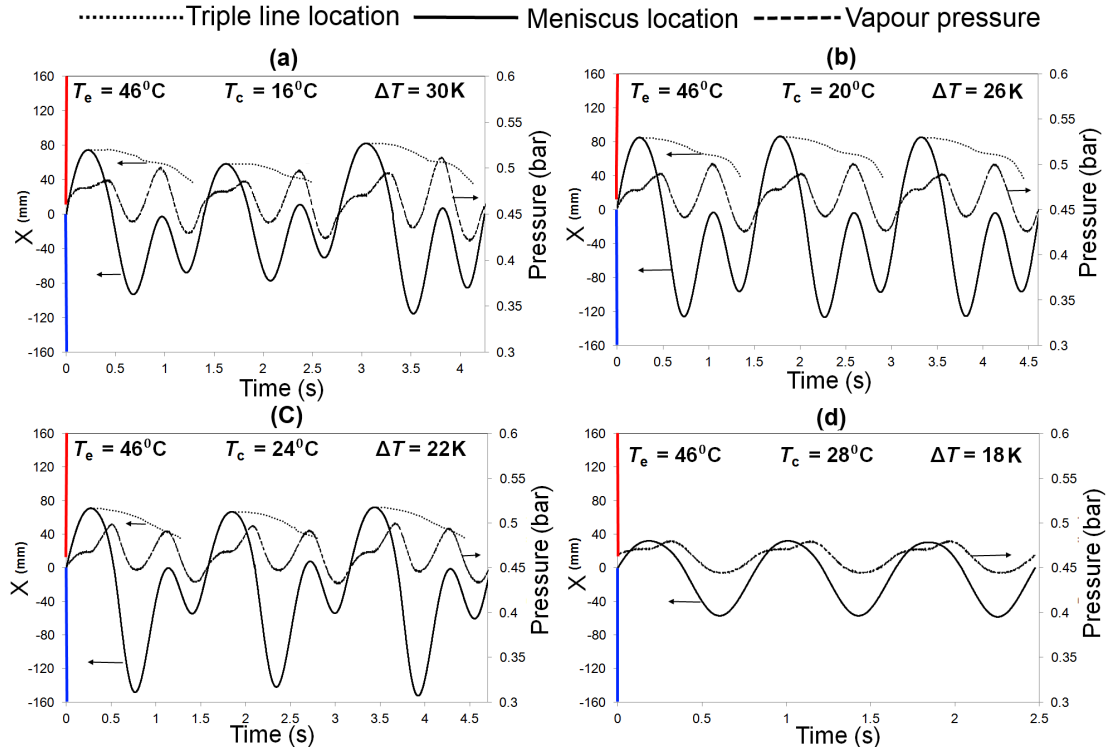


Fig. 4.3: Temporal variations of pressure (right ordinate axis) in the vapour bubble along with location of meniscus (left ordinate axis, solid line) and triple-line (left ordinate axis, dotted line) for experimental condition of $T_e = 46^\circ\text{C}$ and (a) $T_c = 16^\circ\text{C}$, (b) $T_c = 20^\circ\text{C}$, (c) $T_c = 24^\circ\text{C}$ and (d) $T_c = 28^\circ\text{C}$ and $P_r = 0.5$ bar.

For $T_c = 16^\circ\text{C}$ (fig. 4.3-a), $T_c = 20^\circ\text{C}$ (fig. 4.3-b) and $T_c = 24^\circ\text{C}$ (fig. 4.3-c), the meniscus cycle consists of one full stroke inside the evaporator followed by two smaller strokes in the condenser section. During the downward stroke of the meniscus, as noted earlier, it lays down a thin liquid film. Evaporation of this film adds mass to the vapour space and helps in increasing the vapour pressure. Until the time the liquid film laid down by the downward moving meniscus is completely evaporated, the meniscus is not able to re-enter the evaporator, and thus moves back again twice into the condenser. Thus, two strokes are seen to occur in the condenser section. The meniscus re-enters the evaporator section, after the second stroke in the condenser is over, and then the quasi-periodic cycle continues. The maximum high level reached by the meniscus inside the evaporator is rather constant and close to $X = 80$ mm for the different condenser temperatures. This tends to suggest that the amount of vapour generated during one

cycle at the evaporator is rather constant, since it is proportional to the length of the liquid film drained by the meniscus in the evaporator.

Conversely, the maximum level reached by the meniscus inside the condenser increases with the increase of T_c during the first stroke inside the meniscus. Indeed, for smaller condenser temperatures (larger temperature difference), a smaller heat exchange surface area is necessary to condense the vapour generated by the evaporation of the liquid film. The second stroke in the condenser is always shorter than the first one, which can be explained by a smaller amount of vapour generated in the evaporator (the last remnant of the disappearing liquid film), as the remaining liquid film length is much smaller at the end of a cycle. One can also observe that the cycle time-period slightly increases with the increase of T_c .

The qualitative behaviour of the meniscus oscillatory motion is quite different for $T_c = 28^\circ\text{C}$; the meniscus oscillation cycle consisting of a single to-fro stroke in the evaporator (*fig. 4.3-d*), followed by one stroke in the condenser section. Therefore, the net time period of one oscillation cycle is also smaller than for the other condenser temperatures. One can also observe that the amplitude of the signal is much smaller in both the condenser and the evaporator. Above a condenser temperature of 28°C , the energy of the system is not sufficient to maintain the oscillations. It was not possible to distinguish clearly the triple-line evaporation in that case because the length of the film formed due to drainage was very short, compared to other condenser temperatures. Lastly, comparing the pressure signal for the four graphs (*fig. 4.3-a to d*), shows the decrease of its amplitude with the decrease of the difference between T_e and T_c . The maximum of amplitude varies from 0.16 bar to 0.06 bar, when T_c varies from 16°C to 28°C , respectively.

The oscillatory behaviour of the meniscus can be directly and definitely linked with the nature of the liquid film laid by the meniscus while coming down from evaporator. This phenomenon is explained in details in *fig. 4.4-a* where the boundary conditions are $T_e = 46^\circ\text{C}$ and $T_c = 20^\circ\text{C}$. Time evolution of the meniscus from the evaporator (Stage A) as it passes towards the condenser (Stage J) and comes back to the evaporator (Stage T)

is shown. *Fig. 4.4-b* is a typical temporal variation of pressure in the vapour bubble and movement of triple-line depicting several steps of the meniscus motion along with different stages in one cycle (A to T).

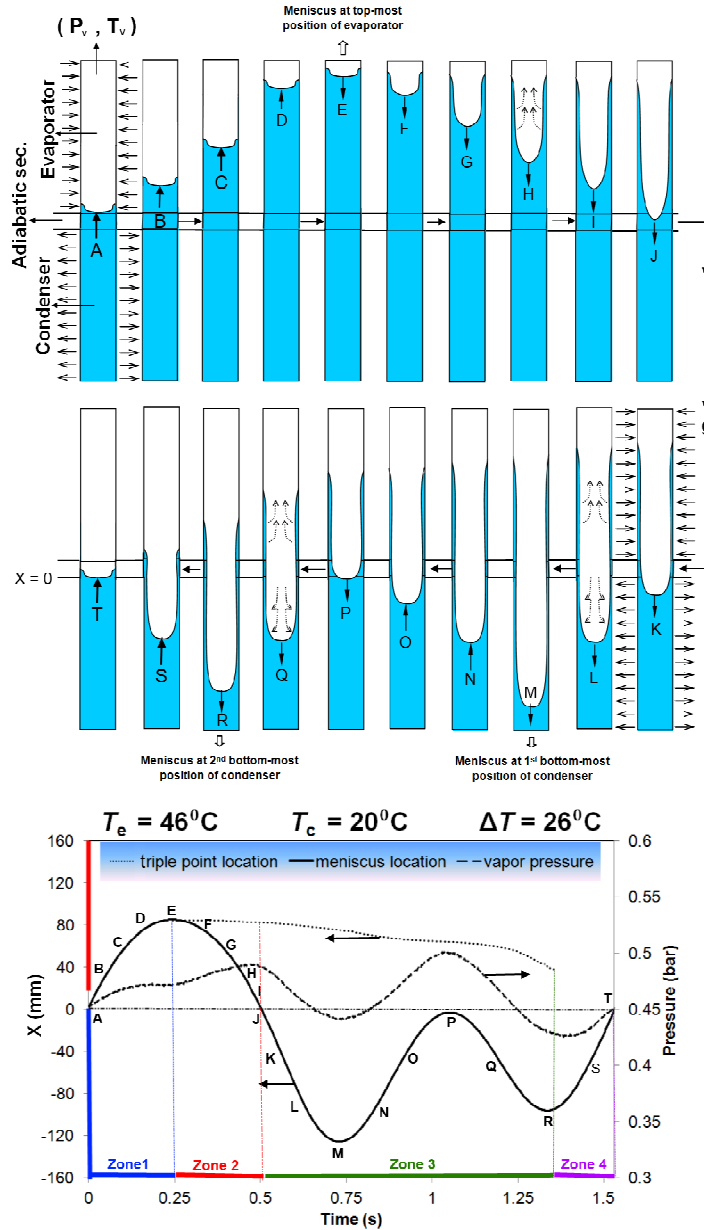


Fig. 4.4: (a) Schematic explaining the events during one cycle of the meniscus motion. (b) Time evolution of the meniscus from the entrance in the evaporator (Stage A) as it passes towards the condenser (Stage J) and comes back to the evaporator (Stage T), is shown. The four zones are also highlighted (will be used in section 1.4.1).

From points A to E, the meniscus is moving upwards in the evaporator and is in the process of approaching the top-most position in the evaporator. During that stage, the vapour space is getting compressed and the pressure of the vapour bubble is simultaneously increasing. At point E, the meniscus reaches the topmost position of evaporator and dwells there for a very short time. This dwelling can be observed both in meniscus location and pressure variations (*fig. 4.4-b*). After point E, the meniscus starts its downward journey. It is observed that a film of liquid is laid on the wall of the tube and the triple-line location coincides with point E. As the meniscus starts moving downwards, this triple-line also starts following it but with a different speed. At point J, the meniscus is about to exit from the evaporator, as it enters the condenser section. It is clearly visible in the figure that at this stage the liquid film still exists in the evaporator section. The maximum value of vapour space pressure is not reached when the meniscus is at its topmost location in the tube, but just before it enters into the condenser. Indeed, the evaporation of the liquid film during the downward movement of the meniscus towards the condenser contributes to the increase of the pressure during the descent of the plug. From points K to M, the meniscus keeps on moving downwards in the condenser and the pressure begins to decrease, due to both, expansion of the vapour bubble and simultaneous condensation. At point M, the meniscus reaches the first bottom-most point in the condenser. The liquid film, albeit thinner, is still in the evaporator. From point N to point P, the vapour-pressure stills decreases, and the meniscus moves towards the evaporator.

During this upward motion of the meniscus in the condenser section, the pressure increases again, clearly indicating that the rate of vapour condensation process is not sufficient to overcome the mass addition rate due to the evaporation of the remaining liquid film. Therefore, the meniscus is not able to reach the adiabatic section, but changes its direction to move downwards again instead of entering the evaporator. This, as explained, happens due to the continued presence of the liquid film in evaporator, which is still continuously evaporating, thus restricting the upward motion of the meniscus. From points P to R the meniscus again re-travels till the bottom-most point of the condenser and very quickly thereafter, the vapour pressure decreases again. Meanwhile, no sooner the liquid film vanishes in between point R to T in the evaporator,

subsequent variation of the mass of vapour is only due to condensation and therefore the pressure of the vapour decreases until a very low value that enables the meniscus to be pulled up into the evaporator section yet again. This process then repeats itself, starting from A to T, with regular repeatable cyclic oscillations.

As has been appreciated, during one complete cycle of meniscus motion, the variation of the vapour pressure is due to both, evaporation and condensation of the fluid and compression or expansion phenomena of the vapour. During the ascent of the meniscus in the evaporator (upward stroke), no thin liquid film is present ahead of the meniscus. Hence during this part of the motion, there is practically no mass addition to the vapour space due to evaporation and the pressure change is directly attributable to compression effect, which results in a small variation of the pressure during that stage. This result undoubtedly highlights the importance of the thin film evaporation and vapour condensation phenomena in the ensuing meniscus oscillations, as compared the purely compression and expansion effects.

Fig. 4.4-b represents the time-evolution of the meniscus location and corresponding variation of vapour pressure during a period of 1.6 seconds. In addition, the location of the moving triple-line, i.e., the edge of the liquid film on the channel wall, is also displayed on this figure. It is clearly visible that the liquid film motion always lags behind the meniscus and takes finite time to evaporate. However, as mentioned earlier, it was not possible to record the variation of liquid film thickness until the very end of the evaporation process, due to photographic limitations. Nevertheless, it is clear that the film lifespan in the evaporator is rather long as compared to the total time period of the oscillation.

Therefore, until the meniscus completes the first part of the cycle of travelling through to the bottom-most point of condenser again coming back to the entrance of evaporator, remnants of the evaporating liquid film still exists in evaporator, thereby restricting the entry of the meniscus into evaporator and pushes it back to the condenser. This behaviour of the meniscus movement is responsible for small and big amplitude oscillations, respectively. As soon as the liquid film completely disappears from the

evaporator, the meniscus is able to re-enter the evaporator again during its return motion from condenser. In this way, regular and repeatable self-sustained thermally driven oscillations go on in the tube at the imposed thermal gradient. With reference to the *fig. 4.3*, it can be said that the film life, i.e., the time period between the film appearing and subsequently completely getting evaporated and vanishing, is of the order of typically between 1.0 s to 1.4 s.

1.3 Actual vapour temperature versus the vapour saturated temperature

Fig. 4.5 presents temporal variations of vapour pressure and temperature in the vapour bubble depicting several cases of the experimentally applied boundary conditions ($T_e = 46^\circ\text{C}$ and $T_c = 16^\circ\text{C}$, 20°C , 24°C and 28°C). The saturation temperature of the working fluid corresponding to the measured pressure is also plotted along with the measured vapour temperature. The measurement of temperature by this micro-thermocouple is critical and requires close scrutiny. Indeed, even if the size of the thermocouple is rather small (bead diameter is $80\ \mu\text{m}$), its frequency response, although much faster than the oscillating frequency of the system, is still finite and non-zero. Furthermore, the micro-thermocouple also exchanges heat by thermal radiation with the inner wall of the capillary tube (although emissivity of both the surfaces is expected to be quite low), which will introduce a non-vanishing bias in the temperature measurement. The precision of the temperature sensor would be lower than $\pm 0.5\ \text{K}$ if it was only based on a calibration process, but the previous described experimental biases increase this uncertainty and make it difficult to estimate properly. However, even with these limitations, the temperature information given by this micro-thermocouple provides some very useful information for qualitative interpretations of the system dynamics.

Secondly, and more strikingly, one major conclusion is that the vapour temperature is always higher than the saturated temperature derived from corresponding vapour pressure measurement, which corroborates the recent results obtained by *Gully et al. [4.4]* in cryogenic conditions. Their study also brings out the existence of superheated conditions of the vapour space during meniscus motion. This is a quite an important conclusion for the proposed modeling of the unit-cell PHP system. The fact that vapour

is seen to be always superheated throughout the cycle of meniscus oscillation provides the first-order justification for using the ideal gas equation for modeling the vapour space, in conjunction with the film dynamics in the evaporator and film condensation in the condenser; the latter two models providing the respective sources and sinks for vapour mass, corresponding to the evaporation and condensation rates, respectively. In the subsequent section, this idealization is used to find the temporal mass variation in the system, and as will be demonstrated, this exercise does provide important insights into the thermal-fluidic behaviour of self-sustained thermally driven oscillatory meniscus motion.

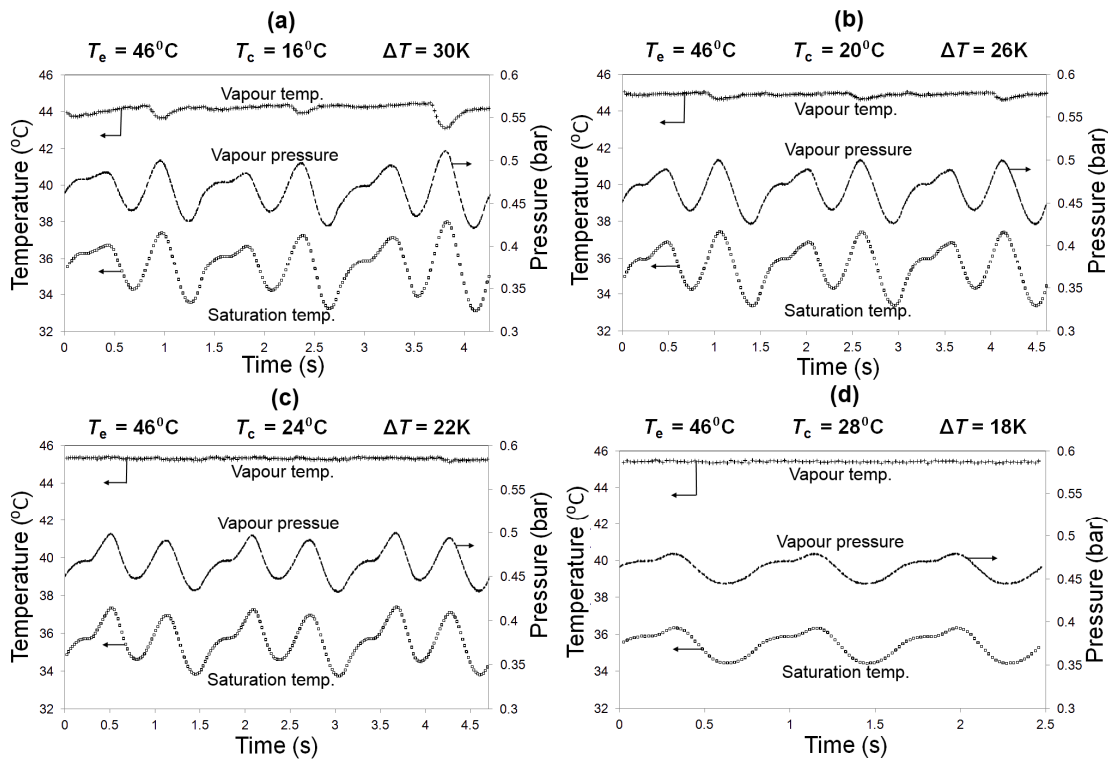


Fig. 4.5: Temporal variations of pressure (right ordinate axis) along with temperature in the vapour bubble and saturation temperature $T_{sat} = f(P_v)$, for experimental boundary condition of $T_e = 46^\circ\text{C}$ and $T_c = 16^\circ\text{C}$, 20°C , 24°C , 28°C , respectively and $P_r = 0.5$ bar.

Firstly, it is seen that the measured vapour temperature is somewhat lower than the maintained evaporator temperature. The variation is extremely small, which can be due to the dampening of the signal due to the non-zero time response of the system.

1.4 Dynamics of the liquid film

The vapour mass dynamics can be estimated using simple assumption of ideal gas equation and the different measurements made via the sensors placed in the vapour space. This information, coupled to the temporal movement of the triple-line, enables to estimate the time-dependent changes of the liquid film thickness. Finally, a simple mass balance equation in the evaporator provides an estimation of the initial thickness of the film. Hence, the dynamics of the film in the evaporator can be completely derived; this procedure is detailed below.

1.4.1 Experimental estimation of the vapour mass dynamics

As discussed in data processing section 1.3 of chapter 3, instantaneous mass of the vapour can be calculated using the following equation.

$$m_v(t) = \frac{P_v(t) \times V_v(t)}{\bar{R} \times T_v(t)} \times \bar{M} \quad 4.1$$

Where, \bar{R} is the universal gas constant and $\bar{M} = 338 \text{ g/mol}$, the molecular weight of FC72.

Fig. 4.6 shows the temporal variations of meniscus location and triple-line locations, respectively, along with the mass of vapour calculated using ideal gas, eq. 4.1, depicting several cases of the applied boundary conditions ($T_e = 46^\circ\text{C}$ and $T_c = 16^\circ\text{C}$, 20°C and 24°C). Vapour mass variation inside the system is a combined effect of evaporation and condensation, respectively, which may be occurring simultaneously. Therefore, any combination of evaporation and condensation rates can produce this variation of vapour mass. One has to develop a heat transfer model to extract these parameters from the experimental data. It is also observed in *fig. 4.6-d* that even a $\pm 10^\circ\text{C}$ variation in vapour temperature measurement affects only $\pm 3\%$ of instantaneous vapour mass calculations. Therefore, even if the temperature measurement by the micro-thermocouple is not highly accurate, the validity of the estimation of the vapour mass certainly remains rather reasonable.

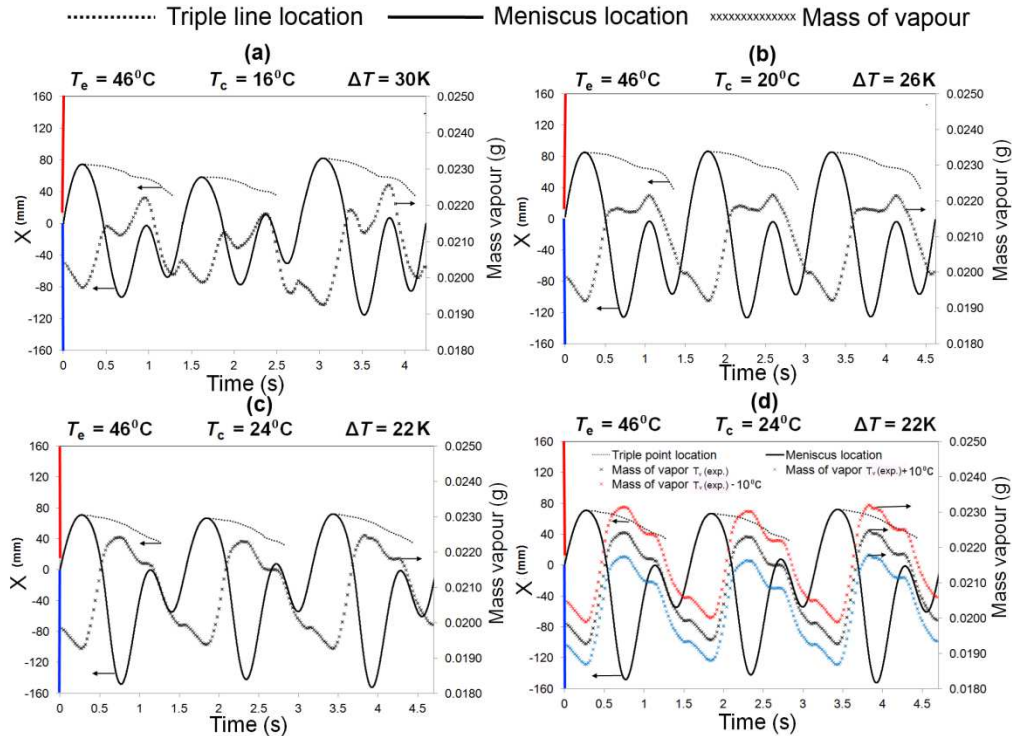


Fig. 4.6: Temporal variations of location of meniscus (left ordinate axis, solid line), triple-line (left ordinate axis, dotted line) and mass of vapour (right ordinate axis) calculated using ideal gas equation (ref. and eq. 4.1) (at $T_e = 46^\circ\text{C}$ and (a) $T_c = 16^\circ\text{C}$, (b) $T_c = 20^\circ\text{C}$, (c) $T_c = 24^\circ\text{C}$, and (d) $T_c = 24^\circ\text{C}$, and $P_r = 0.5$ bar, showing the sensitivity of the vapour temperature on the mass of vapour).

To analyse the experimental data, the oscillation cycle is divided into four different zones that are earlier depicted in *fig. 4.4-b*. In Zone #1, between points A and E, there is no liquid film on the tube wall as the meniscus is moving up in the evaporator. Simultaneously, we observe a decrease of the mass of vapour that can be explained by condensation on the meniscus due to compression of the vapour (ref. *fig. 4.6-b*). From point E to J, referred to as Zone #2, the meniscus is moving down in the evaporator tube section and is laying a liquid film on the evaporator wall. Hence, the length of the liquid film in the evaporator increases due to the downward movement of the meniscus and decreases due to simultaneous evaporation. Zone #3 commences from Point J onwards and terminates when the liquid film cannot be observed anymore. In this operational zone, it is assumed that the length of the liquid film in the evaporator is only decreasing

due to its evaporation at the triple-line. The last zone is Zone #4, where the vanishing liquid film cannot be observed due to the lack of camera resolution. Nevertheless, a few monolayers of liquid film remnants may still remain which will subsequently evaporate. While condensation of vapour occurs primarily on the liquid film in the condenser, it can also be observed on the liquid film in the evaporator. Indeed, the temperature of the liquid plug coming from the condenser region and entering into the evaporator section in the upward stroke (A to E) is much lower than the vapour temperature already present there. Since diffusion time scales in the bulk liquid region are large, the temperature of the liquid film that is laid by the meniscus during its journey towards the condenser is much lower than the adjoining vapour mass, which leads to condensation on the film surface.

After a while, the liquid film temperature increases due to heat conduction from the wall. Then, evaporation of the liquid film begins at the liquid vapour interface. All these physical mechanisms have to be introduced in the heat and mass transfer model to understand the dynamics of the liquid film. The mass transfer interactions due to the liquid film at the evaporator section are complex and its understanding is the key to this analysis.

1.4.2 Modeling of vapour mass dynamics

The variation of vapour mass is estimated from the raw experimental data, as per *fig. 4.6*. This variation is due to four different contributions:

- Condensation of vapour on the liquid film portion in the condenser section.
- Condensation of vapour on the meniscus formed between the vapour plug and the liquid slug.
- Evaporation at the triple-line formed between the liquid film, the wall and the vapour phase.
- Mass transfer (evaporation or condensation) between the liquid film and the vapour in the evaporator section.

The condensation rate due to the first two terms can be obtained by the energy equation:

$$m_c = \frac{1}{\Delta \hat{h}_{lv}} (h_{c,lf} \pi D_{int} L_{c,lf}(t)) [T_{sat}(t) - T_c] + K_c [T_{sat}(t) - T_c] \quad 4.2$$

Where, K_c is the overall thermal conductance of condensation occurring on the meniscus and $h_{c,lf}$, the condensation heat transfer coefficient between the vapour and the condenser; the justification for taking these two terms separately and their relative importance will be clear in the subsequent analysis which follows. In eq. 4.2, T_{sat} is the saturation temperature corresponding to the pressure of the vapour, which will apply at the interface and T_c the temperature of the heat sink, which is controlled by the thermostatic bath. $L_{c,lf}(t)$ is the instantaneous liquid film length in the condenser. In order to simplify the model, we assume that the liquid-vapour interface at the condenser is hemispherical with diameter D_{int} . In reality, the interface area is somewhat smaller due to the thickness of the film on the wall, but based on present experimental evidence too, we can safely assume that this thickness is negligible as compared to the tube diameter.

The overall thermal conductance of condensation, K_c can be estimated by comparison between the mass of vapour (eq. 4.1) calculated from the experimental data during the upward motion of the meniscus inside the evaporator (Zone #1) and eq. 4.2. Indeed, in Zone #1, the vapour mass variation is only due to this term (and therefore, term #1 in eq. 4.2 vanishes in Zone #1 from A to E). The heat transfer coefficient for condensation in the condenser section, $h_{c,lf}$ is linked to the thickness of the liquid film and its order of magnitude can be estimated as $\sim K_l / \delta_{lf,i}$, where K_l is the thermal conductivity of the liquid and $\delta_{lf,i}$ is the initial thickness of the film which is a key parameter for discerning the dynamics of the film [4.4-4.6]. We assume that the variation of the film thickness due to the condensation of the vapour in the condenser is small enough to be neglected; also, the temperature of the wall at the condenser is constant and equal to T_c . The temperature of the liquid plug inside the capillary tube is also taken to be very close to the condenser temperature.

The mass transfer due to the liquid film in the evaporator is more complex and cannot be obtained by the same approach. Two mechanisms have to be taken into account, i.e., the evaporation at the triple-line and the mass transfer at the liquid-vapour interface of the thin film. The temperature of the inner wall of the evaporator cannot be considered as constant, equal to the heat source temperature in this experiment. Indeed, during one cycle, the upper part of the inner tube is always in contact with the vapour plug while the bottom part of the tube is in contact either with vapour or with the liquid film, or with the liquid plug. Furthermore, as the material of the tube is glass, it has a small thermal diffusivity and therefore its time scale is higher than the oscillation period. For all these compelling reasons, the inner temperature of the wall is an unknown function of time and space. Therefore, the modeling of the dynamics of the film cannot be estimated using an evaporating heat transfer coefficient as was possible in the condenser section.

The thickness of the film in the evaporator is varying from a constant value $\delta_{lf,i}$ - when the meniscus begins its journey towards the condenser - to zero at the end of the cycle. This variation is due to two different phenomena: the evaporation at the triple-line and the mass transfer at the liquid-vapour interface of the film. Let us assume that $\delta(t)$ is not a function of the location inside the evaporator, but only a function of time. This hypothesis is reasonable as the temporal variation of the location of the triple-line is much slower than the temporal variation of the meniscus location. Therefore, the mass transfer rate between the liquid film and the vapour plug can be expressed as:

$$\dot{m}_{lf} = -\rho_l \pi D_{int} \left[\delta(t) \frac{dX_{lf}(t)}{dt} + L_{e,lf}(t) \frac{d\delta(t)}{dt} \right] \quad 4.3$$

Where, $X_{lf}(t)$ is the location of the triple-line and $L_{e,lf}(t)$ is the length of the liquid film in the evaporator, which are outputs of the experiments. The minus sign in eq. 4.3 is due to the negative sign of the derivative of X_{lf} and δ during evaporation. The mass variation of the vapour can be expressed as:

$$\dot{m}_v = \frac{dm_v}{dt} = \dot{m}_{lf} - \dot{m}_c \quad 4.4$$

The mass of vapour is known at each time by eq. 4.1, therefore the variation of the film thickness can be estimated by:

$$\frac{d\delta(t)}{dt} = -\frac{1}{L_{e,lf}(t)} \left[\frac{\dot{m}_v + \dot{m}_c}{\rho_l \pi D_{int}} + \delta(t) \frac{dX_{lf}(t)}{dt} \right] \quad 4.5$$

Finally, the equation of $\delta(t)$ can be written as:

$$\delta(t) = \delta_{lf,i} + \frac{d\delta(t)}{dt} \Delta t \quad 4.6$$

This model enables to estimate the complete dynamics of the liquid film by comparison with the experimental data. The initial thickness δ_i can be calculated by integrating the mass balance equation for the liquid film over a complete period of time:

$$\int \dot{m}_{lf} = \int \dot{m}_v + \dot{m}_c = \rho_l \pi D_{int} \delta_{lf,i} L_{lf,max} \quad 4.7$$

One can note that even if one part of the triple-line is not recorded by the high speed camera, eq. 4.7 enables to estimate the initial value of film thickness δ .

1.4.3 Comparison of model predictions with experiments

Fig. 4.7 shows temporal variation of the location of meniscus/triple-line and the film thickness calculated using the described model, for different boundary conditions (keeping $T_e = 46^\circ\text{C}$ constant and T_c varying from 16°C , 20°C and 24°C , respectively).

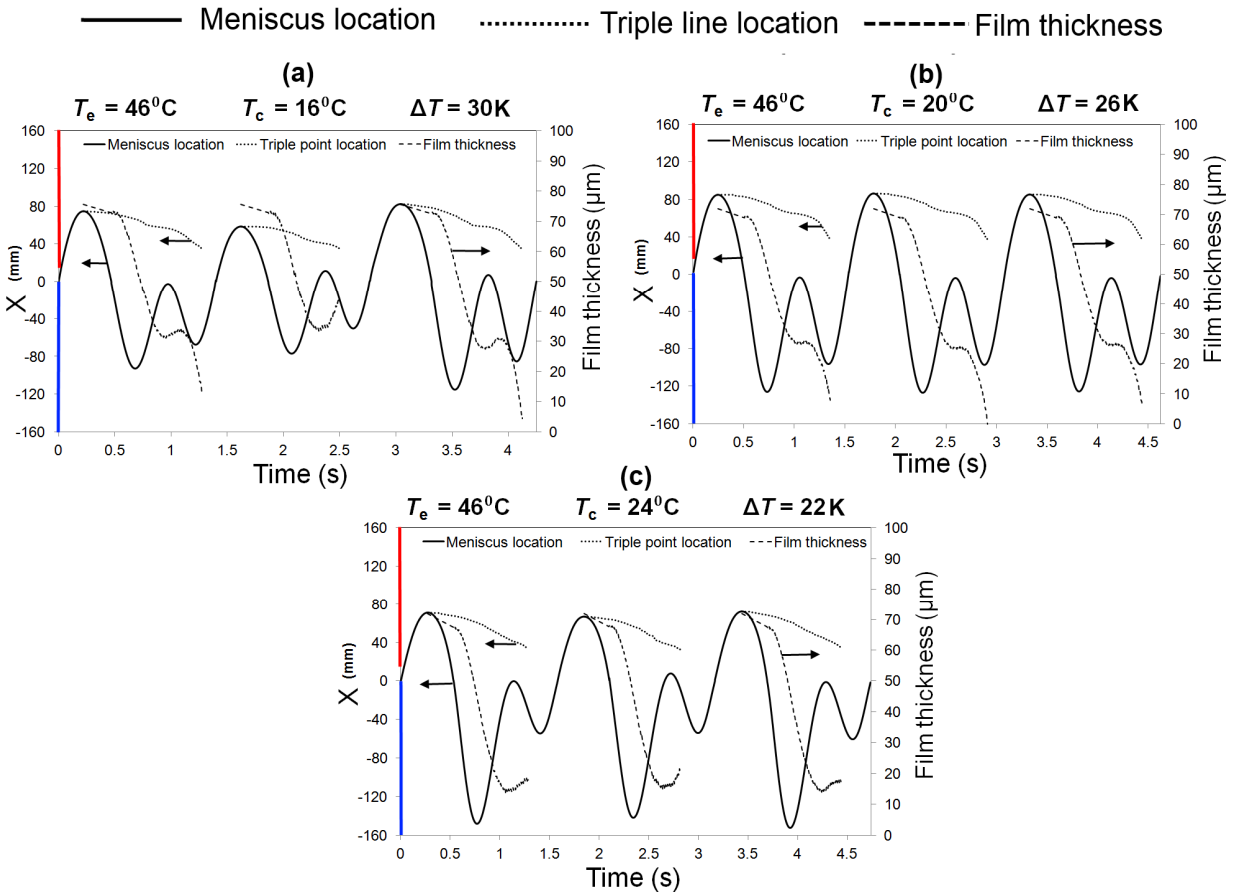


Fig. 4.7: Temporal variations of location of meniscus and film thickness variation calculated using the analytical model as per eq. 4.7 (at $T_e = 46^\circ\text{C}$ and $T_c = 16^\circ\text{C}$, 20°C and 24°C , respectively, and $P_r = 0.5$ bar).

The mean estimated initial liquid film thickness is estimated to be equal to $75\ \mu\text{m}$, $69\ \mu\text{m}$ and $67\ \mu\text{m}$ for T_c equal 16°C , 20°C and 24°C , respectively. The thickness is nearly constant in Zone #2, while at the same time, the triple-line moves towards the condenser; this clearly indicates that two different processes of evaporation occur inside the system, one at the triple-line and the other at the liquid-vapour interface of the liquid film. In Zone #3, the liquid film thickness in the evaporator section decreases rapidly as the meniscus recedes deep into the condenser section towards the reservoir. When the meniscus reaches back to the evaporator section during its first upwards journey, a small increase of the film thickness is observed in some conditions, which is attributed to condensation of compressed vapour on the film. In Zone #4, the thickness

of the film cannot be estimated as the location of the triple-line is not recorded. Nevertheless, the extrapolation of the thickness profile shows that it decreases to zero when the meniscus enters the evaporator in the next cycle.

The initial film thickness estimated by the model described above in section 1.4.3 can also be independently verified by empirical scaling correlations available in the literature; four such correlations are compiled and compared by *Khandekar et al. [4.7]*. These correlations predict the initial thickness of liquid film laid down on a wall by a moving meniscus as a function of the Capillary number (defined as $Ca = \mu U / \sigma$) under adiabatic conditions. While most correlations are applicable to steady motion of the meniscus of wetting fluids at low Capillary numbers, *Han and Shikazono [4.8]* have developed a correlation for a meniscus moving with a constant acceleration also. The effect of the Bond number (defined as $Bo = \rho \cdot \hat{a} \cdot D^2 / \sigma$), is also accounted for in this correlation, which is given as:

$$\frac{\delta_i}{R} = 2 \times \left(\frac{0.968 \times Ca^{2/3} \times Bo^{-0.414}}{1 + 4.838 \times Ca^{2/3} \times Bo^{-0.414}} \right) \quad 4.8$$

The assumptions and conditions under which the above correlation was developed by *Han and Shikazono et al. [4.8]* is probably the closest which we can get from the literature, to the conditions of the present experiments. Needless to say, the assumption of adiabatic flow and constant meniscus acceleration are not applicable to the present experiments. However, as will be demonstrated, application of eq. 4.8 does provide reasonable order-of-magnitude comparison of the initial film thickness laid down by the downward moving meniscus in the evaporator section.

For demonstrative purpose, the time varying Capillary number of the oscillating meniscus in the present experiment is plotted for one complete cycle (for $T_e = 46^\circ\text{C}$ and $T_c = 20^\circ\text{C}$) in *fig. 4.8*. *Fig. 4.9* compares the classical correlations of estimating the film thickness, including eq. 4.8; the correlations are noted on the figure itself. As can be observed, all the correlations are fairly consistent with each other. The most appropriate region to apply eq. 4.8 is when the meniscus commences its downward journey, laying the thin liquid film in the evaporator section. In this zone, as marked by the shaded gray

area in *fig. 4.8*, the average value of Ca is 0.021. With average value of $Bo = 1.72$ in this zone, the initial film thickness estimated by eq. 4.8 comes out to be equal to $\sim 90 \mu\text{m}$. This is within reasonable range of what was earlier predicted by the model described in section 1.4.3, i.e., $\sim 69 \mu\text{m}$.

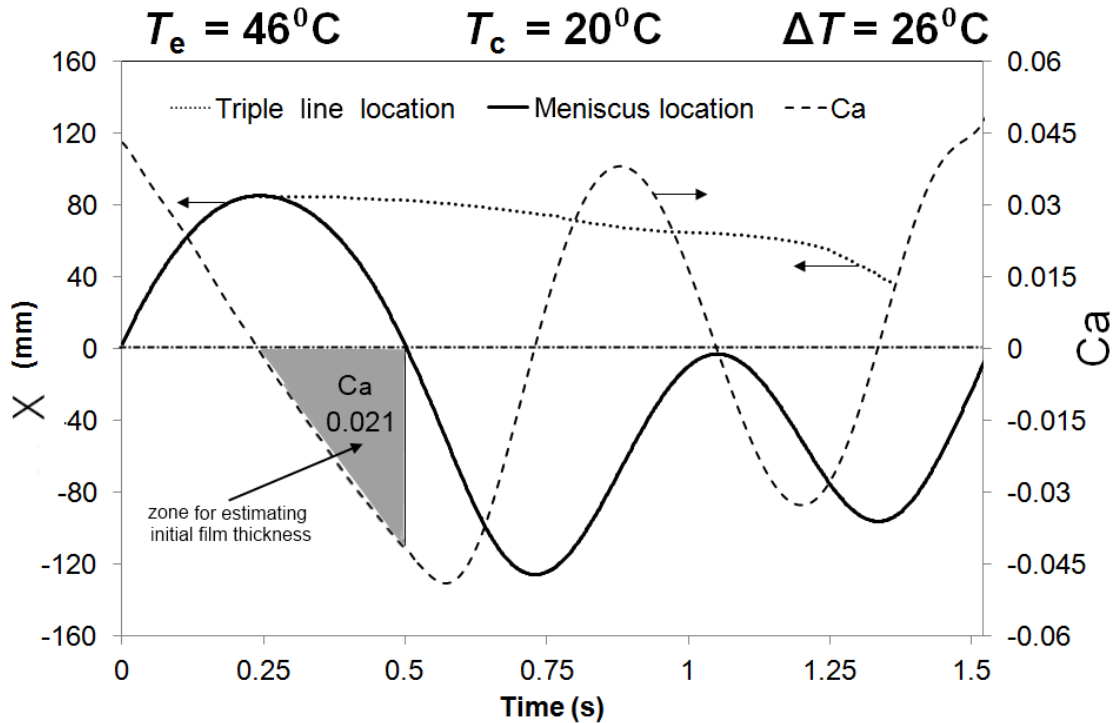
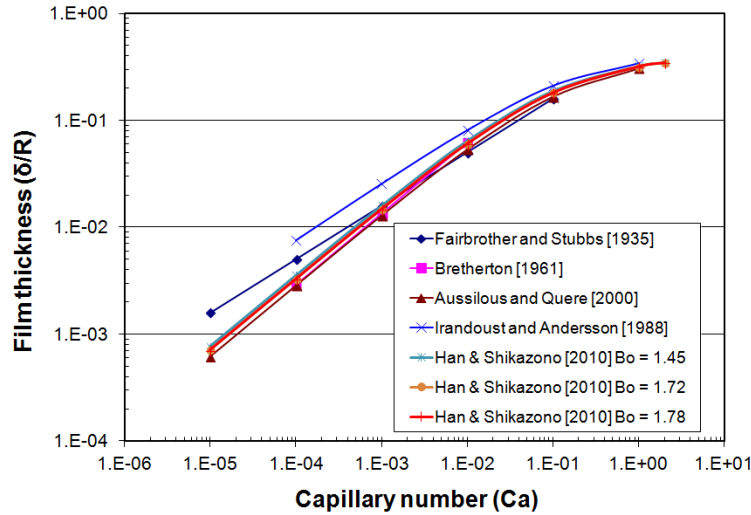


Fig. 4.8: Variation of Capillary number of the meniscus motion during one complete oscillation cycle.

Table 4.1 compares the value of the initial film thickness, as obtained by eq. 4.8 and the model described in section 1.4.3, for the other two boundary conditions of T_e and T_c used in the present work. As noted earlier, given the limitations of assumptions under which the empirical correlations were developed, and the fact that eq. 4.8 has itself an accuracy of $\pm 15\%$ (*Han and Shikazono et al. [4.8]*), it is encouraging to find that reasonable estimates of the initial film thickness can be independently verified, as can be clearly seen in Table 4.1.



Fairbrother and stubbs [1935]

$$\frac{\delta}{R} = 0.50(Ca)^{1/2}$$

Irandoust and Andersson [1988]

$$\frac{\delta}{R} = 0.36[1 - \exp(-3.08(Ca)^{0.54})]$$

Bretherton [1961]

$$\frac{\delta}{R} = 1.34(Ca)^{2/3}$$

Aussilous and Quere [2000]

$$\frac{\delta}{R} = \frac{1.34(Ca)^{2/3}}{1 + 2.5(1.34(Ca)^{2/3})}$$

Han & Shikazono [2010]

$$\frac{\delta}{R} = 2 \cdot \left(\frac{0.968 \cdot Ca^{2/3} \cdot Bo^{-0.414}}{1 + 4.838 Ca^{2/3} \cdot Bo^{-0.414}} \right)$$

Fig. 4.9: Comparison of the empirical scaling correlations for predicting the initial film thickness lay down by a moving meniscus inside a tube

Fig. 4.10 presents the four different explicit contributions to the vapour mass variation during one complete cycle ($T_e = 46^\circ\text{C}$ and $T_c = 16^\circ\text{C}$). Qualitatively similar results are obtained for the other boundary conditions also. The mass due to condensation on the meniscus region is varying nearly linearly because the vapour saturation temperature, which exists on the meniscus, does not vary much during the experiment and therefore, the difference between T_{sat} and T_c remains nearly constant (eq. 4.2). In any case, the amount of condensation on the meniscus is negligible compared to the amount of condensation on the liquid film. This latter component of condensation, which is due to the large variation of the liquid film length in the condenser, is much more critical and important. When the condenser section is full of liquid, its contribution is equal to zero,

while it is maximum, when the meniscus is at the bottom of the condenser section. The evaporation process is more complicated.

Table 4.1: Comparison of initial film thickness²

BC	T_e (°C)	T_c (°C)	Ca	Bo	$\delta_{if,i} \rightarrow$ eq. 4.8 (μm)	$\delta_{if,i} \rightarrow$ Section 1.4.3 (μm)
#1	46	16	0.0198	1.452	93.1	75
#2	46	20	0.0210	1.720	90.1	69
#3	46	24	0.0175	1.782	81.7	67

Fig. 4.10 shows that the amount of vapour generated at the triple-line is significant and equal to more than 1/3 of the contribution of the liquid film evaporation. Furthermore, the evaporation rate at the triple-line can almost be considered as constant during the entire life of the liquid film while the evaporation on the liquid film is highly dependent on the location of the meniscus inside the tube. The net evaporation rate is maximum when the meniscus is at the bottom of the condenser, while it tends to zero or become slightly negative (i.e., condensation occurs on it) when the vapour is being compressed by the upward moving meniscus.

² Values of average Ca and Bo are calculated at mean temperature of T_e and T_c .

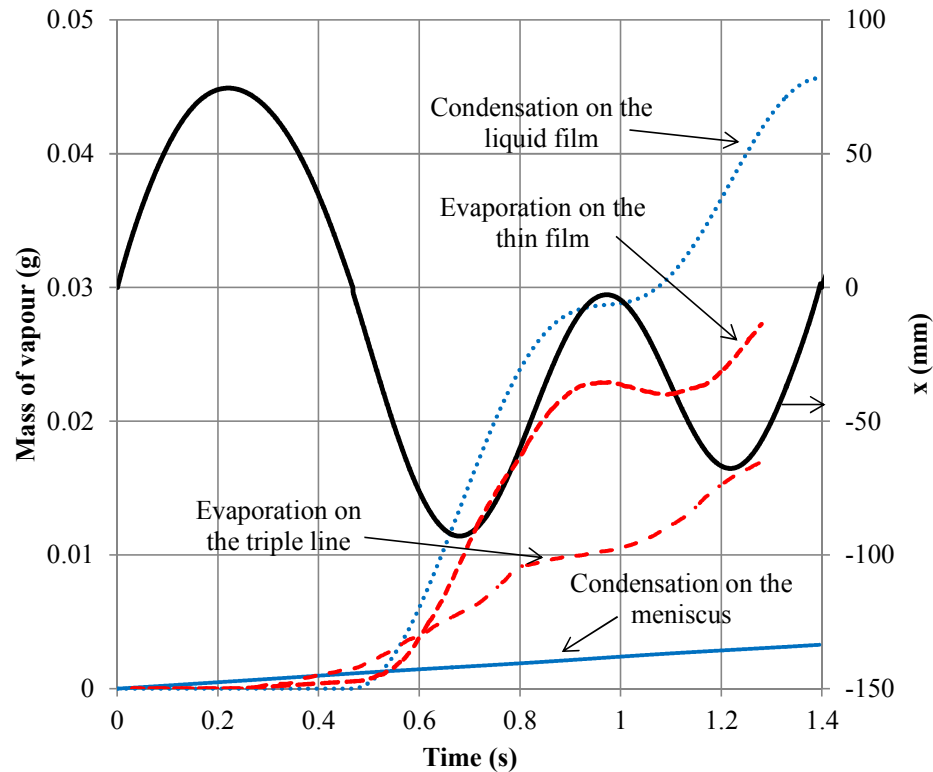


Fig. 4.10: Cumulated variation of vapour mass during one cycle separating four different contributions: Evaporation on the triple-line or on the liquid film in the evaporator and condensation on the liquid film or on the meniscus in the condenser ($T_e = 46^\circ\text{C}$ and $T_c = 16^\circ\text{C}$, first cycle).

2. Theoretical analysis of unsteady heat transfer in the liquid thin film

Looking in the broader prospective of this work is to open way to the predictive modeling of the PHPs. Looking towards the history of the modeling, the joint work of the CEA/ESEME/PMMH and CETHIL teams (*Das et al. [4.5]*) showed that such a simplified model conserves the main features of the multibubble PHP, the most important of which is the existence of self-sustained oscillations. This work showed a strong sensitivity of the modeling results to several parameters (or rather physical phenomena), on which the information is not yet available in the scientific literature. It is believed that the existing theoretical approach of *Das et al. [4.5]* needed to be compared to the experiments for its model validation. As a final step the single bubble model should be integrated into the multibubble approach under development by Nikolayev and his collaborators [4.9-4.12].

It has been conjectured that non-equilibrium states of liquid and vapour are quite likely to exist during the operation of PHPs [4.5, 4.13-4.16]. Conclusive experimental evidence is yet to come; it requires very precise and repeatable dynamic temperature measurements of local vapour and fluid film temperature so as to ascertain non-equilibrium condition and/or metastability. On one asymptote is the assumption that vapour and liquid in the Taylor bubbles are always under thermodynamic equilibrium. This essentially means that the relaxation time-scales of the phase-change by heat addition/subtraction are much faster than the typical characteristics time-scales of internal fluid flow and heat transfer through the walls in the PHP system.

However, the essence of the entire PHP thermal phenomena lies in its transient characteristics. While one can talk about a ‘quasi-steady’ state in a global or lumped sense, nothing is, in fact, steady on the local level inside an operating PHP. Several experimental studies exist which indicate that the typical oscillating frequencies of the self-sustained thermally driven oscillations of a PHP are of the order of 0-5 Hz, which corresponds to fastest time scales of approximately 0.05 s or 0.1 s (Khandekar *et al.* [4.17]). Statistically speaking, given the fact that the local thermodynamic quantities are changing continuously at this characteristic frequency at any given spatial location inside a PHP, the pertinent question to ask is, how different sub-constituents of the unit-cell respond to these changing thermodynamic conditions?

2.1. Scaling arguments

To answer this question, consider a typical PHP made up of copper tube of inside diameter 2.0 mm and outside diameter 3.0 mm, filled with water as the working fluid. Another example can be the glass tube PHP of the previous experiment (ref. section 1.2) with tube ID 2.0 mm and tube OD 6.0 mm, filled with FC72. For such a PHP, the unit cell may look, as depicted in *fig. 4.11*. The four basic constituents of the unit cell, as depicted in the figure are as follows:

1. the vapour bubble
2. the liquid film surrounding the vapour bubble

3. the liquid plug adjacent to the vapour bubble
4. the tube wall of the PHP

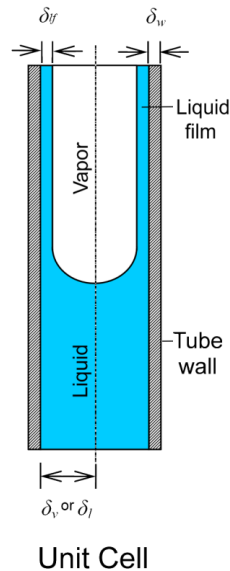


Fig. 4.11: Unit cell of single branch PHP.

Referring to *fig. 4.11*, the characteristic length scale of the liquid slug (δ_l) and vapour bubble δ_v , scales with the radius of the PHP tube, as a first order approximation. The characteristic length scale of the liquid film (δ_{lf}) surrounding the vapour bubble can be estimated from any of the available popular correlations [4.18, 4.19]. The characteristic length scale of the PHP tube (δ_w) scales with the tube thickness.

The thermal response of a material to a change in temperature is indicated by its thermal diffusivity. *Fig. 4.12* compares the thermal conductivity to thermal diffusivity for a wide range of materials on a log-log scale (Salazar [4.20]). The data points noted as condensed matter (liquids and solids) can be described as being near a straight line. As it can be noted, with respect to thermal diffusivity, gases are quite different as compared to the condensed matter. With respect to the transient nature of heat transfer in a PHP, it is worthwhile to note that all the three phases, viz. vapour phase, liquid phase and the solid phase (tube material), having drastically different thermal diffusivities are interacting with each other at all times. In fact, the difference in their respective thermal response, as against the inertia of the working fluid, eventually leads to the oscillating motion inside the device. Estimating the typical characteristics time

scales of these three interacting sub-systems of the unit-cell will be of interest. Table 4.2 summarizes the typical values of the characteristic time scale and the corresponding characteristic frequency of response of the different elements of the unit-cell, as estimated for a copper tube filled with water and for the glass tube filled with FC72, as in the present experiment.

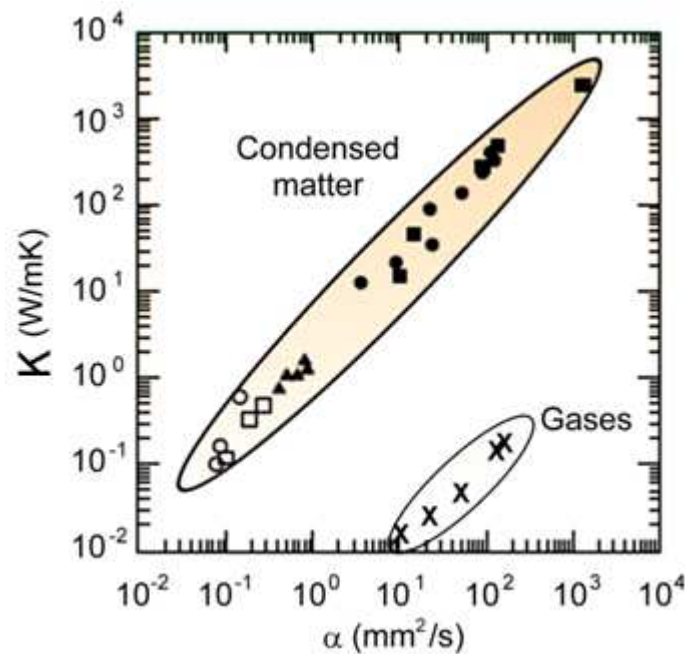


Fig. 4.12: Thermal conductivity versus thermal diffusivity for a wide variety of homogeneous materials (closed circles-metals; squares-ceramics; triangles-glasses; open squares-polymers; open circles-liquids; and crosses-gases) (*Salazar [4.20]*).

If the frequency of any external thermal change imposed on the boundary of these elements exceeds the respective characteristic frequency of the element under consideration, such perturbation information will, in principle, remain largely isolated from the concerned element of the unit-cell. Considering the fact that typical PHPs operate with dominant oscillating frequencies between 0-5 Hz (*Khandekar et al. [4.17]*).

Table 4.2: Order of magnitude of important time scales of the unit-cell elements

Length	Typical length scale (m)	Typical thermal diffusivity (m^2/s)	Characteristics time scale (s)	Characteristics frequency (Hz)
δ_l (FC72)	10^{-3}	3×10^{-8}	33	0.03
δ_l (H_2O)	10^{-3}	1.5×10^{-7}	6.5	0.15
δ_{lf} (FC72)	10^{-4}	$3 \cdot 10^{-8}$	0.33	3
δ_{lf} (H_2O)	10^{-4}	1.5×10^{-7}	0.065	15
δ_v	10^{-3}	2×10^{-5}	0.05	20.0
$\delta_{w\text{-copper}}$	0.5×10^{-3}	1.1×10^{-4}	0.002	500
$\delta_{w\text{-glass}}$	2.0×10^{-3}	3.0×10^{-7}	12.0	0.08

Several observations can be made by looking at the frequency estimates of Table 4.2:

- The liquid plug is the most sluggish in its response to any change in the external or internal thermal perturbations.
- The liquid plug response will be quite slow as compared to the liquid film surrounding the vapour bubble.
- The vapour space temperature change will be relatively quite fast and will largely follow the external imposed frequencies.
- The liquid thin film, as it thins down by evaporation or grows up by condensation, will respond extremely fast to the external stimuli of changing temperatures.
- There is a considerable difference in operating a PHP with glass tubes (representing low thermal conductivity materials) than metal tubes (high conductivity materials). This aspect has been neglected during data interpretation, in many of the earlier experimental studies.

Several other subtle issues get highlighted due to the order of magnitude difference in

the characteristic time-scales of the constituents of the unit cell. For example, in a typical journey from the evaporator to the condenser, while the vapour will quickly respond to the change in temperature of its new colder surroundings, the liquid plug adjoining the vapour bubble will be much slower in losing the sensible heat. From a thermodynamic standpoint, this essentially means that the probability of a temperature difference occurring between the liquid plug and the vapour bubble is quite high. In addition, there is considerable difference between the time response of the vapour and the surrounding liquid film. Thus, the very premise of the assumption of thermodynamic 'equilibrium', in the context of PHPs is rather misleading and inappropriate. In spite of the fact that explicit experimental evidence of non-equilibrium in PHP systems is yet to appear, the arguments presented above clearly indicate that the very nature of PHP heat transfer is guided by this inherent non-equilibrium existing between the vapour bubbles and adjoining liquid plugs.

The system always tries to come to equilibrium locally by either exchanging heat/mass with the wall, or by exchanging heat/mass with the surrounding elements of the unit-cell with which a temperature difference exists so as to rearrange the respective chemical potentials of the two phases. Any change in the respective specific Gibbs free energy, due to a temperature or a pressure imbalance at the interface will lead to a driving potential for local phase-change. Moreover, change in temperature of the vapour can also take place by compression of its volume experienced via the movement of the adjoining liquid plugs. This local compression of a particular unit-cell can be an outcome of events taking place at other locations in the device. If such an event takes place in the adiabatic zone, the temperature of the vapour bubble will rise, depending on the adiabatic index of compression. In such a situation, if the process is fast enough, then there is more likelihood of the liquid film responding to the change in the vapour temperature than the adjoining bulk phase of the liquid plugs.

Considering the fact that non-equilibrium conditions exist inside the system, it is worthwhile to compare the heat transfer resistances experienced by the liquid film surrounding the bubble in getting the required heat of evaporation (or vice-versa). In general, the liquid thin-film essentially interacts with two elements, the vapour bubble

and the tube wall. In the adiabatic zone, it can exchange heat/mass to/from the vapour bubble. Inside the evaporator and the condenser, transport of heat can occur either with the wall or with the vapour bubble. As pointed out earlier, possibility of vapour bubble to have a higher temperature than the tube wall exists due to compression of its volume by the adjoining liquid plugs. In an analogous way, the vapour bubble can become cooler than the adjoining wall due to expansion³. This discussion suggests that, a situation where in a gradient between the wall temperature T_w and the vapour temperature T_v is generated, with the liquid film existing at a different temperature T_f , should be occurring routinely in the transient operation of the PHP system.

2.2. Thermal response time of liquid thin film

Let us consider the temperature in a cross-section of the tube between point states E and I (*fig. 4.4*), wherein the downward motion of the meniscus has just commenced from the evaporator. As has been clearly seen in the experiments and explained in the previous section, a thin liquid film is laid down and remains on the tube wall as the meniscus moves in the downward stroke. The liquid film is bounded by the tube wall on one side and compressed vapour on the other side, as detailed in the unit-cell description of *fig. 4.11*.

Let us assume that the initial temperature of this film is equal to the temperature of the meniscus, which, in turn, can be considered as equal to the condenser temperature T_c as a first approximation, since the time response of the liquid slug is very small compared to the frequency of the meniscus motion. At this very first moment, the liquid film is bounded by the wall at temperature T_w and the vapour at temperature T_v . From the wall side, the liquid film is heated by thermal diffusion due to the strong temperature gradient between the wall and the liquid film. This diffusional heating is not instantaneous, but depends on the thermophysical properties of the liquid film and is guided by the unsteady heat diffusion equation. On the other side of the liquid film, the strong temperature gradient expected between the vapour and the liquid is likely to

³ While in the adiabatic zone, the adiabatic index of compression and expansion can be assumed to be valid for the vapor, it is not possible to ascertain the index of compression under diabatic conditions, in the evaporator or the condenser, wherein compression and/or expansion can take place simultaneously with heat addition/removal.

induce instantaneous heat transfer between the vapour and the liquid film. While thermodynamic considerations are trying to push the system to local equilibrium, there is a strong interplay of kinetic transport limitations which induces heat and mass inertia, thereby creating or sustaining local non-equilibrium conditions. Whether the vapour will condense on the interfacial boundary with the thin liquid film or alternately, the liquid film will evaporate into the vapour space will also be guided by the local degree of superheating/ subcooling vis-à-vis the instantaneous saturation pressure. For example, under a dynamic situation of meniscus motion in the downward stroke in the evaporator, the liquid film may receive thermal energy from the wall as well as the vapour, if the latter is condensing on it. Alternately, the heat received from the wall can evaporate the liquid thin film thereby adding additional mass to the vapour space.

In real time operation, it is indeed possible that due to local distribution/variation of liquid film temperature and vapour temperature respectively, while part of the liquid film experiences condensation, another part gets subjected to vaporization. Such an interfacial transport process suggests that individual fluxes for condensation and vaporization must be derived from kinetic theory considerations, wherein fluxes in each direction are derived separately and results superimposed to obtain the net flux. A simple kinetic model as proposed by Schrage (as reviewed in [4.21]), assuming that both incoming and outgoing molecular fluxes have distinct temperatures and have a Maxwellian distribution, provides the heat transfer between the vapour (at temperature T_v) and the liquid-vapour interface (at temperature T_{lv}), as given by:

$$q''_{\text{int}} = \gamma \cdot \Delta \hat{h}_{lv} \left[\frac{\bar{M}}{2\pi R} \right]^{0.5} \left[\frac{P_v}{T_v^{0.5}} - \frac{P_{\text{sat}}(T_{lv})}{T_{lv}^{0.5}} \right] \quad 4.9$$

Where, γ is the accommodation coefficient. Following the sign convention of (Carey [4.21]), q'' is positive when condensation occurs and negative when vaporization occurs, which depends on the initial temperature of the liquid film. Due to the large difference of state between the vapour and the liquid when the liquid film is laid on the wall, considerably large heat transfer is expected to occur between the liquid film and the surrounding vapour. This relatively large energy exchange at the interface leads to

increase or decrease of temperature in its vicinity, depending on whether local condensation or evaporation occurs. As the time response of the bulk liquid film is constrained by the heat diffusion equation, heat is stored or removed at the liquid-vapour interface until T_{lv} reaches the equilibrium state given by:

$$\frac{P_{\text{sat}}(T_{lv})}{T_{lv}^{0.5}} = \left[\frac{P_v}{T_v^{0.5}} \right] \quad 4.10$$

If the initial temperature of the liquid film is lower than T_{lv} , condensation of vapour occurs as soon as the meniscus moves toward the condenser. Condensation process is replaced by vaporization when the heat coming from the wall reaches the liquid-vapour interface, enabling to change the temperature gradient at the interface. If the initial temperature of the liquid film is higher than T_{lv} , the temperature gradient enables the evaporation as soon as the liquid film is deposited on the wall. In both cases, the evaporation time is principally controlled by the heat diffusion equation in the liquid film, with two Dirichlet boundary conditions on each of its sides. Let us consider the one-dimensional unsteady state heat transfer equation in the liquid film:

$$\alpha \frac{\partial^2 T}{\partial x^2} = \frac{\partial T}{\partial t} \quad 4.11$$

With the following boundary conditions:

$$T|_{x=0} = T_w \quad 4.12$$

$$T|_{x=X(t)} = T_{lv} \quad 4.13$$

Where, $X(t)$ is the location of the liquid-vapour interface. Let us assume that the pressure and the temperature of the vapour are constant, which as a first approximation does not change the essence of the thin film evaporation. Thus, T_{lv} can also be considered as a constant. The location of the liquid vapour interface is given by the following boundary conditions:

$$-K \frac{dT}{dx} \Big|_{X=X(t)} = -\hat{\Delta}h_{lv}\rho_l \frac{dX(t)}{dt} \quad 4.14$$

The initial conditions for thin film are the initial thickness $\delta_{lf,i}$ and the initial temperature field:

$$T(X,0) = T_c \quad 4.15$$

The method of separation of variables leads to the following solution for eq. 4.11:

$$T(X,t) = \sum_{n=1}^{\infty} A_n e^{-\alpha \left(\frac{n\pi}{X(t)}\right)^2 t} \sin\left(\frac{n\pi X}{X(t)}\right) + \frac{T_{lv} - T_w}{X(t)} X + T_w \quad 4.16$$

where,

$$A_n = \frac{2(T_{lv} - T_c)}{n\pi} \cos(n\pi) + \frac{2(T_c - T_w)}{n\pi} \quad 4.17$$

From eq. 4.14, it is possible to derive the time variation of the thickness of the liquid film:

$$\frac{dT}{dX} \Big|_{X=X(t)} = \frac{\hat{\Delta}h_{lv}\rho_l}{k} \frac{dX(t)}{dt} \quad 4.18$$

Where, the temperature gradient at the moving boundary is calculated from eq. 4.16. Thus, the variation of the film thickness can be expressed as:

$$\frac{dX(t)}{dt} = \frac{K}{h_{lv}\rho_l} \left[\sum_{n=1}^{\infty} A_n e^{-\alpha \left(\frac{n\pi}{X(t)}\right)^2 t} \frac{n\pi}{X(t)} \cos(n\pi) + \frac{T_{lv} - T_w}{X(t)} \right] \quad 4.19$$

Eq. 4.19 is a non-linear first order differential equation of the location of the liquid-vapour interface. A time $t = 0$ s, the initial thickness of the film $\delta_{lf,i}$ is the inlet parameter

of the model. It has to be noted that the model can also be used in the condenser area to estimate the time scale of condensation. In that case, the temperature of the wall T_w is equal to T_c .

2.3. Film thickness variation during phase-change

In this section, we present simulations obtained with the analytical model presented above for the experimental conditions, namely $T_e = 55$ °C, $T_c = -3$ °C and $P_r = 0.42$ bar, with FC72 as the working fluid in experimental setup as described in section 1 of chapter 3. Let us assume that the pressure of the vapour is equal to P_r as a first approximation. In reality, the vapour pressure fluctuates around this value during one cycle (*fig. 4.4*). There are two main unknowns in the model: the initial thickness of the liquid film and the temperature of the vapour T_v , which is needed to calculate the liquid-vapour interface temperature T_{lv} . Let us assume that T_v ranges between T_w and $T_{sat}(P_v)$. Within this range of vapour temperature, the interface temperature T_{lv} (eq. 4.10) is ranging between 33.2°C and 34°C. Thus, the superheating of the vapour does not have a strong influence on T_{lv} and we assume that T_v is equal to T_w in the following. Let us also assume that the temperature of the wall is equal to the temperature of the evaporator; the wall poses no thermal resistance.

Fig. 4.13 presents the temperature field of the liquid film at different times assuming an initial film thickness equal to 50 μm . The vapour initially condensates until time $t = 24$ ms, after which the temperature gradient inside the film becomes negative enabling the evaporation of the liquid thin film to begin. Till that time, the thickness of the film has increased to 58 μm due to mass addition due to condensation of vapour. At time $t = 93$ ms, the thickness of the film reaches the initial thickness again, as a result of evaporation. Thus, a time delay of about 100 ms is necessary before the net evaporation of the film begins. This is not at all negligible since it represents 1/5th of the meniscus oscillation period. The liquid film gets totally evaporated at time $t = 0.25$ s, which represents about one half of the period.

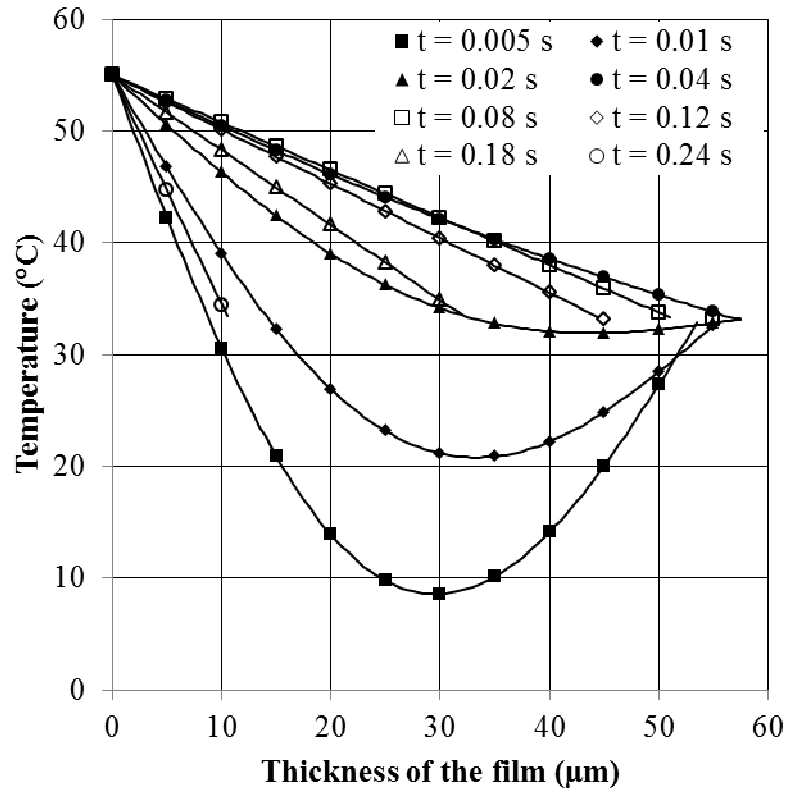


Fig. 4.13: Temporal variation of the liquid film thickness ($\delta_{lf,i} = 50 \mu\text{m}$) and its corresponding temperature at the conditions existing in the evaporator section of the present experiment for FC72 ($T_e = 55 \text{ }^\circ\text{C}$, $T_c = -3 \text{ }^\circ\text{C}$ and $P_r = 0.42 \text{ bar}$).

Fig. 4.14 shows the variation of the liquid film thickness as a function of time in the same conditions corresponding to *fig. 4.13*. One can clearly see two phases: the film thickness increases rapidly due to the large condensation rate which is initially prevalent. When the overall temperature of the film is close to T_{lv} , the thickness stabilizes until the evaporation of the film begins, the heat being now supplied from the elevated wall temperature. With the decrease of the film thickness, the thermal resistance decreases and therefore the evaporation rate increases, until the film completely disappears.

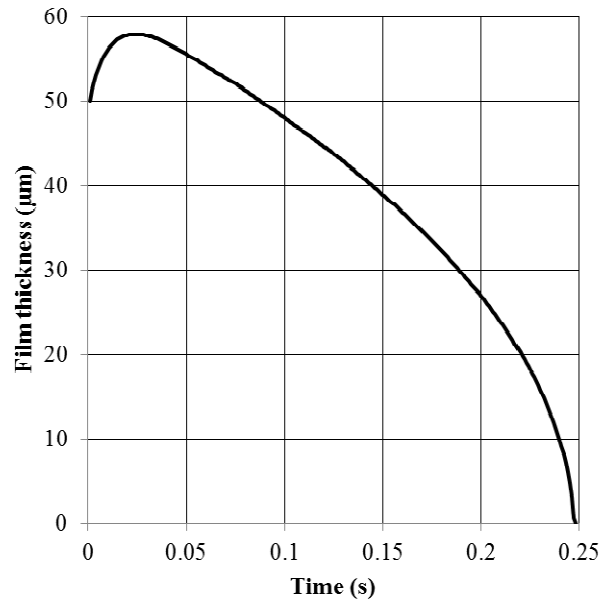


Fig. 4.14: Temporal variation of liquid film thickness ($\delta_{lf,i} = 50 \mu\text{m}$) at the conditions existing in the evaporator section of the present experiment for FC72 ($T_e = 55 \text{ }^\circ\text{C}$, $T_c = -3 \text{ }^\circ\text{C}$ and $P_r = 0.42 \text{ bar}$).

Fig. 4.15 shows the major influence of the film thickness on the time required to evaporate the film. Three initial liquid film thicknesses are compared: $\delta_{lf,i} = 50 \mu\text{m}$, $\delta_{lf,i} = 75 \mu\text{m}$ and $\delta_{lf,i} = 100 \mu\text{m}$. Obviously, the time required to evaporate the film increases with the increase of $\delta_{lf,i}$. The time period for which the initial phase of condensation prevails is equal to 24 ms, 54 ms and 100 ms, and the time period before net evaporation begins is equal to 93 ms, 210 ms and 390 ms for initial film thickness $\delta_{lf,i} = 50 \mu\text{m}$, $\delta_{lf,i} = 75 \mu\text{m}$ and $\delta_{lf,i} = 100 \mu\text{m}$, respectively. For the two last film thicknesses, the delay induced by the condensation is not compatible with the present experiment for FC72 ($T_e = 55 \text{ }^\circ\text{C}$, $T_c = -3 \text{ }^\circ\text{C}$ and $P_r = 0.42 \text{ bar}$) as the frequency is equal to 2 Hz. The next meniscus cycle will commence before the liquid film fully evaporates. The results show that when the thickness of the film is doubled, the delay is multiplied by four. Thus, a very precise estimation of the initial liquid film thickness is required to accurately modeling the PHP behavior.

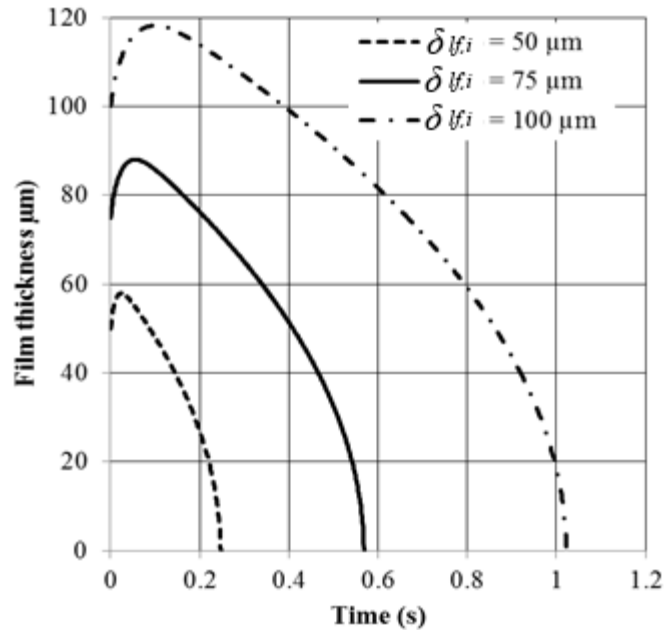


Fig. 4.15: Influence of the initial thickness of the liquid film on its evolution from initial condition to the final state of complete evaporation. During the initial period the film becomes thicker as it experiences condensation of vapour on it.

The physical mechanisms that control the thickness of the liquid film are similar to that encountered into dip coating problems, in which a substrate is withdrawn from a bath, to deposit a liquid film. In the case of a PHP, the tube is stable and the liquid moves but the principles are similar. These kinds of films are described as the Landau-Levich flows (*Mayer et al. [4.22]*) from the names of the two authors who first reported on this problem in 1942. It has been shown that the thickness of the film depends on several non-dimensional numbers like the capillary number and the capillary length (*Mayer et al. [4.22]*). The geometry of the substrate as well as its wettability is also important parameters. Dip coating problems are still an active field of research nowadays. This is the literature that has to be explored to increase the knowledge on such films inside a PHP, but this is beyond the scope of the present work.

The model presented in section 1.4.3 can also be used to study the heat transfer phenomena at the condenser. In that case, the temperature of the wall is set to the condenser temperature (e.g. -3°C in the conditions of the experiment). *Fig. 4.16*

presents the temperature of the film for different times assuming an initial thickness of $50 \mu\text{m}$. One can clearly see that the condensation rate is intense in the early stages and decreases subsequently as the film thickness increases. As the thermal resistance of the film increases, the condensation rate is lower than the evaporation rate. Nevertheless, as there is no delay at the condenser, at time $t = 0.25 \text{ s}$ (which corresponds to the time needed to evaporate a film of thickness $50 \mu\text{m}$), the increase of the film thickness is equal to $50 \mu\text{m}$ at the condenser. Thus, the mean rate of condensation is equal to the mean rate of evaporation, but the dynamics of both heat transfer processes are different, condensation process being more regular.

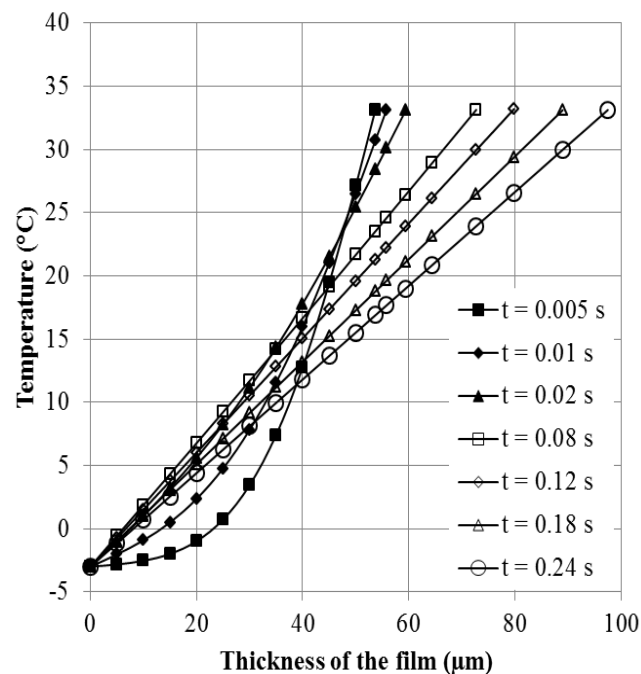


Fig. 4.16: Temperature of the liquid film ($\delta_{l,f,i} = 50 \mu\text{m}$) at different time in the conditions of the experiment at the condenser.

This simple analysis can obviously not describe the entirety of the complex process of heat and mass exchange during the cycle of the vapour bubble - liquid slug interface in an operating PHP. For instance, the above analysis tends to show that during any portion of the cycle, when the meniscus is in the evaporator, the thinnest portion of the liquid film is subject to evaporation while the thickest portion of the film is

simultaneously subjected to condensation (from the vapour) and evaporation (due to the heat flowing from the wall) that eventually results in net evaporation. Taking this observation into account, and the thermally thick character of the liquid film, it is imperative that a comprehensive treatment of the unit-cell is required for deeper understanding of the involved spatio-temporal phenomena. Alternately, just considering evaporation of the film is not sufficient, as part of the film may also be experiencing condensation due to the local spatial thermal non-equilibrium. From an experimental viewpoint, it is now clear that at least two new parameters should be measured as a function of time to describe quantitatively the mechanisms involved in the studied system: the time evolution of the vapour temperature and either the film shape/size or the time required for its evaporation. Proper video-recording could allow characterizing the film geometry and its time-dependant evolution, but measuring the vapour temperature with high time-resolution and with minimal perturbation certainly remains a challenge to be addressed in the future.

3. Closing remarks

- Self-sustained thermally-driven oscillations of a single meniscus can be obtained and efficiently sustained inside a capillary tube over long periods of time by maintaining a step thermal gradient over its length. Associated phase-change processes lead to thermo-mechanical instability in the system which generates continuous auto-oscillations of the meniscus. The amplitude of the oscillations not only depends on the temperature difference between the condenser and the evaporator, but also on their absolute temperature levels. Oscillations are quasi-periodic in nature for a range of imposed temperature gradients; they become more regular and periodic as this gradient decreases. In line with the recent literature (by this group of authors and others), maximum pressure in the vapour space does not occur when the liquid meniscus is at top of evaporator section; it occurs when the meniscus reaches the adiabatic section in the downward stroke while going from the evaporator to the condenser. During this downward motion of the meniscus, a liquid film is laid down on the tube wall and the very high net evaporation rate of this film contributes to rapid increase of the pressure in the vapour space.
- The two processes of evaporation and condensation of vapour to/from the liquid film

and the meniscus respectively, may occur simultaneously during parts of the cycle. Net vapour mass flux is determined from the dominant mechanism out of these two. Condensation of vapour mostly occurs on the liquid film inside the condenser section. A small amount of condensation is also observed on the moving meniscus. For a given boundary condition, the film thickness and its length at a given time determines the overall dynamics of the meniscus. The results show that evaporation takes place at both, the triple-line and the liquid film interface, the continuation of the former mechanism being somewhat higher than the latter. The amount of vapour generated at the triple-line is significant and equal to more than 1/3 of the contribution of the liquid film evaporation. At the triple-line, the evaporation rate is nearly constant during one complete cycle while it depends strongly on the location of the meniscus inside the system for the liquid film evaporation. With average value of Capillary and Bond numbers, the initial film thickness estimated by *Han and Shikazono [4.8]*, is in the range 80 μm to 90 μm . This is in reasonable agreement with the range predicted by our model (65 μm to 75 μm).

- Most of the existing mathematical models fall short of predicting the entire thermo-hydrodynamics of pulsating heat pipes. While some do not include evaporation and condensation processes, others do not appreciate the dominant role of the liquid film in obtaining self-sustained oscillations. The intricate dependency of the net vapour pressure on simultaneous occurrence of evaporation and condensation is also not included by any of the models reported till date. Too, the occurrence of superheated vapour and the possibility of the existence of metastable phase behaviour need further exploration. The experiments reported here helps in understanding these critical issues and will contributed towards improved mathematical modelling of the entire PHP systems. Nevertheless, a predictive theoretical model of both the triple line and thin film evaporation is not easy to develop. It has to include the thermal inertia effects in both the wall and the liquid film, since the thermal problem is highly non stationary. Furthermore, the physics of the triple line - that has been widely studied in the literature - includes several unknown parameters that have to be taken into account (accommodation coefficient, disjoining pressure, contact angle).
- The evaporation mass flux experienced in the vapour space is not only due to the

heat flow by conduction from the wall to the interface, but also to the thermal non-equilibrium between the vapour and the liquid. If the vapour temperature is greater than the liquid temperature, the net mass flux of evaporation will be lower than conduction-induced evaporation mass flux, as the thermal non-equilibrium leads to condensation. Otherwise, the mass flux is due to both conduction through the film and thermal non-equilibrium.

- The simplified analysis of unsteady heat transfer in the liquid thin film shows the importance of measuring the time-evolution of the temperature of the vapour with a high time-resolution and a good accuracy, which remains a challenge today under such experimental conditions.

References

- 4.1 M. Rao, F. Lefèvre, S. Khandekar, J. Bonjour, Understanding transport mechanism of a self-sustained thermally driven oscillating two-phase system in a capillary tube, *Int. J. Heat Mass Transfer*, 65 (2013) 451-459.
- 4.2 M. Rao, F. Lefèvre, S. Khandekar, J. Bonjour, Heat and mass transfer mechanisms of a self-sustained thermally driven oscillating Liquid-Vapour meniscus, *Int. J. Heat Mass Transfer*, 86 (2015) Pages 519-530.
- 4.3 A. Tripathi, S. Khandekar, P. K. Panigrahi, Oscillatory contact line motion inside capillaries, 15th International Heat Pipe Conference (15th IHPC) Clemson, USA, (2010).
- 4.4 P. Gully , F. Bonnet , V.S. Nikolayev, N. Luchier , T.Q. Tran, Evaluation of the vapour thermodynamic state in PHP, 17th International Heat Pipe Conference (17th IHPC), Kanpur, India, (2013).
- 4.5 S.P. Das, V.S. Nikolayev, F. Lefèvre, B. Pottier, S. Khandekar, J. Bonjour, Thermally induced two-phase oscillating flow inside a capillary tube, *Int. J. Heat Mass Transfer*, 53(19-20) (2010) 3905–3913.
- 4.6 F. Bonnet, P. Gully, V.S. Nikolayev, Experimental study of a single branch cryogenic pulsating heat pipe: first results, in: *Proc. Eurotherm Sem. on gravitational effects on liquid-vapour phase change*, IUSTI, Hyeres, France, (2011).
- 4.7 S. Khandekar, Thermo-hydrodynamics of closed loop pulsating heat pipes, Ph.D. thesis, (2004) (available at: <http://elib.unistuttgart.de/opus/volltexte/2004/1939/>).
- 4.8 Y. Han, N. Shikazono, The effect of bubble acceleration on the liquid film thickness in micro tubes, *Int. J. Heat Fluid Flow*, 31(4) (2010) 630-639.S.

- 4.9 V.S. Nikolayev, D.A. Beysens, G.-L. Lagier, J. Hegseth, Growth of a dry spot under a vapour bubble at high heat flux and high pressure. *Int. J. Heat Mass Transfer* 44 (2001) 3499-3511.
- 4.10 V.S. Nikolayev, B. Pottier, Bubble dance in the pulsating heat pipe, « Bubble and drop interfaces » COST P21 workshop, Thessaloniki, Greece, 23-25/9/2009.
- 4.11 V.S. Nikolayev, Comment on “Flow and heat transfer of liquid plug and neighboring vapour slugs in a pulsating heat pipe” by Yuan, Qu, & Ma *Int. J. Heat Mass Transfer*, 54(9) (2011) 2226-2227.
- 4.12 V.S. Nikolayev, A dynamic film model of the Pulsating Heat Pipe *J. Heat Transfer*, 133 (8) (2011) 081504.
- 4.13 S. Khandekar, M. Groll, An insight into thermo-hydraulic coupling in pulsating heat pipes, *Int. J. Therm. Sci.*, 43(1) (2004) 13-20.
- 4.14 R.T. Dobson, Theoretical and experimental modelling of an open oscillatory heat pipe including gravity, *Int. J. Therm. Sci.*, 43 (2) (2004) 113-119.
- 4.15 R.T. Dobson, An open oscillatory heat pipe water pump, *Appl. Therm. Eng.* 25(4) (2005) 603-621.
- 4.16 M. Mameli, M. Marengo, S. Zinna, Thermal simulation of a pulsating heat pipe: Effects of different liquid properties on a simple geometry, *Heat Transfer Engineering*, 33 (14) (2012) 1177-1187.
- 4.17 S. Khandekar, A.P. Gautam, P. Sharma, Multiple quasi-steady states in a closed loop pulsating heat pipe, *Int. J. Therm. Sci.*, 48(3) (2009) 535-546.
- 4.18 P. Aussillous, D. Quéré, Quick deposition of a fluid on the wall of a tube, *Phys. Fluids*, 12 (2000) 2367-2371.
- 4.19 S. Khandekar, P.K. Panigrahi, F. Lefèvre, J. Bonjour, Local hydrodynamics of flow in a pulsating heat pipe: a review, *Front. Heat Pipes*, 1 (2010) 023003(1-20).
- 4.20 A. Salazar, On thermal diffusivity, *European Journal of Physics*, 24 (2003) 351-358.
- 4.21 V.P. Carey, *Liquid-vapour phase-change phenomena*, 2nd ed., Taylor and Francis, (2007).
- 4.22 H.C. Mayer, R. Krechetnikov, Landau-Levich flow visualization: Revealing the flow topology responsible for the film thickening phenomena, *Phys. Fluids*, 24 (2012) 052103(1-33).

Chapter 5

Modeling of single branch PHP

This section presents the thermo-hydrodynamic modeling of the system consisting of a vapour plug and a liquid slug oscillating in a tube closed at one end and connected to a reservoir at a constant pressure P_r at the other end (Fig. 5.1). The equations of the model were already presented in *Das et al. [5.1]*. Some modifications are introduced in this chapter to take into account the peculiarities of the new experimental set-up and improve the liquid film evaporation model in the light of the experimental results. In particular, the equations of the model are developed for the system being in vertical orientation, while in *Das et al. [5.1]*, the system oriented horizontally. Later, we will discuss the results obtained using this model in comparison with the experimental results obtained in chapter 4. Also, a parametric study is carried out to understand the implications of the various factors on the working of such system.

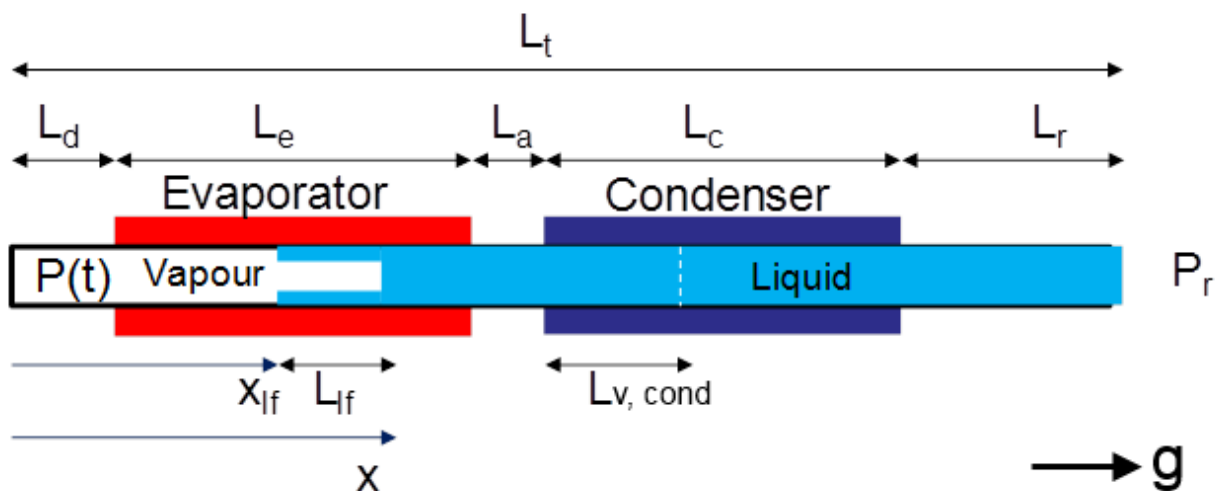


Fig. 5.1: Geometrical properties considered in the model.

1. Modeling of the different components of the unit-cell system

Basically, the system can be divided in 7 main components: the liquid slug, the vapour plug, the liquid film, the reservoir, the tube, the condenser and the evaporator. The liquid slug confines the vapour plug at the closed end of a cylindrical tube of diameter d and cross-section area $A = \pi d^2/4$. The x axis reference is located at the closed end of the tube and the x axis was the orientation as the gravity acceleration (g). The length of the tube is L_t . A dead volume is introduced in the model to take into account the volume of vapour trapped between the evaporator and the end of the tube. This dead volume is due to the presence of the pressure sensor and the connection to the vacuum reservoir. It is modeled by an equivalent length L_d . The evaporator and the condenser length are L_e and L_c respectively. The condenser and the evaporator are separated by an adiabatic length L_a . A part L_r of the capillary tube extends beyond the condenser until the reservoir at a constant pressure P_r .

The pressure of the vapour bubble inside the tube P is a function of time. When the liquid plug leaves the evaporator, a small liquid film is left on the wall. The evaporation of film is responsible for the addition huge amount of vapour in the vapour plug. The location of this film inside the evaporator is x_{lf} and its thickness is δ_{lf} . When the liquid slug is pushed into the condenser, a part of the condenser wall of length $L_{v,cond}$ is in contact with the vapour and condensation occurs. The behavior of each of the different components of the system is described in the next section and the equations and hypotheses of the model are discussed.

Note: For developing the model we have taken x from top of the dead volume as shown in fig. 5.1. Later capital letter X is used to present the results rather than x , with the following relationship between both parameters: $X = -x + L_d + L_e + L_a$. X has for origin the boundary between the condenser and the adiabatic area, following the formalism used in chapter 4 to present the experimental results.

1.1. Reservoir

The volume of the capillary tube is more than 1000 times lower than the volume of the reservoir. Therefore the variation of the reservoir properties during the experiment can be considered as negligible and a constant and known pressure P_r can be applied as one of the boundary conditions of the system, which is verified experimentally with the pressure sensor.

1.2. Liquid slug

The liquid slug moves during the experiment due to the pressure difference existing between the reservoir and the vapour plug. Its velocity u is linked to the location $x(t)$ of the meniscus:

$$u = \frac{dx}{dt} \quad 5.1$$

u is positive when the meniscus moves towards the condenser and negative when it moves towards the evaporator. The movement of the liquid slug inside the tube is described by the momentum balance equation:

$$\frac{d(m_l u)}{dt} = (F_p + m_l g - \text{sign}^*(u) F_\tau) \quad 5.2$$

Where, m_l is the mass of liquid inside the tube, which is derived from geometrical considerations and ρ_l , the density of the liquid, A is internal cross sectional area:

$$m_l = \rho_l A (L_t - x(t)) \quad 5.3$$

We assume that the mass balance of the liquid slug depends only on the velocity. Indeed the evaporation and condensation rates are small compared to the velocity of the meniscus. F_p is the difference of pressure acting on the liquid slug at each of its extremities. F_p is composed of four components. The various components of this analysis are shown schematically in *fig. 5.2*.

* The sign of the F_τ is depends up on the direction of the meniscus velocity.

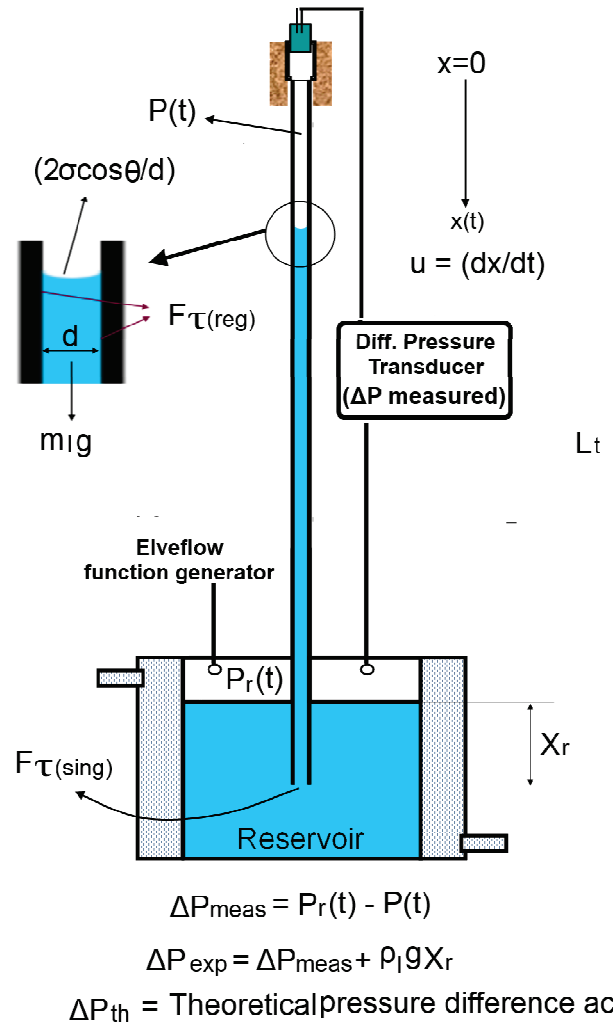


Fig. 5.2: Pressure drop measurement and various components involved in it.

$$F_p = A \left(P(t) - \frac{2\sigma \cos \theta}{d} - P_r(t) - \rho_l g X_r \right) \quad 5.4$$

Where, $P(t)$ is the vapour plug pressure above the meniscus, $2\sigma \cos \theta / d$ is the capillary pressure component due to the curvature of the liquid-vapour interface inside the tube, which depend on the diameter of the tube and the contact angle θ between the triple line and the tube. $P_r(t)$ is the pressure of the reservoir, which is measured in the vapour phase. Therefore, the pressure at the outlet of the tube into the reservoir has to be increased by the hydrostatic component due to the level X_r of the liquid-vapour interface in the reservoir compared to the tube outlet.

F_τ is the sum of regular and singular friction forces between the liquid slug and the tube, $F_{\tau,reg}$ and $F_{\tau,sing}$ respectively:

$$F_\tau = F_{\tau,reg} + F_{\tau,sing} \quad 5.5$$

Its sign depends on the direction of the meniscus movement. F_τ always acts to counterweight the movement, contrary to the weight of the liquid slug mg that contributes to accelerate the meniscus when it moves towards the condenser and on the contrary, prevent its motion back towards the evaporator. Therefore, if the meniscus moves towards the condenser, F_τ is negative, while when the meniscus moves towards the evaporator F_τ is positive.

In the model of *Das et al. [5.1]*, regular friction forces are calculated assuming the flow inside the tube as fully developed. $F_{\tau,reg}$ can therefore be expressed by the following expression that depends on the Reynolds number Re :

$$F_{\tau,reg} = \frac{1}{2} C_f d \rho_l \pi (L_t - x) u^2$$

$$\text{With } C_f = \begin{cases} 0 & \text{if } Re = 0 \\ 16 & \text{if } Re < 1 \\ \frac{16}{Re} & \text{if } 1 < Re < 1180 \\ 0.078 Re^{-0.25} & \text{if } Re \geq 1180 \end{cases} \quad \text{and } Re = \frac{\rho_l |u| d}{\mu} \quad 5.6$$

A singular pressure drop exists at the outlet of the tube in the reservoir due to the contraction or the enlargement. As the diameter of the reservoir can be considered as infinite compared to the diameter of the tube, the following expressions can be used to calculate singular pressure drops:

$$F_{\tau,sing} = \begin{cases} \frac{1}{2} A \rho u^2 & \text{if } u > 0 \text{ (enlargement)} \\ \frac{1}{4} A \rho u^2 & \text{if } u < 0 \text{ (contraction)} \end{cases} \quad 5.7$$

One has to be aware that the flow being oscillating by nature, it cannot be considered as fully developed. Nonetheless, to our knowledge, no correlations are available to calculate the regular pressure drops in these conditions. Therefore, a pure hydrodynamic experiment has been developed to evaluate the validity of the classical correlation in the present experiment. A comparison with the results of the experiment is presented in section 2 of this chapter.

The temperature of the liquid slug is difficult to estimate properly. Indeed, during the experiment, the liquid slug is in contact with the reservoir, the evaporator and the condenser at the same time. Therefore, a temperature gradient certainly exists inside the liquid slug and depending on its location inside the tube. In eq. 5.2, the temperature of the liquid slug is considered as homogeneous to calculate the properties of the liquid (μ and ρ). Both these parameters depending on the temperature, this can lead to an uncertainty on the results of the model.

1.3. Vapour plug

Contrary to the liquid slug, the mass balance of the vapour plug is strongly dependent on the evaporation and condensation phenomena due to the difference of density. The mass balance equation for the vapour is therefore written as:

$$\frac{dm_v}{dt} = \dot{m}_v = (\dot{m}_e - \dot{m}_c) \quad 5.8$$

with \dot{m}_e and \dot{m}_c the flow rates of evaporation and condensation respectively. As it has been shown in chapter 4, the accurate calculation of these flow rates requires the resolution of the transient heat transfer equation in both the tube and the liquid film. The numerical resolution of such a problem will be discussed in the following sections.

Nonetheless, the flow rate of condensation can be simplified, with a reasonable accuracy, using eq. 4.2, developed in chapter 4. The same approach was used in *Das et al. [5.1]*. The flow rate of evaporation is given by the dynamics of the liquid film which is derived in the next section.

The saturation temperature of the vapour is smaller than its temperature since the vapour has been proved experimentally to be superheated. $T_{\text{sat}}(t)$ is a function of the vapour pressure P , which is assumed to be homogeneous inside the vapour plug. Indeed, the frequency of the oscillation is not high enough to create an important pressure gradient inside the vapour plug. The vapour pressure is defined by the equation of state which is assumed to be that of ideal gas:

$$P = \frac{m_v \bar{R} T}{A x} \quad 5.10$$

The calculation of the vapour pressure requires the knowledge of the vapour temperature, which is obtained by writing the energy balance equation for the volume of vapour:

$$\frac{dT}{dt} = \frac{1}{m_v C_{vv}} \left(\dot{m}_v \frac{\bar{R}}{M} T + \Phi_{\text{sens}} - P A u \right) \quad 5.11$$

Where, C_{vv} is the vapour specific heat at constant volume. The sensible heat flux Φ_{sens} is given by:

$$\Phi_{\text{sens}} = h_{\text{sens}} \pi d (L_e - L_{\text{lf}}) (T_e - T) \quad 5.12$$

Where, h_{sens} is the sensible heat transfer coefficient between the tube and the vapour in the part of the evaporator not wetted by the liquid film. Let us assumed that sensible heat is so small compared to latent heat transfer, that it can be neglected as a first assumption.

1.4. Liquid film dynamics

In the model of *Das et al. [5.1]*, the thickness of the film is supposed to be constant while its length L_{lf} varies due to evaporation or rewetting of the liquid slug, when it enters into the evaporator. However, we have seen in chapter 4 that the thickness of the film also increases or decreases in the evaporator and represents an important contribution to the

total evaporation rate. Therefore, the temporal variation of the thickness $\delta(t)$ shall be introduced in the model. The length of the liquid film L_{lf} is defined only in the evaporator section since no evaporation is supposed to occur in the adiabatic section. It is expressed by considering the mass balance equation at the triple line:

$$\frac{dL_{lf}}{dt} = \begin{cases} 0 & \text{if } L_{lf} = 0 \text{ and } u < 0 \\ -\frac{1}{\rho_l \pi d \delta_{lf}(t)} \dot{m}_{e,tl} & \text{if } x > L_e + L_d \\ u - \frac{1}{\rho_l \pi d \delta_{lf}(t)} \dot{m}_{e,tl} & \text{otherwise} \end{cases} \quad 5.13$$

As it has been explained above, the flow rate of evaporation on the triple line $\dot{m}_{e,tl}$ depends on the transient heat transfer equation in both the tube and the wall. In *Das et al. [5.1]*, the same simplified expression as for the condenser was used, introducing a heat transfer coefficient $h_{e,tl}$ at the triple line supposed to be constant:

$$\dot{m}_{e,tl} = \frac{h_{e,tl} \pi d \delta_{lf}}{\Delta \hat{h}_{lv}} (T_e - T_{sat}(P)) \quad 5.14$$

The thickness of the liquid film δ_{lf} can be expressed in the same manner, introducing a heat transfer coefficient $h_{e,lf}$ at the liquid vapour interface of the liquid film, supposed to be constant:

$$\frac{d\delta_{lf}}{dt} = \begin{cases} 0 & \text{if } L_{lf} = 0 \text{ or } \delta_{lf} = 0 \\ -\frac{1}{\rho_l \pi d L_{lf}(t)} \dot{m}_{e,lf} & \text{otherwise} \end{cases} \quad 5.15$$

$$\dot{m}_{e,lf} = \frac{h_{e,lf} \pi d L_{lf}}{\Delta \hat{h}_{lv}} (T_e - T_{sat}(P))$$

δ_{lf} is supposed to be equal to $\delta_{lf,i}$ at the moment the liquid film is deposited on the wall.

1.5. Tube, evaporator and condenser

In the model of *Das et al. [5.1]*, the tube is supposed to be a perfect thermal conductor and the evaporator and the condenser are considered as two perfect heat sources having a constant temperature T_e and T_c . Therefore, the temperature of the tube is supposed to be constant in both the evaporator and the condenser and equal to the temperatures of the heat sources.

In the experiment, the temperatures at the evaporator and at the condenser are controlled by two heat exchangers connected to a thermostatic bath of controlled temperatures T_e and T_c . Therefore, the real boundary condition at the outside periphery of the tube is a Fourier boundary condition between the wall and the heating fluid at temperature T_e or the cooling fluid at temperature T_c . The heat transfer coefficients depend on the cooling or heating fluid properties inside the two heat exchangers as well as the heat exchanger geometry and the velocity of the fluid within it. Inside the tube, the saturation temperature is imposed at the liquid-vapour interface and the liquid film thickness and the temperature of the film are both functions of time. Therefore, the temperature field inside the tube is also a function of time and the transient heat transfer equation has to be solved to take into account both the heat transfer within the tube and the liquid film and the thermal inertia of the system.

A thermal model has been developed in order to evaluate the influence of the nature of the tube and of the heat exchanger on the temperature of the tube and the rate of evaporation. This model does not take into account the triple line, but only the liquid film. It is an extension of the analytical model developed in chapter 4 for the liquid film, which takes into account the tube, the heat exchanger and a variable saturation temperature at the liquid vapour interface of the liquid film.

Fig. 5.3 shows the equivalent electrical representation of the transient thermal model of the system at time j . The tube and the liquid film are discretized in n_{tb} and n_{lf} nodes of temperature $T_{tb,z}^j$ and $T_{lf,z}^j$ respectively and are separated by equivalent thermal

resistances and equivalent thermal capacitors. A perfect contact is assumed between the liquid film and the tube.

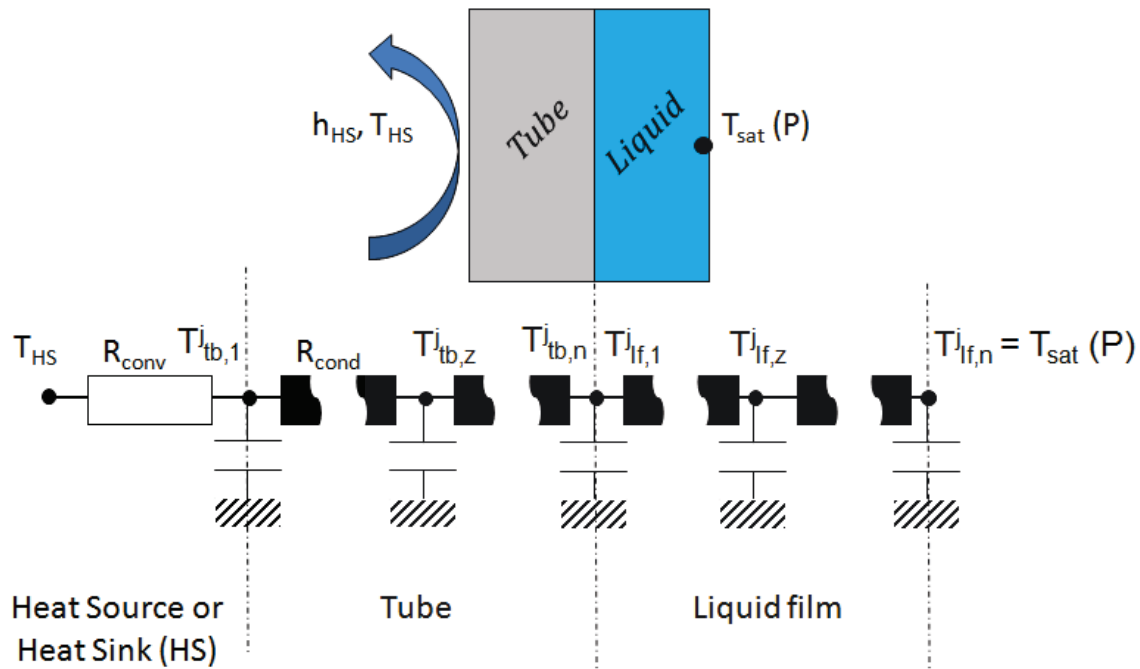


Fig. 5.3: Thermal model of the tube, the evaporator or the condenser.

The conductive thermal resistance (in K.m/W) of the tube is expressed in cylindrical coordinates at node z :

$$\hat{R}_{\text{cond, tb, } z} = \frac{\ln\left(\frac{D_{\text{ext}} - (z-1)\Delta x_{\text{tb}}}{D_{\text{ext}} - z\Delta x_{\text{tb}}}\right)}{2\pi K_{\text{tb}}} \quad 5.16$$

with $\Delta x_{\text{tb}} = \frac{(D_{\text{ext}} - D_{\text{int}})}{n_{\text{tb}} - 1}$

where, D_{int} and D_{ext} are the internal and external diameters of the tube respectively, K_{tb} is the thermal conductivity of the tube and Δx_{tb} the distance between two nodes in the tube. A similar expression is derived for the liquid film.

The thermal capacitance per unit length of the tube C_{tb} (in J/m.K) is expressed as:

$$\begin{aligned}
 C_{tb,z} &= \frac{\rho_{tb} C_{p, tb} \pi \left[\left(D_{ext} - \Delta x_{tb} \left(z - \frac{1}{2} \right) \right)^2 - \left(D_{ext} - \Delta x_{tb} \left(z + \frac{1}{2} \right) \right)^2 \right]}{4} \text{ for } z \neq 1 \text{ and } z \neq n_{tb} \\
 C_{tb,1} &= \frac{\rho_{tb} C_{p, tb} \pi \left[D_{ext}^2 - \left(D_{ext} - \frac{\Delta x_{tb}}{2} \right)^2 \right]}{4} \\
 C_{tb,n} &= \frac{\rho_{tb} C_{p, tb} \pi \left[\left(D_{int} + \frac{\Delta x_{tb}}{2} \right)^2 - D_{int}^2 \right]}{4} + \frac{\rho_{lf} c_{p, lf} \pi \left[D_{int}^2 - \left(D_{int} - \frac{\Delta x_{lf}}{2} \right)^2 \right]}{4}
 \end{aligned} \tag{5.17}$$

where, ρ_{tb} and ρ_l are the density of the tube and the liquid, respectively, $C_{p, tb}$ and $C_{p, lf}$ are the thermal capacity of the tube and the liquid film, respectively. Similar expressions are derived for the liquid film.

At the contact between the heat exchanger and the tube, a convective heat transfer resistance (in K.m/W) is considered:

$$\widehat{R}_{conv} = \frac{1}{h_{HS} \pi D_{ext}} \tag{5.18}$$

where h_{HS} is the convective heat transfer coefficient between the tube and the heat source or the heat sink at temperature $T_{HS} = T_e$ or $T_{HS} = T_c$ respectively. At the liquid vapour interface, a temperature $T_{sat}(P)$ is imposed. The mass flow rate of evaporation or condensation at the liquid-vapour interface \dot{m}_v is calculated as:

$$\dot{m}_v = \frac{1}{h_{lv}} \frac{T_{if, n_{lf}}^j - T_{if, n_{lf}-1}^j}{\widehat{R}_{cond, lf, n_{lf}-1}} \tag{5.19}$$

If \dot{m}_v is negative the liquid film evaporates while if it is positive vapour condensates.

The energy balance equation is written at each node of the system using an explicit scheme. We obtain the following expression for the tube at node z :

$$\frac{T_{tb,z-1}^j - T_{tb,z}^j}{\widehat{R}_{\text{cond,tb,z-1}}} = \frac{T_{tb,z}^j - T_{tb,z+1}^j}{\widehat{R}_{\text{cond,tb,z}}} + C_{\text{tb,z}} \frac{T_{tb,z}^{j+1} - T_{tb,z}^j}{\Delta t} \quad 5.19$$

Where, Δt is the time step between time $j+1$ and time j . Similarly expressions can be derived for the other nodes of the model. We obtain a set of $n_{\text{tb}} + n_{\text{lf}} - 1$ equations with $n_{\text{tb}} + n_{\text{lf}} - 1$ unknowns at each time step.

1.6. Resolution of the equations of the model

Eq. 5.1, 5.2, 5.8, 5.11, 5.13 and 5.15 form a set of six coupled differential equations with six unknowns x , u , L_{lf} , δ_{lf} , m_v and T . These equations are solved using a fourth-order Runge-Kutta method following the same resolution process as in *Das et al. [5.1]*. The heat transfer coefficients $h_{e,\text{tl}}$ and $h_{e,\text{lf}}$ being unknown, they are adjusted to fit with the experimental data. A known initial thickness $\delta_{\text{lf},i}$ (from experimental results obtained in section 1.4.3 of chapter 4) is applied when the meniscus location has reached at top most location inside the evaporator and moves towards the condenser. To begin the resolution, initial conditions are chosen for the six unknowns with value close to the one measured experimentally. Several oscillations are recorded until a stable solution is reached.

The thermal model of the tube and the liquid film at the condenser and the evaporator is solved by considering an a priori initial condition for the entire temperature field in the liquid and in the tube. The heat sink or the heat source temperature is set to T_e or T_c while a constant or a varying saturation temperature is applied at the liquid-vapour interface.

At the evaporator, when the liquid film is totally evaporated, an adiabatic boundary condition is applied at the inner of the tube during a known delay chosen by the user. Then, a new liquid film is deposited on the wall with a known initial thickness $\delta_{\text{lf},i}$ and a temperature equal to T_c . The process is repeated several times until a repeatable solution is obtained.

At the condenser, condensation occurs during a time fixed by the user. Then a constant temperature is applied at the inner of the tube during a known delay chosen by the user corresponding to the presence of the liquid slug inside the condenser. Then, a new liquid film is deposited on the wall with a known initial thickness $\delta_{l,i}$ and a temperature equal to T_c . The process is repeated several times until a repeatable solution is obtained.

The thermal model has been validated by comparison with the analytical model developed in chapter 4, especially for choosing the time step, the spatial step being limited by the maximum acceptable Fourier number for an explicit scheme ($Fo < 0.5$).

A coupling between the thermal model of the tube and the liquid film with the system of differential equations can be considered in the future, but a thermal model of the triple line has to be developed and heat transfer within each section of the tube has to be introduced.

2. Comparison with the experimental data

Let us now compare the results obtained using the model and the experiments to have an idea of the validity of model and also to know the affecting parameters in such single branch PHP system. First we will discuss the single phase pressure drop obtained using model and compare it with the experimental pressure drop measured using experimental setup 2 as described in section 2 of the chapter 3. Later we will discuss the results of thermal model.

2.1. Single phase pressure drop comparison with experiments

As discussed above in section 1.2, a pure hydrodynamic experiment (refer to chapter 3 section 2) has been developed to evaluate the validity of classical correlations for pressure drop calculation in the present experiment. For the sake of comparison the fluids FC72 and Pentane are used at adiabatic conditions (room temperature). The experiments have been performed for 2 frequencies of oscillation (1 Hz and 1.5 Hz) so as to compare to the frequencies obtained in self-sustained thermally-induced oscillation as discussed in chapter 4. The meniscus oscillations recorded during the experiment enable to calculate the temporal variations of liquid slug velocity and its instantaneous

mass. Referring to the eq. 5.2 and then merging it with eq. 5.3-5.7, it is possible to find out the instantaneous differential pressure between reservoir pressure $P_r(t)$ and pressure above the liquid slug in capillary $P(t)$.

The meniscus location and the experimental instantaneous differential pressure drop ($P_r(t) - P(t) + \rho_l g X_r$) are plotted for FC72 (fig 5.4 (a) and (b)) and for Pentane (fig 5.4 (c) and (d)). On the same figure, the theoretical pressure drop including all components for whole tube length L_t is also plotted.

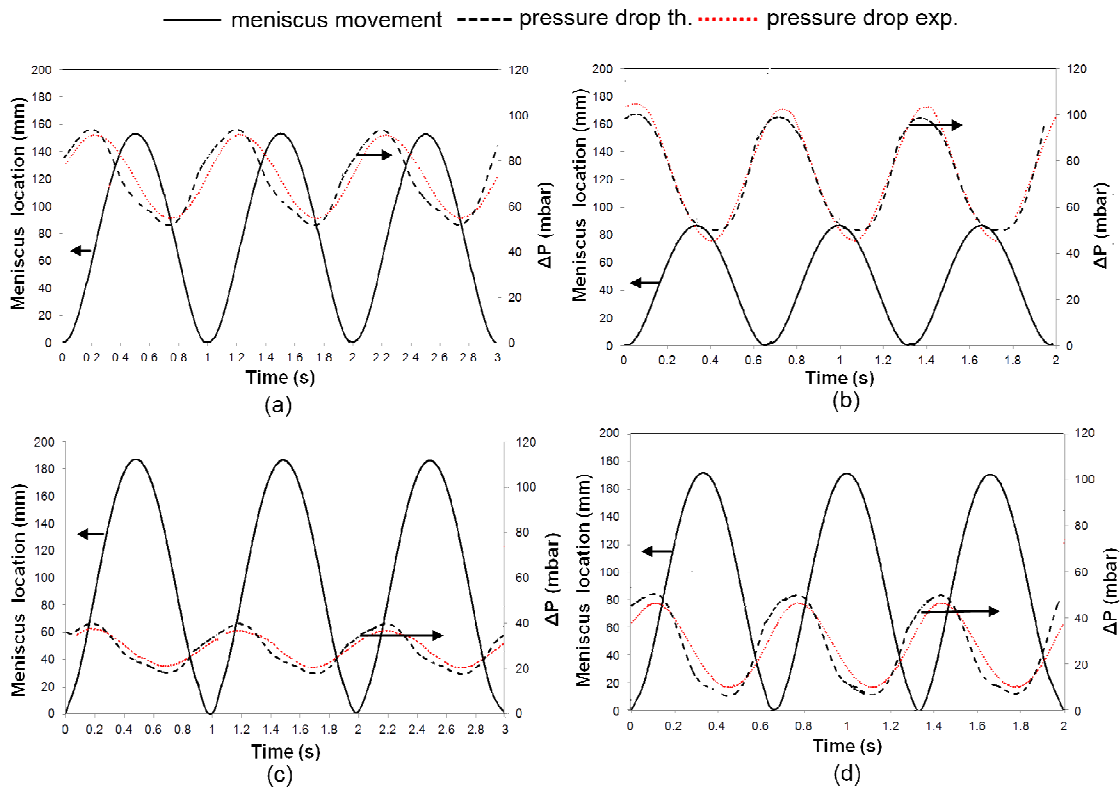


Fig. 5.4: Comparison of temporal variation of analytical and experimental pressure drop for the single phase liquid oscillating inside a capillary tube of 2mm along with the meniscus movement, where (a) for fluid FC72 oscillating at 1 Hz (b) for fluid FC72 oscillating at 1.5 Hz (c) for fluid pentane oscillating at 1 Hz (d) for fluid pentane oscillating at 1.5 Hz (here X-axis represents the location of meniscus in capillary tube, 0 corresponds to the closest location to reservoir during the oscillation).

A good agreement is observed between the theoretical and experimental data, which shows that classical correlations used to calculate pressure drops inside the liquid plug are relevant in the case of an oscillating flow. A closer look in to the results reveal that the pressure drops adds a time delay to on the extremum of the pressure oscillations and slightly increases the amplitude of the pressure variation.

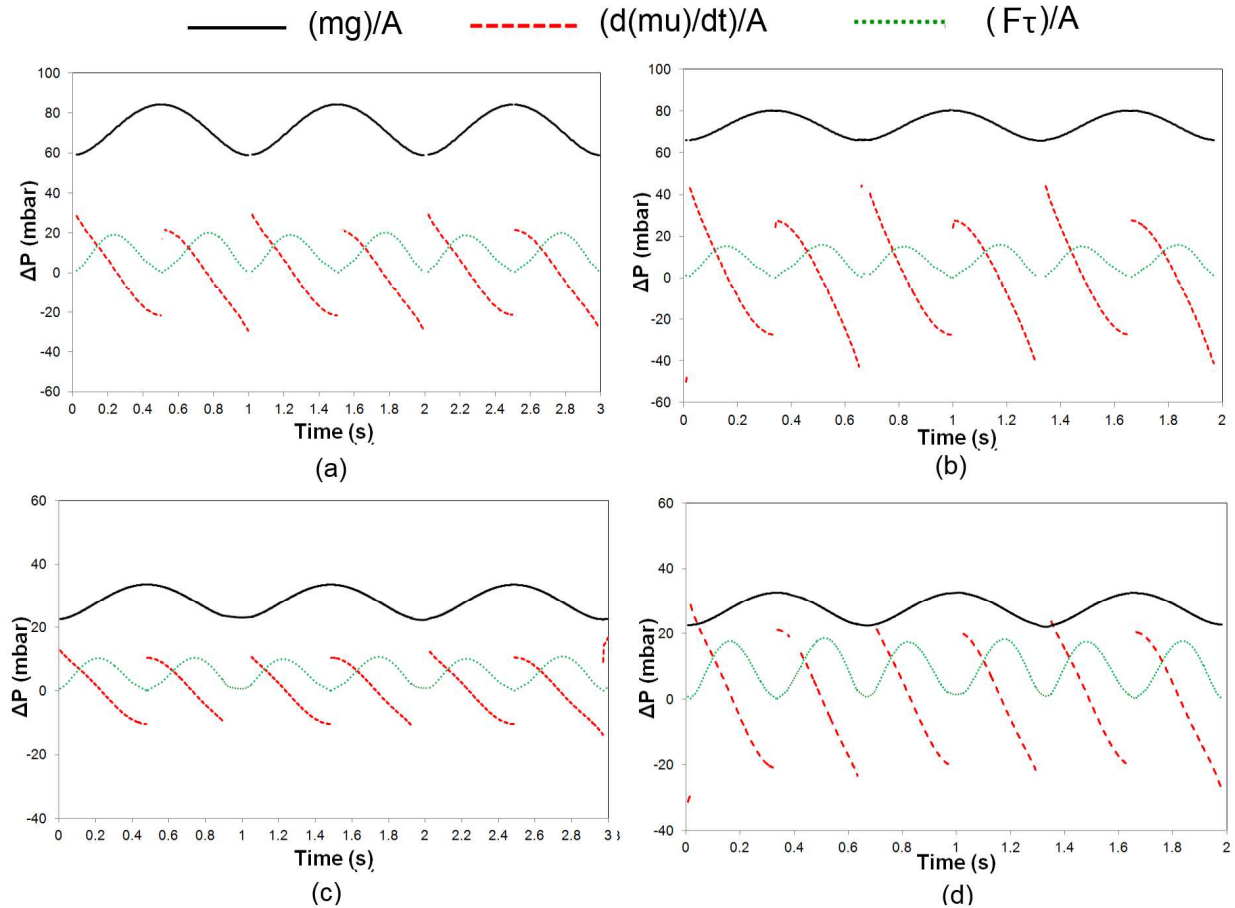


Fig. 5.5: Comparison of three components contributing in theoretical pressure drop across the tube length L_t by dividing them with internal cross sectional area A , (i) Instantaneous momentum of the liquid slug ($d\mu/dt$), (ii) Gravitational term (m_g) and (iii) Shear term (F_τ) for (a) For fluid FC72 oscillating at 1 Hz (b) For fluid FC72 oscillating at 1.5 Hz (c) For fluid pentane oscillating at 1 Hz (d) For fluid pentane oscillating at 1.5 Hz.

We can note that the contribution of capillary pressure component due to the curvature of meniscus ($2\sigma\cos\theta/d$) is negligible as compared to other components. Indeed, let us consider the maximum value of this component for $\cos\theta=1$. For FC72 it is equal to 10 Pa (0.1 mbar) and for Pentane it is 15 Pa (0.15 mbar), which is very less than other components which are in the range of 10 to 100 mbar. As we know from eq. 5.5, F_τ is summation of regular and singular friction forces, we found that in our arrangement (experimental setup 2, as described in section 2 of chapter 3) the singular frictional forces contributes only about 5-10% of total F_τ . This shows that the singular frictional component is not important as compared to the regular frictional component.

Referring to eq. 5.2, the momentum equation of the system is mainly conserved by three components F_p (due to pressure difference across the liquid slug), $m_l g$ (due to the mass of the liquid slug) and F_τ (due to wall shear stress and singularity at the end of capillary inside the reservoir). Let us compare three components contributing in theoretical pressure drop (F_p/A) across the tube length L_t by dividing them with internal cross sectional area A to see their relative contribution in overall pressure drop, (i) Instantaneous momentum of the liquid slug ($(dm/dt)/A$), (ii) Gravitational term ($m_l g/A$) and (iii) Shear term (F_τ/A) for the cases discussed in *fig. 5.4*. This representation gives the idea of the relative influence of these components on the overall pressure drops. *Fig. 5.5* shows the temporal variation of these components for the cases of FC72 (1-1.5 Hz) and Pentane (1-1.5 Hz). By looking at these figures, it is clearly visible that the effect of gravitational force is predominant on other two components. This conclusion may lead to the requirement of performing these experiments in horizontal orientation to increase the accuracy of the measurement.

2.2. Thermal model of the evaporator

In this section, the results obtained with the thermal model developed in section 1.5 for the evaporator are presented with the same geometrical and boundary conditions as in the experimental bench presented in chapter 3 and 4, FC72 being the working fluid. The temperature of the heat source and of the heat sink are equal to 46°C and 20°C respectively, and the saturation temperature is fixed at 35 °C, which corresponds to a mean experimental value with these boundary conditions. The tube is made of

borosilicate glass ($\rho = 2230 \text{ kg/m}^3$; $K = 1.2 \text{ W/m.K}$; $C_p = 830 \text{ J/kg.K}$) and is 2 mm thick with an inner diameter equal to 2 mm. The initial thickness of the liquid film is equal to 70 μm .

Fig. 5.6 shows the effect of the transient heat transfer between the heat source and the liquid film on the inner tube temperature, at the contact with the liquid film. Three different heat transfer coefficients are considered between the heat source and the tube ($h_{HS} = 200 \text{ W/m}^2\text{K}$; $h_{HS} = 600 \text{ W/m}^2\text{K}$ and $h_{HS} = 1000 \text{ W/m}^2\text{K}$). The estimation of the experimental heat transfer coefficient – calculated using a classical correlation of forced convection on a flat plate having a length equal to the length of the evaporator - is close to 200 $\text{W/m}^2\text{K}$. At time $t=0 \text{ s}$, the film is supposed to be deposited by the meniscus on the inner of the tube with a temperature equal to the condenser temperature; at the end of the simulation, it is totally evaporated and a new cycle begins. At the beginning of the cycle (time $t = 0 \text{ s}$), the temperature of the wall decreases brutally due to the presence of the cold liquid film and progressively increases to reach a maximum value varying from 38°C to 39.2°C depending on the value of h_{HS} . For the heat transfer coefficient $h_{HS} = 200 \text{ W/m}^2\text{K}$, the mean temperature of the wall is equal to 37.5 °C, which is much smaller than the temperature of the heat source.

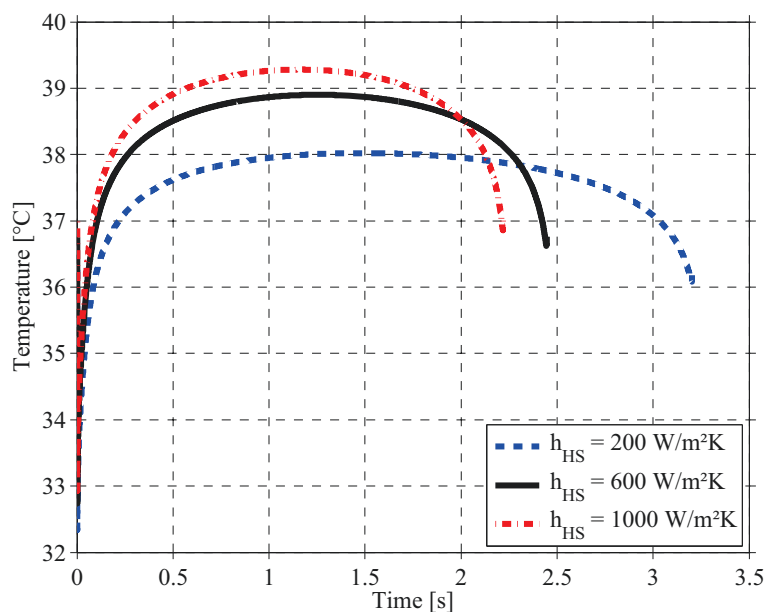


Fig. 5.6: Inner wall temperature of the tube at the contact with the liquid film.

The time required to evaporate the liquid film is equal to 3.2 s, while it lasts about 1.2 s during the experiment. Nonetheless, in the experiments, the film also evaporates at the triple line, which increases the amount of evaporation. Furthermore, one can see that the effect of h_{HS} on the evaporation period is important. Yet, in the condition of the experiment, h_{HS} varies all along the tube. It is higher at the bottom part of the evaporator, close to the adiabatic section than at the top of the evaporator. Indeed, in the experiments, the heating liquid arriving from the thermostatic bath enters into the evaporator heat exchanger perpendicularly to the tube, at the bottom of the evaporator. Therefore, at this location, the heat transfer coefficient is probably much higher than $200 \text{ W/m}^2\cdot\text{K}$. Then, the liquid goes through the heat exchanger in parallel with the tube towards the top of the evaporator and as a consequence, the heat transfer coefficient decreases. Therefore, the liquid film evaporation is more efficient near the adiabatic section than inside the evaporator.

Fig. 5.7 presents the flow rate of evaporation of the liquid film versus time for the three value of h_{HS} . Initially, the liquid film thickness increases due to the condensation of the vapour on the cold liquid as it was already observed in the analytical model developed in chapter 4. Then, the evaporation of the liquid film increases with the increase of the time. This result confirms that liquid film evaporation is not a linear function of time.

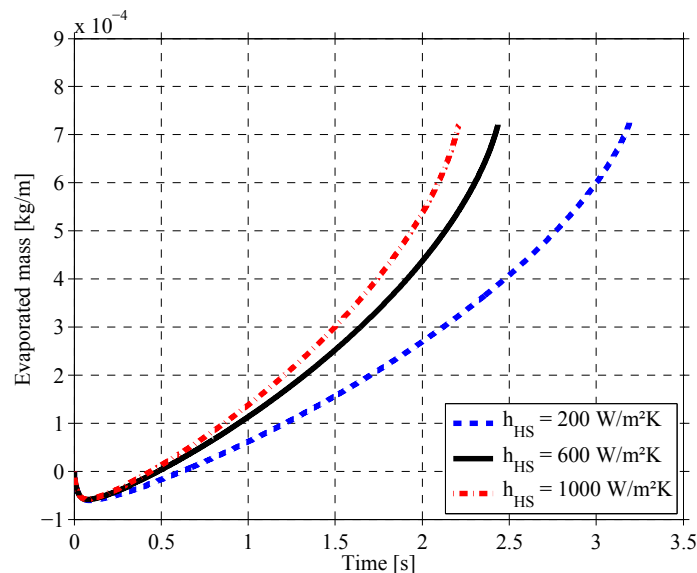


Fig. 5.7: Flow rate of evaporation of the liquid film.

One can conclude from this section that an accurate modeling of the liquid film requires a complete 2D modeling of the thermal system, taking into account the heat transfer between the heating fluid in the evaporator heat exchanger and the tube, and the heat diffusion in the tube and the liquid film. Indeed, both the thermal diffusivity of the tube and the heat transfer coefficient between the heat exchanger and the tube have an influence on the dynamics of the liquid film. In a real PHP, usually made of copper, the thermal diffusivity (and in relation also the effusivity) of the tube would be much higher, leading to a different behavior as it will be explained in section 3 of this chapter.

Anyway, in the next section, the model of the liquid film is simplified using eq. 5.14 to reach some conclusions on the liquid plug, vapour slug and liquid film dynamics. The wall is supposed to be at a constant temperature T_e with a constant heat transfer coefficient between the heat source and the saturation temperature of the vapour.

2.3. Liquid plug, vapour slug and liquid film dynamics

In this section, eq. 5.1, 5.2, 5.8, 5.11, 5.13 and 5.15 are solved and the results compared to the measurements of the vapour pressure, the meniscus oscillation and the liquid film dynamics presented in chapter four. The unknown heat transfer coefficients $h_{e,tl}$ and $h_{e,lf}$ are chosen so that the dynamics of the liquid film thickness and length fits with the experimental data presented in chapter 4. The sensitivity of the model to these parameters is important, as it will be shown in the parametric study.

Fig. 5.8 shows the meniscus location v/s time for different temperatures of the wall: ($T_e = 37.5$ °C, $T_e = 38$ °C, $T_e = 40$ °C and $T_e = 46$ °C), the temperature of the condenser being equal to 16 °C. The fluid is FC72 and the pressure of the reservoir is equal to 0.5 bar. The geometrical parameters are the same as in the experiment. The heat transfer coefficient at the condenser is supposed to be equal to 800 W/m².K, following the same assumption as in chapter 4. One can see that the oscillation pattern obtained by the model is close to that measured experimentally. Depending on the temperature of the evaporator T_e , the frequency of the oscillation and its amplitude are different, both the frequency and the amplitude increasing with the increase of T_e . For a temperature of the evaporator $T_e = 37.5$ °C, the frequency and the amplitude are similar to that observed

experimentally. This temperature is also the mean temperature of the wall calculated with the thermal model, which confirms the conclusions reached with this model.

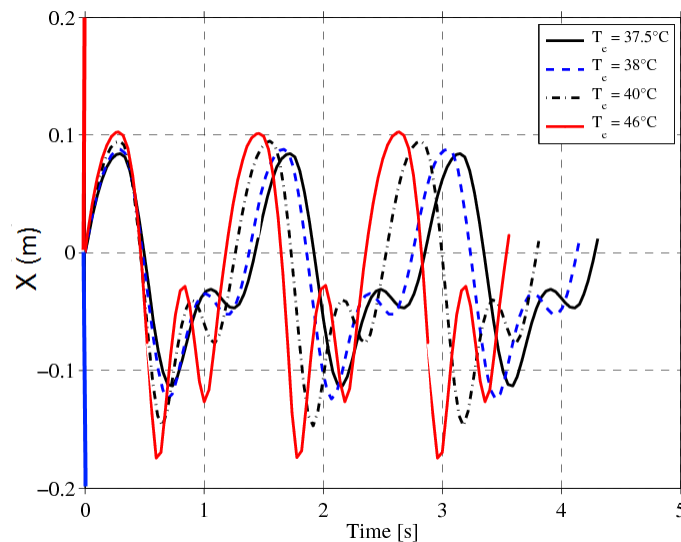


Fig. 5.8: Meniscus movement depending on the evaporator temperature.

Fig. 5.9 shows a comparison of meniscus and triple line dynamics and vapour pressure between the model with $T_e = 37.5^\circ\text{C}$ and the measurements. There is a good agreement between the experimental and numerical results for both the liquid film and oscillation dynamics. The mean vapour pressure on one cycle is similar numerically and experimentally but the time variations are slightly different, which can be explained by the very simple modelling of the dynamics of the liquid film. For example, the numerical vapour pressure increases abruptly as soon as the liquid film is deposited on the wall, while experimentally this growth is smoother. This can be explained by the modelling of the liquid film evaporation. Numerically, evaporation of the liquid film begins as soon as the film is deposited on the wall, while the thermal model shows that there is a delay during which condensation on the film occurs. Therefore, during this delay, evaporation at the triple line is counterbalanced by this condensation phenomenon, which explains why the pressure does not increase so sharply in the experiments.

Note: For the figures (fig.5.8 to 5.13) presented in this section, the location $X = 0$ corresponds to the bottom of the adiabatic section. Locations defined by $X > L_a$ are in the evaporator section (represented by red line on primary Y-axis) while those defined by $X < 0$ are in the condenser section (represented by blue line on primary Y-axis).

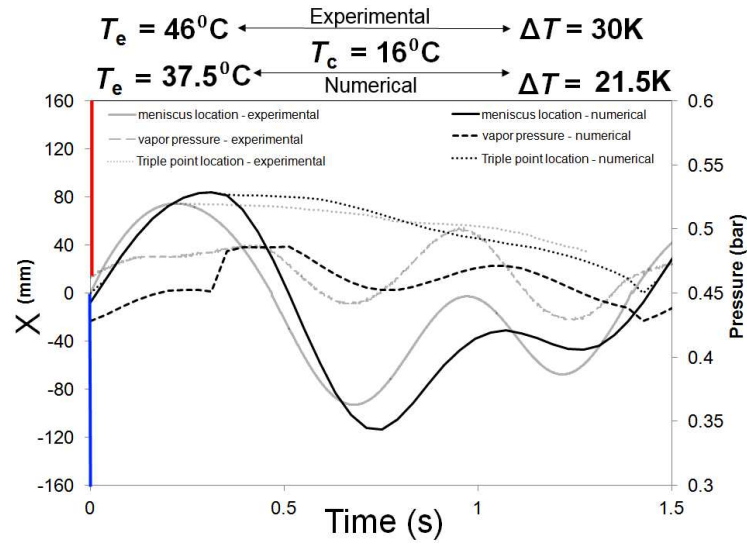


Fig. 5.9: Comparison of meniscus movement, triple line movement and vapour pressure for $T_e = 37.5^\circ\text{C}$ (in thermal model) and $T_e = 46^\circ\text{C}$ (in experiments) for FC72 with $T_c = 16^\circ\text{C}$, $P_r = 0.5$ bar, for similar dimensions as described in chapter 3 experimental setup 1. $h_{e,tl} = 7.348 \times 10^6 \text{ W/m}^2\text{K}$; $h_{e,lf} = 7.273 \times 10^3 \text{ W/m}^2\text{K}$.

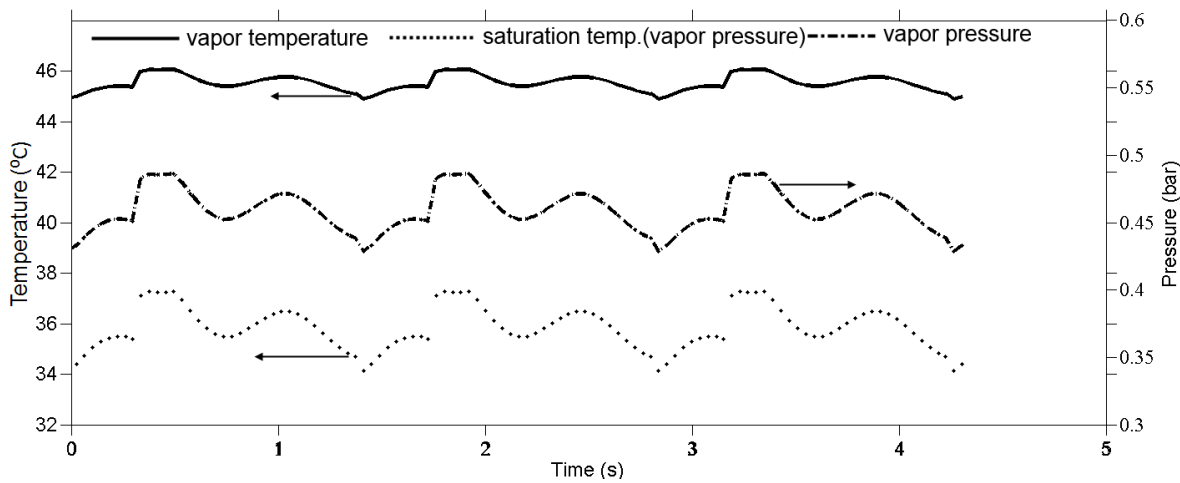


Fig. 5.10: Comparison of vapour temperature and saturation temperature corresponding to the vapour pressure with $T_e = 37.5^\circ\text{C}$, for similar conditions as experimental data presented in fig.4.5-a.

Fig.5.10 presents the vapour temperature, the vapour pressure and its corresponding saturation temperature in the same conditions as in *fig.5.9*. This figure has to be compared to the experimental results presented in *fig.4.5-a*. One can see a good

agreement between the numerical and experimental results. It is clearly visible that the vapour is always in superheated conditions and the hypothesis of using ideal gas equation is within reasonable limits (this holds well as at given P_v , it is very less than the critical point for FC72 and we also have moderate ΔP and ΔT).

Fig. 5.11 to *fig. 5.13* present the temporal variation of the meniscus and triple line dynamics, and vapour pressure for three cases of T_c ($T_c = 16^\circ\text{C}$, $T_c = 20^\circ\text{C}$ and $T_c = 24^\circ\text{C}$) for the sake of comparison with the experimental data presented in *fig. 4.6-a-b-c*. The unknown heat transfer coefficients $h_{e,tl}$ and $h_{e,lf}$ are chosen so that the dynamics of the liquid film thickness and length fit with the experimental data. One can observe the same behavior as in the experimental data: the amplitude of the oscillation in the condenser and the frequency of the oscillation increase with the increase of T_c .

As it was not possible to record the liquid film evaporation in the case of the experimental data of *Fig. 4.6-d*, with $T_c = 28^\circ\text{C}$, it is also not possible to identify the unknown heat transfer coefficients $h_{e,tl}$ and $h_{e,lf}$ using the same procedure. Nonetheless, a parameter study is provided in the next section to show the influence of the heat transfer coefficient on the dynamics of the system.

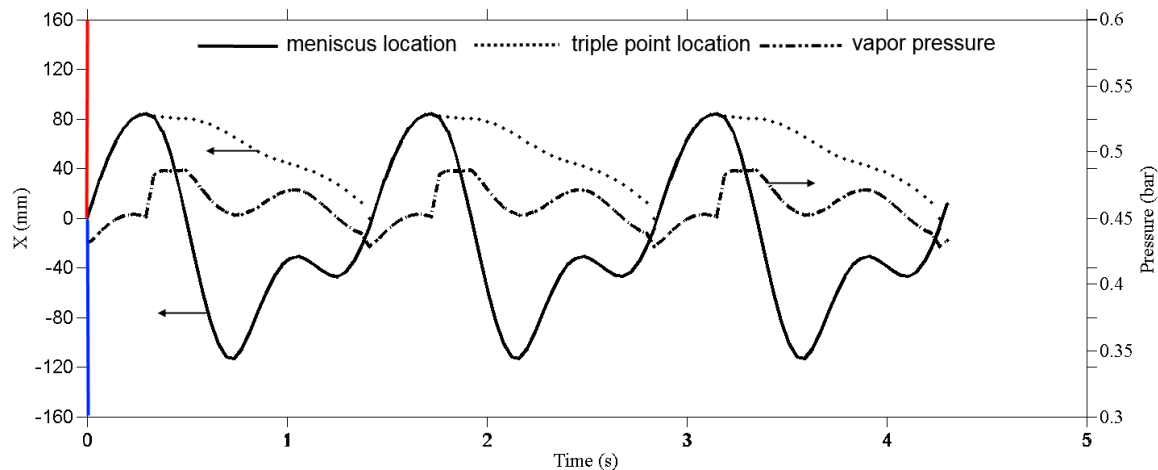


Fig. 5.11: Meniscus movement, triple line movement and vapour pressure with $T_e = 37.5^\circ\text{C}$ and $T_c = 16^\circ\text{C}$, for similar conditions as experimental data presented in *fig.4.6-a*.

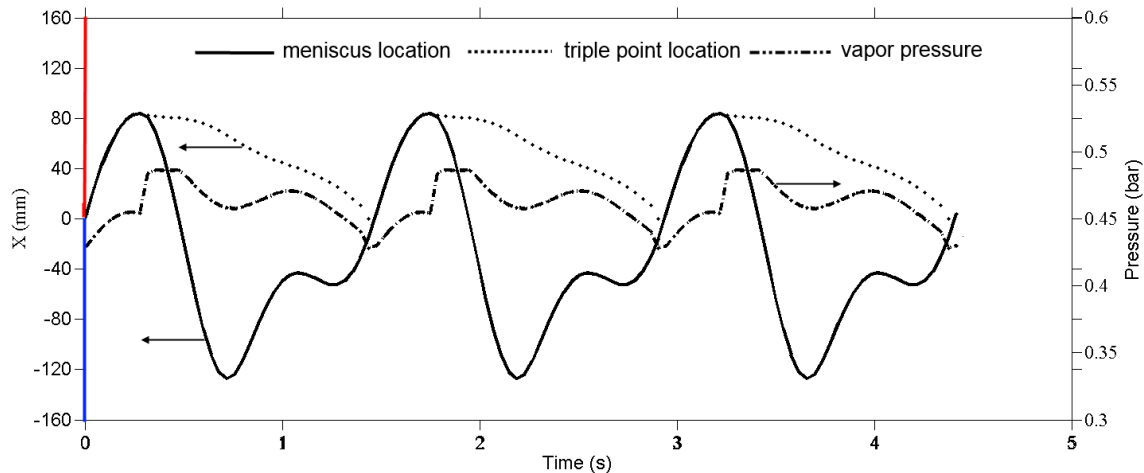


Fig. 5.12: Meniscus movement, triple line movement and vapour pressure with $T_e = 37.5\text{ }^\circ\text{C}$ and $T_c = 20\text{ }^\circ\text{C}$, for similar conditions as experimental data presented in fig.4.6-b.

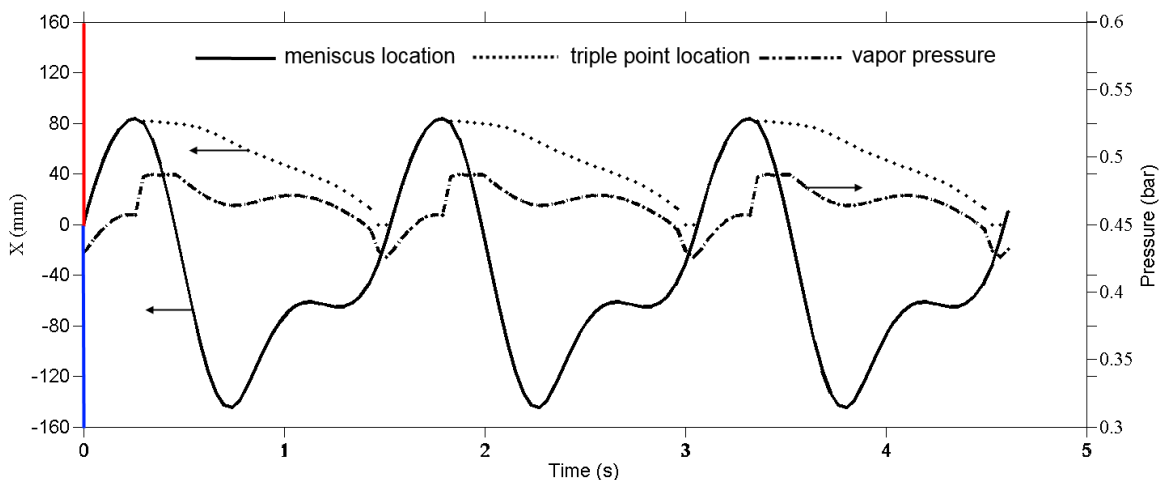


Fig. 5.13: Meniscus movement, triple line movement and vapour pressure with $T_e = 37.5\text{ }^\circ\text{C}$ and $T_c = 24\text{ }^\circ\text{C}$, for similar conditions as experimental data presented in fig.4.6-c.

3. Parameter study

This section presents a parameter study to show the influence of the main parameters on the different models and try to reach some other conclusions on the fundamental mechanisms of Pulsating Heat Pipes.

3.1. Influence of the properties of the fluid and of the tube

The time required to evaporate a liquid film of thickness δ_{lf} depends on the properties of the fluid and can be estimated using an approximation of eq. 5.15:

$$\dot{m}_{e,lf} \cong \frac{m_{e,lf}}{\Delta t} = \frac{\rho_{lf} \pi d L_{lf} \delta_{lf}}{\Delta t} = \frac{h_{e,lf} \pi d L_{lf}}{\Delta \hat{h}_{lv}} (T_e - T_{sat}(P)) \quad 5.20$$

Let us assume that $h_{e,lf}$ is only function of the liquid film thermal conductance (the thermal inertia of the fluid is neglected):

$$h_{e,lf} \cong \frac{K_{lf}}{\frac{\delta_{lf,i}}{2}} = \frac{2K_{lf}}{\delta_{lf,i}} \quad 5.21$$

In this expression, the conductance is calculated by considering a mean value of δ_{lf} which varies from $\delta_{lf} = \delta_{lf,i}$ at time $t = 0$ s to $\delta_{lf} = 0$ when the liquid film vanishes. Introducing eq. 5.21 into eq. 5.20 leads to the following estimation of Δt :

$$\Delta t = \frac{\rho_{lf} \delta_{lf,i}^2 \Delta \hat{h}_{lv}}{2K_{lf} (T_e - T_{sat}(P))} \quad 5.22$$

The thermal properties (K and $\Delta \hat{h}_{lv}$) of FC72 are very poor compared to fluids like water or ethanol. Nevertheless, the comparison of the times required to evaporate both types of fluids shows no major differences since the low value of latent heat of FC72 is counterbalanced by its low thermal conductivity in eq. 5.22. On the contrary, the huge latent heat of water is counterbalanced by its high thermal conductivity. As a result, in the conditions of *fig. 5.6* (with $h_{HS} = 200$ W/m²K and $T_e - T_{sat}(P) = 2.5$ K), $\Delta t = 2.6$ s for FC72 and $\Delta t = 3.3$ s for water (with $T_{sat} = 81^\circ\text{C}$ corresponding to a saturation pressure of 0.5 bar as for FC72).

Using the analytical model developed in chapter 4 (eq. 4.16), the time required to evaporate the liquid film with the same condition and a condenser temperature equal to $T_c = 20 \text{ }^\circ\text{C}$ leads to an evaporation time of 3.05 s for FC72. The difference with the result obtained with eq. 5.22 is due to the thermal inertia of the fluid. For water (with $T_c = 66 \text{ }^\circ\text{C}$), the same model leads to $\Delta t = 3.35 \text{ s}$, which is very close to the result obtained with eq. 5.22. This result is due to the high thermal conductivity of water.

Therefore, this time of evaporation, calculated by considering only the thermal properties of the fluid cannot explain why it was not possible to obtain oscillations with water.

Let us now consider the entire thermal problem and introduce the thermal properties of the tube. *Fig. 5.14* shows the inner temperature of the tube, calculated with the thermal model, the working fluid being water at $T_{\text{sat}} = 81 \text{ }^\circ\text{C}$. For the sake of comparison, let us consider a condenser temperature $T_c = 66 \text{ }^\circ\text{C}$ and an evaporator temperature $T_e = 92 \text{ }^\circ\text{C}$. Therefore, the temperature differences between T_{sat} and T_c and T_{sat} and T_e are similar as the experiment with FC72. The heat transfer coefficient of the heat source has been voluntarily fixed to ($h_{\text{HS}} = 20000 \text{ W/m}^2\text{K}$) so that the results show only the effect of the tube properties since the convective resistance between the tube and the heat source can be considered as negligible. The results show that the time of evaporation is much higher with water than with FC72 (15 s for water and 2 s for FC72) in these conditions. With eq. 5.22, this time of evaporation is obtained for $T_e - T_{\text{sat}}(P) = 0.55 \text{ K}$, which is close to the mean temperature difference observed in *Fig 5.14*. This result is due to both the properties of the fluid and the tube, and can be understood by comparing the thermal effusivity $(K \cdot \rho \cdot C_p)^{1/2}$ of the different materials given in table 5.1.

Table 5.1: Thermal effusivity $(K \cdot \rho \cdot C_p)^{1/2}$ of different substances in $\text{W} \cdot \text{K}^{-1} \cdot \text{m}^{-2} \cdot \text{s}^{1/2}$

Substance	Value
glass	1490
FC72	296
water	1690
pentane	355

By looking at these numerical values, the conclusion is yet to arrive. Water's effusivity tends to impose its temperature to the inner of the tube, which in turn drastically increases the time of evaporation (eq. 5.22). As a result, the dynamics of evaporation is not sufficient to enable the oscillation of the system. On the contrary, for FC72 or even for pentane ($((K.\rho.C_p)^{1/2} = 355 \text{ W}\cdot\text{K}^{-1}\cdot\text{m}^{-2}\cdot\text{s}^{1/2})$), the effusivity of the fluid is small compared to that of glass, which provides a sufficient difference between T_e and $T_{\text{sat}}(P)$ to evaporate with a high flow rate the liquid film and therefore to generate the oscillation of the meniscus.

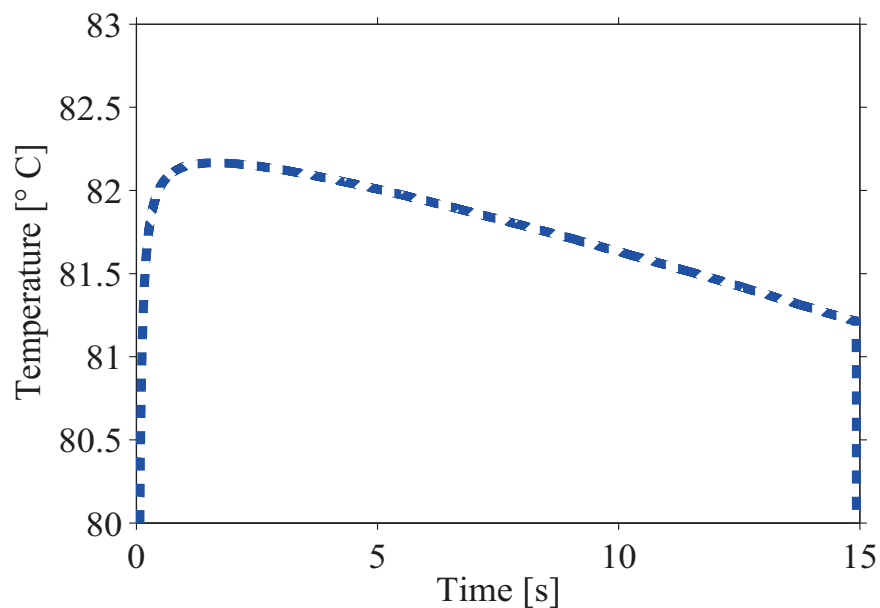


Fig. 5.14: Inner wall temperature of the tube made of glass at the contact with the liquid film for water ($T_{\text{sat}} = 81 \text{ }^\circ\text{C}$; $T_e = 92 \text{ }^\circ\text{C}$; $T_c = 66 \text{ }^\circ\text{C}$; $h_{\text{HS}} = 20000 \text{ W/m}^2\text{K}$).

In most of the applications, Pulsating Heat Pipes are made of copper whose thermal effusivity is always huge ($((K.\rho.C_p)^{1/2} \sim 37000 \text{ W}\cdot\text{K}^{-1}\cdot\text{m}^{-2}\cdot\text{s}^{1/2})$) compared to the fluids. Therefore, the difference between T_e and $T_{\text{sat}}(P)$ is less dependent on the nature of the fluid and we can conclude that the time required for the liquid film evaporation is similar for most of the fluids. As an illustration, *fig. 5.15* shows the same study as *fig. 5.14*, but with a tube made of copper.

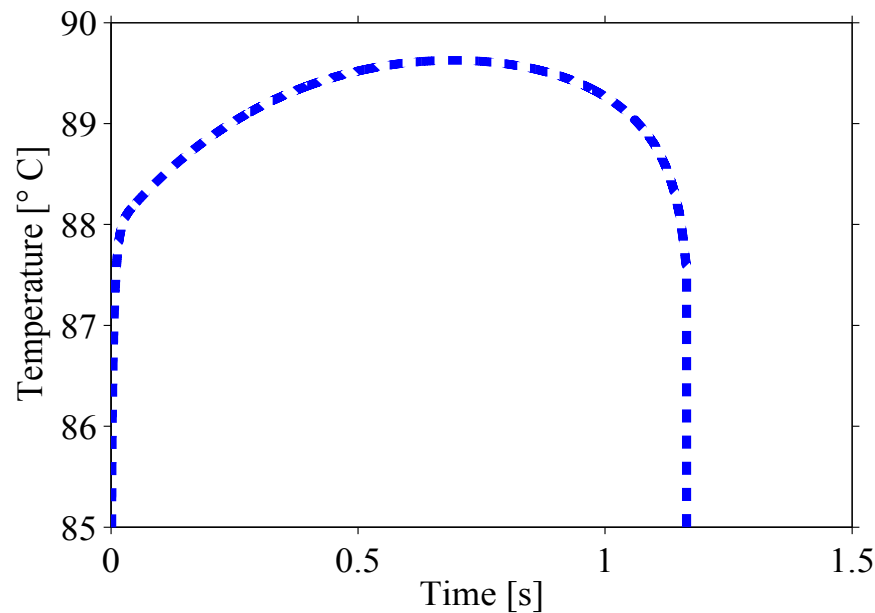


Fig. 5.15: Inner wall temperature of the tube made of copper at the contact with the liquid film for water ($T_{\text{sat}} = 81 \text{ }^\circ\text{C}$; $T_e = 92 \text{ }^\circ\text{C}$; $T_c = 66 \text{ }^\circ\text{C}$; $h_{\text{HS}} = 20000 \text{ W/m}^2\text{K}$).

3.2. Influence of $h_{e,tl}$ and $h_{e,lf}$ and h_c on the dynamics of the system

Fig. 5.16 presents the effect of $h_{e,tl}$ and $h_{e,lf}$ on the dynamics of the meniscus. The conditions are the same as in *fig 5.9* ($T_e = 37.5^\circ\text{C}$; $T_c = 16^\circ\text{C}$; $P_r = 0.5 \text{ bar}$, fluid FC72). The black curve is the meniscus oscillation calculated with heat transfer coefficients ($h_{e,tl} = 8.638 \times 10^6 \text{ W/m}^2\text{K}$; $h_{e,lf} = 3.212 \times 10^3 \text{ W/m}^2\text{K}$) chosen so that the dynamics of the liquid film thickness and length fits with the experimental data presented in chapter 4. The blue and red curves are the meniscus oscillations obtained nullifying $h_{e,lf}$ and $h_{e,tl}$, respectively. Therefore, the effect of each component on the shape of the oscillation can be evaluated. One can see that each phenomenon taken individually leads to an oscillation shape totally different with a frequency two times lower than the black curve. This result shows that the dynamics of the film fully controls the oscillation parameters.

For the triple line, the heat transfer coefficient is huge. It however corresponds to standard values available in the literature (*Stephan and Busse [5.2]*). The heat transfer coefficient for the liquid film is twice the one calculated using the liquid film thermal conductance ($h_{e,lf} \sim 1600 \text{ W/m}^2\text{K}$ with equation 5.21). It has to be noted that it is not possible to fit the experimental data using a smaller heat transfer coefficient for the

liquid film. This result can be explained by the temperature of the wall which is probably underestimated. With a wall temperature $T_e = 38.4$ °C, the same pattern (fig. 5.17) as with $T_e = 37.5$ °C is obtained but the heat transfer coefficients are lower ($h_{e,tl} = 5.579 \times 10^6$ W/m²K; $h_{e,lf} = 1.605 \times 10^3$ W/m²K) and more coherent with the heat transfer model. A higher wall temperature leads to a smaller heat transfer coefficient.

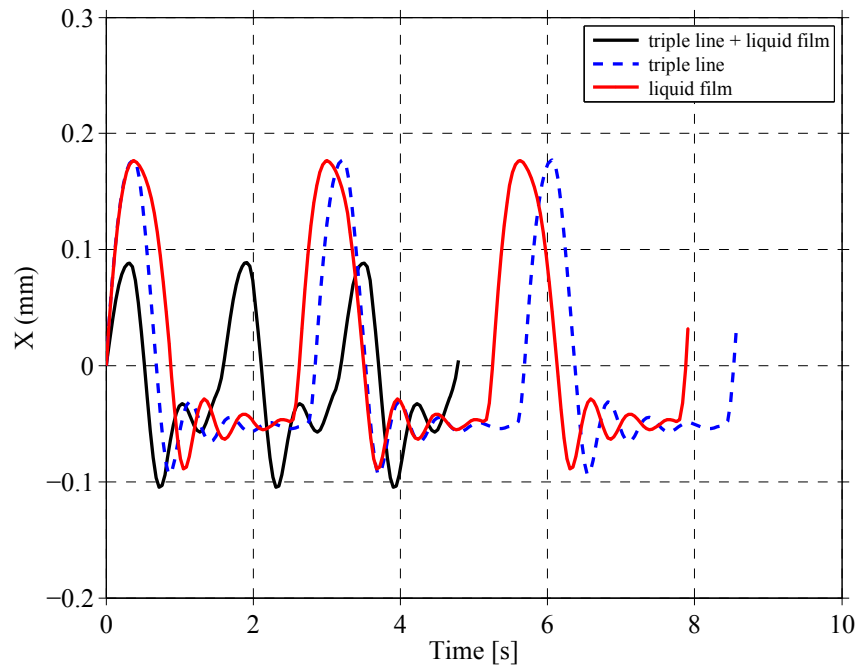


Fig. 5.16: Meniscus dynamic for $T_e = 37.5$ °C and $T_c = 16$ °C; $h_{e,tl} = 8.638 \times 10^6$ W/m²K; $h_{e,lf} = 3.212 \times 10^3$ W/m²K; $h_c = 800$ W/m²K.

Fig. 5.18 shows that it is possible to find another pair of heat transfer coefficients ($h_{e,tl} = 7.348 \times 10^6$ W/m²K; $h_{e,lf} = 7.273 \times 10^3$ W/m²K) that fit with the experimental data. By comparison with fig 5.16, the shape of the oscillation is similar, but the heat transfer at the triple line is lower to compensate for the higher value of the heat transfer coefficient for the liquid film. This result also shows the complexity of the model.

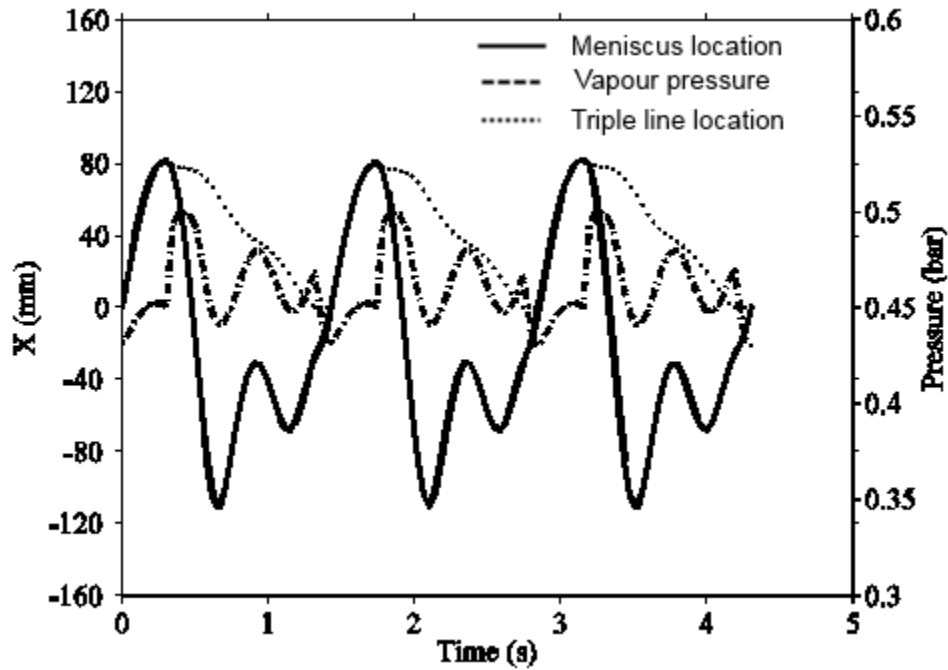


Fig. 5.17: Meniscus movement, triple line movement and vapour pressure with $T_e = 38.4 \text{ }^\circ\text{C}$; $T_c = 16 \text{ }^\circ\text{C}$; $h_{e,tl} = 5.579 \times 10^6 \text{ W/m}^2\text{K}$; $h_{e,lf} = 1.605 \times 10^3 \text{ W/m}^2\text{K}$; $h_c = 800 \text{ W/m}^2\text{K}$.

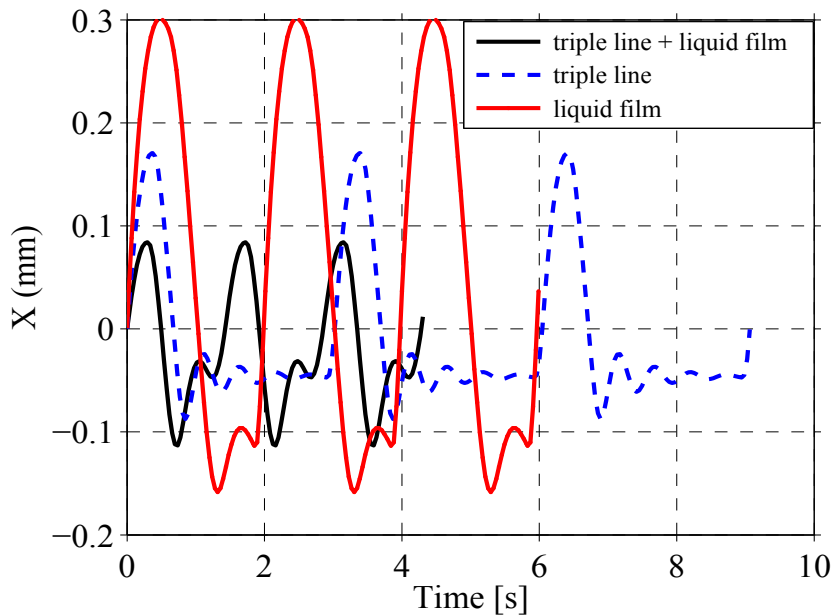


Fig. 5.18: Meniscus dynamic for $T_e = 37.5 \text{ }^\circ\text{C}$ and $T_c = 16 \text{ }^\circ\text{C}$; $h_{e,tl} = 7.348 \times 10^6 \text{ W/m}^2\text{K}$; $h_{e,lf} = 7.273 \times 10^3 \text{ W/m}^2\text{K}$; $h_c = 800 \text{ W/m}^2\text{K}$.

Fig 5.19 shows the effect of the condensation heat transfer coefficient on the oscillation shape. Increasing the condensation heat transfer decreases the frequency and the amplitude of the oscillation inside the condenser and increases the amplitude inside the evaporator.

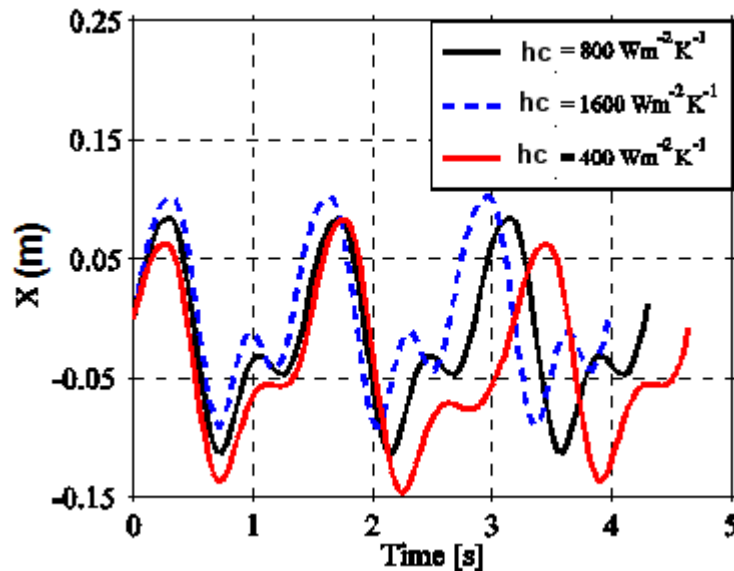


Fig. 5.19: Meniscus dynamic depending on the condensation heat transfer; $T_e = 37.5 \text{ }^\circ\text{C}$, $T_c = 16 \text{ }^\circ\text{C}$; $h_{e,tl} = 7.348 \times 10^6 \text{ W/m}^2\text{K}$; $h_{e,lf} = 7.273 \times 10^3 \text{ W/m}^2\text{K}$.

4. Closing remarks

In this last chapter, numerical simulations have brought some new insights of the fundamental nature on the single branch Pulsating Heat Pipe, especially following:

- The results show that the classical correlations used to calculate pressure drops inside the liquid plug in the model are relevant in the case of an oscillating flow.
- The results confirm that the dynamics of the film is the most important parameter of the system and has to be modeled by taking into account the nature of the liquid but also the nature of the wall. Therefore, the heat transfer equation in the wall has to be solved and coupled to the hydrodynamic behavior of the system.

References

- 5.1. S.P. Das, V.S. Nikolayev, F. Lefèvre, B. Pottier, S. Khandekar, J. Bonjour, Thermally induced two-phase oscillating flow inside a capillary tube, *Int. J. Heat Mass Transfer*, 53 (2010) 3905–3913.
- 5.2. P.C. Stephan, C.A. Busse, Analysis of grooved heat pipes evaporators walls, *Int. J. Heat Mass Transfer*, 35(2) (1992) 383-391.

Chapter 6

Conclusion and future scope

Now it is time to conclude a work that is hoped to be a substantial contribution to the pioneering efforts to develop a literature relevant to single branch PHP. Hence a summary of historical work was presented and the unit-cell of the PHP was looked from a point of extended meniscus theory in general. Das developed the first experimental of such kind which later became the basis of my work. One of the important experimental limitations was addressed; the new experimental setup now fully transparent. Also now the connection between evaporator and the condenser section is smooth so that it does not induce flow perturbations. Furthermore, experiments are done with synchronization of the internal pressure measurements with the videography. The experiments were performed to analyse the behavior of the wetting films, in particular their thickness and length. Das also developed a simplified model based on the balance equations. Some modifications were introduced in this work to take into account the peculiarities of the new experimental set-up and improve the liquid film evaporation model in the light of the experimental results. Parametric study was also carried out to understand the implications of the various factors on the working of such system. Lastly, the pressure drop for single phase oscillating liquid was measured and compared it with which was taken by the model of Das.

1. Conclusions

- The self-sustained thermally-driven oscillations of a single meniscus can be obtained and efficiently sustained inside a capillary tube over long periods of time by maintaining a step thermal gradient over its length. Associated phase-change processes lead to thermo-mechanical instability in the system which generates continuous auto-oscillations of the meniscus. The amplitude of the oscillations not only depends on the temperature difference between the condenser and the evaporator, but also on their absolute temperature levels.

- Oscillations are quasi-periodic in nature for a range of imposed temperature gradients; they become more regular and periodic as this gradient decreases.
- Maximum pressure in the vapour space does not occur when the liquid meniscus is at top of evaporator section; it occurs when the meniscus reaches the adiabatic section in the downward stroke while going from the evaporator to the condenser. During this downward motion of the meniscus, a liquid film is laid down on the tube wall and the very high net evaporation rate of this film contributes to rapid increase of the pressure in the vapour space.
- The two processes of evaporation and condensation of vapour to/from the liquid film and the meniscus respectively, may occur simultaneously during parts of the cycle.
- Net vapour mass flux is determined from the dominant mechanism out of these two. Condensation of vapour mostly occurs on the liquid film inside the condenser section. A small amount of condensation is also observed on the moving meniscus.
- For a given boundary condition, the film thickness and its length at a given time determines the overall dynamics of the meniscus. The results show that evaporation takes place at both, the triple-line and the liquid film interface, the continuation of the former mechanism being somewhat higher than the latter. The amount of vapour generated at the triple-line is significant and equal to more than $1/3$ of the contribution of the liquid film evaporation. At the triple-line, the evaporation rate is nearly constant during one complete cycle while it depends strongly on the location of the meniscus inside the system for the liquid film evaporation.
- The evaporation mass flux experienced in the vapour space is not only due to the heat flow by conduction from the wall to the interface, but also to the thermal non-equilibrium between the vapour and the liquid. If the vapour temperature is greater than the liquid temperature, the net mass flux of evaporation will be lower than conduction-induced evaporation mass flux, as the thermal non-equilibrium leads to condensation. Otherwise, the mass flux is due to both conduction through the film and thermal non-equilibrium.

- The simplified analysis of unsteady heat transfer in the liquid thin film shows the importance of measuring the time-evolution of the temperature of the vapour with a high time-resolution and a good accuracy, which remains a challenge today under such experimental conditions.
- The results show that the classical correlations used to calculate pressure drops inside the liquid plug are relevant in the case of an oscillating flow.
- The results confirm that the dynamic of the film is the most important parameter of the system and has to be modeled by taking into account the nature of the liquid but also the nature of the wall. Therefore, the heat transfer equation in the wall has to be solved and coupled to the hydrodynamic behavior of the system.
- Considering that no comprehensive model of PHP system is available, the conclusions and directions provided in this study are important for building a broad understanding.

2. Future scope

- Evaporator wall temperature measurement needs to be performed to understand the PHP phenomenon critically.
- In this experimental setup the vapour temperature is measured only at one point, it will be interesting to know about the existence of temperature gradient in it.
- Measurement of film thickness experimentally will also verify the thin film dynamics given in this work.
- Parametric study with varying the evaporator, condenser and adiabatic dimension may also give some insight in to the physics.
- Developing a method to dynamically calibrate temperature sensor would give more reliability to results.
- There is also a need to perform experiments in various orientations to see the effect of gravity on working of such PHP systems.
- This setup can be further modified to incorporate two tubes with two bubbles, so that it can reach closer to actual PHPs.

Appendix A

Dimensionless numbers

Dimensionless number	Ratio	Formula
Reynolds number 'Re'	$\frac{\text{Inertia forces}}{\text{Viscous forces}}$	$\frac{\rho U D}{\mu}$
Capillary number 'Ca'	$\frac{\text{Viscous forces}}{\text{Surface tension forces}}$	$\frac{\mu U}{\sigma}$
Bond number 'Bo' or Eötvös 'Eo'	$\frac{\text{Surface tension forces}}{\text{Body forces}}$	$D \sqrt{\frac{(\rho_1 - \rho_g) \cdot g}{\sigma_1}}$
Webber number 'We'	$\frac{\text{Inertia force}}{\text{Surface tension}}$	$\frac{\rho U L}{\sigma}$
Marangoni number 'M'	$\frac{\text{Surface tension forces}}{\text{Viscous forces}}$	$\frac{d\sigma L \Delta t}{dt \alpha \mu}$
Fourier number 'Fo'	$\frac{\text{diffusive transport rate}}{\text{heat storage rate}}$	$\frac{\alpha t}{L^2}$
Poiseuille number 'Po'		$C_f \cdot Re$
Geometries aspect ratio	$\frac{\text{Length}}{\text{Diameter}}$	
	$\frac{\text{Perimeter of shape}}{\text{Perimeter of circle}}$	

When dealing with additional time scales in the system, for example arising due to externally imposed oscillations, Strouhal or Womersley number need to be considered for appropriate scaling. Additional non-dimensional numbers appearing for non-isothermal cases, without phase-change, are Peclet number ($Re \cdot Pr$) and Nusselt number. If the axial conduction in the substrate is important under given boundary conditions, the Biot Number of the wall material also needs to be considered.

The issues become more complicated with phase-change phenomena of evaporation and condensation occurring simultaneously in the Taylor bubble system. Above non-dimensional numbers are shown in below table;

Dimensionless number	Ratio	Formula
Biot number	$\frac{\text{heat transfer resistance in body}}{\text{heat transfer resistance on surface}}$	$\frac{hL}{K}$
Strouhal or Womersley number	$\frac{\text{transient inertia forces}}{\text{viscous forces}}$	$\frac{\omega L}{\nu}$
Prandlt number	$\frac{\text{viscous diffusion rate}}{\text{thermal diffusion rate}}$	$\frac{\mu C_p}{K}$
Peclet number	$\frac{\text{advective transport rate}}{\text{diffusive transport rate}}$	$Re \cdot Pr$
Nusselt number	$\frac{\text{convective heat transfer}}{\text{conductive heat transfer}}$	$\frac{hL}{K}$

Appendix B

Image processing algorithm

```
%%%%%%%%%%%%%%%%%%%%%%%%%%%%%%%%%%%%%%%%%%%%%%%%%%%%%%%%%%%%%%%%%%%%%%%%%
%
%   MATLab program of image processing of meniscus B/W images for oscillations   %
%
%%%%%%%%%%%%%%%%%%%%%%%%%%%%%%%%%%%%%%%%%%%%%%%%%%%%%%%%%%%%%%%%%%%%%%%%%

clear
close all
clc
%emplacement fichiers

fileFolder = fullfile('E:\ ');
dirOutput = dir(fullfile(fileFolder,'*.jpg' ));
fileNames = {dirOutput.name}';

NbrelImages = numel(fileNames);
cd(fileFolder);

Image = imread(fileNames{1});
[NbrePixelY NbrePixelX] = size(Image); %Nbre de pixel en x des images

%%%%%%%% Boucle de traitement des images

Num = 1;

for NumImage = 1 : NbrelImages-500;

    Image1 = imread(fileNames{NumImage});
    Image2 = imread(fileNames{NumImage+3});
```

```

DiffImage = ((Image2-Image1)+(Image1-Image2))*5;
DiffImage = im2bw(DiffImage);
se = strel('diamond',1);
DiffImage = imerode(DiffImage,se);
DiffImage = imdilate(DiffImage,se);
Profile = sum(DiffImage(:,:));
[Max location] = max(Profile);
I2 = sum(Image2(:,:));

```

NumImage

```

if Max > 0 ;
    SaveLocation(Num)=location;
    Savet(Num)=NumImage;
    Num=Num+1;
end

```

```

image(1)
subplot(1,4,1)
imshow(DiffImage)
subplot(1,4,2)
imshow(Image2)
subplot(1,4,3)
plot(Profile)
subplot(1,4,4)
plot(I2)

```

end

```

figure
plot(Savet/1000, SaveLocation)
xlswrite('Name.xls', [Savet' SaveLocation'])

```

Appendix C

Uncertainty Analysis and calibration

C.1 Experimental uncertainty analysis

All the scientific and engineering experimental observations are prone to different types of error. The degree of inaccuracy, also called total measurement error is the difference between measured value and the true value. The total error is the summation of the bias error and precision error. Bias error is the fixed, systematic and constant component of the total error and precision error (also called repeatability error) is the random component of the total error. Experimental data are generally of two types, single sample and multi-sample data. The single sample experiments are those where a single instrument is used to measure a certain property, then some of the error present will be sampled only once, no matter how many times the reading is repeated. However, if several numbers of instruments are used for the same total set of observation, then it called multi-sample experiment. Then the success of the multi sample experiment will be determined by the number of observation made in accordance with applied statistical principle. Due to the financial and time constraint, most of the scientific and engineering observations are of single sample type. Hence a single sample uncertainty analysis proposed by *Kline and McClintock [C.1]*, are applied to data acquired in this work. Considering a general case, where the desired result R of the experiment is a function of X_i and can be represented as:

$$R = R(X_1, X_2, X_3, X_4 \dots X_n) \quad \text{C.1}$$

Where, X_i is the measured variable in the experiment. Then the uncertainty in the results can be expressed with good accuracy in terms of the effects of each individual input by a root-sum-square combination:

$$U_R = \left\{ \sum_{z=1}^{z=n} \left(U_{Xz} \frac{\partial R}{\partial Xz} \right)^2 \right\}^{1/2} \quad \text{C.2}$$

U_{X_i} is the uncertainty of the measured quantity X_i and each term in the above equation represents the contribution in uncertainty in the result by each measured variable. It is assumed that the given relationship in eq. C.1 is continuous and has continuous derivative in the domain of interest, that the measured quantities are independent of one another and the uncertainty in each quantity are independent of each other.

For the vapour mass dynamics, using the eq. 4.1 of chapter 4, the uncertainty ($\Delta m_v(t)$) of vapour mass dynamics can be estimated using eq. C.1;

$$\Delta m_v(t) = \left\{ \left(\frac{\partial m_v(t)}{\partial P_v(t)} \Delta P_v(t) \right)^2 + \left(\frac{\partial m_v(t)}{\partial V_v(t)} \Delta V_v(t) \right)^2 + \left(\frac{\partial m_v(t)}{\partial T_v(t)} \Delta T_v(t) \right)^2 \right\}^{1/2} \quad \text{C.3}$$

Similarly for dynamics of the thin film using eq. 4.5 of chapter 4, the uncertainty of the film thickness ($\Delta \delta(t)$) can be estimated using eq. C.1;

$$\Delta \delta(t) = \left\{ \left(\frac{\partial \delta_v(t)}{\partial L_{e,lf}(t)} \Delta L_{e,lf}(t) \right)^2 + \left(\frac{\partial \delta_v(t)}{\partial (m_v(t) + m_c(t)) m_v(t)} \Delta (m_v(t) + m_c(t)) m_v(t) \right)^2 + \left(\frac{\partial \delta_v(t)}{\partial X_{lf}(t)} \Delta X_{lf}(t) \right)^2 \right\}^{1/2} \quad \text{C.4}$$

C.2 Estimation of uncertainties

While calculating the uncertainty of various experimental measurements, we need to assume that the hypothesis used here (Ideal gas equation) is still valid and all these uncertainties are based upon this. For the estimation of the uncertainties, we have neglected the error occurring due to the change of physical properties of fluids in spite of variation of system temperature. Table C.1 represents the uncertainties and maximum output speed in various quantities.

Table C.1 Uncertainty in the measured variables

S. No.	Measured quantity	Range	Accuracy	Max. reliable reading per second
1	Meniscus location	0-200 mm	±5 mm	1000
2	Film location	0-200 mm	±5 mm	1000
3	Vapour temperature	-200 to 1000 °C	± 0.3 K	Unknown
4	Vapour pressure	0-5 bar	± 0.3 % of FS	5000
5	Differential pressure	0-1 bar	± 0.1 % of FS	1000

While calculating the uncertainty in the mass, the uncertainty due to the meniscus tracking by high speed camera is calculated by the resolution of the image and the limitation of image processing software which could not differentiate the intensity in about 10-15 pixels around the meniscus. This in turn, contributed in uncertainty of vapour volume calculation.

Using eq. C.3, we found that there is uncertainty of ±5% in the calculation of the vapour mass dynamics. Similarly using eq. C.4 the uncertainty in film thickness calculation is believed to be 15%. For the pressure drop calculation there is no other variable involved in estimating it, hence the accuracy of the differential pressure transducer itself depicts the uncertainty in this case.

One more important observation is that all of these calibrations are being performed in static conditions. Two examples of calibration curves are given on [fig. C.1](#) and [fig. C.2](#)

however, in the future, dynamic calibration of these instruments may also differ the results in amplitude as well as phase.

C.3 Calibration curves of measuring devices

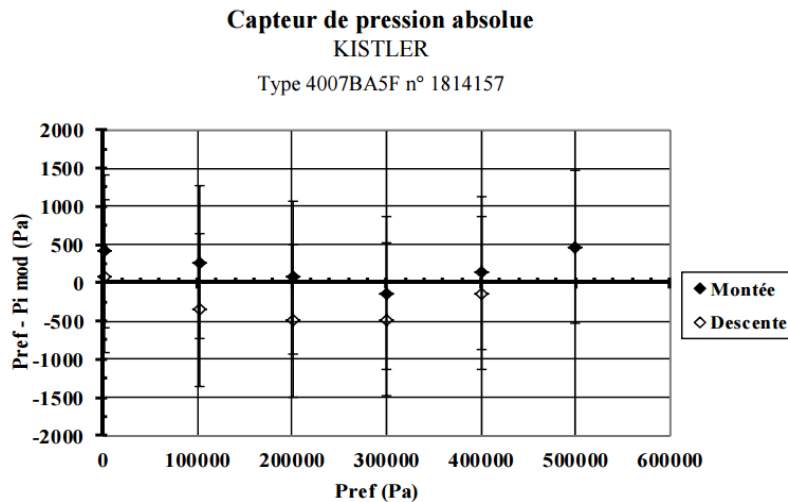


Fig. C.1: Calibration curve absolute pressure transducer

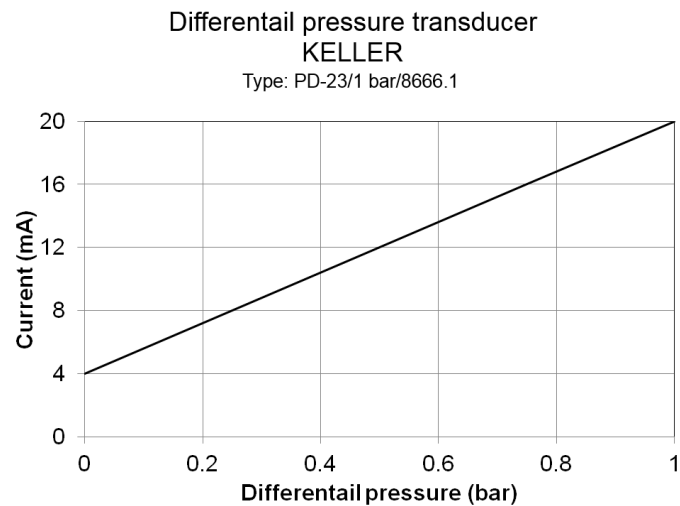


Fig. C.2: Calibration curve differential pressure transducer

References

- C.1 S.J. Kline and F.A. McClintok, Describing uncertainties in single sample experiments, Mech. Engg., (1953) 3-8.

Appendix D

Pentane results

In the following, experimental results are displayed for various operating boundary conditions of Pentane as working fluid using experimental setup 1 as discussed in section 1 of chapter 3. The reservoir is maintained at a constant pressure of 0.5 bar, corresponding to a saturation temperature of 37.2°C. The evaporator temperature T_e is kept constant at 42°C while the condenser temperature T_c is varied from -4 °C to -16 °C. For these condenser temperatures systematic repeatable oscillations of vapour pressure and meniscus movement and thin film movement are observed.

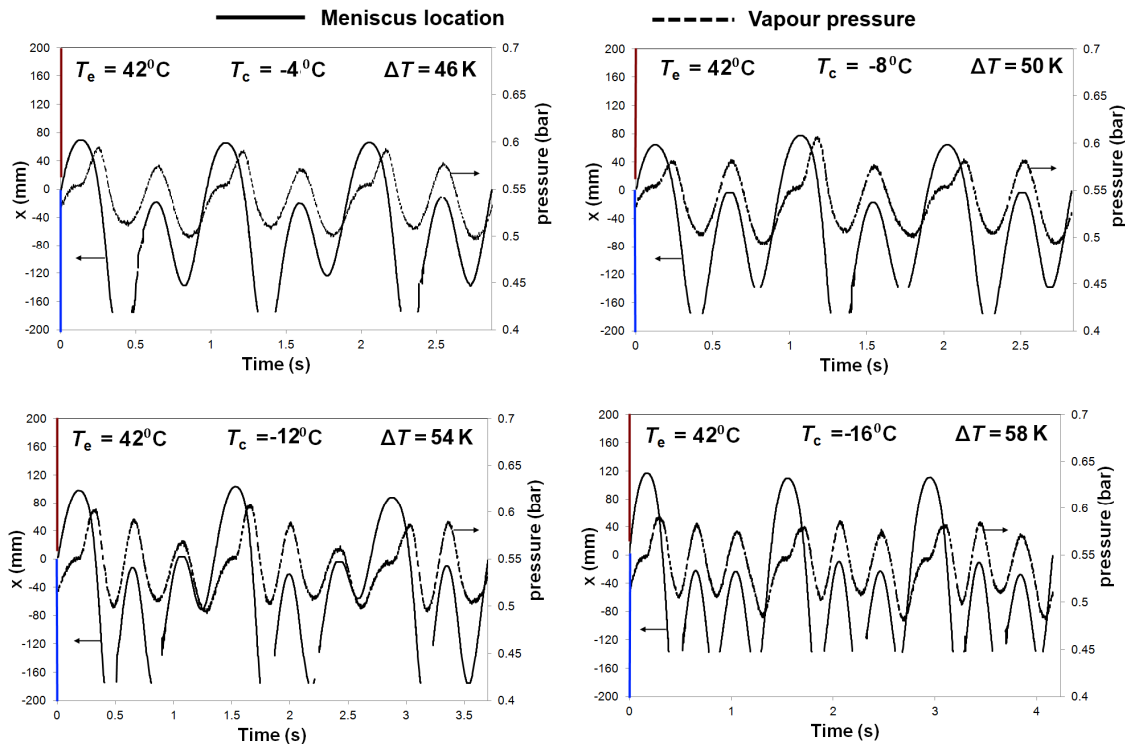


Fig. D.1: Pentane results (meniscus location cannot be tracked completely because it was beyond the range of camera)